

# **Computational Studies of Point Defects in Aluminium Nitride**

*Lei Zhu*

A dissertation submitted  
in partial fulfilment of  
the requirements for the degree of  
**Doctor of Philosophy**

Department of Chemistry  
**University College London**

May 2022

# Declaration

I, Lei Zhu, confirm that the work presented in this thesis is my own. Where information has been derived from other sources, I confirm that this has been indicated in the thesis.

# Abstract

The aim of this work is to investigate intrinsic point defects systematically in the wide band gap semiconductor material aluminium nitride (AlN) by means of computational molecular modelling techniques. Molecular mechanical (force field method) and the embedded cluster hybrid molecular quantum mechanics/molecular mechanics (QM/MM) method are the two key techniques applied in this study. By using GULP (the MM code), new 2-body and 3-body interatomic potentials for AlN are developed. A broad range of physical properties predicted through the two interatomic potentials agree well with experiment data and other theoretical results. The new interatomic potentials are applied to further investigate the lattice stability, physical properties, defect energetics and defect migration barriers of AlN. The work using the molecular mechanical tool lays the foundation of the subsequent QM/MM studies. By using Chemshell (the QM/MM interface), embedded defective AlN clusters in the QM/MM environment are treated with the density functional theory (DFT) methods with the PBE0, B97-2 and BB1K hybrid functionals to obtain the formation energies of native vacancy, interstitial, and anti-site point defects. We find nitrogen vacancy and N split interstitial are the two most favourable defects in both N-rich and N-poor conditions. Relevant diffuse states, thermodynamic concentrations, and ionization transition processes are discussed. Finally, by constructing the configuration-coordinate diagrams, we are able to assign the luminescence and absorption bands to some of defect states. The optical bands from the electron vertical processes of N vacancy and Al vacancy agree well with many previous experiment and theoretical results. The results of other types of defects also bring new insight into resolving the long-term debate around the role of defects in the material.

# Impact Statement

The property of point defects in AlN has been explored frequently in a number of experimental and theoretical studies. Yet, there is still unclear territory in the fields of both the experimental observation and the computational prediction. For the theoretical part, the common periodic boundary condition DFT method has the limitation of the ambiguity of the vacuum level, which results in an incorrect representation of the electron ionization process. The QM/MM embedded cluster method applied throughout this work fixes such problem, so that the electronic transitions can now have a real representation in the calculations. Therefore, the method and the results presented in this work will have a direct impact on all the theoretical point-defect-related electronic studies of AlN, and perhaps other solid-state materials. It can also clear the misunderstanding and inaccurate statements about the role of the point defects established from the experimental observations.

As part of theme of this QM/MM study, a new set of interatomic potential for point defect in AlN has been developed. The agreement with the wide range of experimental results will have direct relevance to the other interatomic potential models that are widely developed for molecular dynamic studies.

The realization of the QM/MM method will also have impact to the developers and the communities of computational chemistry software.

AlN has now regained attention due to the successful application of the deep-UV light emitting diode and the single photon emitter. The optical transition energies predicted in this work will shed some light on and lead to a better understanding of the point-defect-related photoluminance nature of the material, and the design of the application on the atomistic level.

# Acknowledgements

First and foremost, the deepest appreciation must be given to my supervisor Prof. Sir. Richard Catlow, for giving me the chance of stepping into the world of computational chemistry and material science, and for the invaluable guidance and the tremendous support throughout my PhD study.

I would like to extend my sincere thanks to Dr. Alexey Sokols for his extensive guidance throughout every stage of the research, from the numerous discussions about computational chemistry techniques, physics and chemistry theories, and the fun facts about the history of Europe of the past century.

Thanks should also go to Dr. John Buckeridge and Dr. Qing Hou for the helps at many critical moments during the study. Many sections in this thesis would not be completed without your guidance of the methodologies in the QM/MM chapter.

I'd like to recognize the assistance I received from Prof. Scott Woodley, Xingfan Zhang, Dr. Jingcheng Guan, Jamal Abdul Nasir, and Dr. Alex Ganose. It would not be the same without you.

To the past and current colleagues and friends in 349 and 351 KLB offices, such as, Alec, Erze, Woongkyu, Isa and Tonggih, I had a great pleasure of working and exchanging life and study experiences with you.

Finally, a special thanks to my parents, my wife, and my close friends for their unwavering support.

For all the people that I mentioned above, I would like to stress that this journey will not be fulfilled without your mental supports every day.

# Contents

<b>List of Figures</b>	<b>1</b>
<b>List of Tables</b>	<b>7</b>
<b>List of Abbreviations</b>	<b>11</b>
<b>Chapter 1 Introduction</b>	<b>14</b>
<b>Chapter 2 Theory of Material Properties and Defects</b>	<b>16</b>
2.1 Structural properties	16
2.2 Elastic properties	18
2.3 Dielectric properties	20
2.4 Piezoelectric properties	21
2.5 Phonon (lattice dynamics)	22
2.6 Band structure	25
2.7 Ionic bonding and lattice energy	27
2.8 Defects in crystals	30
2.8.1 Types of defects	32
2.8.2 Defect energy levels	34
2.8.3 Charged defects	36
2.8.4 Electronic transitions between charged defects	38
2.8.5 Defect diffusion	39
2.9 Summary	40
<b>Chapter 3 Background on Computational Methods</b>	<b>41</b>
3.1 Molecular mechanics methods	41
3.1.1 Madelung energy and interatomic potentials	42

3.1.2	Shell model and polarization	45
3.1.3	Parameterization	45
3.1.4	Molecular mechanics software	46
3.2	Quantum mechanical methods	47
3.2.1	Hartree-Fock theory	48
3.2.2	Density functional theory	50
3.2.3	Basis sets	54
3.3	Optimization methods	57
3.3.1	Steepest Descent	57
3.3.2	Quasi-Newton Methods	58
3.3.3	Transition state search	59
3.4	QM/MM methods	59
3.4.1	Region Partitioning	60
3.4.2	Energy calculation in Chemshell	63
3.4.3	Geometry optimization in Chemshell	64
3.4.4	Jost correction	65
3.5	Summary	65
	<b>Chapter 4 The MM Model and Defect Energetics of AlN</b>	<b>66</b>
4.1	Background	66
4.2	Methodology	68
4.2.1	Two-body interatomic potential	68
4.2.2	Three-body interatomic potential	73
4.2.3	Mott-Littleton calculations	76
4.3	Defect energetics	77
4.3.1	Defect energies from Mott-Littleton calculations	77
4.3.2	Electron and hole formation	79
4.3.3	Vacancy defect reaction energies	80
4.3.4	Formation of Frenkel and Schottky defects	83
	<b>Chapter 5 Point Defect Migration</b>	<b>85</b>

5.1	Background	85
5.2	Results	86
5.2.1	Vacancy migration	86
5.2.1	Interstitial migration	89
5.3	Summary and conclusion	93
<b>Chapter 6 QM/MM Study of Defects in AlN</b>		<b>94</b>
6.1	Introduction	94
6.2	Computational techniques	96
6.3	Calculation of defect formation energies	99
6.4	Results and discussion	101
6.4.1	Ionization potentials	101
6.4.2	Formation energies of intrinsic defects	104
6.4.3	Diffuse states of intrinsic defects	132
6.4.4	Defect concentrations	138
6.4.5	Defect processes of intrinsic defects	140
6.5	Conclusion	155
<b>Chapter 7 Summary and Conclusions</b>		<b>157</b>
<b>Appendices</b>		<b>161</b>
A.1	GULP input script for physical property prediction	161
A.2	QM/MM basis set	165
A.3	QM/MM ECP	167
<b>Bibliography</b>		<b>168</b>



## List of Figures

<b>Figure 2.1</b> Wurtzite, zinc-blende and rock-salt unit-cell structures of AlN.....	16
<b>Figure 2.2</b> Wurtzite (top) and zinc-blende (below) and ABC stacking. ....	18
<b>Figure 2.3</b> The Brillouin zone of a wurtzite crystal (from <sup>22</sup> ).....	23
<b>Figure 2.4</b> The normal optical modes in wurtzite AlN. ....	24
<b>Figure 2.5</b> Band structure of: (a) metal, (b) insulator and (c) semiconductor	25
<b>Figure 2.6</b> The evolution of band structure from tight-binding band theory....	26
<b>Figure 2.7</b> One-dimension illustration of short-range and long-range interactions on ions. ....	29
<b>Figure 2.8</b> The Born-Haber cycle of AlN formation. ....	30
<b>Figure 2.9</b> Gibbs free energy $\Delta G$ , enthalpy ( $\Delta H$ ) and entropy ( $\Delta S$ ) with respect to defect concentration. ....	31
<b>Figure 2.10</b> 2D representation of basic types of intrinsic point defects. ....	33
<b>Figure 2.11</b> Defect energy level in the band gap: donor level, acceptor level and deep level.....	34
<b>Figure 2.12</b> Fermi levels in semiconductor band structures. ....	36
<b>Figure 2.13</b> Schematic diagram of charged defect. ....	37

---

<b>Figure 2.14</b> A configuration-coordinate diagram according to the Franck–Condon principle.....	39
<b>Figure 2.15</b> 2D diagram of interstitial diffusion and vacancy diffusion.....	40
<b>Figure 3.1</b> The diagram of embedded QM/MM cluster in Chemshell. ....	60
<b>Figure 4.1</b> The calculated phonon dispersion curve (black) using our 2-body interatomic potential model (the red curves indicate the “problematic” part which causes the discrepancies in the off-diagonal elastic constants). The experimental data is also presented for comparison.....	72
<b>Figure 4.2</b> Tetrahedral (T) and octahedral (O) site for interstitial defect in wurtzite AlN (Al is in blue, N is in purple and interstitial site is in pink).....	78
<b>Figure 4.3</b> The N interstitial defect after relaxation. (N1 is the introduced interstitial defect, N2 is the host atom).....	79
<b>Figure 5.1</b> Horizontal and vertical directions of vacancy migration in wurtzite AlN (noted that these arrows are not actual paths, merely an illustration of migration directions).....	86
<b>Figure 5.2</b> The lattice geometry of Al vacancy migration: horizontal migration in (a) & (b); vertical migration in (c) & (d). ....	88
<b>Figure 5.3</b> Atomic visualisation of horizontal Al Interstitial migration (looking through hexagonal channel): (a) initial ground state; (b) transitional state (saddle point) .....	90
<b>Figure 5.4</b> Atomic visualisation of the transition state of N Interstitial defect migration through hexagonal channel: see from z-axis (above); see from x-axis (below).....	90
<b>Figure 5.5</b> Atomic visualisation of the “hand-over” mechanism of N Interstitial defect migration (looking from x-axis): (a) initial state; (b) transitional state (saddle point); (c) final state .....	91

- Figure 6.1** Hole polaron in AlN shown with spin density (yellow isosurfaces of 0.05, 0.01, and 0.0025 a.u.) of an ionised cluster using B97-2 functional in QM/MM method. (N atoms in blue, and Al atoms in red) ..... 103
- Figure 6.2** The defect transition diagram showing formation energies of intrinsic defects in AlN as function of Fermi level in the band gap (functionals used --- top: B97-2; middle: PBE0; bottom: BB1K). The Fermi level starts from the valence band maximum (VBM) on the left of the x-axis and ends at the conduction band minimum (CBM) on the right of the x-axis. The slopes of the lines indicate different charge states of the defect..... 107
- Figure 6.3** Al vacancy in different charge states (-2 to +3). The spin density (yellow isosurfaces of 0.05, 0.025, and 0.01 a.u.), looking from the [011] direction, shows hole(s) localisation..... 108
- Figure 6.4** Spin density of *VA11* – using different functionals (yellow isosurfaces of 0.05, 0.03, and 0.02 a.u.), looking from the [011] direction. The N12 atom has lower share of the spin population as the HF exchange portion in the functional increases. .... 109
- Figure 6.5** Optical energy levels of Al vacancy with respect to band edges (based on vertical ionisation potential with respect to vacuum), calculated using the B97-2 and BB1K hybrid functionals. The vertical red lines indicate electron ionisation processes into the conduction band, and the vertical black lines the hole ionisation in the valence band..... 110
- Figure 6.6** N vacancy in charge states +2 and 0 in AlN. Electron localisation is shown with spin density of (yellow isosurfaces of 0.01, 0.005, and 0.0025 a.u.), looking from the [001] direction..... 113
- Figure 6.7** Optical energy levels of N vacancy with respect to band edges (based on vertical ionisation potential with respect to vacuum), calculated using the B97-2 and BB1K hybrid functionals. .... 115

- Figure 6.8** Optimized geometry of Al interstitial defect at the octahedral site in charge states +3 and +1, looking from [001] and [100] directions. “Al1” label shows the interstitial defect species. .... 117
- Figure 6.9** Spin density of charge state +2 of Al interstitial at the octahedral site (yellow isosurfaces of 0.02, 0.01, and 0.005 a.u.). .... 118
- Figure 6.10** Optical energy levels of Al interstitial with respect to band edges. .... 119
- Figure 6.11** Optimized geometry of N interstitial defect at the octahedral site in the -3 state, looking from [001] and [100] directions. The atom labelled “N1” is the interstitial defect species. .... 121
- Figure 6.12** N interstitial defect at the octahedral site in charge states -2, -1, and 0. Electron localisation is shown with spin density of (yellow isosurfaces of 0.1, 0.05, and 0.025 a.u.). .... 121
- Figure 6.13** Optical energy levels of N interstitial defect at the octahedral site with respect to band edges. .... 122
- Figure 6.14** Optimized geometry of N split interstitial defect site in the charge states of -1, 0, +1, +2, and +3. The split N-N configuration ions are shown in green. The atom labelled “N1” is the interstitial defect species, and “N11” is the bonded N atom from the lattice. .... 124
- Figure 6.15** N split interstitial defect in charge states 0, +1, and +2. Electron localisation is shown with spin density (yellow isosurfaces of 0.1, 0.05, and 0.025 a.u.). .... 124
- Figure 6.16** Optical energy levels of N split interstitial defect with respect to band edges. .... 125
- Figure 6.17** Optimized geometry of N antisite defect in “Configuration A” in the charge states -2, -1, and 0. The spin density is presented for the

defect in charge states -2 and -1 (yellow isosurfaces of 0.1, 0.05, and 0.025 a.u.).	128
<b>Figure 6.18</b> Optimized geometry of N antisite defect in “Configuration B” in charge states +1, +2, and +3. Electron localisation in charge states +1 and +3 is shown with the spin density (yellow isosurfaces of 0.1, 0.05, and 0.025 a.u.).	129
<b>Figure 6.19</b> Optical energy levels of N antisite defect with respect to band edges.	130
<b>Figure 6.20</b> The calculated equilibrium concentrations of charge carriers (electrons and holes) and the intrinsic defects as a function of temperature in N-rich and N-poor condition using B97-2 and BB1K hybrid functionals. The calculated self-consistent Fermi energies in each condition are also presented in black lines.	139
<b>Figure 6.21</b> Configuration-coordinate diagram for <i>Val</i> using BB1K functional. The coloured vertical arrows indicate the optical transitions of visible light. The grey curves are the diffuse states of corresponding compact defect states.	142
<b>Figure 6.22</b> Configuration-coordinate diagram for <i>VN</i> using BB1K functional. The coloured vertical arrows indicate the optical transitions of visible light. The grey curves are the diffuse states of corresponding compact defect states.	144
<b>Figure 6.23</b> Configuration-coordinate diagram for <i>Ali</i> using BB1K functional. The coloured vertical arrows indicate the optical transitions of visible light. The grey curves are the diffuse states of corresponding compact defect states.	146
<b>Figure 6.24</b> Configuration-coordinate diagram for <i>Ni<sub>oct</sub></i> using BB1K functional. The coloured vertical arrows indicate the optical transitions of	

visible light. The grey curves are the diffuse states of corresponding compact defect states.....148

**Figure 6.25** Configuration-coordinate diagram for  $Ni, split$  using BB1K functional. The coloured vertical arrows indicate the optical transitions of visible light. The grey curves are the diffuse states of corresponding compact defect states.....149

**Figure 6.26** Configuration-coordinate diagram for  $NAl, A$  using BB1K functional. The coloured vertical arrows indicate the optical transitions of visible light. The grey curves are the diffuse states of corresponding compact defect states.....151

**Figure 6.27** Configuration-coordinate diagram for  $NAl, B$  using BB1K functional. The coloured vertical arrows indicate the optical transitions of visible light. The grey curves are the diffuse states of corresponding compact defect states.....152

## List of Tables

<b>Table 2.1</b> The structural parameters, angles and fractional coordinates of AlN unit cell.....	17
<b>Table 4.1</b> The 2-body short-range interatomic potential parameters of wurtzite AlN. ....	71
<b>Table 4.2</b> The 2-body and 3-body short-range interatomic potential parameters of wurtzite AlN. ....	74
<b>Table 4.3</b> Calculated and experimental properties of wurtzite AlN. ....	75
<b>Table 4.4</b> Intrinsic defect energies in AlN. ....	77
<b>Table 4.5</b> Electron and hole formation energy in wurtzite AlN. ....	80
<b>Table 4.6</b> Formation energies of Al vacancy ( $Val'''$ ), N vacancy ( $VN \cdots$ ), Al interstitial ( $Ali \cdots$ ), and N interstitial ( $Ni'''$ ) in wurtzite AlN (units in eV). (The calculation results from other studies are obtained approximately from their defect transition energy figures. The “CBM” and “VBM” in the table indicate the location of Fermi level in the bandgap at which the formation energy is calculated.) ....	82
<b>Table 4.7</b> Frenkel and Schottky Defect formation energies, and results from previous studies using interatomic potential methods.....	84
<b>Table 5.1</b> Results of activation energies (eV) of vacancy migrations in AlN and other calculated results on AlN and GaN. ....	87
<b>Table 5.2</b> Results of activation energies (eV) of interstitial point defect migrations in AlN and other calculated results on GaN ....	89
<b>Table 6.1</b> Structural data after geometry optimisation calculated by Chemshell using four different hybrid functionals (PBE0, B97-2, BB1K and HSE03 (with	

---

tuned 33% HF exchange)), compared with MM results, experimental results, and other DFT results. $d$ is the bond length in Å.....	98
<b>Table 6.2</b> Ionisation potentials (eV) calculated using the hybrid QM/MM method, and comparison with other calculated and experimental results. The minus sign in the bracket indicates that the corresponding (ionised) electron levels are below the vacuum level. ....	102
<b>Table 6.3</b> Bond lengths (Å) between the $VAl$ site and the neighbouring N ions in the defect charge states -3, -2, -1, and 0. The last row is for the bond length between the central Al ion and its surrounding N ions without the defect in the cluster. The percentage number in parentheses indicates how much the bond length changes relative to corresponding perfect bond length. ....	111
<b>Table 6.4</b> An overview of the defect energy level (eV) at the $VAl$ defect charge transition position with respect to the VBM. ....	112
<b>Table 6.5</b> Formation energies (eV) of $VAl0$ . Previous calculated values reported in the literature as graphs are directly measured . (*The HSE functional is an HSE06 type ( $\omega = 0.11$ ), with HF exchange fraction of 33%, as implemented in other recent work <sup>106</sup> .).....	112
<b>Table 6.6</b> Bond lengths (Å) between the $VN$ site and the neighbouring Al ions in the defect charge states +3, +2, +1, 0, and -1. The positive percentage number in the parentheses indicates how much the distance is increased relative to corresponding perfect bond length. The minus percentage number indicates how much they contract.....	114
<b>Table 6.7</b> Defect energy levels (eV) of $VN$ with respect to the VBM. ....	116
<b>Table 6.8</b> Formation energies (eV) of $VN0$ .....	116
<b>Table 6.9</b> Off-centre displacements (Å) of $Ali$ in charge states +2, +1, and 0 from the ideal $Ali3$ +position . ....	118
<b>Table 6.10</b> Defect levels (eV) of $Ali$ with respect to the VBM.....	119
<b>Table 6.11</b> Formation energies (eV) of $Ali0$ .....	120



---

<b>Table 6.12</b> Bond lengths (Å) of the N-N dimer struture of the N split interstitial in charge states -2, -1, 0, +1, +2, and +3, calculated by B97-2 and BB1K functionals.....	126
<b>Table 6.13</b> Defect energy levels (eV) of <i>Ni, split</i> and <i>Ni, oct</i> with respect to the VBM. ....	126
<b>Table 6.14</b> Formation energies (eV) of <i>Ni, split0</i> and <i>Ni, oct0</i> . ....	127
<b>Table 6.15</b> Bond lengths (Å) of the N-N dimer struture of the N antisite defect in two different configurations in charge states -2, -1, 0, +1, +2, and +3, calculated by B97-2 and BB1K functionals. ....	130
<b>Table 6.16</b> Defect energy levels (eV) of N antisite with respect to the VBM. ....	131
<b>Table 6.17</b> Formation energies (eV) of N antisite. ....	131
<b>Table 6.18</b> The binding energies (eV) of the diffuse electrons in AlN with respect to CBM. ....	133
<b>Table 6.19</b> The binding energies (eV) of the diffuse holes in AlN with respect to VBM. ....	133
<b>Table 6.20</b> Formation energies (eV) of compact and diffuse states of <i>VAl</i> in AlN. The compact state energies are taken from the defect formation energies at VBM level. The hydrogenic state energies for diffuse electrons and holes are calculated with respect to the corresponding formation energies at VBM. ....	134
<b>Table 6.21</b> Formation energies (eV) of compact and diffuse states of <i>VN</i> in AlN. The compact state energies are taken from the defect formation energies at CBM level. The hydrogenic state energies for diffuse electrons and holes are calculated with respect to the corresponding formation energies at CBM. ....	134
<b>Table 6.22</b> Formation energies (eV) of compact and diffuse states of <i>Ali</i> in AlN. The compact state energies are taken from the defect formation energies at CBM level. The hydrogenic state energies for diffuse electrons and holes are calculated with respect to the corresponding formation energies at CBM. ....	135
<b>Table 6.23</b> Formation energies (eV) of compact and diffuse states of <i>Ni, oct</i> . The compact state energies are taken from the defect formation energies at VBM	

---

level. The hydrogenic state energies for diffuse electrons and holes are calculated with respect to the corresponding formation energies at VBM. .135	
<b>Table 6.24</b> Formation energies (eV) of compact and diffuse states of <i>Ni, split</i> . The compact state energies are taken from the defect formation energies at CBM level. The hydrogenic state energies for diffuse electrons and holes are calculated with respect to the corresponding formation energies at CBM. .136	
<b>Table 6.25</b> Formation energies (eV) of compact and diffuse states of <i>NAl, A</i> . The compact state energies are taken from the defect formation energies at CBM level. The hydrogenic state energies for diffuse electrons and holes are calculated with respect to the corresponding formation energies at CBM. .136	
<b>Table 6.26</b> Formation energies (eV) of compact and diffuse states of <i>NAl, B</i> . The compact state energies are taken from the defect formation energies at CBM level. The hydrogenic state energies for diffuse electrons and holes are calculated with respect to the corresponding formation energies at CBM. .137	
<b>Table 6.27</b> Ionization energies of <i>VAL</i> in all charge states using B97-2 and BB1K functional. The underlined $E_{PL}$ values are the energies falling in the visible light range (1.6-3.1 eV). .143	
<b>Table 6.28</b> Ionization energies of <i>VN</i> in all charge states using B97-2 and BB1K functional. The underlined values are the energies falling in the visible light range (1.6-3.1 eV). .145	
<b>Table 6.29</b> Ionization energies of <i>Ali</i> in all charge states using B97-2 and BB1K functional. The underlined values are the energies falling in the visible light range (1.6-3.1 eV). .147	
<b>Table 6.30</b> Ionization energies of <i>Ni, oct</i> and <i>Ni, split</i> in all charge states using B97-2 and BB1K functional. The underlined values are the energies falling in the visible light range (1.6-3.1 eV). .150	
<b>Table 6.31</b> Ionization energies of <i>NAl, A</i> and <i>NAl, B</i> in all charge states using B97-2 and BB1K functional. The underlined values are the energies falling in the visible light range (1.6-3.1 eV). .153	

## List of Abbreviations

<b>AB</b>	Absorption
<b>AO</b>	Atomic orbital
<b>BFGS</b>	Broyden–Fletcher–Goldfarb–Shanno
<b>CBM</b>	Conduction band minimum
<b>DFT</b>	Density functional theory
<b>DOS</b>	Density of states
<b>DUV</b>	Deep-UV
<b>ECP</b>	Effective core potential
<b>ENDOR</b>	Electron–nuclear double resonance
<b>EPR</b>	Electron paramagnetic resonance
<b>FF</b>	Force field
<b>GGA</b>	Generalised gradient approximation
<b>GTO</b>	Gaussian-type orbitals
<b>GULP</b>	General utility lattice program
<b>HF</b>	Hartree-Fock
<b>IR</b>	Infra-red
<b>L(S)DA</b>	Local (spin) density approximation
<b>LCAO</b>	Linear combination of atomic orbital

<b>LED</b>	Light-emitting diode
<b>LO</b>	Longitudinal optical modes
<b>MM</b>	Molecular mechanical
<b>MO</b>	Molecular orbital
<b>MOCVD</b>	Metalorganic chemical vapor deposition technique
<b>NEA</b>	Negative electron affinity
<b>NEB</b>	Nudged elastic band
<b>NR</b>	Newton-Raphson
<b>PBC</b>	Periodic boundary condition
<b>PES</b>	Potential energy surface
<b>PGTO</b>	Primitive GTO
<b>PL</b>	Photoluminescence
<b>QM</b>	Quantum mechanical
<b>RFO</b>	Rational function optimizer
<b>RHF</b>	Restricted Hartree-Fock
<b>RMS</b>	Root mean square
<b>ROHF</b>	Restricted opens-shell Hartree-Fock
<b>SAW</b>	Surface acoustic wave
<b>SCF</b>	Self-consistent field
<b>SP</b>	Single-point energy and gradient
<b>SPE</b>	Single-photon emitter
<b>STO</b>	Slater-type orbitals

<b>TO</b>	Transverse optical modes
<b>UHF</b>	Unrestricted Hartree-Fock
<b>UV</b>	Ultraviolet
<b>VASP</b>	Vienna Ab initio Simulation Package
<b>VBM</b>	Valence band maximum
<b>XC</b>	Exchange-correlation
<b>ZPL</b>	Zero-phonon line

# Chapter 1

## Introduction

Since the first discovery of aluminium nitride (AlN) in 1862<sup>1,2</sup>, it has taken more than a century for people to finally grasp the true potential of this material. Thanks to the early studies of the physical properties of AlN by Slack and his co-workers<sup>3-6</sup>, many key properties such as the thermal conductivity, thermal expansion, and elastic properties are measured experimentally in high purity AlN crystal. These ground-breaking studies pave the way to the applications such as the heat sink component for electronic devices<sup>7</sup> and surface acoustic wave (SAW) devices made of AlN. Furthermore, AlN is found to have high dielectric and piezoelectric coefficients<sup>8-12</sup>, which makes it a suitable material for high power transistors and energy devices. After Nakamura and his group successfully fabricated the blue-light-emitting diode (LED) using the metalorganic chemical vapor deposition technique (MOCVD) from two other nitride materials of GaN and InGaN<sup>13</sup>, the wide-band-gap semiconductor materials (Al-, Ga-, and InN) and their optical properties instantly become a popular subject for the researchers. It had been previously reported from experiment that, by tuning the Al proportion in the  $\text{Al}_x\text{Ga}_{1-x}\text{N}$  alloy from  $x = 0$  to  $x = 1$ , the bandgap of the material can vary from 3.4 to 6 eV<sup>14</sup>. Such finding makes the AlGaN as one of the most important materials for ultraviolet (UV) and deep-UV (DUV) opto-electronic devices<sup>15</sup>. Recently, with the multi-national wave of the quantum computer development, AlN has gained even more attention due to its very wide bandgap where highly localized, defect-related deep states can be formed to house the qubit spins<sup>16,17</sup>.

The driving force of the latest research and development outcome around AlN is the growing understanding of the role of defects in the material, both experimentally and theoretically. Early work by Slack and McNelly found that defects, which are mostly formed during crystal growth, show a strong correlation with the optical properties of AlN<sup>18</sup>. Over the years, many experiments have been

done to investigate the subject. A good review summarising the latest experimental results of the defect-related optical transitions has been created by Koppe et al.<sup>2</sup> To better understand the physical properties observed from experiment, computational-assisted analysis is now becoming common in both areas of academia and industry. However, there is still a large portion of mismatch between the theoretical prediction and the experimental observation, owing to the inaccurate simulation model used for those predictions. On this topic, we will have a more detailed discussion in **Chapter 4** and **Chapter 6**.

Therefore, the aim for this work is that, by using a wide range of computational methods, we can gain a better understanding of the role of the defects in AlN. By using both classical and quantum mechanical methods, more accurate predictions of the defect formation, defect dynamic, and defect-related electronic structures will be made.

In **Chapter 2**, the physical properties of AlN and the theory of defect will be explained. In **Chapter 3**, the theory of all the computational methods applied in this work will be introduced. In **Chapter 4** and **Chapter 5**, the classical interatomic potential model for the defect calculation will be presented, and the energetics and the migration of the intrinsic point defects in AlN will be investigated by using such models. In **Chapter 6**, we will use the QM/MM embedded cluster method to investigate the formation energies, configurations, electronic structures, equilibrium concentrations, and optical transitions of all the intrinsic point defects in AlN, before summarising the main findings of the thesis.

## Chapter 2

# Theory of Material Properties and Defects

In this chapter, some key properties of AlN are introduced, consisting of two parts: bulk physical properties of AlN and defect properties of the material. These properties of AlN are central to our research, i.e., computational simulation of the material, and will appear repeatedly in the chapters afterwards. Our discussion focuses on the essential features necessary for the work reported in later chapters.

### 2.1 Structural properties

AlN crystal can be formed in three main phases (polymorphs): wurtzite (most stable), zinc-blende (meta-stable) (**Figure 2.1**) and rock-salt (only seen under high pressure). In this work, calculation will mostly be on wurtzite AlN due to its widest applications. AlN in rock-salt phase is not relevant here, so it will not be discussed further.

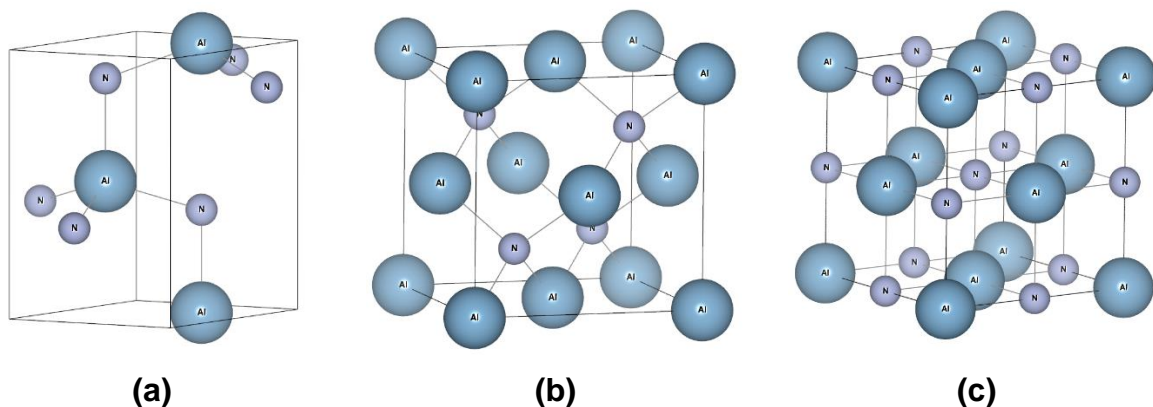


**Figure 2.1** (a) wurtzite, (b) zinc-blende, and (c) rock-salt unit-cell structures of AlN (prepared in VESTA).

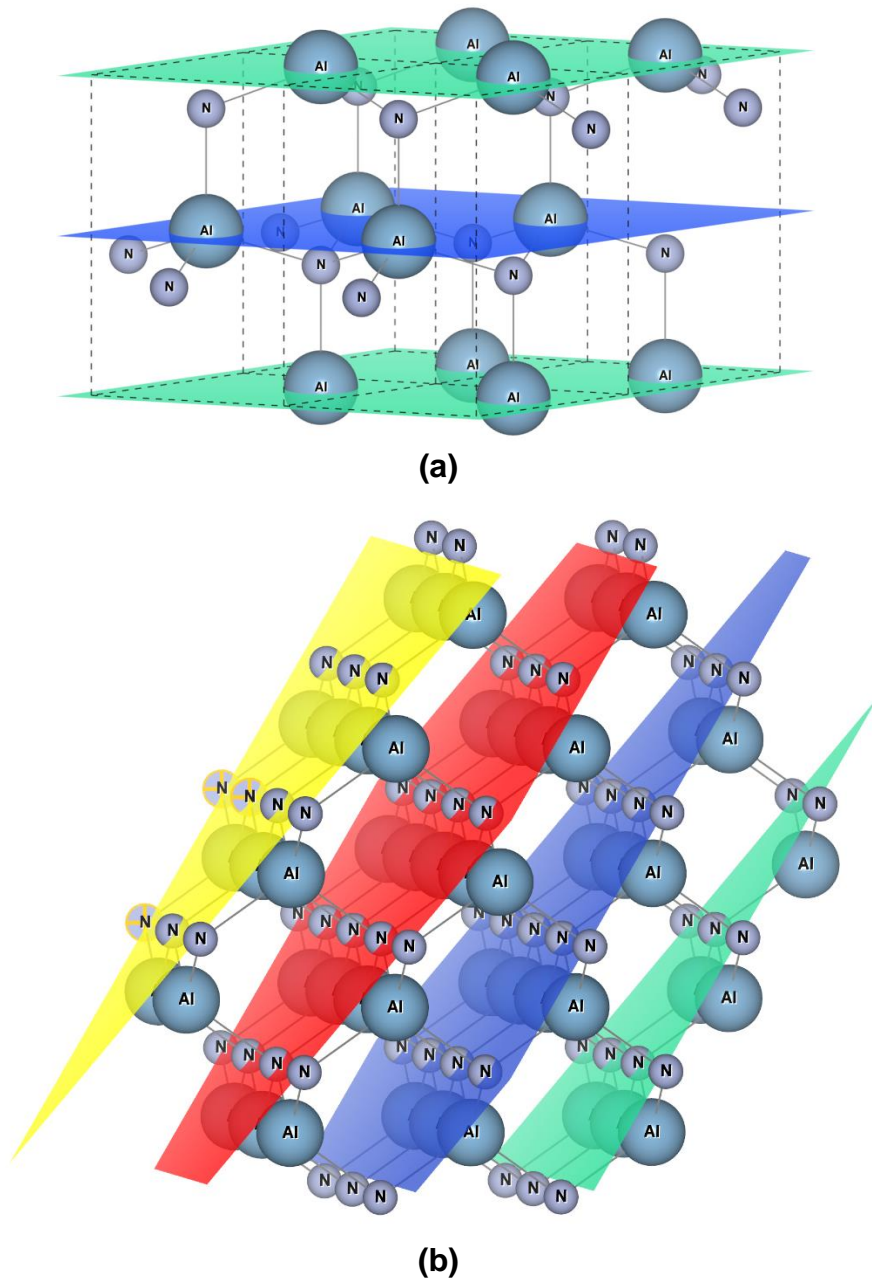


The wurtzite structure has a hexagonal unit cell and space group of  $P6_3mc$  (in Hermann–Mauguin notation), while the zinc-blende structure has a cubic unit cell and space group of  $F\bar{4}3m$ . The structural parameters, angles and fractional coordinates are listed in **Table 2.1**.

**Table 2.1** The structural parameters ( $a$ ,  $b$ , and  $c$ ), angles ( $\alpha$ ,  $\beta$ , and  $\gamma$ ), and fractional coordinates of AlN unit cell.

UNIT CELL LENGTHS	UNIT CELL ANGLES	FRACTIONAL COORDINATES
Wurtzite		
$a = b = 3.11 \text{ \AA}$ ,	$\alpha = \beta = 90^\circ$	Al (2/3, 1/3, 1/2)
$c = 4.97 \text{ \AA}$	$\gamma = 120^\circ$	Al (1/3, 2/3, 0)
		N (1/3, 2/3, $u$ )
		N (2/3, 1/3, $1/2 + u$ )
Zinc-blende		
$a = b = c = 4.37 \text{ \AA}$	$\alpha = \beta = \gamma = 90^\circ$	Al (0, 0, 0)
		N (1/4, 1/4, 1/4)

Another way to look at the difference between wurtzite phase and zinc-blende phase is through close packing models. We can envisage close packed structures in three dimensions, as multiple sheets of atoms stacked together to form a stacking sequence. The hexagonal wurtzite structure forms a repeated stacking sequence of the type “ABABABA...”, while the cubic zinc-blende structure in “ABCABCABCA...” (illustrated in **Figure 2.2**). Both structures have one important feature: voids between atoms. If we envisage the structure being based on close-packed nitrogen ions, these voids provide the space for interstitial defects to be trapped or diffuse in the lattice, which is the starting point for our investigation of point defects and their dynamics (see **Chapter 3 & 4**).



## 2.2 Elastic properties

In solid-state materials, the physical property of elastic strain and stress describes the stiffness of a material under the action of external forces. These properties are essential especially at a nanometre scale level, because the sensitivity of deformation could have enormous influence on a real device. For semiconductor materials like AlN, in device applications, the external force comes from various

sources such as epitaxial fabrication process, lattice mismatch between heterostructure layers, etc. More generally, understanding, and matching elastic data from experiments are always crucial at the initial stage of any computational simulation.

The elastic constant tensor  $C_{ijkl}$  is defined in a generalised form of Hooke's Law (Newton's second law applied):

$$\sigma_{ij} = C_{ijkl} \varepsilon_{kl} \quad . \quad (2.1)$$

The formula shows the relationship of strain ( $\varepsilon_{kl}$ ) is linearly proportional to stress ( $\sigma_{ij}$ ) in a bulk, solid-state material. The subscript “ $ijkl$ ” under each variable implies the direction of stress and strain, where normally in three-dimensional system they are  $x$ ,  $y$  &  $z$ . To simply the formula, we define “ $ij$ ” and “ $kl$ ” to be:

$$1 \equiv xx ; 2 \equiv yy ; 3 \equiv zz ; 4 \equiv yz ; 5 \equiv zx ; 6 \equiv xy \quad .$$

For stress, the first letter  $i$  indicates the direction of force and the second letter  $j$  indicates which axis the plane encountered such force is normal to. The definition of strain tensor is:

$$\varepsilon_{kl} = \frac{1}{2} \left( \frac{\partial u_k}{\partial r_l} + \frac{\partial u_l}{\partial r_k} \right) \quad , \quad (2.2)$$

where  $u_k$  is deformation displacement in  $r_k$  direction.

This makes a total number of elastic constants 81, but it can be reduced to 21 truly independent ones due to the condition of zero total torque (e.g., “ $xy$ ” and “ $yx$ ”) and cancellation of inversed numbered subscript (e.g.,  $C_{12} = C_{21}$ ); and because of the symmetry relationships in certain structures. For the wurtzite structure,  $C_{11}$ ,  $C_{12}$ ,  $C_{13}$ ,  $C_{33}$  and  $C_{44}$  are the only independent terms, whereas for zinc-blende structure, they are  $C_{11}$ ,  $C_{12}$  and  $C_{44}$ .

The relationship between elastic energy ( $U$ ), elastic constant and strain in a bulk, homogeneous, solid-state material with volume  $V$  is formulated as:

$$U = V \int C_{ijkl} \partial \varepsilon_{ij} \partial \varepsilon_{kl} \quad , \quad (2.3)$$

or

$$C_{ijkl} = \frac{1}{V} \left( \frac{\partial^2 U}{\partial \varepsilon_{ij} \partial \varepsilon_{kl}} \right) . \quad (2.4)$$

The formula is used in our molecular mechanical simulation for calculating elastic constants.

### 2.3 Dielectric properties

Understanding dielectric properties is essential as semiconductor materials play a key role in electronic devices. Generally, dielectric properties describe the change of the material's internal electric field (or the polarisation), resulting from external electric field. In the case of an atom or an ion in a crystal structure, the definition of the local electric field ( $E_{loc}$ ) is the sum of contributions of applied electric field, depolarisation field from the surface of the crystal, Lorentz cavity field and electric field within the atom itself. In a cubic system, the electric field within the atom (induced by dipole moment) can be all cancelled out becoming effectively zero, while in hexagonal structure atom's polarisation is considered unneglectable.

The definition of polarisation ( $P$ ) is given as the product of dielectric susceptibility ( $\chi$ ) and local electric field:

$$P = \chi E_{loc} . \quad (2.5)$$

And the dielectric constant is:

$$\epsilon = 1 + \chi . \quad (2.6)$$

However, in general the concept is more complicated, and is given in the form of tensor:

$$P_i = \chi_{ij} E_j^{loc} . \quad (2.7)$$

And therefore, the dielectric constant tensor is:

$$\epsilon_{ij} = \delta_{ij} + \chi_{ij} , \quad (2.8)$$

where  $\delta_{ij}$  is a term called "Kronecker delta" (equals to 0 if  $i \neq j$ , and to 1 if  $i = j$ ).

This formula is the theoretical foundation of the dielectric constant calculation in molecular mechanics. And the tensor expression of dielectric constant is

important to us, as in wurtzite system the dielectric property on  $x$ - $y$  plane should be treated differently from that in the  $z$ -axis.

At a microscopic level, the total polarisation in a solid-state material comprises three main types: the strength and orientation of dipole moments (dipolar polarisation); the displacement of ions (ionic polarisation); the displacement of electrons with respect to nuclei (electronic polarisation). The frequency dependent polarisation results in frequency dependent dielectric constants, among which the static dielectric constant ( $\epsilon_{ij}^0$ ) and high frequency dielectric constants ( $\epsilon_{ij}^\infty$ ) are the two extremes particularly important and are calculated in this work. Especially, the latter high frequency term is closely related to key optical properties.

We will be back on this topic from a computational perspective in **Chapter 3**.

## 2.4 Piezoelectric properties

Piezoelectric effect in AlN is important to us, as AlN in heterojunction structures tends to bear stress or strain over the lattice. Recently, there are reports on AlN-based thin-film biochemical piezoelectric applications such as acoustic sensor<sup>19</sup> and pressure sensor<sup>20</sup>. Combining the formular of elasticity and dielectric in the last two sections, we have the coupled, strain-charge form of the piezoelectric polarisation ( $P$ ) in one-dimension as:

$$P = \sigma d + E\chi , \quad (2.9)$$

or in a converse form (strain  $\epsilon$ )

$$\epsilon = \sigma S + Ee , \quad (2.10)$$

where  $d$  is the piezoelectric strain constant and  $S$  is the elastic compliance constant.  $e$  is the piezoelectric constant which can be transformed from  $d$  mathematically. From these equations, in three-dimension system, the piezoelectric constant and the piezoelectric strain constant can be calculated (in the form of tensor):

$$e_{\alpha i} = \frac{\partial P_\alpha}{\partial \epsilon_i} , \quad (2.11)$$

Or

$$d_{\alpha i} = \frac{\partial P_{\alpha}}{\partial \sigma_i}, \quad (2.12)$$

depending on the direction of interest.

## 2.5 Phonon (lattice dynamics)

Lattice dynamics in solid-state is a massive physical chemical topic crossing over quantum mechanics and classical thermodynamics. The motion of particles at a nanometre level in the system is described by the highly celebrated Heisenberg uncertainty principle, and the energy of such motion can be quantized (multiplied by the  $\hbar$  constant) and packaged in the name of “phonon”. However, as the number of particles increases in solid-state system and the electronic structure gets more complex in larger atoms and molecules, the exact result of the phonon energy is extremely difficult to solve straight from the Schrödinger equation. Therefore, considering the nature of symmetry in the crystal lattice, group theory is introduced to transform the Hamiltonian of individual particle in the system into a symmetrically dependent one so that it can bypass some irrelevant physical difficulties. The hard theory of group theory and quantum mechanics is too big for us to discuss and it is not the aim in this section, so the readers are recommended to check the famous work by Tinkham<sup>21</sup> to get more fundamental knowledge. This section may primarily focus on the part which is relevant to our wurtzite phase system.

The space group of our wurtzite structure is  $C_{6v}^4$  (in the language of group theory, equivalent to the previous “ $P6_3mc$ ” notation). And there are four atoms (two formula) in the unit cell. According to the group theory<sup>21,22</sup>, this yields a total of nine normal phonon modes, in which there are six optical modes and three acoustic modes (analogue to sound waves). By taking the Fourier transform of the “real” Bravais lattice space, the resultant reciprocal space (**Figure 2.3**) is more convenient for the problems related to propagating waves in the periodic lattice system, since one can transform into a finite wavenumber (variable  $k$ ) dependent problem, which is beneficial to the interpretation of how phonons propagate in the lattice. Frequencies of phonons in solid-state system can be

completely described in the primitive cell of the reciprocal space (the 1<sup>st</sup> Brillouin zone), i.e., the phonon dispersion relationship. This relationship can clearly illustrate the optical and acoustic information within the lattice and predicts results from Raman and IR (infra-red) spectroscopy which are two key tools for characterising materials experimentally.

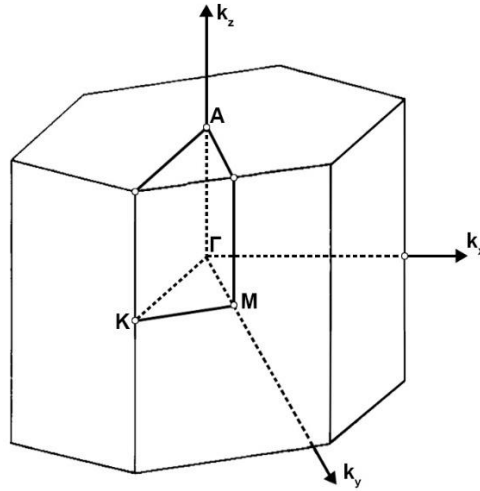


**Figure 2.3** The Brillouin zone of a wurtzite crystal (based on paper<sup>23</sup>).

At the origin of the reciprocal wurtzite lattice (where  $k = 0$ ,  $\Gamma$  point), only the six optical modes have non-zero energy values. These can be represented in an irreducible way<sup>24</sup>:

$$\Gamma_{opt} = A_1 + 2B_1 + E_1 + 2E_2 \quad . \quad (2.13)$$

The letters indicate the vibration modes, and the subscript number indicates the direction of the vibration. As they are all optical modes, the vibrations of atoms are all out-of-phase, as illustrated in **Figure 2.4**. The  $A_1$  and  $E_2$  modes can be detected by Raman and IR spectroscopy (or Raman/IR active), and  $E_2$  modes are Raman active only, and the  $B_1$  modes are inactive to either Raman scattering or IR radiation. These optical modes can be further split into longitudinal (LO) and transverse modes (TO) due to the macroscopic electric field on the system, and the magnitude of such splitting is related to the static and high-frequency dielectric constant from the polarisation in the material.

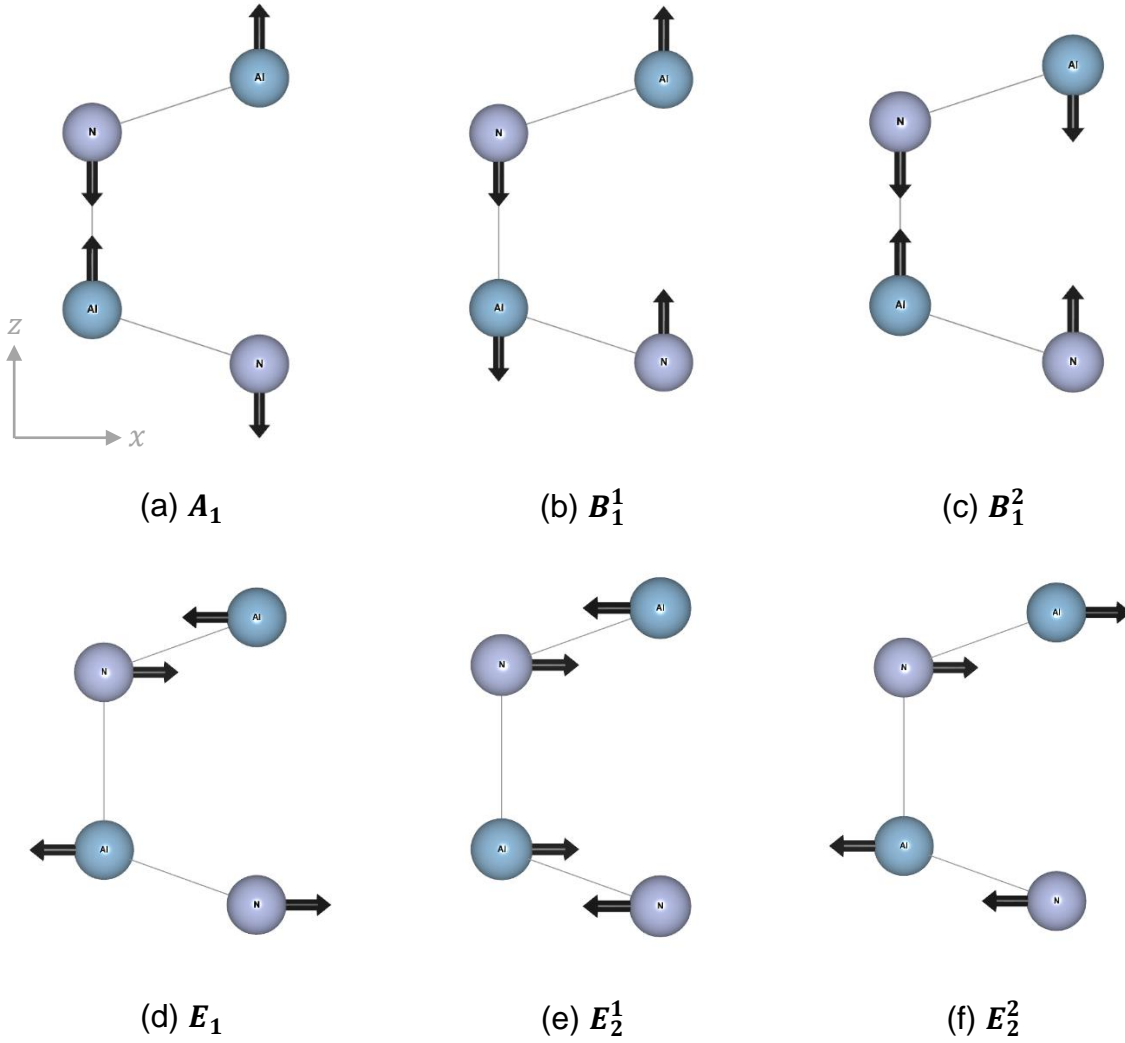


**Figure 2.4** The normal optical modes in wurtzite AlN (prepared in VESTA).

For solid-state systems, assuming the motions between atoms are harmonic around the minimum energy positions, lattice dynamics can be treated using interatomic potential models with the displacements of atoms controlled by Hooke's Law. In calculations, the phonons of the system are calculated via the force constant matrix, which is second derivatives of the energy with respect to the Cartesian coordinates of the atoms' positions. By taking a Fourier transform on the force constant matrix, one can get a dynamical matrix in  $k$  space, which its eigenvalue solution corresponds to the vibrational modes. For the shell model (the model we will be using for molecular mechanical study in **Chapter 3**), as the shell has no mass, the force information of the core-shell and shell-shell interactions is integrated into the force constant matrix before the transformation



of the dynamical matrix. However, such method has a weakness on calculating LO and TO modes at the  $\Gamma$  point because of the lack of electronic information, and the approach is more suitable for calculating average frequency of phonons, unless corrections are made.

## 2.6 Band structure

As we regard AlN as a semiconductor material, we will introduce some key concepts of band theory. The electron configuration of Al atom is comprised of localised core electrons comprising  $1s$ ,  $2s$  and  $2p$  orbitals and outermost delocalised valence electrons comprising  $3s$  and  $3p$  orbitals. The counterpart N atom comprises core  $1s$  orbital and delocalised  $2s$  and  $2p$  orbitals. In a AlN molecule, the  $3s$  atomic orbital in Al atom will form a pair of  $\sigma$  molecular orbitals (MO) with the  $2s$  atomic orbital in N atom, and a pair of  $\pi$  MOs are formed by the  $3p$  in Al and  $2p$  in N. In a single AlN molecule, discrete AOs form discrete MOs. As the number of molecules increases, in the case of the AlN crystal lattice, the number of MOs increases up to a point that the discrete orbitals become continuum of energy states, i.e., energy band. The energy band formed by bonding orbitals is called the valence band which in a non-metal is fully occupied at 0 K, and the energy band formed by anti-bonding orbitals is the conduction band to which electrons can be excited to and move (the electron conduction). This band theory of “squeezing” MOs is known as “tight-binding band theory”, and its theoretical foundation is the linear combination of atomic orbital method (LCAO) of computational chemistry.

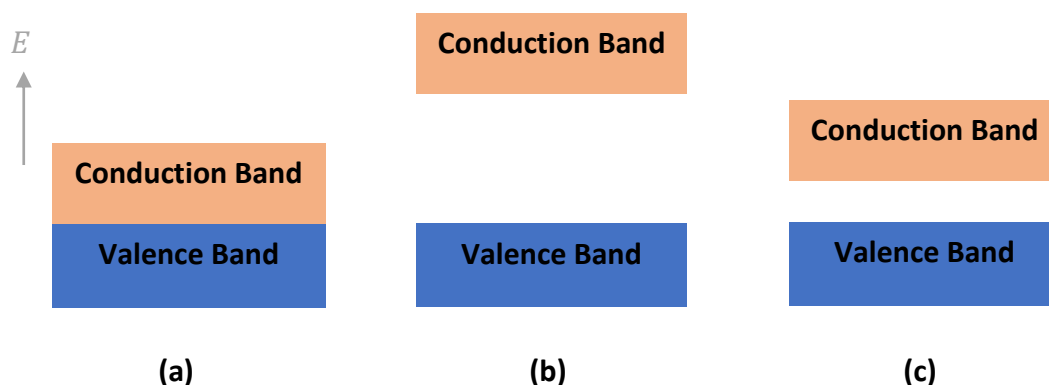


**Figure 2.5** Band structure of: (a) metal, (b) insulator and (c) semiconductor.

The split between valence band and conduction band, energy band gap, is what distinguishes semiconductors from metals (**Figure 2.5**). The energy of band gap is the distance between valence band maximum (VBM) to conduction band minimum (CBM). In typical semiconductor materials like Si and Ge, the band gap energy is  $< 2$  eV, but the band gap energy of AlN (and also for GaN) is higher than this range and therefore termed “wide band gap semiconductor material”. At room temperature, the experimental band gap value for AlN is reported around 6.2 eV<sup>25</sup>. The relatively large value reduces the occupancy of the conduction band resulting in many benefits for practical applications such as high voltage endurance and high heat capacity. And according to the Planck-Einstein relation ( $h$  the Planck constant,  $\nu$  the frequency of photon,  $c$  the speed of light and  $\lambda$  the wavelength of photon),

$$E_g = h\nu = \frac{hc}{\lambda} \quad , \quad (2.14)$$

the luminescence and photon absorption are around the frequency of ultra-violet radiation, which makes AlN a natural candidate to UV-LED devices.

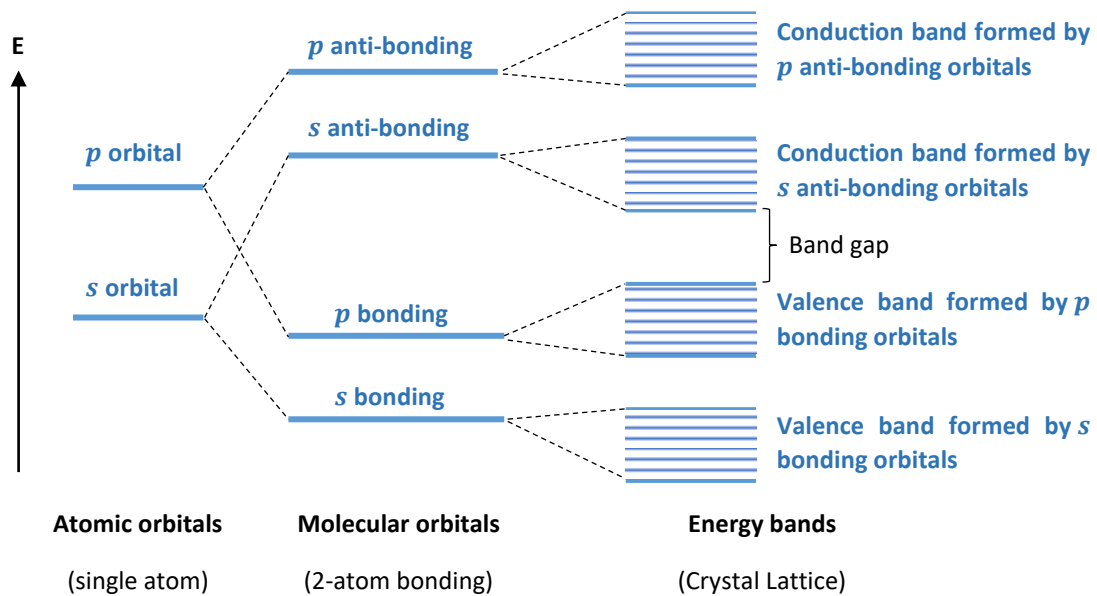


**Figure 2.6** The evolution of band structure from tight-binding band theory

While tight-binding band theory has its origin in computational chemistry, an alternative approach is based on the concept of the “nearly free electron theory.

Starting from the classical “free particle in a box” problem, the electrons are represented by plane waves (Bloch’s Theorem) moving under the influence of periodic potential from the cores in the crystal lattice. The physical origin of band gap in this context comes from the total energy difference between the forward propagating and the reflected electrons at the edge of 1<sup>st</sup> Brillouin zone. The nearly free electron theory provides an accurate density of state (DOS) diagram where the relationship between the energy ( $E$ ) and the momentum ( $k$ ) is presented, providing a complete description of band structure, charge carrier (electron/hole), effective mass, spin density, etc. The approach is more appropriate for metals and narrow gap semiconductors, while tight-binding band theory is more suitable for wide gap semiconductors or insulators. It is still possible to use the tight-binding band theory to plot the accurate DOS diagram and band structure. **Figure 2.6** attempts to link the two approaches to band structure.

## 2.7 Ionic bonding and lattice energy

AlN in this work is modelled as an ionic compound, so our interatomic potentials are based on the interaction between  $\text{Al}^{3+}$  and  $\text{N}^{3-}$  ions interacting via electrostatic and short-range forces, of which the former is the Coulomb interaction:

$$v_{ij} = \frac{q_i q_j}{r_{ij}} \quad , \quad (2.15)$$

where  $v_{ij}$  here is the electrostatic potential from the interaction between ion  $i$  and  $j$ ,  $r$  is the ion distance, and  $q$  is the ion charge. Ions with opposite charge attract each other to be packed as close as possible consistent with their relative sizes; ions with like charges repel. Therefore, an ionic crystal is stably formed at a state when all the attractive forces can counter-balance with all the repulsive forces.

The sum of all the electrostatic energy in the ionic crystal is denoted the Madelung energy, but such summation over all the ions in an infinite 3-D crystal lattice is difficult. To simplify the problem, if one takes a single ion in an infinite crystal lattice as central reference point and calculate the sum of electrostatic potential energy acting on it, the resultant energy can become:

$$V_i = \sum_{j \neq i} v_{ij} = \frac{q_i}{r_0} M_i \quad , \quad (2.16)$$

where  $M_i$  is the Madelung constant, which is solely determined by the crystal structure (or the coordination number), and  $r_0$  is the nearest neighbour distance. Electrostatic summations are, however, conditionally convergent – a problem that is generally solved by a partial transformation onto reciprocal space known as the Ewald summation to which we return with more detail in **Chapter 3**.

While the electrostatic forces are still the main contribution to the cohesion of the crystal, we must consider the non-bonded interactions. The Born repulsive force is often modelled in the form of an exponential function (particularly in the case of solid-state system) and the energy of interactions between one ion pair now becomes:

$$v_{ij} = \frac{q_i q_j}{r_{ij}} + B \exp\left(\frac{-r_{ij}}{\rho}\right) \quad . \quad (2.17)$$

The  $B$  and  $\rho$  in the Born model are both normally empirical parameters. Apart from these two interactions, there are other contributions such as van der Waals attractive force (from dipole-induced dipole interaction) which are described by an  $r^{-6}$  term (with an empirical constant  $C_6$ ) giving rise to the widely used “Buckingham potential” (more detail in **Chapter 3**):

$$V_{\text{Buckingham}} = B \exp\left(\frac{-r_{ij}}{\rho}\right) - \frac{C_6}{r^6} \quad . \quad (2.18)$$

Therefore, the lattice energy (**Figure 2.7**) can be defined as the sum of all the long-range interactions (electrostatic) and all the short-range interactions ( $\varphi(r_{ij})$ ):

$$U = \sum_{i,j} v_{ij} = \sum_{i,j} \left( \frac{q_i q_j}{r_{ij}} + \varphi(r_{ij}) \right) \quad . \quad (2.19)$$

In practice, the short-range interaction could take other forms to predict the most precise results, which will be discussed in **Chapter 3**.

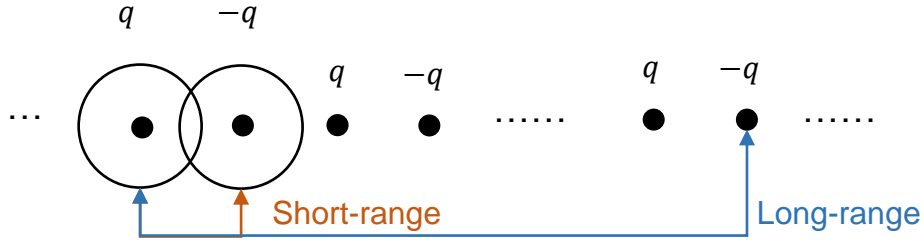


**Figure 2.7** One-dimension illustration of short-range and long-range interactions on ions.

The Lattice energy is equivalent to the energy needed for the hypothetical process of separating the crystal into individual ions at infinity, and therefore, lattice energy is a theoretical concept rather than an experimental observable. However, the lattice energy can be evaluated via a thermo-chemical Born-Haber cycle. For example, the reaction of AlN formation can be written as:



where  $\Delta H_f$  is the enthalpy of formation. From solid metal aluminium atom and nitrogen gas molecule to the final product of AlN, the reaction can be further divided presented in **Figure 2.8**.

According to Hess's law, the energies of these sub-reactions can be written as:

$$\Delta H_{f/AlN} = H_{S/Al} + \sum_1^3 IE_{Al} + \frac{1}{2}E_{D/N} + \sum_1^3 EA_N + U_{lattice} \quad , \quad (2.21)$$

where

- $H_{S/Al}$ : enthalpy of sublimation for metal aluminium;
- $IE_{Al}$ : ionization energy of one electron in aluminium atom;
- $E_{D/N}$ : dissociation energy for nitrogen gas molecule;
- $EA_N$ : electron affinity of one electron in nitrogen atom;
- $U_{lattice}$ : lattice energy.

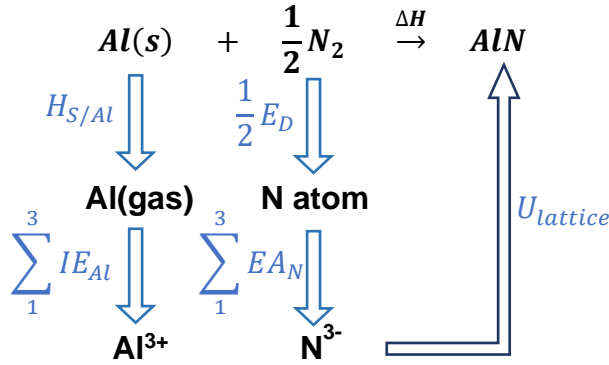


**Figure 2.8** The Born-Haber cycle of AlN formation.

The sign before each item in this equation may vary depending on the definition of individual energy term. Normally, lattice energy can be calculated readily using current modelling software allowing predictions of the chemistry and hence stability of compounds.

However, in the case of AlN, the sum of electron affinities of three outer electron in nitrogen atom ( $\sum_1^3 EA_{\text{N}}$ ), is not available. Experimental data are only available for the 1<sup>st</sup> electron affinity as both the doubly and triply charged species are unstable as isolated ions. The Born-Haber cycle, however, allows us to explore such terms.

Kapustinskii suggests an approach to calculating approximate for lattice energies using the radii of both cation ( $r_{\text{cation}}$ ) and anion ( $r_{\text{anion}}$ ), giving Kapustinskii's equation:

$$U_{\text{Kapustinskii}} = 1200.5 \cdot \frac{|q_i| \cdot |q_j|}{r_{\text{cation}} + r_{\text{anion}}} \left( 1 - \frac{0.345}{r_{\text{cation}} + r_{\text{anion}}} \right) \text{ kJ mol}^{-1} \quad (2.22)$$

The Kapustinskii's equation is a good reference for our results, because it often gives consistent, yet higher predictions of the lattice energy.

## 2.8 Defects in crystals

All materials are inevitably defective. Previous sections were based on the concept of the perfect crystal, which can only exist at absolute zero temperature for a crystal with no impurities. Both thermal effects and impurities will result in

the creation of defects Some types of defects can be detrimental to the material, while some others are beneficial to the fundamental properties of the material. For example, in AlN fabrication, defect control is the fundamental principle of tuning frequency and intensity of light emission in AlN-based LEDs.

The existence of defects in crystals has a fundamental thermodynamic basis (**Figure 2.9**). Introducing defects into a crystal is an endothermic process (requiring energy), which means during the process (reaction of defect formation) the enthalpy ( $H$ ) of the system increases. However, owing to the disorder introduced by the defects, the entropy ( $S$ ) in the system also increases. And there will always be a finite defect concentration for which the change in the Gibbs free energy owing to defect creation is negative:

$$\Delta G = \Delta H - T\Delta S \quad . \quad (2.23)$$

Thermodynamic theory therefore requires a non-zero-defect concentration, and the defects present due to this factor are known as “intrinsic defects”.

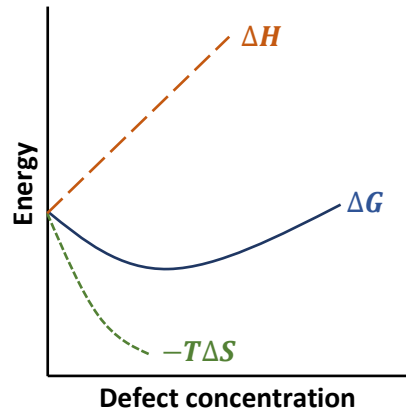


**Figure 2.9** Gibbs free energy  $\Delta G$ , enthalpy ( $\Delta H$ ) and entropy ( $\Delta S$ ) with respect to defect concentration.

If we ignore the vibrational entropy associated with defect formation, the concentration of a certain defect in the crystal per unit volume is given as (in Boltzmann’s way),

$$\frac{n_i}{N-n_i} = \exp\left(-\frac{E_i^f}{2kT}\right) \quad , \quad (2.24)$$

where  $N$  is the number of cation (or anion) per unit volume and  $E_i^f$  is the enthalpy of defect forming, i.e., defect formation energy. In most cases, the number of defects is much less than the total number of atoms in crystal ( $n_i \ll N$ ), so we can have:

$$n_i \approx N \exp\left(-\frac{E_i^f}{2kT}\right) \quad . \quad (2.25)$$

It is worth noting that this prediction may underestimate defect concentrations because of the neglect of lattice vibrational entropy associated with defect formation. However, the formation energy is the dominant term controlling the defect concentration.

### 2.8.1 Types of defects

Different schemes have been used to classify the defects in crystal. Defects which are comprised solely of the native atoms of the original crystal with concentrations governed by the thermodynamic theory outlined above, denoted intrinsic defects. Defects which are formed as a result of dopants or impurities are denoted extrinsic defects. In this thesis we focus on intrinsic defects, although we have some discussion of extrinsic, impurity induced defects.

The thesis is concerned mainly with point defects which comprise one atom or one site (or a small cluster of atoms/site) in the crystal, including, *vacancies*, (*self-interstitials*) or an antisite point defects as illustrated in (**Figure 2.10**). Other types of defects are known as extended defects, including line defects (dislocations), plane defect (e.g., grain boundary) and large clusters which can be considered as nuclei of a different phase. In **Chapter 4, 5** and **6**, the species that we are studying are primarily intrinsic point defects.



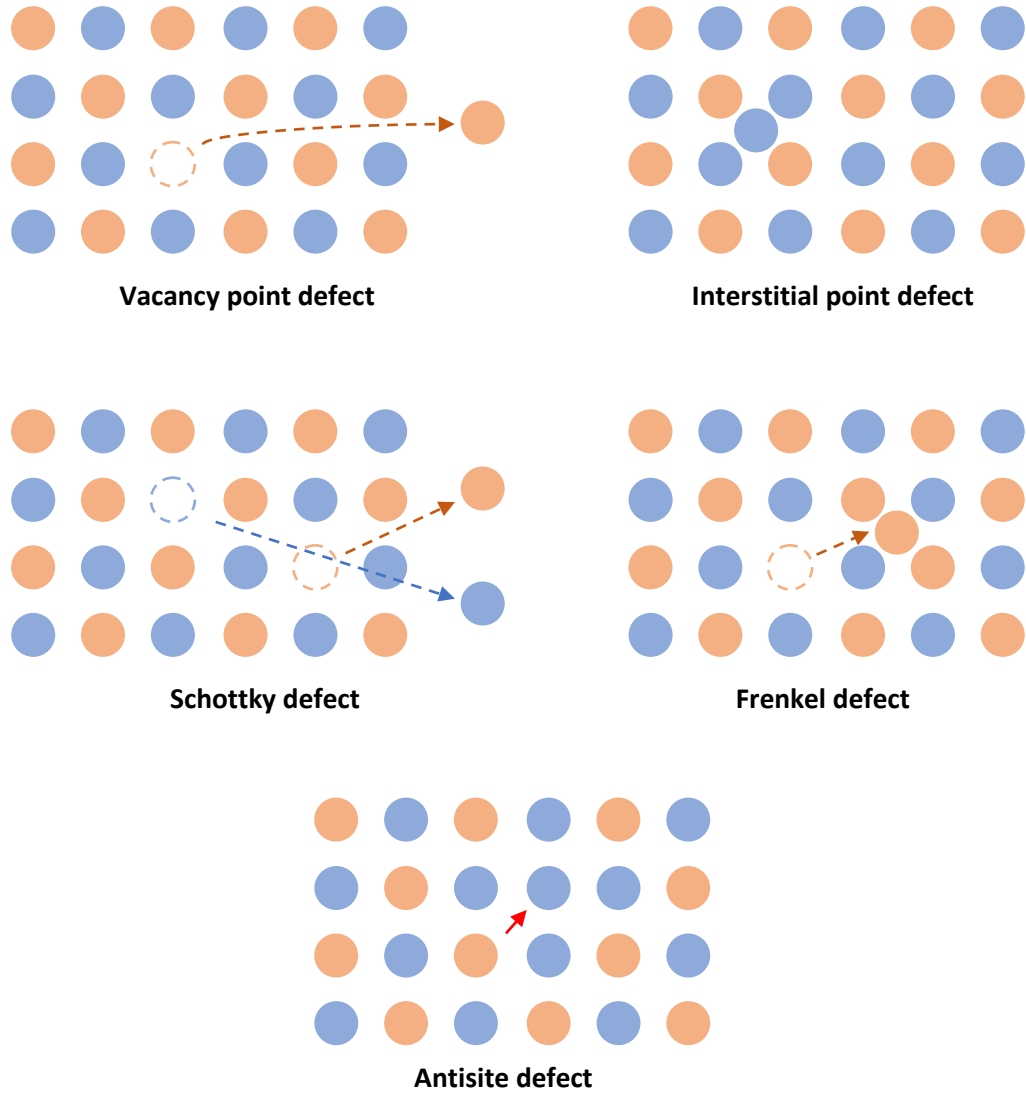


**Figure 2.10** 2D representation of basic types of intrinsic point defects.

*Schottky* defects and *Frenkel* defects are two key types of intrinsic defect complexes. In AlN, a pair of Al vacancy and N vacancy forms one Schottky defect pair. The formation of the Schottky pair can be envisaged as involving the migration of the cation and anion leave their own lattice sites and migrate to the surface. The concentration of Al and N vacancies is controlled by the Schottky equilibrium is given as,

$$n_{Schottky} \approx N \exp\left(-\frac{E_{Schottky}^f}{2kT}\right) \quad , \quad (2.26)$$

where  $N$  is either the number of cation or anion in the crystal. If the solely the Schottky equilibrium is operative, the concentrations of Al vacancies and N vacancies are equal.

The Frenkel defect is a pair of vacancy and interstitial point defects of the same species. The formation of Frenkel defect can be envisaged as an atom leaving its own lattice site and then re-locating at a non-interacting interstitial site, *i.e.*, an empty void between atoms. The concentration of vacancies and interstitials if controlled by the Frenkel equilibrium is given as,

$$n_{Frenkel} \approx (NN')^{\frac{1}{2}} \exp\left(-\frac{E_{Frenkel}^f}{2kT}\right) \quad , \quad (2.27)$$

where here  $N'$  is the total number of available interstitial void in the lattice. Which of the two defect equilibria dominates depends on the defect formation energies which in turn will be dependent on structural and other properties.

### 2.8.2 Defect energy levels

The band theory (**Section 2.6**) for a perfect crystal has no states in the band gap between. A valence band maximum (VBM) and conduction band minimum (CBM). However, the presence of defects can lead to states in the gap. (**Figure 2.11**).

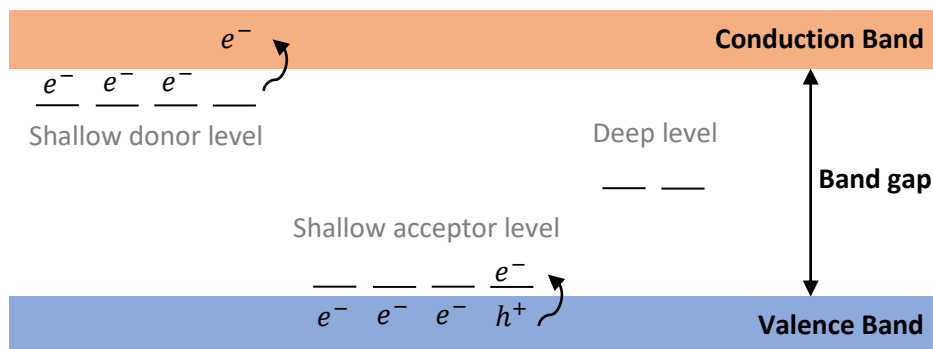


**Figure 2.11** Defect energy level in the band gap: donor level, acceptor level and deep level.

Depending on the distance from the edge of band gap, a shallow level is an energy state close to either VBM or conduction band minimum (CBM), and a deep level is the energy state near the middle of the band gap. The shallow energy levels close to the CBM are often formed by introducing excessive valence electrons, and these additional loose electrons at the shallow states can easily be excited into conduction band (normally by heat), so they are also called donor states (“electron donation”). The shallow energy states closed to VBM are often formed by the deficit of electron in the system, and these empty states can be occupied by electrons already in valence band leaving behind holes, so they are called acceptor states (“accepting electrons”). The deep levels, because the distance to the band gap edge is much larger than normal thermal energies, cannot be effective donors or acceptors; instead, they are most likely to act as traps for electrons. They may also act as recombination centres. Donor and acceptor behaviour is commonly discussed as originating from impurities. However, intrinsic point defects, by modifying the number of valence electrons and breaking bonds in the lattice, can induce both shallow and deep energy levels in the band gap region.

Indeed, in many semiconductors the electron conductivity is mainly controlled by defects in the material. The Fermi level ( $E_F$ ), a concept originally from the Fermi-Dirac distribution function, is the highest energy level that an electron can occupy in a solid-state material at absolute zero temperature. In intrinsic semiconductor (no impurities), as the numbers of electrons and holes are equal, the Fermi level locates at the centre of band gap. And because no electron is allowed in the band gap, the highest occupied level is at the top of the valence band. The Fermi-Dirac distribution function,

$$f(E) = \frac{1}{1 + e^{(E - E_F)/kT}} \quad , \quad (2.28)$$

shows the probability ( $f(E)$ ) of electrons appearing at certain energy level. If the temperature is high enough, the distribution will result in a finite electron concentration in the conduction band. As previously stated, defects in semiconductor will create donor states or acceptor states in the band gap region. If the semiconductor has a majority of donor states (states close to CBM), the increased electron population in the CB induces the Fermi level approaching

closer towards CBM. The semiconductor with appreciable occupancy of the CB is denoted and “n-type” (negative-type) semiconductor. In contrast, a “p-type” (positive-type) semiconductor is one that has excess holes in the material, where the Fermi level falls towards VBM. Such properties are illustrated in **Figure 2.12**. The Fermi level is extremely useful for semiconductor device design, as engineers can use Fermi level as representation of electron potential to build interfaces as their building blocks, for example the “p-n junction” structure.

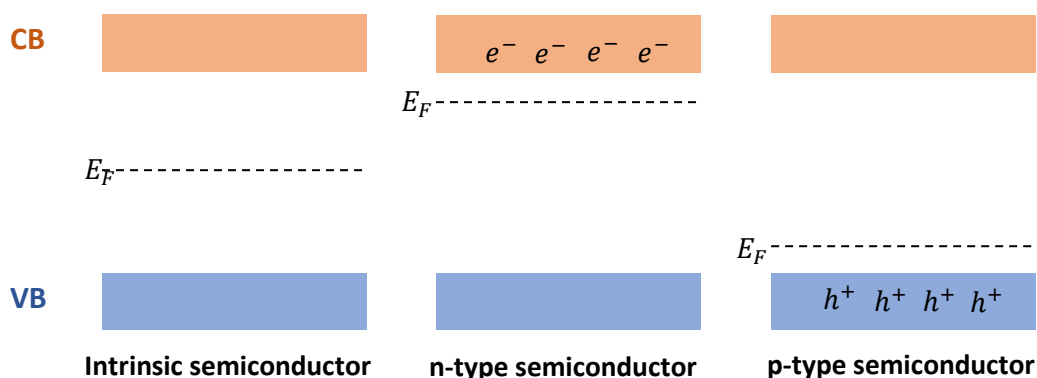


**Figure 2.12** Fermi levels in semiconductor band structures.

For computational chemists who study defects in solid-state material, Fermi level is an important quantity since the Zhang-Northrup defect formation energy scheme<sup>26</sup> can be utilised to calculate the theoretical defect shallow and deep states in semiconductor materials. We discuss this topic in more detail in the next chapter.

### 2.8.3 Charged defects

Point defects may have different charge states. The loosely bonded valence electrons of the defects may be ionised. A neutral point defect ( $X^0$ ) does not change the neutrality of the overall crystal lattice. In an ionic crystal, a neutral point defect generally involves trapping of holes or electrons. It is slightly more complex for the case of neutral antisite defects, although again for ionic crystals such defects can only be neutral by trapping electrons or holes. And the mobility of the additional electrons or holes is determined by their surrounding Coulomb potential<sup>27</sup>.

We can write the reaction of defect ionisation of singly charge carrier (**Figure 2.13**):

$$X^0 \rightarrow X^{+1} + e^- \quad (\text{for donor}), \quad (2.29)$$

or,

$$X^0 \rightarrow X^{-1} + h^+ \quad (\text{for acceptor}). \quad (2.30)$$

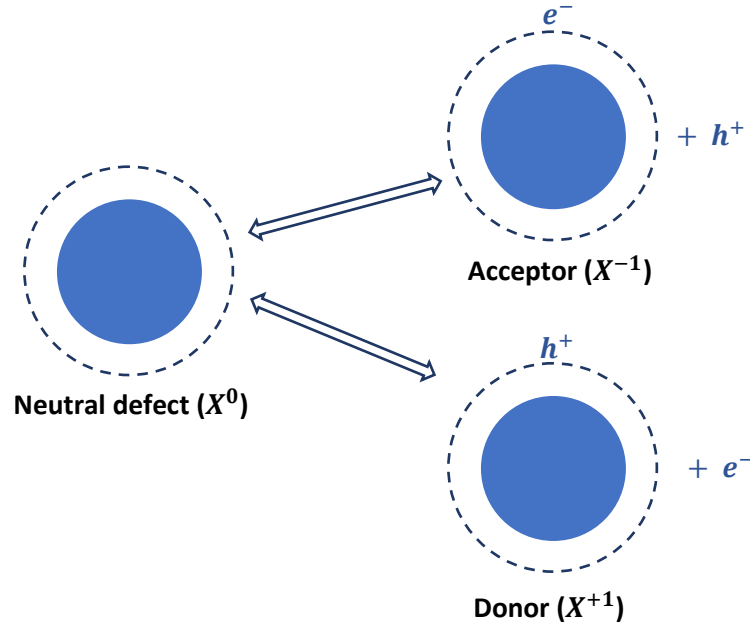


**Figure 2.13** Schematic diagram of charged defect.

Therefore, from the reactions, the concentration of charged defects respect to the number of neutral defects can be written in the way of Boltzmann's distribution:

$$\frac{[X^{+1}]}{[X^0]} = \frac{\theta_{X^{+1}}}{\theta_{X^0}} \exp \left[ \frac{E_{X^{+1}}^f - E_F}{kT} \right] \quad (\text{for donor}), \quad (2.31)$$

or,

$$\frac{[X^{-1}]}{[X^0]} = \frac{\theta_{X^{-1}}}{\theta_{X^0}} \exp \left[ \frac{E_F - E_{X^{-1}}^f}{kT} \right] \quad (\text{for acceptor}), \quad (2.32)$$

where the square bracket indicates the concentration and the  $\theta$  is related to the spin degeneracy of certain species.

As these neutral defects ionised, the distribution of excess electrons (or holes if missing electrons) still obeys the Fermi-Dirac distribution function. The Fermi

level in such ionisation process acts as the chemical potential for these charge carriers. Therefore, the change of the Gibbs free energy of formation of ionising an electron from the neutral state defect can be written as:

$$\Delta G_{X^{+1}}^f = E_F - E_{X^{+1}}^f \quad (\text{for donor}), \quad (2.33)$$

or

$$\Delta G_{X^{-1}}^f = E_{X^{-1}}^f - E_F \quad (\text{for acceptor}). \quad (2.34)$$

If the defect is doubly or triply ionised, like the case of Al and N atoms in AlN, the Gibbs free energy is:

$$\Delta G_{X^q}^f = qE_F - \sum_q E_{X^q}^f \quad (\text{for donor}), \quad (2.35)$$

Or

$$\Delta G_{X^q}^f = \sum_q E_{X^q}^f + qE_F \quad (\text{for acceptor}), \quad (2.36)$$

where  $q$  is the charge of the defect, which shows for each charge state, the Gibbs formation energy relates to the addition of its last ionised state. We determine energy states in the band gap by using thermodynamic statistic theory to calculate the chemical potential of each ionised carrier. For each carrier, Fermi level is always the reference point for the relative Gibbs free energy.

#### 2.8.4 Electronic transitions between charged defects

We now consider electronic transitions involving defect species. Some of the energy states are in the band gap region creating shallow and deep levels, while some are in the valence band and conduction band.

Electrons in defects can be excited to higher energy states, and the transitions will need to be modelled using a quantum mechanical approach. The excitation process involves a vertical transition – the Franck-Condon principle as illustrated in the **Figure 2.14**. After the excitation, the system may relax to the lowest vibration states on the same excited electronic state. The system may then emit a photon and return to a higher vibrational level of the ground state. This full cycle of excited electron lifetime is presented in the configuration–coordinate diagram (**Figure 2.14**).

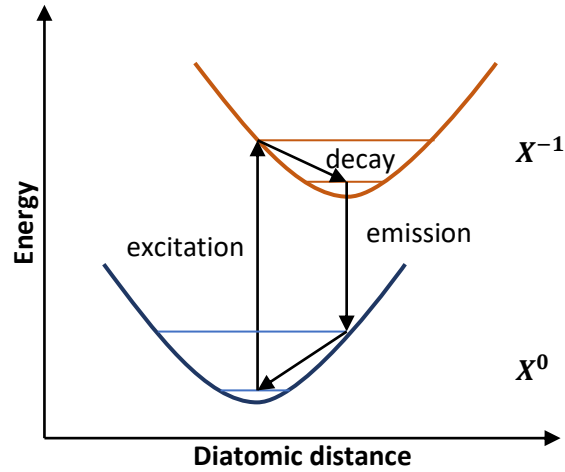


**Figure 2.14** A configuration-coordinate diagram according to the Franck–Condon principle.

### 2.8.5 Defect diffusion

So far in this section we have discuss stationary point defects. However, defects can undergo thermally activated migration, hence effecting atomic transport in the solid. To study atomic diffusion in the lattice, one approach is to consider the diffusing atoms as a flux of particles ( $J$ ) related to the gradient of atom concentration ( $C$ ), regardless of the physical and chemical properties of the lattice:

$$J = -D \cdot \text{grad}C \quad . \quad (2.37)$$

This is the phenomenological description of diffusion flux (Fick's law), which gives the definition of the diffusion coefficient (or diffusivity,  $D$ ). As atomic migration is thermally activated, it normally has an Arrhenius like temperature dependence:

$$D = D_0 \exp \left( -\frac{E_A}{kT} \right) \quad . \quad (2.38)$$

Here  $D_0$  is the pre-factor and  $E_A$  is the activation energy of diffusion, *i.e.*, the minimum energy barrier for migration. As migration is commonly affected by defects, the activation energy will correspond to the energy barrier for defect migration.

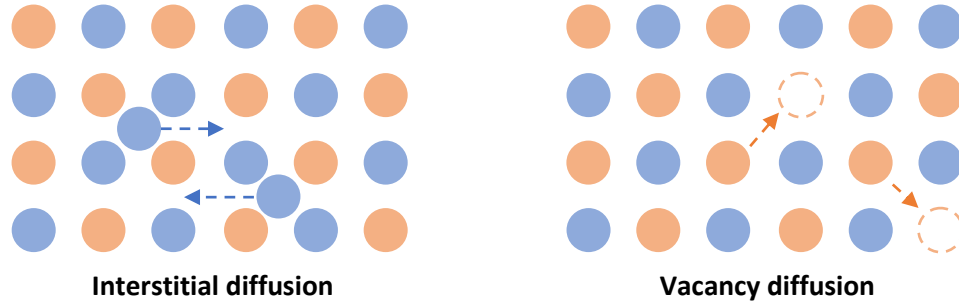


**Figure 2.15** 2D diagram of interstitial diffusion and vacancy diffusion.

Two types of the defect migration are illustrated in **Figure 2.15**. **Chapter 5** will discuss the self-diffusion of wurtzite AlN, which the diffusion only involves Al and N native point defects, in much more detail and we will report results of calculations of defect migration barriers.

## 2.9 Summary

In this chapter, we have introduced some of the key materials properties of aluminium nitride, especially of the wurtzite structured phase which is the most stable structure for crystalline AlN. These properties are not only critical to the applications of the material, but also are the quantities that we will be probing into by using our computational methods. Computational techniques can both calculate quantities like lattice constants and dielectric constants, for comparison with experiment and hence validation; and can also predict some which are not available from experiment such as the higher electron affinities of nitrogen atom. Basic concepts of band structure and point defects in solid-state materials have been outlined in the second half of the chapter. Defects are particularly important contribution to the photoluminescent properties of the wide band gap aluminium nitride semiconductor, and they also effect atomic migration. They would form the basis if extensive computational studies reported in this thesis.

The brief summary we have presented provides the context for the later chapters in the thesis. More details of the topics discussed can be found in the bibliography below.



## Chapter 3

### Background on Computational Methods

In this chapter, theories of computational methods, which are extensively used in this work, will be introduced. The aim here is to explain the essential features of the concepts and methodologies. The chapter starts from the classical approach, molecular mechanical (MM) or interatomic potential method, to the non-classical one, the quantum mechanical (QM) electronic structure method. The actual method applied for our electronic study of defects in AlN, i.e., the hybrid QM/MM method, inherits the advantages from both MM and QM approaches. In the final section, different structural optimisation methods are discussed.

#### 3.1 Molecular mechanics methods

In molecular mechanics, the atom is the “smallest” element of the theory. This means molecular mechanic methods can only deal with the system larger than one atom, like molecule or crystal lattice, or with the problems not related to smaller particles, like electronic structure (related to electrons). Although one might see attempts appearing in the **Chapter 4** where we try to use MM methods to calculate electronic energy level, they are either crude predictions or approximate evaluations of the enthalpy of certain reactions involving electronic species.

Because atoms are the “building blocks” in the MM methods, how they interact with one another must be specified when setting up the calculations. These interactions are commonly modelled by interatomic potential functions. Interatomic potential, or force fields (FF), containing information about bonding, and non-bonding interactions between atoms. Calculating the sum of all the interatomic potentials with respect to the atomic positions, one can get the potential energy surface (PES) of the whole system. From the PES, we can

predict many other important properties, including vibrational frequencies and activation energies of diffusion.

In modelling covalently bonded systems, it is usual to include terms representing of bending and rotation of (organic) molecules (see one example<sup>28</sup>). For the AlN crystal lattice, where the bonding is predominantly ionic, we found that two-body interactions may be sufficient to conduct accurate simulation (particularly for defects, which is the main topic of this thesis). In **Chapter 4**, we will implement a form of three-body interatomic potential for improving our prediction of the physical properties, but it will be proved that such model is not good for the defect calculation without additional correction term. Details of the interatomic potentials used in modelling AlN are given in the following section.

Once the appropriate interatomic potentials are in place, the MM code can evaluate the energy of the system and search for the energy minimum, i.e., undertake energy minimisation. The first test of the quality of a potential model is its ability to reproduce the structure of the molecule or material, but a good model should also predict elastic, vibrational and dielectric properties.

For a periodic crystal lattice, the energy term is effectively the lattice energy introduced in **Chapter 2**. In this work, AlN is, as noted, considered as an ionic compound. Therefore, the lowest lattice energy from MM simulation is obtained when the sum of all the repulsive forces balances the sum of all the attractive forces between charged atoms (ions). The lattice energy is the sum of all potentials of the long-range interactions and the short-range interactions in the lattice (see chapter 2). The long-range interactions are predominantly coulomb or electrostatic interactions. And the short-range interactions originate from the repulsive and van de Waals non-bonded interactions between atoms, which are modelled by Morse potential, Buckingham potential and Lennard-Jones potential, as discussed in detail below.

#### 3.1.1 Madelung energy and interatomic potentials

The predominant contribution of the lattice energy in ionic material is electrostatic potential, and the sum of all electrostatic potential of an infinite crystal lattice is known as Madelung energy. Both concepts have been discussed in detail in **Chapter 2**. For computational chemistry codes, the direct sum of electrostatic

potentials is still a difficult task. For example, for a reference ion at the 3-D lattice centre, the Coulomb force is weaker as the distance between the reference ion and the other ions increase. However, the number of ions increases further away from the reference ion. This means the sum of electrostatic potentials can only converge conditionally. Therefore, in most cases, the summation is calculated through a method called Ewald summation<sup>29,30</sup> which can accelerate the convergence of the calculation. In such a method, Coulomb interactions are subjected to a Laplace transformation. The original interaction term is separated into a real component corresponding to real space and a component corresponding to reciprocal space. The use of the reciprocal space component is beneficial in calculating long-range electrostatic interactions as it can quickly converge. The mathematical formulation is presented in other work<sup>30</sup>.

However, although the electrostatic interaction is the predominant contribution in ionic material, the crystal structure is largely controlled by the short-range interactions. One of the most widely used forms of the short-range interatomic potential is the Buckingham potential:

$$V_{Buckingham} = Ae^{-r/\rho} - \frac{C_6}{r^6} \quad , \quad (3.1)$$

where  $A$ ,  $\rho$  and  $C_6$  are all parameters which depend on the atom types. The Buckingham potential consists of an exponential term, a classical form of Born repulsive potential, which prevents two atoms from overlapping (**Chapter 2**), and another  $r^{-6}$  attractive term. The power of minus 6 is appropriate for the dispersion energy originating from the dipole-induced-dipole moments between molecules (London dispersion force) in the lattice. However, when the  $C$  parameter is fixed by empirical fitting, the term may include other attractive interactions.

Another similar potential function is the Lennard-Jones potential, in which the repulsive terms in the Buckingham potential is replaced by an  $r^{-12}$  term:

$$V_{Lennard-Jones} = \frac{C_{12}}{r^{12}} - \frac{C_6}{r^6} \quad . \quad (3.2)$$

The use of an  $r^{-12}$  term gives a steeply repulsive potential but in some cases the power could be any integer number from 9 to 12. In the MM code used in this

work, minus twelve is the default power in the first term, as it is more computationally friendly (six times two). The Buckingham potential is more flexible as it employs three parameters instead of two, and the exponential form for repulsive interaction may in ionic systems be a better description than  $r^{-m}$ . Therefore, even though the exponential component makes it more expensive computationally, the Buckingham potential is still the preferred short-range potential for ionic solids. In some cases, the attractive  $r^{-6}$  term is omitted and the function is then referred to as the Born-Mayer potential.

Another important short-range interatomic potential is the Morse potential:

$$V_{Morse} = D_e (1 - e^{-a(r-r_e)})^2, \quad (3.3)$$

where  $D_e$ ,  $a$  and  $r_e$  are all variable parameters. A simple bond harmonic function can be used to describe bonding or stretching interaction between atoms:

$$V_{Harmonic} = \frac{1}{2} k r^2. \quad (3.4)$$

The Morse potential is, however, in general superior to the harmonic oscillator, because the former potential converges to the dissociation energy ( $D_e$ ) as  $r$  increases. There are variations of Morse potential by adding/subtracting a constant after the above equation. In the MM code we used, another  $D_e$  is subtracted on the right side of the equation by default:

$$V_{Morse} = D_e \left( (1 - e^{-a(r-r_e)})^2 - 1 \right), \quad (3.5)$$

to keep all the interatomic potential consistently converged to zero (like Lennard-Jones potential). This alternative form has its minimum point at  $-D_e$ .

One further type of potential functional is the polynomial potential, which has the form:

$$V_{polynomial} = c_0 + c_1 r + c_2 r^2 + \dots + c_i r^i, \quad (3.6)$$

where  $c_i$  are constants. The polynomial potential sometimes is an alternative for modelling bond stretching interaction. The foundation of polynomial function as interatomic potential is from the Taylor expansion at the equilibrium diatomic distance. However, in this work at key interatomic distances no polynomial potential is employed. It is only used as inter-potential linkage function between

different functional forms to make sure the overall interatomic potential profile is smooth, without discontinuities.

### 3.1.2 Shell model and polarization

The ionic system cannot be completely described without introducing polarizability. In this work, Dick and Overhauser's shell model<sup>31</sup> is employed for the representation of polarization. Unlike the single point dipole moment approach ( $\mu = \alpha E$ ), the shell model divides a single charged atom into two species - a core and a shell. A core species represents the nucleus and the innermost electrons closely bound to the nuclei. A shell species represents the outermost valence shell electrons loosely bound to the rest of the atom. The shell has its own charge ( $Y$ ), and the sum of the charges of core and shell must equal to the formal charge of the atom or ion. The assumption here is that most contribution of the polarization is from the shell<sup>31</sup>. Therefore, the polarizability ( $\alpha$ ) of a free ion is given by:

$$\alpha = \frac{Y^2}{k} \quad . \quad (3.7)$$

Within a single atom, the shell and the core are connected by spring constants  $k$  (Hooke's Law):

$$V_{spring} = \frac{1}{2}k_2d^2 + \frac{1}{24}k_4d^4 \quad , \quad (3.8)$$

where  $k_2$  and  $k_4$  are spring constants for the quadratic and the quartic terms, and  $d$  is the intraatomic distance between the core and the shell. The quartic term is only employed when ions are very strongly polarised when it prevents the shell from moving too far from the core.

However, reader must be aware that the "shell" in Dick and Overhauser's shell model is not equivalent to electron shell or electron cloud in quantum mechanics theory. Here "shell" and "core" are mimicking the atomic structure of valence electrons and nucleus, and they are interacting through a classical force. A clearer example of an unphysical model occurs when one allows positively charged "shell" species.

### 3.1.3 Parameterization

Once the functional forms of the force field are decided for a system (in this case crystalline AlN), fitting the right parameters is the final task in completing the description of the interatomic potential. Generally, the parameters of interatomic potential are obtained through numerical fitting against the external referencing data, which can be from reliable experimental results (ideally) or other higher-level computational results of a similar system (for example: results from *ab-initio* calculations).

In the present work, due to the ample availability of experimental data for AlN (also for GaN and InN), the parameters of our interatomic potential are mainly fitted empirically. It is always good practice to choose as large range of the experimental data as possible, ideally including lattice constants (in this case  $a$  and  $c$  for wurtzite AlN), elastic constants, dielectric constants, piezoelectric constants, bulk moduli, phonon frequencies and lattice energy. All these different types of data together can reflect a PES which can match the one reproduced by suitable interatomic potentials and their parameters.

To perform a parameterization of interatomic potential, an error function is normally applied here<sup>32</sup>:

$$F = \sum_{i=1}^{N_{obs}} w_i (f_i^{obs} - f_i^{calc})^2 \quad (3.9)$$

where  $N_{obs}$  is the number of observables,  $w_i$  is the weight factor,  $f_i^{obs}$  is the value of the observable, and  $f_i^{calc}$  is the calculated value. Here parameter fitting is becoming a problem of  $F$  minimisation where mathematical optimisation methods are employed. In our case, the Newton-Raphson minimisation process along with Broyden–Fletcher–Goldfarb–Shanno algorithm (BFGS) is applied here (**section 3.3**). Further detail can be found in other work<sup>32</sup>.

#### 3.1.4 Molecular mechanics software

The software used for the force field method is the GULP Program (The General Utility Lattice Program)<sup>29</sup>. It has been widely used in modelling crystalline materials using interatomic potential parameters and can calculate physical properties, defect energetics, surfaces, and interface, and can be applied to solid solutions. Moreover, it can be used in “inverse mode” in order to fit potential

parameters to observed data. Calculations on AlN using GULP are reported in **Chapters 4 and 5**. In the framework of the present work, which also employs the QM/MM method, the “MM” environment is constructed and executed using GULP. Therefore, it is crucial to start with molecular mechanics to ensure the embedded environment is reliable for the central cluster.

### 3.2 Quantum mechanical methods

While shell model in the molecular mechanic method can give good description of ionic polarizability, it cannot give information on the electronic structure of the material. Electrons are in the realm of quantum particles, so quantum mechanical methods are necessary to probe electronic structure. Because the methods are at the most fundamental level of physical theory, such calculations are also called “first principle” or “*ab initio*” calculations, unless they are approximated by using empirical parameters.

The core of any quantum mechanical method is the Schrödinger equation. Unless one cares time-evolution of a quantum system, a time-independent Schrödinger equation in the form of Hamiltonian and eigenvalue is:

$$\hat{H}\Psi = E\Psi, \quad (3.10)$$

where  $\Psi$  is the wavefunction,  $\hat{H}$  is the Hamiltonian and  $E$  is the corresponding energy (eigenvalue) of the Hamiltonian operator. All the quantum mechanical calculations try to solve this equation by using different degrees of approximation, as apart from one electron systems, we are dealing with many body systems. The first level approximation theory is the Born-Oppenheimer approximation, where the motion of nuclei and the motion electrons are assumed to be separable, independent in the system. The nuclei are much heavier than electrons, so for any one nuclei configuration, the distribution of electrons can be obtained according to the configuration of the nuclei, assumed to be stationary. The Born-Oppenheimer approximation is only the first step towards the more practically used quantum mechanical methods.

Next, the Hamiltonian  $\hat{H}$  is expanded into sub-level kinetic ( $\hat{T}$ ) and potential energy operators ( $\hat{V}$ ):

$$\hat{H} = \hat{T}_n + \hat{T}_e + \hat{V}_{nn} + \hat{V}_{ee} + \hat{V}_{ne} \quad , \quad (3.11)$$

where the  $n$  represents nucleus and  $e$  represents electron indicating the particle that the operator is acting on. Within the Born-Oppenheimer approximation, the most difficult task concerns the electron-electron interaction. As more and more electrons are added to the system, the exchange and correlation effects between electrons becomes more apparent. Different approaches employ different philosophies to the treatment of electron exchange and correlation. The most popular theories used for solid-state material calculations are the wavefunction method (the Hartree-Fock theory) and the Density Functional Theory (DFT).

### 3.2.1 Hartree-Fock theory

Hartree-Fock (HF) theory is based on solution of the Schrödinger equation for a many electron wave function that is consistent with the “Pauli exclusion principle” which says the same-spin electrons cannot occupy same atomic orbital simultaneously. The principle limits the localisation of the electrons and dictates the final distribution of electrons.

Next, solving the wavefunction needs the variational principle, which proves the energy of any trial wavefunction will always be higher than the real ground state energy of the real wavefunction. This is useful because one can use a trial wavefunction at the start (often called “initial guess”) and can obtain the lowest energy in an iterative mechanism. The resultant energy is always higher than the “real” energy but will approach the latter as the quality of the wave function improves.

The Pauli exclusion principle arises from a very important property of wavefunction of fermions, i.e., anti-symmetry. Antisymmetric property of the wavefunction says that the exchange of any two electrons will change the sign of the total wavefunction. In practice, to form a such wavefunction for two electron system (like the case in helium atom), one utilised the form:

$$\Psi_{TOT} = \psi_1\psi_2 - \psi_2\psi_1 \quad , \quad (3.12)$$

where exchanging the electron positions (swapping “1” and “2” in this case) makes the wavefunction change sign. As the number of electrons in the system



increases, it is more convenient to use an  $N \times N$  matrix determinant form to construct the wavefunction:

$$\Psi_{TOT,SD} = \frac{1}{\sqrt{N!}} \begin{vmatrix} \chi_1(1) & \chi_2(1) & \dots & \chi_N(1) \\ \chi_1(2) & \chi_2(2) & \dots & \chi_N(2) \\ \vdots & \vdots & \ddots & \vdots \\ \chi_1(N) & \chi_2(N) & \dots & \chi_N(N) \end{vmatrix}, \quad (3.13)$$

where  $N$  is the total number of electrons in the system, and  $\chi_N$  is the spin-orbital function containing both the spatial and spin information of the corresponding electron orbital. This is called the Slater determinant form of the wavefunction, and it is the foundation of the HF method. As required by the variational principle, the HF wavefunction is above the true energy and an intrinsic limitation of the single determinantal HF method is the omission of the electron correlation energy, which is included in higher-level *ab initio* methods.

In practice, the determination of the minimum energy of the Slater determinant completes through an iterative process, the self-consistent field (SCF) technique. Such technique starts from constructing a new Fock matrix from the initial trial wavefunction. The Fock matrix will be diagonalized and the density of molecular orbitals is calculated. The new molecular orbitals replace the last ones and a new Fock matrix is formed based on these new orbitals. Such process will continue iteratively until the before/after densities of molecular orbitals are identical or within acceptable convergence threshold. In most case, to accelerate the SCF process, the initial trial functions are specified as some form of atomic orbital functions (initial guesses). As the initial atomic orbitals gets more complex, SCF will yield a more accurate energy, but this also comes with a cost of an increase in the computer resources needed. One of the researcher's responsibilities is to choose suitable initial guess functions to achieve accurate enough energy while using a reasonable amount of computational resource.

So far, there is no restriction on the trial wavefunction. In the Slater determinant above, the spin-orbitals are the product of spin function and spatial orbitals. The spin in the spin-orbital function is either spin-up or spin-down. However, the form of spatial orbital varies according to the quantum states. As the system is in singlet quantum state, where there is no unpaired electron on the orbitals, one

can restrict the trial wavefunction to be that there must be both spin-up and spin-down on the spatial orbitals. This is known as restricted Hartree-Fock (RHF) wavefunctions. If the system has one and more unpaired electrons, the restriction can be lifted and such wavefunction becomes unrestricted Hartree-Fock (UHF) type. There is also another in-between type known as restricted opens-shell Hartree-Fock (ROHF) wavefunctions, in which the spatial orbitals are the same if doubly occupied and different if singly occupied. The SCF process treats the two types of wavefunctions differently in the variational calculation. In principle, if the system is singlet, there should not be any difference on the two energies calculated via between R(O)HF and UHF. If the system has unpaired electron, UHF wavefunctions always lead to a lower orbital energy than R(O)HF ones do.

To compensate the energy error in the HF theory, many efforts have been done to recover the correlation energy without sacrificing too much computer resource. These are sometimes called electron correlation method. They are not used in our work, so we will not cover them here.

### **3.2.2 Density functional theory**

The density functional theory (DFT) is a better model to consider both the electron exchange and the correlation interactions. In our work, both the Hartree-Fock method and DFT are employed. The former is often served as a pre-optimizing calculation to improve the performance on the final DFT calculations.

Compared with the wavefunction method where orbital energies are calculated from explicit electronic wavefunctions, the energy calculation by the density functional theory is with respect to electron densities. The wavefunction of a single electron contains four variables (spatial coordinates ( $x$ ,  $y$  &  $z$ ) and spin information). As the total number of electrons in the system becomes larger, calculating on the electronic wavefunctions can be difficult. The electron density only contains the three spatial coordinates, so the reduction in the variables increases calculation speed. Additionally, the meaning of electron density is much closer to physical observables. Therefore, introducing electron density makes the quantum mechanical calculation much simpler.

As previously mentioned, the HF wavefunction method can obtain quite reasonably accurate molecular orbital energies by constructing matrixes of

wavefunctions that obey the Pauli exclusion principle and the variational principle. The main flaw to the HF method is that it does not compute electron correlation energy well. This omission is rectified in DFT by using the electron density with an “exchange correlation function”. The breakthrough of the DFT that led to becoming the predominant tool for today’s computational studies rested on two important theorems proved by Hohenberg and Kohn in 1964<sup>33</sup>. They proved, firstly, that the quantum mechanical observables can be calculated by ground state electron density; and secondly that the energy calculated from the electron density can obey the variational principle. The two theorems proved the electron density can be used for quantum mechanical calculation in a similar fashion of the HF method if the right electron density is given. Yet, DFT is a different method from HF, as the former can in principle be an exact theory, and the latter is an approximate theory (but solved exactly).

The real practicality of DFT is shown by the theory introduced by Kohn and Sham<sup>34</sup>. They state that the real quantum mechanical system will be regarded as a fictitious system where all the electrons are not interacting, and the electron density (which contains interaction information) will be constructed by all these non-interacting electrons. In this way, the eigenfunction can still apply the same form of one-electron Slater determinant (same as the HF method). It is only the form of the Hamiltonian changes, where it includes the additional information of electron interaction. The new Kohn-Sham Hamiltonian is written as:

$$\hat{H}_{K-S}[\rho(\mathbf{r})] = \hat{T}[\rho(\mathbf{r})] + \hat{V}_{ne}[\rho(\mathbf{r})] + \hat{V}_{ee}[\rho(\mathbf{r})] + \hat{V}_{xc}[\rho(\mathbf{r})] \quad , \quad (3.14)$$

where  $\rho(\mathbf{r})$  is the electron density function, which is calculated from all the non-interaction orbitals (initial guesses):

$$\rho(\mathbf{r}) = \sum_{i=1}^N |\chi_i(\mathbf{r})|^2 \quad . \quad (3.15)$$

The kinetic energy, nuclei-electron energy and electron-electron energy of the system can all be calculated via the electron density. The additional exchange-correlation energy is calculated separately to add a correction on the former kinetic and potential energies. The amount of correction is dependent on the method of approximation (exchange-correlation functional) used, but normally it only takes up a very small portion of the total energy. This is the reason why the lower-level HF method can still approximate an energy of good quality.

The inter-correlation of non-interaction orbitals and electron density in the Kohn-Sham DFT method shows that the minimum ground-state energy calculation can still employ the SCF approach. Initial guesses of molecular orbitals are used as a starting point and the initial electron density is calculated from them. It will go through the same process of diagonalizing of the Fock matrix, and a new set of molecular orbitals and electron density will be formed. If the difference between the input and the resultant densities (energies) are larger than threshold, the process will continue iteratively until the self-consistency is fulfilled.

### 3.2.2.1 Exchange-correlation functional

In principle there is an exchange-correlation functional that can give us the real ground state energy. However, the real exchange-correlation energy is still unknown, and one can only compute this term by using different methods of approximation. They are called exchange-correlation functionals (XC functionals), as they are functionals in terms of electron density functions. Much effort in the last few decades has been devoted to developing the right XC functionals for the right problems and there are many different XC functionals, so choosing which one to use is a key decision.

The exchange-correlation energy can be formulated as a single energy term form, or separate exchange energy term and correlation energy term form:

$$E_{xc}[\rho(\mathbf{r})] = \int \rho(\mathbf{r}) \cdot \varepsilon_{xc}[\rho(\mathbf{r})] d\mathbf{r} \quad , \quad (3.16)$$

or,

$$E_{xc}[\rho(\mathbf{r})] = \int \rho(\mathbf{r}) \cdot \varepsilon_x[\rho(\mathbf{r})] d\mathbf{r} + \int \rho(\mathbf{r}) \cdot \varepsilon_c[\rho(\mathbf{r})] d\mathbf{r} \quad , \quad (3.17)$$

where  $\varepsilon_{xc}$ ,  $\varepsilon_x$  and  $\varepsilon_c$  is the energy density functional as a function of electron density. The key difference between different XC functionals is how to construct  $\varepsilon_{xc}$ . Starting from the simplest type, the local (spin) density approximation (LDA or LSDA) employs the energy density form determined by the local electron density directly. However, though such an implementation proved to yield a very good approximation on geometry, it is very poor on the energy estimation. Therefore, a step forward is to use the generalised gradient approximation (GGA) method, where it adds an energy density term dependent on the gradient of the local density. GGA methods can improve results on energy to the level of HF

calculations, and at the same time estimates much more accurately the geometry. The next level of the evolution is called the meta-GGA methods, where it includes second derivatives of electron density and kinetic energy density. At this point, it is obvious that the higher orders of expansion the method involved, the more accurate it becomes. Such a hierarchy of different levels of DFT methods is named as “Jacob’s ladder” of chemical accuracy, where the HF methods sits at the lowest rung and the highest rung represents methods for the ultimate chemical accuracy.

The next rung above the meta-GGA methods is the hybrid functional methods, which are primarily adopted for the defect calculations of AlN in this work. The idea of hybrid functional DFT method is the inclusion of HF exchange energy term in the XC energy. The concept can be formulated as:

$$E_{xc} = E_x^{HF} + z(E_{xc}^{DFT} - E_x^{HF}) \quad , \quad (3.18)$$

or replacing  $z = 1 - a$ ,

$$E_{xc} = (1 - a)E_{xc}^{DFT} + aE_x^{HF} \quad . \quad (3.19)$$

The HF exchange energy  $E_x^{HF}$  is the energy that electrons in the system do not correlate at all (when  $a = 1$ , pure exchange behaviour), and the DFT XC energy  $E_{xc}^{DFT}$  is the energy that the electrons are fully correlated (when  $a = 0$ ). The real situation of the system must fall somewhere between the two extremes, where electrons are semi-local and partially correlated. The form of  $E_{xc}^{DFT}$  can be any one from the lower rungs of the “ladder” and the key is to find the right proportion  $a$ . Below are the hybrid functionals used in our work:

**PBE0**<sup>35,36</sup>: The functional uses the PBE (Perdew–Burke–Ernzerhof, GGA type) exchange energy mixed with exact HF exchange (in 3:1 ratio) and the full PBE correlation energy. The “0” in the name means that the parameter  $a$  (which is  $\frac{1}{4}$ ) is pre-determined and unchanged. This is the simplest type of hybrid functional used for the DFT calculations in this work.

**B97-2**<sup>37</sup>: The functional uses the idea that Becke adopted in his work published in 1997 (the “97” in the name)<sup>38</sup>, in which the ratio between the GGA type Becke XC contribution and the HF exact exchange contribution is refitted with broad range of thermodynamic data. This hybrid functional was refitted

with even larger sets of thermodynamic data in 2001 to produce better energy barriers and was named B97-2 with 21% of HF exact exchange energy. The “2” in the name stands for the 2<sup>nd</sup> generation from the original B97 functional.

**BB1K**<sup>39</sup>: The hybrid functional starts from combining the ideas of the original Becke’s GGA type functional<sup>40</sup> and another Becke’s GGA functional in 1995 adjusted to the kinetic energies<sup>41</sup>; and then with exact HF exchange, the hybrid functional was refitted with energy barrier data and kinetic data for reactions. The resultant proportion of exact HF exchange is 42%, which is the highest among all the functionals used in our work. The high exchange proportion means it will result in the least localised description of the system, so it normally performs very good for saddle point estimation. It also means that it is the most expensive hybrid functional among all in this work.

**HSE03**<sup>42</sup>: The functional adopts the PBE0 functional and divides only the exchange part into short-range and long-range Coulomb components and adds an additional variable of Coulomb screening factor  $\omega$  (ranging from 0 to  $\infty$ ) to control the contribution of long-range Coulomb potential. It has been widely used in periodic boundary condition calculations (like those employed in the VASP code) for many solid-state semiconductor materials. The data obtained by the embedded cluster method in this work via the functional will offer us a direct comparison with most of the data in the literature by PBC methods. Its name comes from the authors first invented the functional (Heyd, Scuseria and Ernzerhof) in 2003 (“03”).

### 3.2.3 Basis sets

Both the HF and the DFT methods are the *ab initio* means to solve Schrödinger equation, and the basis sets are the “ingredients” of the calculations. Basis sets are sets of basis functions representing wavefunctions or electronic orbitals of atoms or molecules in terms of known equations so that they provide an entry for the *ab initio* calculations. The form and the size of the basis sets varies according to the target of the calculation. In principle, there exists a complete set of basis functions that reflects the exact wavefunction of the species, but it would be either too large size or could not be represented by any known formalism. Just like choosing the suitable hybrid XC functionals for the DFT calculation, selecting and

comparing different basis sets is also important for getting maximum accuracy and highest efficiency of the calculations (although these two normally conflict each other in computational chemistry).

There are two forms of functions for constructing the basis sets, Slater-Type Orbitals (STO) and Gaussian-Type Orbitals (GTO). The form of the STO is much closer to the real atomic orbitals and it can yield very accurate results, but it is very difficult to compute relevant integrals using STOs in *ab initio* calculations. The GTO is therefore a more common form of basis sets for more complicated systems. The idea behind the usage of GTO is that one can construct a linear combination of different Gaussian-type functions so that it can mimic the profile of STO and obtain similar resultant energy. Also, Gaussian-type functions are much easier for computer to calculate integrals and derivatives (as they are continuous functions) than Slater-type functions (they are discontinuous functions). Therefore, most of the calculations for multi-electron system utilize the GTO form basis sets.

The class of basis set that is mainly used in this work is named *def2-TZVP*<sup>43</sup>. Def2-TZVP contains a large database of basis sets for chemical elements from H to Rn. It has been re-optimized (2<sup>nd</sup> time, “def2”) against 300 compounds using different computational methods such as HF, DFT and MP2 (the method which deals with electron correlation directly). Therefore, it is a widely applicable basis set for more than half of the elements in the periodic table, and it is useful for calculating properties of correlated molecular systems. From this point in this section, we will be considering the construction of basis sets according to the def2-TZVP.

**TZV** (*triple zeta valence*): The primary identification of the basis set is by indicating how many basis functions describe electronically occupied orbitals or valence orbitals. *Triple zeta* indicates that there are triple number of GTO functions to the actual number of occupied orbitals. And *triple zeta valence* indicates that only the outer valence orbitals are represented by triple number of basis functions. For example, for nitrogen atom, there are one inner core 1s orbital, one valence 2s orbitals and one valence 2p orbital that are occupied by electrons, so there will be one basis function describing the core 1s orbital, and three basis functions for each of the valence 2s orbital and 2p orbital. The accuracy increases when there are more basis functions (like quadruple zeta, 5Z,

6Z, etc.) describing each orbital, but the cost of the calculation also increases dramatically.

In fact, in the TZV basis sets for nitrogen atom, there are five basis functions for the  $s$  orbitals instead of four. A single basis function for the core  $s$  orbital did not yield a successful energy optimization<sup>44</sup>, so it was deliberately split into two parts, one for inner core orbital and the other for orbital below the valence orbitals.

In the TZV basis sets for aluminum atom, there are five basis functions for the  $s$  orbitals instead of eight (the  $3s$  valence orbital should have added 3 more functions compared with N atom), because it has been proved that the  $3s$  orbital is inert and is not involved in most of the chemical reactions<sup>44</sup>. As for the functions for  $p$  orbital, there are five instead of four. This is a special re-optimization for Al (and other elements afterwards until Ar)<sup>44</sup>.

The notation for characterizing the basis functions with respect to atomic orbitals is:  $[klmn]$ , which denotes the number of basis functions for  $s$ ,  $p$ ,  $d$ , and  $f$  orbitals respectively. The notation of TZV type basis sets for nitrogen atom is then:  $[53]$  or  $[5s, 3p]$ ; similarly for the aluminum atom:  $[55]$  or  $[5s, 5p]$ .

**P (polarization):** For these basis sets there will be additional basis functions for higher orbital(s) that describes the polarization effect of the species. They add greater flexibility and improve the description of polarizability. In the convention of TZVP basis sets for N atom and Al atom, the additional polarization functions in addition to the TZV are  $[2d, 1f]$ <sup>43,45,46</sup>. Altogether, the TZVP type basis functions for N atom and Al atom are:  $[5s, 3p, 2d, 1f]$  and  $[5s, 5p, 2d, 1f]$  respectively.

Sometimes, the polarization functions only describe a small diffuse “tail” of the orbital far from the nuclei and unimportant to the energy we are interested, but it enlarges the size of the basis sets and prolongs the calculation time. In such cases, we would remove 1-2 outermost polarization functions which saves time without damaging the final energy.

**Basis set contraction:** If the form of a basis function has the linear combination of many GTO basis functions, it is called the contracted basis functions (CGTOs). They normally appear on the inner orbitals and less on the outer valence ones. As previous mentioned, the linear combination of GTOs can be very similar to STO, which yields a more accurate resultant energy. Also, the total energy of the



atom is mainly determined by the orbitals closer to core, and is not influenced much by chemical reactions, which are primarily related to valence orbitals. Therefore, the most inner orbitals are often contracted with a set of GTOs, and coefficients of these GTOs are optimised to lowest total energy. For example, in the TZVP basis sets of N atom, the core orbital ( $1s$ ) consists of 6 GTOs. The contraction of basis sets can be formulated as:

$$\chi_{CGTO} = \sum_i^k a_i \chi_{i,PGTO} \quad , \quad (3.20)$$

where PGTO stands for primitive (GTOs) which are the components of CGTO.

In the database of basis sets, the total number of PGTOs used are often given along with the number of CGTO to provide information on the degree of contraction. For example, in the TZVP basis sets for  $N$  atom, there are 11 PGTOs for  $s$  orbitals, 6 PGTOs for the  $p$  orbital, 2 PGTOs for  $d$  orbital, and 1 PGTOs for  $f$  orbital. They are contracted into [5321] formation. The notation of the contraction denotes as:  $(11s, 6p, 2d, 1f) \rightarrow [5s, 3p, 2d, 1f]$ .

### 3.3 Optimization methods

The term “optimization” here indicates the process of finding the minimum energy of all the atoms with respect to their coordinates in the system, *i.e.*, finding lowest points in the potential energy surface (PES in **Section 3.1**). This is achieved by searching for zero first derivatives of the energy for all the atoms. Though this seems like a very simple idea,  $N$  atoms means that there are  $N$  number of variables ( $3N$  if consider three coordinates) which must be optimized, for which it is very time-consuming. There is also the complication that there may be many local minima and the objective is usually to identify the global minimum. Therefore, many algorithms have been developed for finding the global minimum. However, this does not mean that lower-level algorithms which identify local minima may still be useful. Different algorithms are introduced in this section, although this is a large field, and we only select those approaches that are relevant to our study.

#### 3.3.1 Steepest Descent

Steepest descent is the simplest optimization method. In every step, the search direction vector is directly to the opposite of the gradient vector (first derivative of

energy) at that point. Therefore, it ensures that the next geometry must be a lower energy than the last one. This process is repeated iteratively until the gradient is zero. Steepest descents method is particularly useful if the potential surface is relatively simple and the slope around the minimum point is steep. However, if the gradient around the minimum point is relatively low, e.g., “valley” shape surface, such method is becoming dramatically slow (the search step is short). Normally, for finding global minima in a complex system, steepest descents method is not recommended, but for some cases like finding local minimum around the transition state, the method can be very useful.

Here in the study of point defect migration in the crystal lattice, after the transition states are found, a steepest descents search starts from the transition state. It searches for local minimum for finding next lower energy transition state, or it searches for global minimum proving the saddle point identified is on the migration path between two global minima.

### 3.3.2 Quasi-Newton Methods

The quasi-Newton methods are the upgraded methods of the original Newton’s method (or the Newton-Raphson method, NR). In NR, the energy function at current point is expanded to second order function (Taylor expansion function), and the searching step is determined by the first order ( $g$ ) and second order (the Hessian,  $H$ ) derivatives of energy at that point. The step is determined by:

$$x - x_0 = -H^{-1}g \quad . \quad (3.21)$$

One of the most used quasi-Newton methods is the Broyden-Fletcher-Goldfarb-Shanno (BFGS) method. It has been adapted as the default optimizer for shell relaxation and geometry optimisation in both the MM software, GULP, and the QM/MM software, Chemshell. In the original NR method, the exact Hessian needs to be calculated in each step, and this can be very time-consuming and memory demanding. In BFGS method, the Hessian  $H$  is updated in every step (therefore also named the Hessian updated method). The starting Hessian does not need to be an exact one, and the updated Hessian is approximated to the exact one along the optimization process. The use of an approximate Hessian might result in more steps to reach optimization convergence, but it might cost

less computational resource in total. Therefore, it is favourable in many computational chemistry software packages.

### **3.3.3 Transition state search**

In some cases, optimisations are not necessarily for finding energy minima for the system. The optimization algorithms can be used for finding the transition state of some reaction mechanism or the transition state location along the path of atom migration (diffusion) in the system. The two most widely used methods for transition state search are the Rational Function Optimizer (RFO) and the Nudged Elastic Band (NEB) techniques. Later in this work, transition state searching techniques are extensively used in the investigation of defect migration. We find in the contemporary literature that the NEB method is more frequently employed in transition state searches, but we were not able to use it because the MM software, GULP, had not implemented NEB in the Mott-Littleton functionality.

At the transition state (the saddle point) on the PES, the configuration of the system is a semi-local minimum except for to only one direction the configuration is energy maximum. RFO is a similar approach to NR, in which they both use the exact Hessian in their processes. RFO decides the optimisation direction based on the signs of the eigenvalues in the Hessian, so that it can control the optimization either towards energy minima (all positive eigenvalues) or the saddle point (only one negative eigenvalues). When RFO is used for a transition state search, it searches towards the direction where the eigenvalue is negative. Since this is a type of local optimization technique, the starting configuration of the system should be as close to the transition state configuration as possible. A distant starting configuration would result in arriving at random local energy minimum instead of transition state.

## **3.4 QM/MM methods**

In this work, we are interested in problems related to defects located at a specific site in a group of atoms. Lower-level MM methods (interatomic potential methods) have the advantage of being able to handle large scale systems including thousands of atoms, but they lack the capability of dealing with complex electronic level problems. Higher-level QM methods (HF, hybrid DFT, etc.) for

large system are often unaffordable. Here a hybrid QM/MM embedded cluster method, inheriting both the ability of dealing with large scale system from the MM methods, and the capability of electronic treatment from the QM methods, will be presented.

In this thesis, the implementation of the QM/MM method uses the Chemshell software<sup>47–49</sup>. It takes a five-concentric-region large cluster (usually of around ten thousand atoms), where a small central QM region is surrounded by a larger MM environment. Earlier implementations<sup>50–52</sup> of the embedded QM cluster method were using fewer layers for their system construction, but the more sophisticated partitioning is significant to the development of the approaches used in Chemshell.

### 3.4.1 Region Partitioning

In Chemshell, the system is partitioned into 5 concentric regions, where the innermost 3 (region 1, 2 and 3) are “active region” and outer 2 (region 4 and region 5) are inactive (**Figure 3.1**). In the active region, atoms are treated explicitly, and total energy of each region is calculated. Atoms can interact with other atoms in other active regions in the geometry optimization process using standard optimization algorithms (**Section 3.3**). In inactive regions, atoms are frozen during the calculation. They bear fixed charges and provide a background of bulk lattice and the vacuum level for the inner active regions.

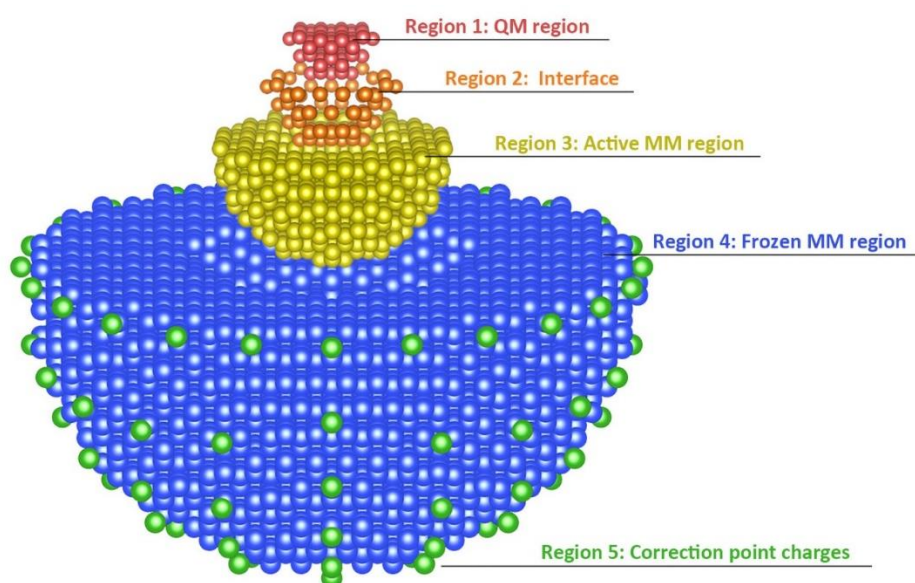


**Figure 3.1** The diagram of embedded QM/MM cluster in Chemshell.

**Region 1:** This is the most central region of the local state (for example, the defect site). It is the most important region, as all the atoms in this region are treated quantum mechanically and acquire the highest computational accuracy. Because the site of interest should normally be positioned as close to the central point as possible, the size of the region should be as large as possible to reflect the real material. However, in practice, the size of the region 1 bears up to 100 atoms, as higher volume might require too much computational resource.

The rim of the region 1 cluster is chosen to consist of cation species solely rather than anion or mixed ones. All the electrons should be mostly confined in region 1. Any electronic spill from the region 1 would deteriorate the resultant QM energy, especially LUMO and HOMO energies. Therefore, terminating region 1 with electron-deficient species prevents the electronic spill problem, as negatively charged electrons are attracted by the positively charged cations at the periphery of region 1 while being repelled by the negatively charged nearest neighbour anions positioned outside region 1.

**Region 2:** This is the “interface” region between the QM region and the MM region. How to construct the transition layer is always the most difficult part in the field of the QM/MM theory, as it is the key to maintain the chemical environment correct. The forces acting on the electrons in region 1 are from both QM (including both the electrostatic and exchange-correlation interactions) and MM regions (via the electrostatic and short-range interatomic interactions). These forces can be mismatched, so additional adjustment must be made in this region to achieve a chemical equilibrium.

In our case, the cations in region 2 are not treated using wavefunctions. Instead, the region comprises a set of pseudo-potentials in the form of the effective core potentials (ECP). ECPs are widely used in molecular quantum mechanical calculations as a form of supplement to large atom basis sets. For large atoms (often referred to as atoms in the 5<sup>th</sup> rows and after), the electrons occupying innermost orbitals (core orbitals) are chemically inactive and can be represented by a form of a core potential. The ECP approach is also often seen in calculations on solid-state materials again as the cores are relatively inert and only the valence electrons are involved in many chemical problems. Here in the QM/MM theory in Chemshell, ECPs are a suitable tool for the intermediate-level atomic

representation between QM and MM theory, as it can effectively model all the core electrons of the cations. Sometimes, common, or standard ECP needs to be refitted to achieve the chemical equilibrium of the system. Complementary to providing a chemically balanced environment on the cations in region 2, ECP also contribute to electron confinement for the central cation-terminated cluster. In such case, the electron can be localized better inside the QM region.

In the current approach, the anions in region 2, however, are not modelled by the ECP theory. Instead, they are described by the same short-range interatomic potentials as for the other atoms in the MM regions.

**Region 3:** This is the outermost active region, where the atoms are treated using the molecular mechanics approach. The suitable force field is developed separately in the MM software (GULP) to ensure that it can evaluate appropriate physical properties. The shell model is applied alongside to represent the polarization effects. The atoms in region 1 are subject to the field of the charges in region 3, 4 and 5 via the electrostatic potentials, and *vice versa*. On atoms in region 1 acts the potential generated by the environment referred to as embedding potential, which includes a field of background charges to the inner atoms. Thus, the interaction energy between atoms in region 1 and atoms in region 2-5, performs not only as the embedding potential for atoms in region 1 but also as the “polarization potential” on the outer atoms. A suitable force field should not distort neither the QM cluster nor the outer regions. Sometimes, the force field can be very versatile reflecting experimental data but not at all usable for the QM/MM application. If after geometry optimisation process, the implemented force field distorts the QM cluster badly, the force field needs to be adjusted.

**Region 4:** This is an inactive MM region that is pre-optimised using GULP but frozen in QM/MM calculations. At the outermost rim of region 4, the charges of some atoms are adjusted to maintain the charge neutrality of the whole QM/MM system and so minimise the effect of the cluster termination. The thickness of the region 4 is chosen to be greater than the longest cut-off distance in the force field, so that the missing atoms do not affect the inner active regions via short-range forces.

**Region 5:** The outermost region is for reproducing the Madelung field on the active region (region 1-3), mimicking the environment of infinite crystal remainder. It is accomplished by putting model “fluoride” ions around the whole cluster (region 1-4) equidistantly. The charges on these fake ions are fitted to affect the Madelung field on the active regions. There are six more model charges positioned on the poles around the cluster at long separation distances (they are not shown in **Figure 3.1**) to control the vacuum potential and mean electrostatic field.

The five-region QM/MM cluster is generated in a software called *construct*. It takes a geometry optimized unit cell structure from the pre-calculation on bulk material in MM software (GULP) and builds the QM/MM cluster from a selected central atom outward.

### 3.4.2 Energy calculation in Chemshell

In *Chemshell*, the total QM energy of all atoms in region 1 will be calculated first using a QM software (*Gamess-UK* or *NWChem*). The QM software calculates the lowest energy from the wavefunctions (spanned over basis sets) starting from initial guesses on region 1 atoms via the SCF process. The ECPs on region-2 atoms and point charges on region-3, -4, -5 atoms (core and shell species) contribute through the background potential to the total QM energy.

As the SCF process converges, the analytic energy gradients (forces) for all region-1 atoms with respect to their coordinates are calculated based on the resultant charge distribution. Forces on atoms in regions 2 and 3, due to their interactions with region-1 atoms are also calculated in the QM code. These gradient data are recorded and passed (via *Chemshell*) to the MM code.

In the initial stage of the calculation, the MM part of the calculation performs only shell relaxation. The MM analytic gradients are calculated first from the force field used here and recorded by *Chemshell* as MM gradient data; after which they are added with the gradients data passed from QM calculations. The MM code then evaluates the resultant gradients on shell species and optimises positions of shells accordingly.

After MM calculation, *Chemshell* continues a self-consistent iterative process to find the best solution for shell positions and the wavefunction. The RMS (the root

mean square) displacements of shell species on relaxation are evaluated to decide if the QM/MM convergence is achieved by *Chemshell*. If the RMS shell displacements are still high, Chemshell passes the new positions of shells to the QM code to start another cycle of the QM/MM calculation. The iterative process stops once the RMS of shell displacements reaches the required threshold.

The final total QM/MM energy is expressed in an additive form:

$$E_{total} = E_{QM} + E_{MM} + E_{QM/MM} + E_{corr.} \quad , \quad (3.22)$$

where  $E_{QM/MM}$  is the energy of interaction between QM and MM atoms, and  $E_{corr.}$  is the correction energy that sometimes applied in cluster calculations, e.g., the Jost correction.

Note that at this point, the centres of all atoms are frozen, i.e., no QM/MM geometry optimisation has yet been performed. In *Chemshell*, the calculation only involving shell relaxation is called *single-point energy and gradient* (SP) calculation. SP calculation is good for testing if the QM/MM environment setup is appropriate, as most of the convergence problems appear in the first cycle of geometry optimisation. On the other hand, as the shell positions can influence the gradients in region 1, a successful SP calculation can also improve the time spent on the subsequent QM SCF process and save resources.

### 3.4.3 Geometry optimization in Chemshell

The geometry optimization process is completed using the *DL-FIND*<sup>53</sup> package in Chemshell. The optimization is also iterative. There are 5 different types of criteria to determine whether the cluster is optimised. They are the change in energy value, maximum step, RMS of steps, maximum gradient component, and RMS of gradients. In each optimisation cycle, an SP calculation cycle is carried out, from which the energy and gradient values are used for calculating optimisation steps. Once it meets the minimum thresholds of the five criteria, the corresponding QM/MM cluster is said to be fully optimised. The SP calculation in geometry optimisation normally employs fewer shell relaxation cycles (4-5 shell cycles) to prevent excessive shell displacements. As the atoms are approaching the configuration of energy minimum, it is believed that the positions of the shells would already been optimized to a good degree, so there is no need for full shell relaxation during the geometry optimization process. However, after the end of



geometry optimization calculation, one should conduct another SP calculation of the optimized configuration for full shell relaxation to make sure the system is at absolute chemical equilibrium.

#### 3.4.4 Jost correction

For the defect at the centre area of the cluster, there is polarization effect appearing across the 3 active regions. Such a change in the shell positions does not happen explicitly in the outer frozen region 4 and 5. QM/MM model in theory ought to mimic an infinite environment for the defect species and in practice there should also be polarization contribution to the total energy from the outer regions. Instead of directly calculating the term atomistically, here a Jost correction<sup>54</sup> is introduced to estimate the sum of the polarization energy to infinity:

$$E_{jost} = -\frac{q^2}{2R} \left(1 - \frac{1}{\epsilon_r}\right) \quad . \quad (3.23)$$

Here we use the net charge,  $q$ , of the whole inner active region and  $\epsilon_r$  is the dielectric constant of the material (an arithmetic mean of the principal values of the dielectric tensor obtained from the MM calculation). For SP calculations that account for electronic polarisation, the high frequency  $\epsilon_r$  should be used. For geometry optimisation calculations, the static  $\epsilon_r$  should be used instead.

### 3.5 Summary

In this chapter, a wide range of computational techniques have been introduced, although mathematical details have in general been avoided. All the methods mentioned in this chapter are directly relevant to calculations that will appear in the following result chapters. Greater details of the techniques discussed will be found in the references.

## Chapter 4

# The MM Model and Defect Energetics of AlN

The MM study of AlN will be divided into two chapters. In this chapter, our focus is primarily on the development of our interatomic potential model that will be used for the Mott-Littleton point defect calculations of AlN. At the beginning of this chapter, the related background is illustrated including the literature review on both the experimental and other theoretical studies about the point defects in AlN. After that, the methodology that is applied in both chapters is introduced in detail. Our prediction of a wide range of physical properties is presented, which will be compared and discussed with other experimental and theoretical results.

### 4.1 Background

AlN, together with GaN and InN and in solid solution with various compositions of group-III nitrides (AlGa<sub>x</sub>N<sub>1-x</sub>, etc.), is one of the key materials for semiconductor light emitting devices. Having had the least attention among the three nitrides, AlN has started to gain more interest owing to its application in deep ultraviolet (wavelength shorter than 300 nm) light-emitting diodes (LEDs)<sup>15,55,56</sup>, due to its very wide band gap characteristic (6.07-6.28 eV measured from 5K to room temperature<sup>57-59</sup>, equivalent to around 197-204 nm of wavelength). The state-of-the-art AlN-based deep-UV lab LED was successfully made with a lowest possible wavelength of 210 nm<sup>56</sup>, the potential of which has stimulated great interest in the material. Some additional advantages, such as high thermal conductivity (285-320 W/m•K)<sup>3,6</sup> and high thermal stability, make AlN increasingly important in the fabrication of electronic devices.

There have been several publications reporting point-defect-related emission and absorption in AlN experimentally and theoretically. Identification of Al vacancy and N vacancy brings new insights into AlN<sup>6,60,61</sup>. It is generally suggested that

most of the emissions are attributed to deep states induced by Al vacancy defects, which often form Al-vacancy-O-impurity defect complexes. Numerous detected photoluminescence (PL) peaks have been assigned to either standalone Al vacancy or Al vacancy related complexes in AlN crystals from red light to deep-UV region: 1.4-2.4 eV by Lamprecht et al.<sup>62</sup>, 1.4-3.65 eV (“white light”) by Liu et al.<sup>63</sup>, 2 eV by Aleksandrov et al.<sup>64</sup>, 2.78 eV by Sedhain et al.<sup>65</sup>, 3.3 eV by Tojo et al.<sup>66</sup>, 3.6 eV by Mäki et al.<sup>67</sup>, 3.2-3.7 eV by Harris et al.<sup>68</sup> and Ichikawa et al.<sup>69</sup>. However, there have been several studies reported that the N vacancy, often associated with carbon impurities, can also be the origin of deep state emission<sup>70,71</sup>. Alden et al speculates the source of their measured 2.7 eV and 3.9 eV emission is N vacancy induced deep states<sup>70</sup>. Recently, AlN based single-photon emitter (SPE) at 550-1000 nm was successfully fabricated; Liu proposed point defects and their complexes play a significant role<sup>72</sup> in this property.

In this chapter and in **Chapter 5**, we report a computational study using the Mott-Littleton methods on wurtzite AlN and its extended defects, particularly the formations of Al vacancy and N vacancy, including both defect formation and migration energies. Computational studies on AlN in the last three decades were predominantly *ab initio* calculations, primarily the Density Functional Theory (DFT)<sup>71,73–81</sup>, but, in order to balance better results with reasonable computational expense, such methods often bear a limitation of no more than 200 atoms. Our method based on an empirical interatomic potential model is able to contain a system up to thousands of atoms. Though such classical approach will not give us any information on electronic structure, given an accurate set of potential models, we can obtain reliable defect energies and geometries as has been demonstrated by a large number of studies of oxides<sup>82–84</sup>. And owing to the development of the quantum mechanical/molecular mechanical (QM/MM) method in the last two decades, interatomic potential methods can contribute to hybrid approaches to defect modelling.

Since the first reported interatomic potential model for wurtzite AlN in the last century<sup>85</sup>, there has been a number of evolutions over the last two decades. The earliest pair-wise Coulomb and Buckingham potential implementations originated from the ionic properties of AlN<sup>85,86</sup>, where such constructions of the models can retain low number of empirical parameters, and in the meantime obtain an

accurate prediction on defect energetics and the physical properties including lattice constants, elastic constants and dielectric constants<sup>86</sup>. However, since then, the ionic study on the material has halted, and, due to the vast popularity of lattice dynamic studies, all the later developed AlN interatomic potential models took the route of covalent property of the material. Accurate predictions on physical properties have been seen from these molecular mechanic methods of bond order Tersoff potential models<sup>87–92</sup>, three-body potential models<sup>93,94</sup> and other many-body models<sup>95</sup>. Over the years, these more complex interatomic potentials are increasing their numbers of parameters, but the differences in their outcomes are marginal. In AlN, a simple 2-body interaction model still proves to be quite effective, especially in investigating defect energetics in the material. In this work, we present a new pair-wise interatomic potential model for wurtzite AlN system, from which we will present a comprehensive study on intrinsic defects in the material.

## 4.2 Methodology

### 4.2.1 Two-body interatomic potential

As noted, our approach uses the Mott-Littleton methodology, for which it is necessary to derive a suitable interatomic potential. The first interatomic potentials for AlN were reported by Cormack<sup>85</sup>, using a shell model with formal charges. Later models include those of Chisholm<sup>86</sup> which employed partial charges. In both works, only a Buckingham potential was used whereas in our work a set of functionals was used, giving a more accurate and smooth potential profile, which has been successfully applied to oxides lately<sup>83</sup>. All the parameterisations were completed via empirical fitting using the GULP code<sup>96</sup>. **Table 4.1** shows the fitted potential parameters used in the present work.

The classical interatomic potential model in this work is based on Born model<sup>97</sup> of the ionic solid. Both the wurtzite structure adopted by AlN, and the dielectric properties of the material are consistent with the use of the ionic model. In this work, to obtain a precise and smooth profile of interatomic potentials across short-range and long-range distances, we fitted a combination of pair-wise Coulomb, and short-range Buckingham, Lennard-Jones, and polynomial

potentials, to experimental data including lattice constants, elastic constants, dielectric constants, and piezoelectric constants.

Regarding the short-range potentials, for the interaction between the cation and anion, here we employ the Buckingham potential which is the most used form in modelling ionic solids:

$$V_{Buckingham} = Ae^{-r/\rho} - \frac{C}{r^6} \quad (4.1)$$

The Lennard-Jones potential is applied here covering the whole interatomic short range, with  $C_6$  to be zero, to prevent atoms collapsing from getting too close:

$$V_{Lennard-Jones} = \frac{C_{12}}{r^{12}} - \frac{C_6}{r^6} \quad (4.2)$$

Polynomials are applied connecting the different Buckingham potentials, where the atoms are not observed:

$$V_{polynomial} = C_5r^5 + C_4r^4 + C_3r^3 + C_2r^2 + C_1r + C_0. \quad (4.3)$$

$r$  is the internuclear distance between two atoms. And  $A$ ,  $\rho$ ,  $C$ ,  $C_{12}$ ,  $C_6$ ,  $D_e$  and the polynomial  $a_n$ ,  $b_n$ ,  $C_n$  constants are all variable parameters that are adjusted by either manually or automatically during the fitting process. The chosen values for these parameters will be discussed in the later paragraph.

Between anions, GULP has the 4-range Buckingham (Buckingham-4) potential of separated Born-Meyer (for 1<sup>st</sup> neighbouring atoms) and dispersion (for 2<sup>nd</sup> neighbouring atoms) terms,

$$V_{Buckingham-4} = \begin{cases} Ae^{-r/\rho}, & r_{min} < r < r_{cut1} \\ a_5r^5 + a_4r^4 + a_3r^3 + a_2r^2 + a_1r + a_0, & r_{cut1} < r < r_{cut2} \\ b_3r^3 + b_2r^2 + b_1r + b_0, & r_{cut2} < r < r_{cut3} \\ -\frac{C}{r^6}, & r_{cut3} < r < r_{max} \end{cases} \quad (4.4)$$

where same concept of treating active and inactive atomic regions separately is adopted here achieved in a condense form.

Here we apply the *pair potential approximation*, which is normally an acceptable approximation for ionic solids. In addition, polarisation of the nitride ions is included via the shell model<sup>31</sup>, which provides a simple mechanical model of polarizability in which the ion is divided into a core linked by an harmonic spring to

a shell and which has proved effective in modelling dielectric properties of ionic materials. The polarizability of the free ion is given by:

$$\alpha = \frac{Y^2}{k} \quad , \quad (4.5)$$

where  $Y$  is the charge of the shell and  $k$  is the spring constant. The energy from such spring interaction can be formulated in squared and quartic terms:

$$V_{spring-2} = \frac{1}{2}k_2r^2 \quad \text{and} \quad V_{spring-4} = \frac{1}{4}k_4r^4 \quad . \quad (4.6)$$

As noted, in our model, the aluminium ion is treated as unpolarizable, i.e., core only, whereas the nitride ion is polarisable with both a core and a shell. Two main short-range interactions are considered, i.e. “Al-core-N-shell” and “N-shell-N-shell”. For many ionic materials, Buckingham potential is still proved to be an effective model, so here it is used within all the distance ranges where atoms are observed. The parameters of the potential for “Al-core-N-shell” interaction are all fitted empirically against experimental properties. The attractive parameters  $A$  and  $\rho$  in the “N-shell-N-shell” Buckingham potential are obtained from the previous Buckingham potential for binary oxides, which successfully predicts defect properties and defect diffusion<sup>98</sup>. For the dispersion parameter  $C$  in the “N-shell-N-shell” Buckingham potential, we applied the theory first introduced in the work by Pyper<sup>99</sup>. According to the Slater-Kirkwood formula<sup>100</sup>, the dispersion parameter is determined by the polarizability and the shell effective electron number of the species. For  $N^{3-}$  ion, the effective electron number is chosen to be 4.455, same as the Ne atom and  $O^{2-}$  ion<sup>99</sup>. The dispersion constant  $C$  must be smaller than the one previously fitted for GaN<sup>101</sup>, to match the smaller anion polarizability in AlN. The parameter is therefore downscaled by 1/4.455 from the one used in GaN<sup>101</sup>. The polynomial functions do not affect material properties. They are calculated to connect all the regions in the Buckingham potentials, under the condition that the 1<sup>st</sup> and 2<sup>nd</sup> derivatives at both end points must be matched. The cut-offs of both short-range potentials are 10Å, which is ~3 times the experimental lattice constant  $a$  and twice the constant  $c$ . Between “N core” and “N shell”, the interactions are controlled solely by harmonic spring (including squared and quartic terms). The resulting parameters are reported in **Table 4.1**.

**Table 4.1** The 2-body short-range interatomic potential parameters of wurtzite AlN. (Al core charge: +3; N core charge: +1.4; N shell charge: -4.4.)

Species	Potential functions	Parameters	$r_{min}$ - $r_{max}$ (Å)	
Al core - N shell	Born-Meyer	$A = 1400.00$ eV $\rho = 0.3350$ Å	0.0 - 2.2	
	Polynomial	$C_0 = 0.65$ eV	0.0 - 2.2	
	Polynomial	$C_0 = 4639.62$ eV $C_1 = -9312.72$ eV•Å <sup>-1</sup> $C_2 = 7473.93$ eV•Å <sup>-2</sup> $C_3 = -2992.99$ eV•Å <sup>-3</sup> $C_4 = 597.52$ eV•Å <sup>-4</sup> $C_5 = -47.55$ eV•Å <sup>-5</sup>	2.2 - 2.8	
		Born-Meyer	$A = 640.00$ eV $\rho = 0.382$ Å	2.8 – 3.3
		Polynomial	$C_0 = -0.07$ eV	2.8 – 3.3
		Polynomial	$C_0 = 122628.01$ eV $C_1 = -180945.37$ eV•Å <sup>-1</sup> $C_2 = 106770.43$ eV•Å <sup>-2</sup> $C_3 = -31492.42$ eV•Å <sup>-3</sup> $C_4 = 4643.11$ eV•Å <sup>-4</sup> $C_5 = -273.75$ eV•Å <sup>-5</sup>	3.3 – 3.5
			Lennard-Jones	$C_{12} = 10.42$ eV•Å <sup>12</sup>
	N shell - N shell		Buckingham-4 $A = 22764.3$ eV $\rho = 0.1490$ Å $C = 74.00$ eV•Å <sup>6</sup>	0.0 – 10.0 ( $r_{cut1} = 3.5$ , $r_{cut2} = 4.0$ , $r_{cut3} = 5.0$ )
	N core - N shell		Spring $k_2$	$63.00$ eV•Å <sup>-2</sup>
Spring $k_4$		$50000.00$ eV•Å <sup>-4</sup>	0.0 – 0.5	

The resulting structural parameters for the wurtzite structure elastic constants, bulk modulus and lattice energy are obtained are shown in the **Table 4.3**: the lattice constants and dielectric constants agree well with experimental and other *ab initio* computational results, although there are significant discrepancies in the off-diagonal elastic constants. We note that other groups had reported better reproduction of the off-diagonal elastic constants by employing three-body, bond-order, or other many-body types of interatomic potential models<sup>87–95</sup>. However, in those models, they do not include proper charge of the species and other means of dielectric contribution, so they are not suitable for defect calculations. We also note that although the previous two-body interatomic potential model presented a

slightly better fitting of elastic constants, the lattice energy is particularly low<sup>86</sup>, as a result of the choice of partial charge resulting in a much lower Madelung potential. A reliable lattice energy value is crucial in our calculation of defect energy as presented in the following sections.

We also calculate the phonon dispersion curve using our 2-body potential model (**Figure 4.1**) to find the source of the discrepancies in the off-diagonal elastic constants. At the  $\Gamma$  point, the calculated phonon frequencies agree well with the experimentally measured frequencies of E2 (low), A1 (LO), and E1 (LO) modes. However, the calculated frequency of mode A1 (TO) is higher than the ones of E2 (high) and E1 (TO), whereas from the experiment the former frequency is lower than latter two frequencies. As shown in **Figure 4.1**, the two red curves representing the A1 (TO) phonon mode propagating along  $\Gamma - K - M$  (the “ab-plane”) and  $\Gamma - A$  (the “c-axis”) are both steeper than the experimental measurement, which in turn makes the values of  $C_{12}$  and  $C_{13}$  higher. This proves that our 2-body model is incapable of predicting off-diagonal properties.

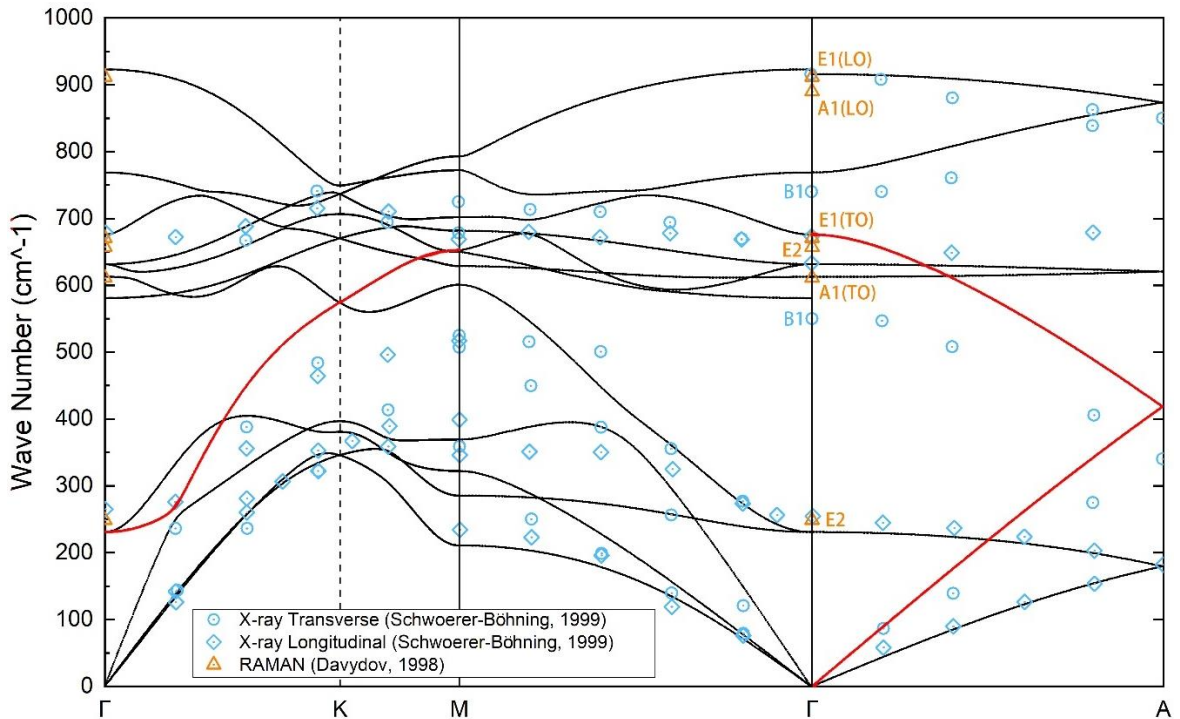


**Figure 4.1** The calculated phonon dispersion curve (black) using our 2-body interatomic potential model (the red curves indicate the “problematic” part which causes the discrepancies in the off-diagonal elastic constants). The experimental data is also presented for comparison. (Reference for



experimental data: X-ray by Schwoerer-Bohning et al.<sup>102</sup>, and Raman by Davydov et al.<sup>103</sup>)

#### 4.2.2 Three-body interatomic potential

For proving 3-body interatomic potential can improve the prediction of the elastic constants, we fit another set of potential by adding a 3-body potential to the same 2-body ones. Here the 3-body interatomic potential takes the form of:

$$V_{3-body} = K e^{-\rho_2(r_{12}-R_0^{12})} e^{-\rho_3(r_{13}-R_0^{13})} , \quad (4.7)$$

where  $K$ ,  $\rho_2$ , and  $\rho_3$  are the constants fitted empirically,  $R_0^{12}$  and  $R_0^{13}$  are the bond lengths of Al-N of perfect lattice, and  $r_{12}$  and  $r_{13}$  are the interatomic distances between Al and different neighbouring N atoms. Here we assume that the “Al core” interacts equally with the two neighbouring “N shell”, so  $\rho_2$  and  $\rho_3$  are fixed to be the same. As introducing additional potential, in order to calculate the properties correctly, the parameters of our 2-body interatomic potential for “Al core” and “N shell” interaction must be refitted. The 2-body Buckingham potential of “N shell” and “N shell” remains unchanged. **Table 4.2** presents all the parameters of the potential, and **Table 4.3** shows the prediction of the properties using the new 3-body potential model. Now all the properties agree well with experimental and *ab initio* results, except for one of the piezoelectric constants. However, as we will discuss in the following section, the adopted 3-body model is not suitable for defect calculations without some additional compensating terms in the force field. And such a compensation can in turn worsen the predicted physical properties. Therefore, for our defect study, the 2-body form of potential is applied primarily.

The GULP input scripts for the physical property calculation using the 2-body and 3-body interatomic potential model are both presented in Appendices.

**Table 4.2** The 2-body and 3-body short-range interatomic potential parameters of wurtzite AlN. (Al core charge: +3; N core charge: +1.4; N shell charge: -4.4.)

Species	Potential functions	Parameters	$r_{min}$ - $r_{max}$ (Å)		
Al core - N shell	Born-Meyer	$A = 1776.79 \text{ eV}$ $\rho = 0.3270 \text{ Å}$	0.0 - 2.2		
	Polynomial	$C_0 = 0.35 \text{ eV}$	0.0 - 2.2		
	Polynomial	$C_0 = 2032.03 \text{ eV}$ $C_1 = -3965.36 \text{ eV} \cdot \text{Å}^{-1}$ $C_2 = 3110.78 \text{ eV} \cdot \text{Å}^{-2}$ $C_3 = -1222.38 \text{ eV} \cdot \text{Å}^{-3}$ $C_4 = 240.12 \text{ eV} \cdot \text{Å}^{-4}$ $C_5 = -18.84 \text{ eV} \cdot \text{Å}^{-5}$	2.2 - 2.8		
		Born-Meyer	$A = 2222.25 \text{ eV}$ $\rho = 0.3277 \text{ Å}$	2.8 – 3.3	
		Polynomial	$C_0 = -0.07 \text{ eV}$	2.8 – 3.3	
		Polynomial	$C_0 = -16719.30 \text{ eV}$ $C_1 = 24150.45 \text{ eV} \cdot \text{Å}^{-1}$ $C_2 = -13939.89 \text{ eV} \cdot \text{Å}^{-2}$ $C_3 = 4019.23 \text{ eV} \cdot \text{Å}^{-3}$ $C_4 = -578.88 \text{ eV} \cdot \text{Å}^{-4}$ $C_5 = 33.32 \text{ eV} \cdot \text{Å}^{-5}$	3.3 – 3.5	
			Lennard-Jones	$C_{12} = 10.42 \text{ eV} \cdot \text{Å}^{12}$	0.0 - 10.0
			N shell - N shell	Buckingham-4	$A = 22764.3 \text{ eV}$ $\rho = 0.1490 \text{ Å}$ $C = 74.00 \text{ eV} \cdot \text{Å}^6$
	Al core - N shell 1 - N shell 2		3-body exponentials	$K = -0.1442 \text{ eV}$ $\rho_2 = 4.73 \text{ Å}^{-1}$ $R_{12} = 1.89 \text{ Å}$ $\rho_3 = 4.73 \text{ Å}^{-1}$ $R_{13} = 1.89 \text{ Å}$	0.0 – 12.00 (Both bonds)
	N core - N shell	Spring $k_2$	$63.00 \text{ eV} \cdot \text{Å}^{-2}$	0.0 – 0.5	
Spring $k_4$		$50000.00 \text{ eV} \cdot \text{Å}^{-4}$	0.0 – 0.5		
Correction term for the Mott-Littleton defect calculation					
Al core – N core	Born-Meyer	$A = 1776.79 \text{ eV}$ $\rho = 0.3270 \text{ Å}$	0.0 – 12.00		

**Table 4.3** Calculated and experimental properties of wurtzite AlN.

Property	Present 2-body	3-body	Experimental	Other IP	DFT
Lattice constant, $a$ (Å)	3.11	3.10	3.11 <sup>a</sup>	3.11 <sup>a</sup> ,	
Lattice constant, $c$ (Å)	4.98	4.98	4.98 <sup>a</sup>	5.00 <sup>i</sup> , 4.97 <sup>a</sup> , 4.98 <sup>j</sup> , 5.07 <sup>k</sup> , 5.04 <sup>m</sup>	
Special position, $u$ (Å)	0.380	0.379	0.382 <sup>b</sup>	0.380 <sup>j</sup> , 0.375 <sup>k</sup>	
<b>Elastic constants</b>					
$C_{11}$ (GPa)	515.9	365.1	345 <sup>c</sup> , 411±10 <sup>d</sup>	417 <sup>a</sup> , 293 <sup>j</sup> , 392 <sup>k</sup> , 435 <sup>l</sup> , 463 <sup>m</sup>	464 <sup>n</sup> , 398 <sup>n</sup> , 396 <sup>n</sup>
$C_{12}$ (GPa)	274.3	117.3	125 <sup>c</sup> , 99±4 <sup>d</sup>	178 <sup>a</sup> , 161 <sup>j</sup> , 137 <sup>k</sup> , 148 <sup>l</sup> , 92 <sup>m</sup>	149 <sup>n</sup> , 140 <sup>n</sup> , 137 <sup>n</sup>
$C_{13}$ (GPa)	261.8	105.1	120 <sup>c</sup> , 99±4 <sup>d</sup>	152 <sup>a</sup> , 151 <sup>j</sup> , 101 <sup>k</sup> , 108 <sup>l</sup> , 104 <sup>m</sup>	116 <sup>n</sup> , 127 <sup>n</sup> , 108 <sup>n</sup>
$C_{33}$ (GPa)	564.7	460.6	395 <sup>c</sup> , 389±10 <sup>d</sup>	432 <sup>a</sup> , 303 <sup>j</sup> , 428 <sup>k</sup> , 356 <sup>l</sup> , 437 <sup>m</sup>	409 <sup>n</sup> , 382 <sup>n</sup> , 373 <sup>n</sup>
$C_{44}$ (GPa)	138.1	135.6	118 <sup>c</sup> , 125±5 <sup>d</sup> , 122±1 <sup>e</sup>	125 <sup>a</sup> , 96 <sup>j</sup> , 114 <sup>k</sup> , 81 <sup>l</sup> , 194 <sup>m</sup>	128 <sup>n</sup> , 96 <sup>n</sup> , 116 <sup>n</sup>
$C_{66}$ (GPa)	120.8	123.9		120 <sup>a</sup> , 129 <sup>j</sup> , 128 <sup>k</sup> , 144 <sup>l</sup>	
<b>Dielectric constants</b>					
$\epsilon_{11}^0$	10.52	9.78	8.8 <sup>a</sup> , 9.14 <sup>f</sup> , 8.5 <sup>g</sup> , 8.0 <sup>h</sup>	8.07 <sup>a</sup>	
$\epsilon_{33}^0$	11.90	10.53	9.5 <sup>h</sup>	11.22 <sup>a</sup>	
$\epsilon_{11}^\infty$	4.64	4.60	4.7 <sup>a</sup> , 4.84 <sup>f</sup> , 4.6 <sup>g</sup>	4.46 <sup>a</sup>	
$\epsilon_{33}^\infty$	4.79	4.72		4.85 <sup>a</sup>	
<b>Piezoelectric constants</b>					
$e_{33}$ (C/m <sup>2</sup> )	3.58	1.22	1.55 <sup>h</sup>		1.80 <sup>p</sup> , 1.50 <sup>p</sup> , 1.50 <sup>q</sup>
$e_{31}$ (C/m <sup>2</sup> )	-2.25	-4.52	-0.58 <sup>h</sup>		-0.64 <sup>p</sup> , -0.53 <sup>p</sup> , -0.60 <sup>q</sup>
<b>Bulk modulus, <math>B_0</math></b>	354.4	203.5	201 <sup>c</sup> , 210 <sup>d</sup>	248 <sup>a</sup> , 202 <sup>j</sup> , 210 <sup>k</sup> , 211 <sup>l</sup> , 218 <sup>m</sup>	228 <sup>n</sup> , 218 <sup>n</sup> , 207 <sup>n</sup>
<b>Lattice energy (eV)</b>	-90.07	-90.07		-98.209 <sup>i</sup> , -43.50 <sup>a</sup>	

(a <sup>86</sup>, b <sup>104</sup>, c <sup>9</sup>, d <sup>105</sup>, e <sup>106</sup>, f <sup>12</sup>, g <sup>107</sup>, h <sup>108</sup>, i <sup>85</sup>, j <sup>94</sup>, k <sup>91</sup>, l <sup>93</sup>, m <sup>95</sup>, n <sup>109</sup>, o <sup>110</sup>, p <sup>111</sup>, q <sup>112</sup>)

### 4.2.3 Mott-Littleton calculations

Our potential is implemented in Mott-Littleton<sup>113</sup> calculations of defect energies. The method which is discussed in detail in<sup>96</sup> divides the lattice around the central defect into 3 regions. In the inner region (region I), displacements of the atoms are calculated by explicit energy minimisation. Secondly, the displacement of atoms in the middle region (region IIa) is calculated by harmonic interactions with respect to the central defect, but with explicit calculation of the interaction energy with region 1. The outer region is treated as a dielectric continuum which responds to the effective charge of the defect. In this work, the radii of region I and region IIa are 21 Å and 36 Å respectively; with these values all defect energies have converged to within 0.1 eV with respect to subsequent expansion. All the potential fitting and defect calculation in this work were done by using the GULP code<sup>29</sup>.

Using the 3-body potential in **Table 4.2**, we found that the Mott-Littleton defect energy cannot converge for all four intrinsic defects without the additional correction in the force field. The pre-exponential parameter  $K$  is fitted empirically to be negative, which indicates the 3-body potential acts as an attractive force. As a defect is introduced, the cluster is likely to contract due to the additional attractive force, which leads to abnormally high potential gradients at energy minimum position. As a result, a repulsive term must be added in the force field to counteract the force. We employ a form of the Buckingham repulsive force between the Al core and the N core:

$$V_{3-body,corr.} = D e^{-r/\rho_D} \quad , \quad (4.8)$$

where constants  $D$  and  $\rho_D$  are first determined analytically and then fitted empirically.  $\rho_D$  needs to be smaller than  $1/(\rho_2 + \rho_3)$  (same  $\rho_2$  and  $\rho_3$  in the 3-body potential). And  $D$  must be big enough to counteract the 3-body potential, so we have the formular by equating the correction term to the 3-body potential and we get:

$$D \geq (m - 1) K \rho_2 \rho_D e^{(2\rho_2(R_0^{12} - R_D) + \frac{R_D}{\rho_D})} \quad , \quad (4.9)$$

where  $m$  is the maximum coordination number of the defect (6 for the interstitial defect),  $R_D$  is the shortest bond length of the defective cluster ( $\sim 1.7$  Å), and the

rest of the parameters are from the 3-body potential. However, the compensation term results in worsening the physical properties. We further adjust the  $D$  and  $\rho_D$  value to reduce the deviation of the observing physical properties while the Mott-Littleton calculation can still converge. Both parameters are presented in **Table 4.2**.

### 4.3 Defect energetics

We first apply our approach to obtaining estimates of electron and hole formation energies, then calculate formation energies for both vacancy and interstitial species, before modelling defect migration processes.

#### 4.3.1 Defect energies from Mott-Littleton calculations

The intrinsic point defect energies of AlN are presented in **Table 4.4**. Owing to the nature of our method and potentials, all point defect energies are calculated with their formal charges. We note that the energies are all with respect to the perfect lattice and ions at infinity.

**Table 4.4** Intrinsic defect energies in AlN.

Defect type	Present		Cormack <sup>85</sup>
	2-body	3-body	
$N_i'''$	-32.43	-32.21	-12.561
$V_N'''$	51.49	53.12	52.108
$Al_i'''$	-32.98	-32.24	-40.694
$V_{Al}'''$	51.51	53.06	62.998

There are two distinctive sites/voids for the Al interstitial in the wurtzite structure adopted by AlN: the T (tetrahedral) and O (octahedral) sites (**Figure 4.2**). An interstitial in the T “chamber” has four cations and four anions as the nearest neighbours, while at the O site has two nearest neighbours (one cation and one anion) and six next nearest neighbours. An alternative approach to envisaging the O interstitial sites is from the perspective of the  $z$ -axis, where the interstitial at O

site sits around the centre of the “channel” (It should be noted that the defect will not be stabilised at the exact centre of the channel, so the “O’ site” is used in other works, e.g.<sup>114</sup>. In our work, we use “O site” for this defect). Previous work found the interstitial at the O site is more stable than at the T site in AlN<sup>76</sup> and also in GaN<sup>78,114</sup>. In our work, when the Al interstitial is initially located at a T site it moves during the minimisation to the O site. Hence, only results for this configuration are presented here.

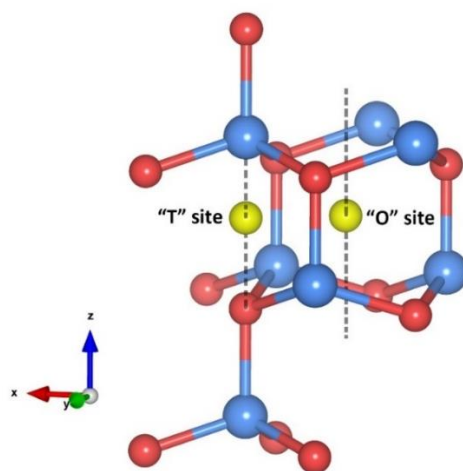


**Figure 4.2** Tetrahedral (T) and octahedral (O) site for interstitial defect in wurtzite AlN (Al is in blue, N is in purple and interstitial site is in pink).

For the N interstitial, our calculation using both the 2-body and the 3-body potential shows the defect energy is close to its cation counterpart (**Table 4.4**). The introduced  $N^{3-}$  ion (N1 in **Figure 4.3**) is positioned at the “O site” as the Al interstitial does. The introduced interstitial pushes another on-site  $N^{3-}$  ion away from its original position (N2 in **Figure 4.3**) due to the large repulsive force between the two  $N^{3-}$  ions. The distance between the two N ions is calculated to be  $2.47\text{\AA}$ . The two N ions shown in **Figure 4.3** indicate a split interstitial configuration, which two bonded N atoms share the same N lattice site. The configuration is widely reported in other *ab initio* studies, but in those literature the split interstitial in the charge state -3 is not discussed due to the high formation energy<sup>76,81,110,115</sup>. Cormack<sup>85</sup>, using the shell model and interatomic potential,

reports that the  $N^{3-}$  interstitial defect energy is much higher than the cation counterpart (**Table 4.4**). The report admits its large difference between the results of both interstitials and speculates that the source could be from the different sizes of both species<sup>85</sup>. However, the interatomic potential in that report does not calculate as good elastic, piezoelectric, and dielectric constants as that used in this work.

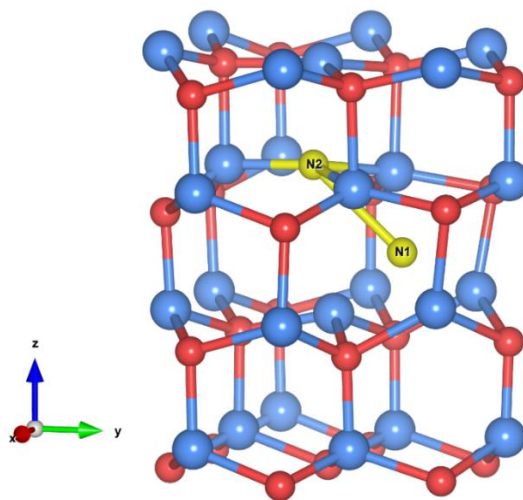


**Figure 4.3** The N interstitial defect after relaxation. (N1 is the introduced interstitial defect, N2 is the host atom)

#### 4.3.2 Electron and hole formation

Computational models based on interatomic potentials cannot provide accurate estimates of electronic energies calculations, but a useful estimate of hole and electron energies is still possible. We assume that the conduction band minimum (CBM) can be represented by an electron localising on a cation (Al) and the valence band maximum (VBM) by a hole on an anion (N), *i.e.*, the electron state is thus approximated as a localised  $Al^{2+}$  state, and the hole state as a localised  $N^{2-}$  state. By using our interatomic potential model and Mott-Littleton method in GULP, defect energies of  $Al^{2+}$  and  $N^{2-}$  are calculated. To model optical excitations, only shells are relaxed during these calculations, *i.e.*, there is no thermal relaxation of the lattice. In addition, we must include appropriate intra-atomic terms. Here we make another simplification that such intraatomic energies are equal to their respective ionisation energies as free ions. The third ionisation

potential of Al is available for experiment. The third electron affinity of N is not a measurable quantity but has been calculated using the QM/MM techniques<sup>48</sup>. All the energy terms are presented in **Table 4.5**.

**Table 4.5** Electron and hole formation energy in wurtzite AlN.

	eV
$Al^{2+}$	32.46
$N^{2-}$	34.68
$Al^{2+} \rightarrow Al^{3+} + e'$	29.89
$N^{2-} + e' \rightarrow N^{3-}$	27.44
Calculated CBM (localising $e'$ )	2.57
Calculated VBM (localising $h'$ ) ( $-E_h$ )	-7.24
Calculated bandgap	9.81
Experimental bandgap (at low temperature)	6.23 <sup>25</sup>
Revised CBM ( $-E_e$ )	-1.01

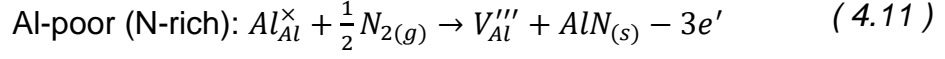
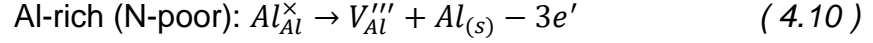
The calculated VBM is 0.96 eV lower than the experimental ionization potential on the AlN surface of 8.2 eV<sup>116</sup>. We obtain a higher bandgap energy (9.81 eV) than reported experimentally (6.23 eV at low temperature). The calculated CBM value is clearly problematic, which can be attributed to our assumption of a localised  $Al^{2+}$  state. The experimental value of the electron affinity of AlN is uncertain with estimates, ranging from 0.25-1.9 eV<sup>116–118</sup>, but our calculated CBM value is still far from these data. As our approach appears to be more reliable for estimating a hole state, we can get the revised CBM value by adding experimental bandgap energy at low temperature over to our VBM value. The revised CBM now falls within the range of experimental values.

#### 4.3.3 Vacancy defect reaction energies

In this section, the reaction energies for formation of the N and Al vacancy point defects, corresponding to different conditions will be discussed.



The reaction forming an aluminium vacancy in the AlN lattice is represented by the following equations depending on the Al and N chemical potentials, assuming the three electrons are localized at the CBM:



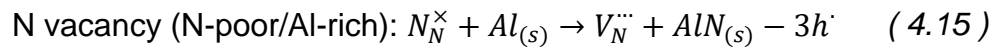
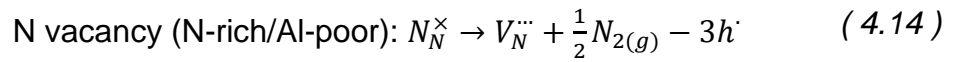
where we use the Kröger–Vink notation. The “Al-rich” or “Al-poor” conditions indicate the respective reactions occurring in the case of either Al excess or Al deficiency, (as in the environment of semiconductor doping in a MOCVD fabrication system). The Born-Haber cycles for these reactions are as follows:

$$\text{Al-rich (N-poor): } E_{V_{Al}, \text{ Al-rich}} = E[V_{Al}'''] - \frac{H_{S/Al}}{Al} - \sum_1^3 IE_{Al} + 3E_e \quad (4.12)$$

$$\text{Al-poor (N-rich): } E_{V_{Al}, \text{ Al-poor}} = E[V_{Al}'''] - \frac{H_{S/Al}}{Al} - \sum_1^3 IE_{Al} + \Delta H_{AlN(s)} + 3E_e \quad (4.13)$$

where  $E[V_{Al}''']$  is the defect energy of Al vacancy in table,  $H_{S/Al}$  heat of sublimation of Al solid (3.43 eV<sup>119</sup>),  $IE_{Al}$  the ionisation energy of Al,  $\Delta H_{AlN(s)}$  the experimental value of enthalpy of AlN formation (-3.296 eV<sup>119</sup>) and  $E_h$  the energy creating a hole in valence band from vacuum (7.24 eV, as given in **Table 4.5**). The experimental ionisation energies of Al can be extracted from the database (53.26 eV<sup>119</sup> for sum of the 3 outer electrons).

Applying the same approach to the nitrogen vacancy, assuming three holes are localized at the VBM, the following defect reactions can be formulated:



And the respective formation energies are as following:

$$\text{N vacancy (N-rich/Al-poor): } E_{V_N, \text{ N-rich}} = E[V_N'''] - A_N^{1-3} - \frac{1}{2}D_{N_2} - 3E_h \quad (4.16)$$

$$\text{N vacancy (N-poor/Al-rich): } E_{V_N, \text{ N-poor}} = E[V_N'''] + \Delta H^0(AlN) - A_N^{1-3} - \frac{1}{2}D_{N_2} - 3E_h \quad (4.17)$$

where  $A_N^{1-3}$  is the sum of the three electron affinities of N atom. The experimental electron affinity energies of nitrogen atom are not readily available yet, but one

can estimate the sum of three electron affinities via the Born-Haber cycle for AlN formation ( $Al_{(s)} + \frac{1}{2}N_{2(g)} \rightarrow AlN_{(s)}$ ). Our energy of three electron affinities of N atom is calculated as 25.19 eV. The dissociation energy of  $N\equiv N$  pair ( $D_{N_2}$ ) is chosen to be 9.79 eV<sup>119</sup>.

**Table 4.6** Formation energies (eV) of Al vacancy ( $V_{Al}'''$ ), N vacancy ( $V_N''''$ ), Al interstitial ( $Al_i''$ ), and N interstitial ( $N_i'''$ ) in wurtzite AlN (units in eV). (The calculation results from other studies are obtained approximately from their defect transition energy figures. The “CBM” and “VBM” in the table indicate the location of Fermi level in the bandgap at which the formation energy is calculated.)

	Present	Other calc. approx.
<b><math>V_{Al}'''</math> (CBM)</b>		
Al-poor/N-rich	-5.46	~-2.90 <sup>a</sup> , ~-3.60 <sup>b</sup>
Al-rich/N-poor	-2.16	~-0.40 <sup>a</sup> , ~-0.20 <sup>b</sup>
<b><math>V_N''''</math> (VBM)</b>		
Al-poor/N-rich	-0.31	~-0.20 <sup>a</sup> , ~0.40 <sup>b</sup> , ~0.20 <sup>c</sup>
Al-rich/N-poor	-3.61	~-3.00 <sup>a</sup> , ~-3.00 <sup>b</sup> , ~-3.00 <sup>c</sup>

(a:<sup>110</sup>, b:<sup>71</sup> & c:<sup>80</sup>)

**Table 4.6** summarises our calculated formation energies. For  $V_N''''$ , formation energy is higher in N-rich condition, while the formation energy of  $V_{Al}'''$  is higher in Al-rich condition, which agrees with other works using first-principle methods<sup>71,77,80,110,120,121</sup>. Direct comparison with experiment is difficult and comparison with earlier electronic structure calculations is not straightforward as the latter are often reported as a function of the position of the Fermi level. In **Table 4.6**, we compare reported formation energies at the edges of the band gap. The energy for the N vacancy agrees well with other DFT calculations in either environment conditions. Our energies for Al vacancy are 2.06-2.76 eV lower than DFT results in Al-poor condition (2.17-2.77 eV in Al-rich condition). The Al ionization potential and the N electron affinities are linearly correlated with each other in the Born-Haber cycle of AlN formation, determined by the value of the

lattice energy calculated from GULP. Therefore, the formation energies of N vacancy and Al vacancy are also linear dependent with the Al ionization energy (or N electron affinity) in the defect reactions above.

#### 4.3.4 Formation of Frenkel and Schottky defects

From the energies reported in (**Table 4.4**) we can calculate energies of the Schottky and Frenkel pairs listed below:

Schottky defect:



Anti-Schottky defect:



Anion Frenkel defect:



Cation Frenkel defect:



From these reactions we have the formation energies per defect of each type ( $E[AlN]$  is the lattice energy of AlN in **Table 4.3**):

$$E_{Schottky,AlN} = \frac{1}{2} (E[V_{Al}'''] + E[V_N'''] - E[AlN]) \quad (4.22)$$

$$E_{Anti-Schottky,AlN} = \frac{1}{2} (E[N_i'''] + E[Al_i'''] - E[AlN]) \quad (4.23)$$

$$E_{Anion\ Frenkel,AlN} = \frac{1}{2} (E[N_i'''] + E[V_N''']) \quad (4.24)$$

$$E_{Cation\ Frenkel,AlN} = \frac{1}{2} (E[V_{Al}'''] + E[Al_i''']) \quad (4.25)$$

All the energies are summarised in **Table 4.7**. For AlN, Schottky disorder has the lowest energy, suggesting that Al and N vacancy pairs will be the dominant disorder type in the material. The finding is in good agreement with the previous works by Cormack<sup>85</sup> and Chisholm<sup>86</sup> using interatomic potential methods, although these authors did not report results for the “Anti-Schottky” energy. The considerably higher Schottky defect energy here compared with that reported by Chisholm, et al., reflects the choice of interatomic potential, especially the differences in ionic charges.

**Table 4.7** Frenkel and Schottky Defect formation energies per defect (in eV), and results from previous studies using interatomic potential methods.

Defect type	Present		Previous calculations	
	2-body	3-body	Cormack <sup>85</sup>	Chisholm, et al. <sup>86</sup>
Schottky	6.46	8.99	8.45	5.17
Anti-Schottky	12.33	11.57	22.48	
Al Frenkel	9.26	10.55	11.15	6.62
N Frenkel	9.53	10.01	19.77	7.40

In summary, in this chapter, we develop two sets of interatomic potential, a two-body type and a three-body type. For predicting the physical properties, our three-body interatomic potential is superior to our two-body potential, particularly on the off-diagonal elastic constant prediction. However, for the point defect Mott-littleton calculations, additional correction term must be added to the three-body interatomic potential, whereas our two-body type does not have such problem.

All types of intrinsic defects have been calculated using the MM theory. The Schottky pair defect complex is the most energetically likely that would appear in AlN. We have also tried to calculate the VBM electronic level and defect formation energies by using our two-body potential, and their results are comparable to other existing DFT results. The CBM level, however, is poorly reproduced, which shows the limitation of predicting electronic states using such method.

Next chapter, we will be discussing the migration of the intrinsic point defects.

# Chapter 5

## Point Defect Migration

Following the development of interatomic potential and the calculations of defect energetics in the last chapter, here we will be focusing on the point defect migration in AlN.

### 5.1 Background

The motion of native defects controls atomic transport, material growth and degradation. However, there is very little information on this aspect of AlN, despite the extensive interest in III-V nitride semiconductor materials over the last few decades. Experimental studies have been limited to oxygen<sup>122</sup> or dopant diffusion<sup>123,124</sup>, but none is on intrinsic defect diffusion. After Limpijumnong & Van de Walle's comprehensive theoretical study on intrinsic defect migration in GaN using DFT, several other studies followed<sup>81,125–129</sup>. But there has not been a comprehensive computational investigation on intrinsic defect migration in AlN, only some comparisons with GaN<sup>81,128</sup>. Here we will present our computational results of a systematic study of defect migration in AlN and compare with currently available data from studies on GaN.

Our approach is to perform a comprehensive search of the energy landscape for the migrating species. Along each path, 10-20 points with equal distance are marked and RFO transitional energy calculation are conducted at each point until a suitable transition state is identified. The transition states are further confirmed by the single negative vibrational frequency of the defect. A final check involves a steepest descent optimisation from each transitional state on both directions (to initial ground state and to final ground state). Hence, we define a valid migration path as that involving a continuous route which can be successfully connected by steepest descent minimisation via one or multiple transitional states. We note the

need for the Mott-Littleton defect cluster centre to be at the mid-point of the path so that the activation energies are accurate and reliable.

## 5.2 Results

### 5.2.1 Vacancy migration

The migration of vacancy involves a neighbouring ion moving into the vacancy. We investigate the migration of  $V_{Al}'''$  and  $V_N^{\bullet\bullet}$  in wurtzite AlN lattice on vertical direction (out-of-plane) and horizontal direction (in-plane, perpendicular to  $c$  axis, **Figure 5.1**). Although we note vacancy self-diffusion in similar materials was reported to be isotropic in previous reports<sup>114,126,127</sup>, here the two directions will be studied separately. In **Table 5.1** we present our activation energies and other currently available related data on AlN, GaN and InN for comparison.

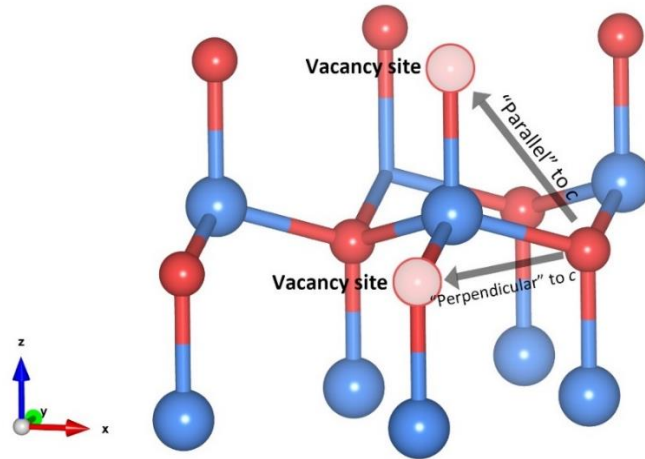


**Figure 5.1** Horizontal and vertical directions of vacancy migration in wurtzite AlN (noted that these arrows are not actual paths, merely an illustration of migration directions)

Our results for the energy barrier of 1.67 eV with Al migrating vertically and 2.62 eV horizontally. Such difference in energy barriers on different directions originates from the different interatomic distances between the migrating species and its neighbouring atoms. As the Al ion departs from its ground state position horizontally, it approaches a single N ion at 4.96 Å away and two N ions at ~ 3.7 Å. As Al departs vertically, it moves towards two furthest N ions both at 4.51 Å

away and a single N ion at 3.12 Å. The different starting local geometries around the moving Al ion cause the different geometries and different energies at their transition states. The initial ground state positions, transition state positions and the interatomic distances are presented in **Figure 5.2**. Our higher horizontal barrier of Al vacancy migration matches the results from the work of Aleksandrov, et al.<sup>128</sup>, where by using first-principle method the barrier for the Al vacancy migration is higher than that for the Ga vacancy migration in GaN. In addition, Hrytsak, et al.<sup>130</sup> calculates higher vertical migration barrier in InN for both cation and anion. However, Warnick, et al.<sup>126</sup> presents a lower barrier (1.6 eV) of Al vacancy migration in AlGaN alloy than in pure GaN, which agrees with our lower barrier results. Our results show, Al vacancy migration can occur with a relatively modest activation energy 1.67 eV in energy, and the migration would preferably occur perpendicular to the “ $a - b$ ” plane.

**Table 5.1** Results of activation energies (eV) of vacancy migrations in AlN and other calculated results on AlN and GaN.

	This work		Other Calculations			
	Horizontal	Vertical	AlN <sup>128</sup>	GaN <sup>114,125–128,130</sup>	InN <sup>130</sup>	
Direction	Horizontal	Vertical	V	unclear	H	V
Cation vacancy	2.62	1.67	2.33, 2.53	1.9, 2.0, 2.01, 2.24, 2.1, 2.28	2.12	2.27
Anion vacancy	2.92	2.20		2.0, 2.6, 2.7, 2.47	1.80	2.34

We found a similar mechanism for the N vacancy migration. Our calculated N vacancy migration barrier is 2.92 eV horizontally and 2.20 eV vertically. Even though there is no available data for AlN for us to compare, our results are higher than the calculated activation energies in GaN, which agrees with the reported higher barrier trend of N vacancy in the AlGaN alloy<sup>126</sup> and the previous DFT calculation results<sup>81</sup>. Compared with the ionic radii of Al<sup>3+</sup> and Ga<sup>3+</sup> ions, the N<sup>3-</sup> ion is much bigger (by a factor of three compared with Al<sup>3+</sup> and of two for Ga<sup>3+</sup>), so it is expected the migration will be more hindered in AlN, with higher migration barriers. To our knowledge, no experimental data are available to compare to date.

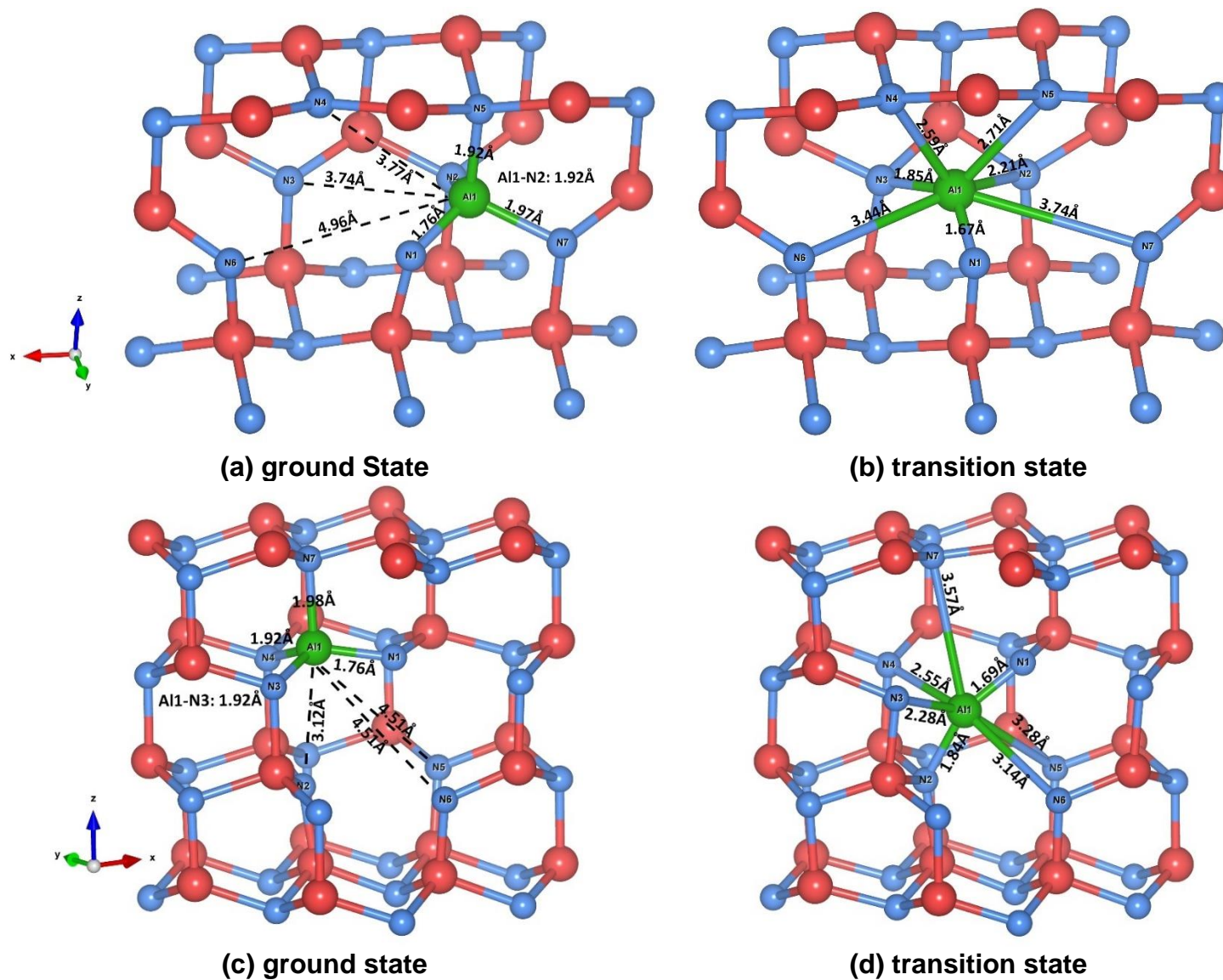


**Figure 5.2** The lattice geometry of Al vacancy migration: horizontal migration in (a) & (b); vertical migration in (c) & (d).



### 5.2.1 Interstitial migration

We first discuss Al interstitial migration, and then later N interstitial migration; different approaches are needed for the two species.

As stated in **Chapter 4**, Al interstitials are stable at the O-site. Therefore, the migration path between two nearest neighbour O-sites can either be along the hexagonal channel (along the  $c$ -axis) or horizontally passing the T-site. Here we apply the same methodology as for the vacancies where steepest descent search follows valid saddle point identification. From our calculation, the latter motion involves an “interstitialcy” mechanism in which the migrating Al interstitial knocks on and replaces a host Al ion, with the “knocked-out” Al ion becoming a new interstitial defect moving towards its closest neighbouring O-site (**Figure 5**). This horizontal migration is energetically more favourable than the vertical migration through the hexagonal channel (**Table 5.2**). Our activation energy is very close to that of Ga interstitial migration in GaN, which again supports our reasoning in **Section 5.2.1**.

**Table 5.2** Results of activation energies (eV) of interstitial point defect migrations in AlN and other calculated results on GaN

		This work	GaN <sup>114,127</sup>
<b>Cation interstitial</b>	C-axis channel path	1.42	3.00
	Interstitialcy mechanism	0.93	0.90, 0.7
<b>Anion interstitial</b>	C-axis channel path	2.04	
	Interstitialcy mechanism	1.32	1.4

Migration of the N interstitial has a more complex mechanism due to the large double-N bonding energy. The N interstitial is easily pulled or dragged by other on-site N ions resulting in the distortion around the introduced defect. Like the investigation of Al interstitial migration, we assume that there could also be parallel and perpendicular motion for N interstitial migration with respect to  $c$  axis, so saddle point and initial/final stable states searches are also undertaken here for both. A more detailed account of the procedure is given below.

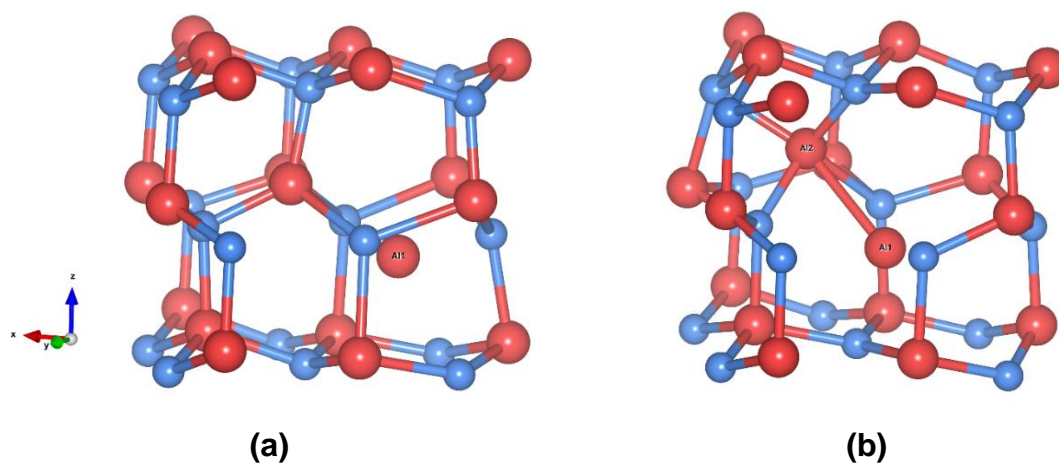


**Figure 5.3** Atomic visualisation of horizontal Al Interstitial migration (looking through hexagonal channel): (a) initial ground state; (b) transitional state (saddle point)

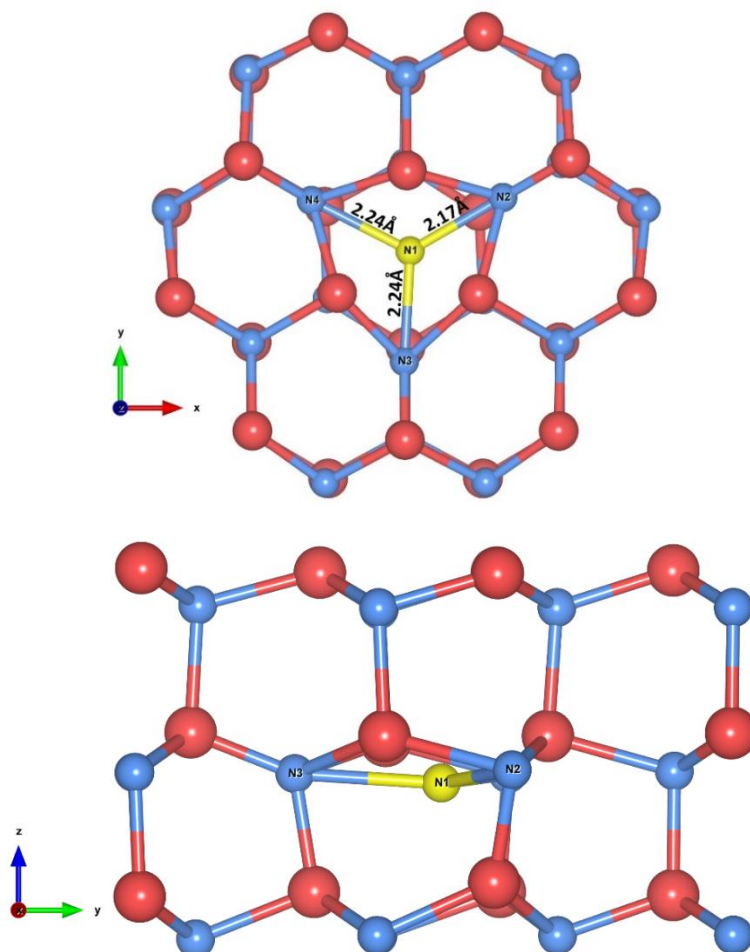


**Figure 5.4** Atomic visualisation of the transition state of N Interstitial defect migration through hexagonal channel: see from z-axis (above); see from x-axis (below)

For the migration through the hexagonal channel, at the saddle point three nearest neighbouring N ions are pushed away by the defect forming three “split-interstitial” configurations with different bond lengths—all three are shorter than stable split-interstitial defect (**Figure 5.4**). This interaction between three N ions makes it more difficult for the defect to return to the initial/final stable configuration, inducing a higher migration barrier.

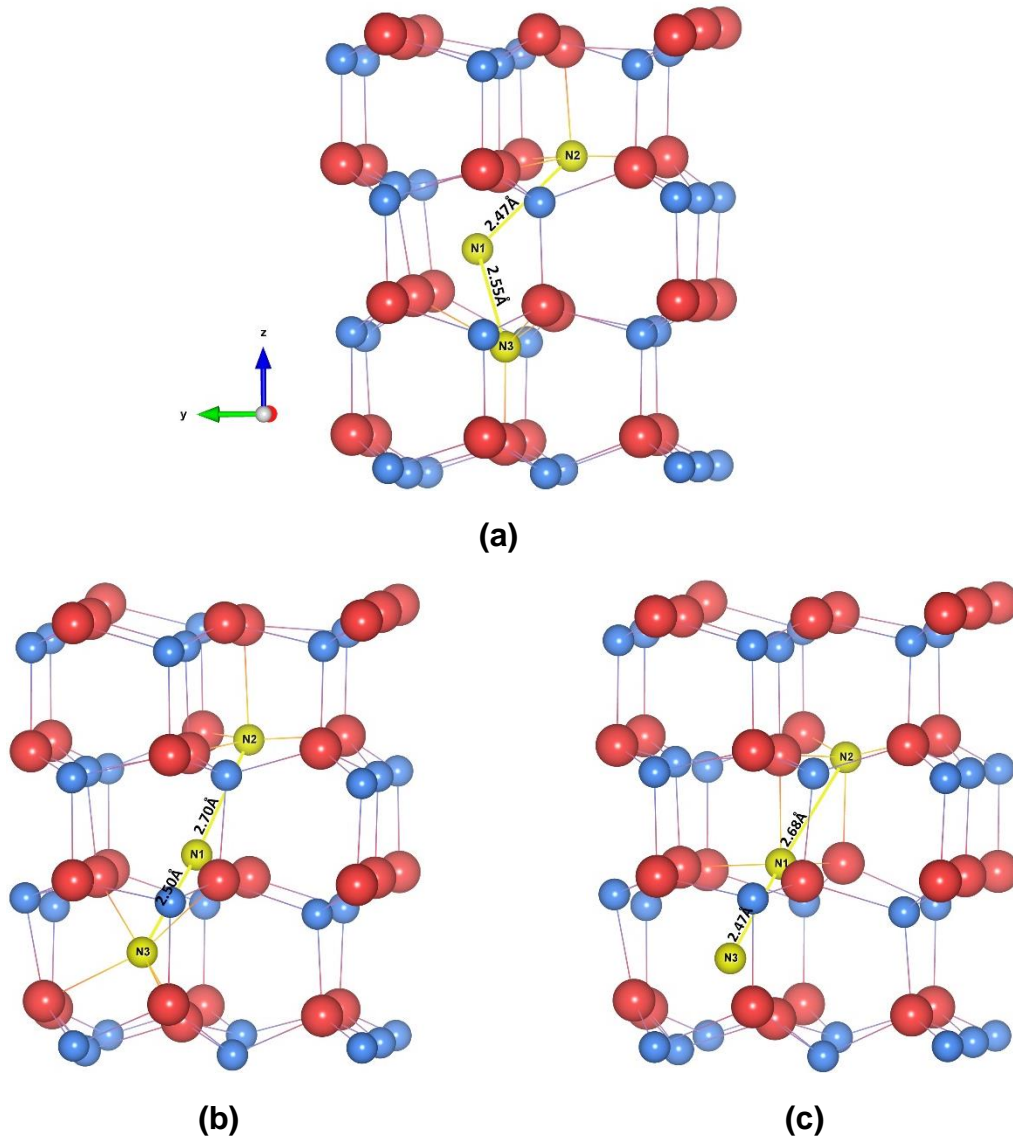


**Figure 5.5** Atomic visualisation of the “hand-over” mechanism of N Interstitial defect migration (looking from x-axis): (a) initial state; (b) transitional state (saddle point); (c) final state

For the other migration mechanism, we found a path in single unit cell with a much lower barrier. Here we applied an iterative approach to find the transition state. At first, we located two closed stable split-interstitial defect configurations at neighbouring lattice layers. These two configurations are rotational symmetric, so they are likely to be the initial and final states of the path. At the first time, the interstitial N defect (N1 in **Figure 5.5**) is moved along the straight line from N2 to N3. N1 is kept fixed on the path, as we relaxed only the surrounding ions to give us energy potential surface with respect to N1. Afterwards, we conducted RFO transition state search on each resulting configuration until a transition state (proved by single negative vibrational frequency) is found. Now we have a new possible migration path of two straight lines connecting three points (N1 to N2 and N1 to N3). We then again move the defect along this new path and repeat the same process iteratively until the highest saddle point is found. At the end, as with all other types of migration, a steepest descent optimisation is conducted to verify the path.

The resultant migration motion is illustrated in **Figure 5.5** and is close to previous reports on GaN<sup>14</sup>. The path has two rotationally symmetric split-interstitials as its initial and final stable configurations. At the saddle point, another nearest neighbouring N ion (N3) is pushed away from its original position while the initial split-interstitial configuration maintains with a stretched bond. As the defect approaches its final position forming a new stable pair, the “left-over” N (N2) ion slowly moves back to a closest lattice site. This “hand-over” motion between three N ions is significantly different from the “knock-on” mechanism of the Al interstitial, where the former is due to attraction between N ions and the latter one repulsion between Al ions.

The migration barriers/activation energies for both mechanisms are presented in **Table 5.2**. Our result shows the “hand-over” mechanism is energetically more favourable than the hexagonal channel migration. This barrier is also comparable to the result of the same migration mechanism in GaN, which supports the earlier reasoning related to the N ion size.

### 5.3 Summary and conclusion

Following Chapter 4, we have implemented our interatomic potential model to further investigate the point defect migration. A comprehensive atomistical investigation of point defect migration suggests that the energy barriers and migration paths of self-diffusion behaviour in AlN are overall closed to the counterparts in GaN. The migration barrier of Al vacancy is 1.67 eV, at least 0.23 eV lower than the calculated results of Ga vacancy migration barrier in GaN. Different to previous calculations, the migration of vacancy is not isotropic in our calculation. Different heights of migration barriers are assigned to the vertical and the horizontal directions. For the interstitial defect migration, the energy barrier of *c*-channel Al interstitial migration is 1.42 eV, 1.58 eV lower than the GaN counterpart. Different “interstitialcy” migration mechanisms are seen in cation and anion interstitial migration. For the Al interstitial, the on-site Al atom can be “knocked-out” and replaced by the approaching interstitial defect. And for the N interstitial, to maintain the stable split-interstitial configuration, the interstitial first bonded with one on-site N atom is handed-over to the other closest on-site N atom. The study of point defect migration here not only proves the integrity of our new interatomic potential model, but also introduces another approach to the study of defect diffusivity.

# Chapter 6

## QM/MM Study of Defects in AlN

### 6.1 Introduction

In the last two chapters, the energetics and mobility of the point defects is investigated by the means of MM methods, but all the defects are in their formal charges. As discussed in **Chapter 2**, defects can be in different charge states. The charge state plays a key role in determining the donor/acceptor nature of the defect, and in affecting the thermal and optical transitions of the material. Here in this chapter, using the embedded QM/MM technique, a systematic study of differently charged intrinsic point defects in AlN is presented.

Experiment has identified both cation and anion vacancies as the most common native defects in AlN, and they are the most investigated ones in the literature<sup>2</sup>. These native vacancies<sup>65,131–139</sup>, as well as related defect complexes with oxygen impurities<sup>131,132,135,140–156</sup> (mostly Al-vacancy-O-substitution), are proposed to be a possible source of deep-state luminescence from the band gap. Other unintentional or intentionally doped impurities include silicon<sup>133,157,158</sup> and carbon<sup>158–163</sup> that are also found to be stable in the material. All these defects can act as either donors (donating electrons) or acceptors (accepting electrons and creating holes) in the material, and they can change their role between donor and acceptor by changing their charge. And different charges on the same defect give rise to different energy states in the band gap region. The complex physics and chemistry of such defects can be explored by the state-of-the-art computational techniques.

Density functional theory (DFT) is the best tool so far to probe into the realm of charged state defects in AlN. There has been already a few theoretical reports of comprehensive investigation on defect types such as native vacancies, interstitials, anti-sites, impurities, and defect complexes. The early computational works on AlN were ground-breaking, providing insights into atomic and electronic

configurations of defects in the material, but they all suffered from band gap underestimation, which is inherent to local density approximation (LDA) used in their calculations<sup>76,164</sup>. Nevertheless, these works were able to confirm that vacancies should be dominant in the material, and which vacancy species will be dominant would depend on environment (whether it is N-rich or Al-rich)<sup>76,164</sup>. Moreover, they were able to explore the types of defects in AlN that have not been seen in experiment, like nitrogen split-interstitials, anti-sites and many other impurities<sup>53</sup>.

More recently, DFT calculations tend to use hybrid functionals that improve on the old LDA and GGA functionals that underestimate the band gap energy<sup>76,164</sup> and poorly reproduce related physical properties<sup>53</sup>. Further, the fast improvement in computer power allows one to use the “higher-rung” DFT functionals in calculations on larger system. Some popular hybrid functional options for solid-state material include the Heyd–Scuseria–Ernzerhof (HSE)<sup>68,70,71,80,81,110,115,165–170</sup> and the Perdew–Burke–Ernzerhof (PBE0)<sup>14,16,57</sup> functionals. In particular, for wide-gap AlN, HSE is more favourable as its Hartree-Fock portion is tuneable for reproducing the more accurate physical properties such as lattice constants, enthalpy of formation, and band gap<sup>110</sup>. In addition, these later works calculate configuration-coordinate diagrams of defect processes trying to match optical transition predictions with experimental photo-absorption and photoluminescence energy bands, although their findings may vary.

In both experimental and theoretical studies of defects in AlN, there remain unsolved problems. Differences in positions of the photo-absorption/luminescence bands and conclusions drawn often vary from study to study, despite already much experimental effort on the topic. One of the key reasons is the unprecise control over eliminating unwanted and introducing intended impurities and native defects. It is often difficult to identify whether it is a particular type of defects or a group of different defects causing a certain wavelength of photo-response. In theoretical studies, current DFT methods are mostly implemented for a system constructed based on periodic boundary condition (PBC) in the plane-wave based software. In the problem of charged defects, such an implementation gives an ambiguous description of the reference potential level, and therefore unreliable description of electron ionisation

processes. Additionally, supercell system, which is often constructed for these DFT calculations, suffers from the finite-size effect<sup>172</sup>. For defect calculations, the defect is periodically repeated in each supercell causing spurious interactions between defects in adjacent supercells, which requires the system being corrected upon the calculation of charged defects. Moreover, the choice of hybrid functionals has strong influence on the results. The reasons above cause a wide spread of results from different computational studies, which makes the interpretation of the experimental data even more difficult and unclear.

In this chapter, instead, we are using a hybrid quantum mechanical/molecular mechanical (QM/MM) embedded cluster method for the investigation of electronic and optical properties of point defects in AlN. In the method, localised defect has real interactions with surrounding environment, governed by short-range and long-range electrostatic forces and polarization effects. The surrounding reacts to a perturbation from the central active region, as the charge of the defect changes. In this way, the ionization process of the defect will no longer be ambiguous as in the PBC method, so it has a real reference, or vacuum level and correct ionisation energy. In principle, there are also limitations in our method, where it is difficult to calculate a highly diffuse defect state. The diffuse electronic part of the defect will be confined due to the nature of embedded system, which might cause electron over-localisation and wrong electronic exchange-correlation energy. The goal of this chapter is to report a body of systematic work on charged defects in AlN using the hybrid QM/MM method. There will be three hybrid functionals used here. We will compare our results with other reports in the current literature using other hybrid functionals, and, where available with experiment.

## **6.2 Computational techniques**

There are three levels of theory employed in the hybrid QM/MM embedded cluster technique. At the central region, where the localised defect state is positioned, QM theory is applied. The choice of our QM method is DFT, which is the most widely used method for materials electronic studies. Outside of the QM region, the surrounding environment is treated with MM theory, which includes the interatomic potentials and polarisable shell model. At the interface between



QM and MM theory, some of the cations are treated with semi-local pseudopotentials (effective core potentials, ECP). The ECPs act as a compensation for the mismatch in the QM and MM environment for the outermost QM atoms, so that it minimises the stress on the QM cluster. In general, the ECPs need to be adjusted to work with the force field implemented in the technique. The outer layer of the environment includes a frozen MM region. And at last, at the rim of the whole QM/MM system, there are intentionally put point charges to reproduce the Madelung potential of the infinite crystal around the defect site. A more detailed discussion of the technique is in **Chapter 3** and in the original publication of the method<sup>48</sup>.

The final results are taken from the calculation of the 86-atom ( $\sim 5\text{\AA}$ ) QM cluster of the wurtzite structured AlN, which is pre-optimized in GULP using the MM model. The cluster is centred on an aluminium atom and terminates with cations. The choice of cation termination is to prevent the electronic spill from the QM region, so that the electrons are more likely to localize, and the HOMO value is more reliable. In principle, it is desirable to use as big cluster as possible, we find that the 86-atom cluster is sufficient to obtain reasonable results without spending too much computer resources (see previous works<sup>173–175</sup>). Smaller sized clusters (usually of 42 or 43 atoms depending on whether it is cation- or anion-centred) is also used for some trial runs before the actual production calculations.

The QM cluster is treated with three different DFT hybrid functionals, PBE0<sup>35,36</sup>, B97-2<sup>37</sup> and BB1K<sup>39</sup>. The 25% Hartree-Fock (HF) exchange portion for PBE0 is the same as for the HSE functional used in many recent reports. The 21% HF exchange for B97-2 was fitted by the authors to a broad range of thermodynamic data, which would give accurate prediction of defect formation energies. And BB1K bears the highest portion of HF exchange (41%) in this work, which can give a more accurate description of the electronic processes in the material, such as defect transition levels. The goal of using three hybrid functionals is to see how they will perform on different tasks, compared with other theoretical and experimental results. The type of basis set for both Al and N is def2-TZVP<sup>43</sup>. The outer most diffuse as well as high angular momentum basis functions are removed for both species ( $f$  or N, and  $d$  &  $f$  for Al), as they contribute very little to the results while contributing to unwanted electron spillage to the environment and

waste computational time. Both the active and frozen MM regions are treated with same two-body interatomic potential that is fitted empirically to a broad range of structural and physical properties of bulk wurtzite AlN (see **Chapter 4**). The thickness of both MM regions is about 15 Å (containing atoms at the order of 10000 for both regions), which is the largest cut-off of the short-range interatomic potentials. To solve the mismatch between the QM region and MM region, a local ECP is fitted separately in the *FIT\_MY\_ECP* software<sup>176</sup> for the Al atoms at the interface region, minimising: (i) the gradients on the atoms in the QM, interface and active MM region; (ii) energy scatter of innermost localised states on anions<sup>174</sup>. The fitted parameters of the ECP are presented in the *appendix*. **Table 6.1** shows the calculated structural results and bond lengths after geometry optimisation using our QM/MM setup. Our results are in good agreement with experiment and other computational results using different techniques. One should note that the lattice constants  $a$ ,  $c$  and internal structural parameter  $u$  in **Table 6.1** are characteristics of an infinite periodic crystal, so they are only meaningful in comparison of experimental, MM and DFT PBC results. For a small cluster in Chemshell calculation, these values are measured at the central region (sometimes called central cell), so that we can make sure the cluster is not distorted against the embedded environment.

**Table 6.1** Structural data after geometry optimisation calculated by Chemshell using four different hybrid functionals (PBE0, B97-2, BB1K and HSE03 (with tuned 33% HF exchange)), compared with MM results, experimental results, and other DFT results.  $d$  is the bond length in Å.

	Chemshell				GULP	Exp.		DFT calc.
	PBE0	B97-2	BB1K	HSE03 (33% HF)	Forcefield (This work)	300 K <sup>25</sup>	90 K <sup>177</sup>	HSE03 (33% HF) <sup>110</sup>
$a$	3.148	3.148	3.148	3.112	3.112	3.112	3.115	3.107
$c$	4.976	4.976	4.976	4.983	4.983	4.982	4.988	4.974
$u$	0.385	0.385	0.385	0.380	0.380	0.382	0.379	0.382
$c/a$	1.581	1.581	1.581	1.601	1.601	1.601	1.601	1.601
$d_{cluster}^{central}$	1.915	1.915	1.915	1.928	$d$	1.894	1.903	1.893
$d_{cluster}^{rim}$	1.906	1.915	1.906	1.878				

The hybrid QM/MM method is realised in the Chemshell software (TCL version<sup>47,53</sup> and Python version<sup>49</sup>). The QM software is NWChem<sup>178</sup> (main production calculations) and GAMESS-UK<sup>179</sup> (for ECP fitting). The MM software for pre-optimisation and the hybrid technique is GULP<sup>29</sup>. A number of reports have been published using the same method for GaN<sup>173,180,181</sup> and for other ionic materials<sup>175,182–185</sup>.

To account for the missing polarisation effect in the frozen MM region and beyond to infinity, a correction term is applied on any non-neutral charged defects states. Such correction is formulated by Jost<sup>54</sup>,

$$E_{Jost} = -\frac{q^2}{2R} \left(1 - \frac{1}{\varepsilon_r}\right) . \quad (6.1)$$

where  $q$  is the charge of the defect,  $R$  is the radius of the active region (region I, II, and III), and  $\varepsilon_r$  is the dielectric constant of the material. In the case of an adiabatic process (e.g., the fully optimised states),  $\varepsilon_r$  equals to the static dielectric constant,  $\varepsilon_0$ . In the case of a vertical process (e.g., electron ionisation and optical excitation) where relaxation only involves electrons, an appropriate form of Jost's correction is applied involving the high-frequency dielectric constant  $\varepsilon_\infty$ ,

$$E_{Jost}^{vertical} = -\frac{(q+\Delta q)^2}{2R} \left(1 - \frac{1}{\varepsilon_\infty}\right) + \frac{q^2}{2R} \left(\frac{1}{\varepsilon_\infty} - \frac{1}{\varepsilon_0}\right) . \quad (6.2)$$

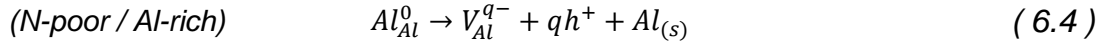
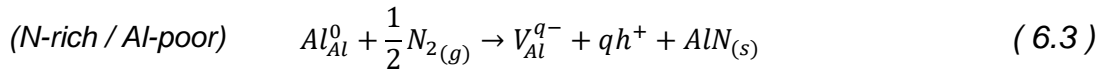
which describes the vertical transition from  $q$  to  $q + \Delta q$ . Here our  $\varepsilon_0$  is 10.98, and  $\varepsilon_\infty$  is 4.68. These values are found by averaging over dielectric tensors components calculated in GULP (see **Chapter 4**). As the QM cluster is a part of the infinite pre-optimised in the MM software environment, to keep the calculation consistent, it is reasonable to use the corresponding calculated values of the dielectric constants instead of, for example, experimental values (with which our calculation shows good agreement).

### 6.3 Calculation of defect formation energies

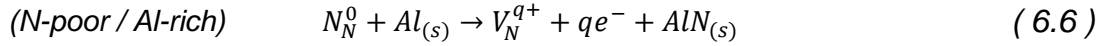
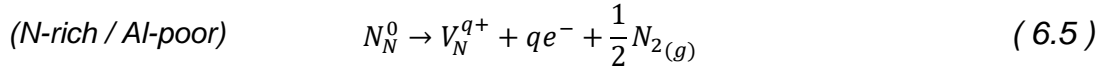
The formation energy of a defect is calculated as the enthalpy of each defect reaction. To distinguish the growth condition during defect forming process, the terms “N-rich/Al-poor” and “N-poor/Al-rich” are used to indicate which species is dominate in the ambient environment. Below all types of defects discussed in this chapter and their defect reactions are presented, in which  $q$  is the charge

(magnitude) state of the defect,  $e^-$  is an electron and  $h^+$  is a hole. Unlike the Kröger-Vink notation used in Chapter 4, we are using a new form to represent all the defect reactions, as it is more convenient to consider all the charge states of each defect in a single formular. For example,  $Al_{Al}^0$  is equivalent to  $Al_{Al}^\times$  in the Kröger-Vink form representing an Al on the Al lattice site in neutral charge,  $V_{Al}^{q-}$  represents a negatively  $q$  charged Al vacancy point defect ( $V_{Al}^{3-}$  is equivalent to  $V_{Al}'''$  in the Kröger-Vink form), and  $Al_i^{q+}$  represents a positively  $q$  charged Al interstitial point defect ( $Al_i^{3+}$  is equivalent to  $Al_i^{\cdot\cdot\cdot}$  in the Kröger-Vink form).

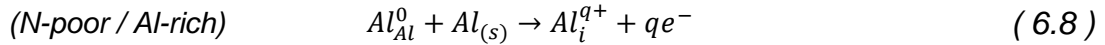
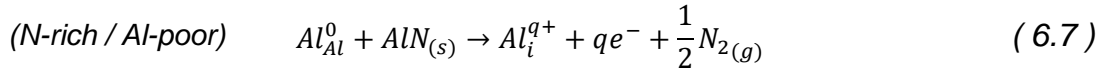
For Al vacancy:



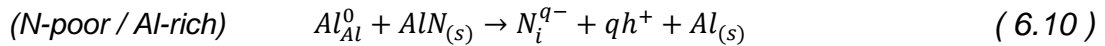
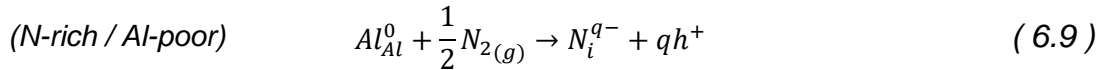
For N vacancy:



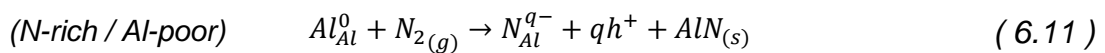
For Al interstitial:

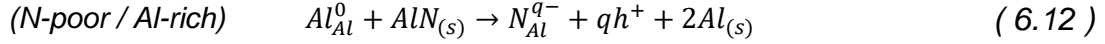


For N interstitial:



For N antisite:





Here the Al antisite defect is not considered. The Al ion is three times smaller than the N ion. Additionally, Al metal is not likely to be in an anionic state, and the regular positively charged Al ion will be highly instable if surrounded by four other  $Al^{3+}$  ions in the lattice. Moreover, the formation energy of neutral Al interstitial defect calculated in Chemshell is around 14.21eV, about 4eV higher than that of a neutral Al interstitial at the octahedral site.

The total energy of a perfect cluster (energies of  $N_N^0$  and  $Al_{Al}^0$ ) and the total energy of defective clusters (energies of  $V_N^{q+}$ ,  $V_{Ga}^{q-}$ ,  $N_i^{q-}$ ,  $Al_i^{q+}$ , and  $N_{Ga}^{q-}$ ) are calculated using the hybrid QM/MM technique. For the intrinsic defects in chemical equilibrium, the source (or the sink) for their formation is  $N_2$  gas, solid metallic Al, and solid AlN. Here we calculate the heat of formation of the  $N_2$  gas in NWChem using the three different functionals (PBE0: -109.44 Ha; B97-2: -109.529 Ha; BB1K: -109.521 Ha). The heat of formation of solid Al is calculated starting from the gas phase in NWChem (PBE0: -242.248 Ha; B97-2: -242.367 Ha; BB1K: -242.383 Ha), and then subtracting the experimental enthalpy of sublimation of Al (0.1257 Ha<sup>186</sup>). Depending on the ambient environment, formation energy can also include the formation of a solid compound. Here, we use the experimental enthalpy of formation of solid AlN (-0.121 Ha<sup>186</sup>), which is the energy difference between the defect forming under the two conditions. The basis set using to calculate all above energies is the same (with the diffuse and high angular moment polarisation functions removed).

Here for convenience, the charge transition process is denoted as<sup>181</sup>:  $X(Q_1|Q_2)c$ , where  $X$  indicates the type of defect,  $c$  is the carrier type ( $e$  for electron and  $h$  for hole),  $Q_1$  is the initial charge state, and  $Q_2$  is the final charge state. Thus, the notation is shorthand for the reaction process:



## 6.4 Results and discussion

### 6.4.1 Ionization potentials

As the description of the vacuum level is not ambiguous in our hybrid QM/MM method, the ionisation potential of the material (IP) can be calculated directly using the formula:

$$E^{IP} = E^{ionised} - E^{perfect} + E^{corr.}, \quad (6.14)$$

where  $E^{perfect}$  and  $E^{ionised}$  are the QM/MM total energy before and after an electron is ionised, respectively, and  $E^{corr.}$  is the polarisation correction energy, which equals to the vertical Jost correction for the “+1” charge state ( $E^{corr.} \approx -0.38$  eV from eq. (6.2)). As shown in **Table 6.2**, our calculated IP (and thus the VBM level) values sit around the middle of the experimental reported values. The large variation of the experimental VBM values is mainly due to the surface composition, orientation, and dipole moment of the measured samples, as proved by many theoretical studies<sup>166,187,188</sup>. As in our method, the electron is ionised from the centre of the cluster, this is termed as “bulk ionisation potential”<sup>174</sup>. Experimentally measured VBM is affected by either upwards or downwards surface bending depending on the surface condition, so it is normal that their values are lower and higher to ours. Large variation can also be seen between the calculated results, which are mostly by DFT methods, but the ambiguity of their vacuum level, finite-size effects, and broad choice of hybrid functionals leaves reported results under debate. The B97-2’s VBM is higher (closer to vacuum level) than BB1K’s VBM, which should be expected due to the different electronic localisation performance of the two hybrid functionals. Similar trend is also found in GaN using the same QM/MM method (*cf.* **Table 6.2**).

**Table 6.2** Ionisation potentials (eV) calculated using the hybrid QM/MM method, and comparison with other calculated and experimental results. The minus sign in the bracket indicates that the corresponding (ionised) electron levels are below the vacuum level.

	B97-2	BB1K	PBE0	Previous calc.	Exp.
AlN	(-)7.63	(-)8.38	(-)7.98	6.9-9.1 <sup>166,187,188</sup>	6.5-8.3 <sup>117,189–192</sup>
GaN <sup>181</sup>	(-)6.625	(-)7.340	N/A	6.8, 7.2	6.8

The electron affinities (also CBM level) of AlN, however, cannot be predicted accurately using the same approach, as high electron delocalisation of the conduction band states is a long-standing issue for the embedded cluster method. Therefore, a correction to the calculated EA has to be applied. Here, EA of AlN can be calculated by subtracting the experimental bandgap (6.2 eV) from the VBM level (B97-2: 1.167 eV; BB1K: 1.437 eV; PBE0: 1.584 eV). In our case, no negative electron affinity (NEA) behaviour<sup>193</sup> is observed for the pure AlN cluster, which is in good agreement with experimental reports<sup>117,189</sup>.

**Figure 6.1** shows the cluster geometry and spin density of a hole polaron as an electron is ionised from the cluster. A hole is well localised at the N atom (“N16” in **Figure 6.1**) near the central Al atom, with a  $p_z$  orbital shape spin density around the N atom (the z direction is parallel to the optically active c axis of wurtzite). The bond between the N atom and the vertical neighbouring Al atom (“Al31”) is stretched (by 0.358 Å) due to the localised hole. This is expected that, as positively charged hole and Al cation repel each other due to Coulomb forces. The bond distances between the hole localising N and the surrounding Al atoms in the same basal plane are not affected much (increased by 0.064 Å on average), which shows the local deformation mainly in the z-direction.

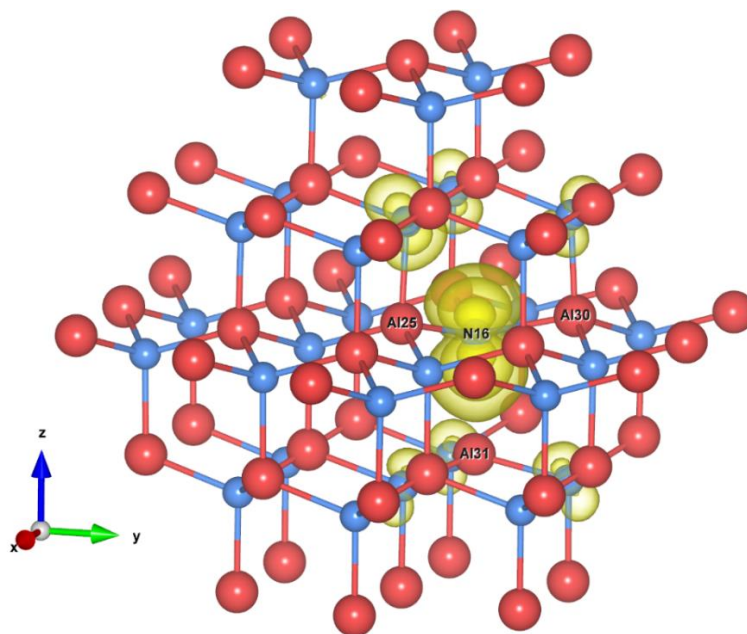


**Figure 6.1** Hole polaron in AlN shown with spin density (yellow isosurfaces of 0.05, 0.01, and 0.0025 a.u.) of an ionised cluster using B97-2 functional in QM/MM method. (N atoms in blue, and Al atoms in red)

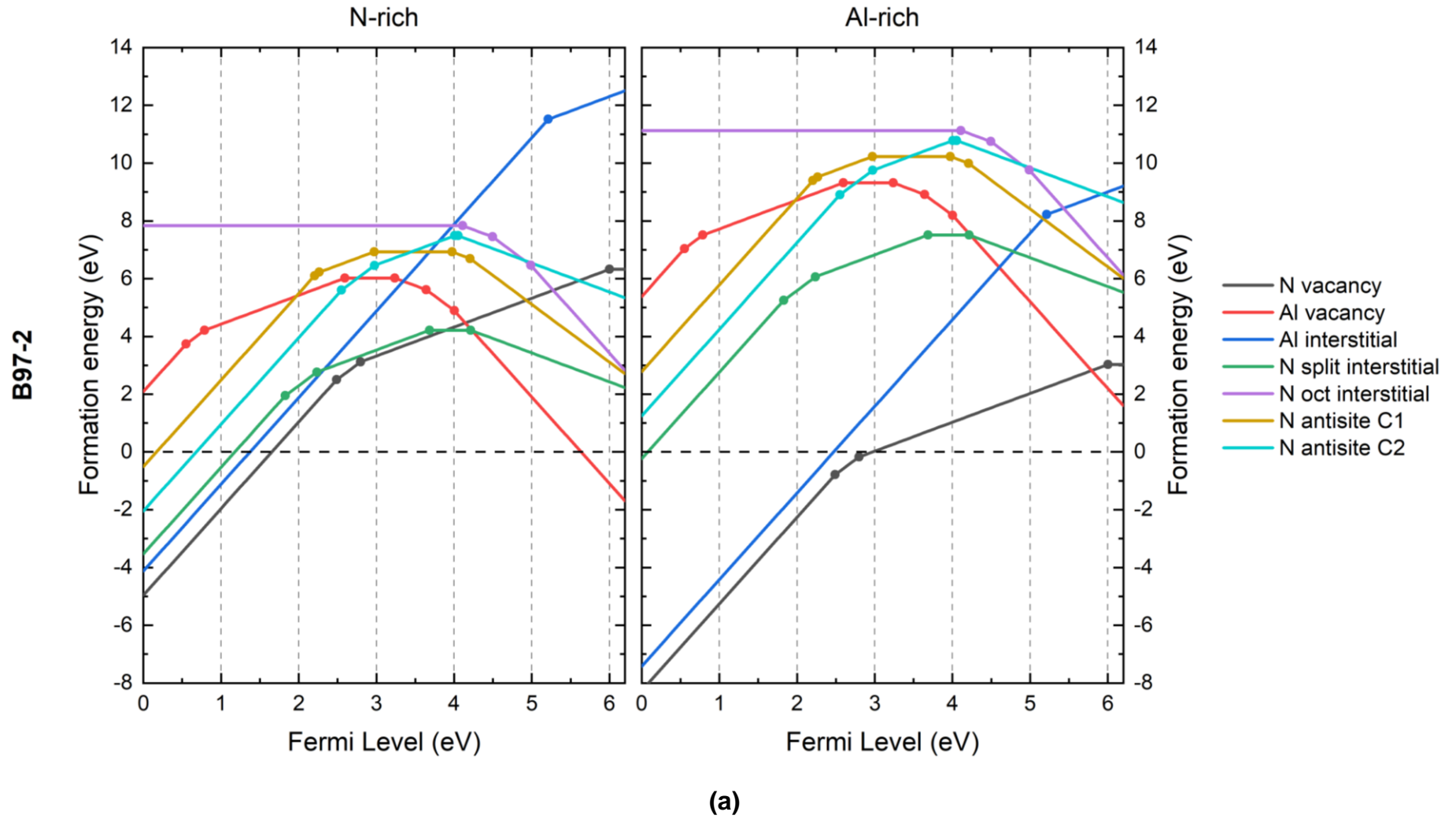
### 6.4.2 Formation energies of intrinsic defects

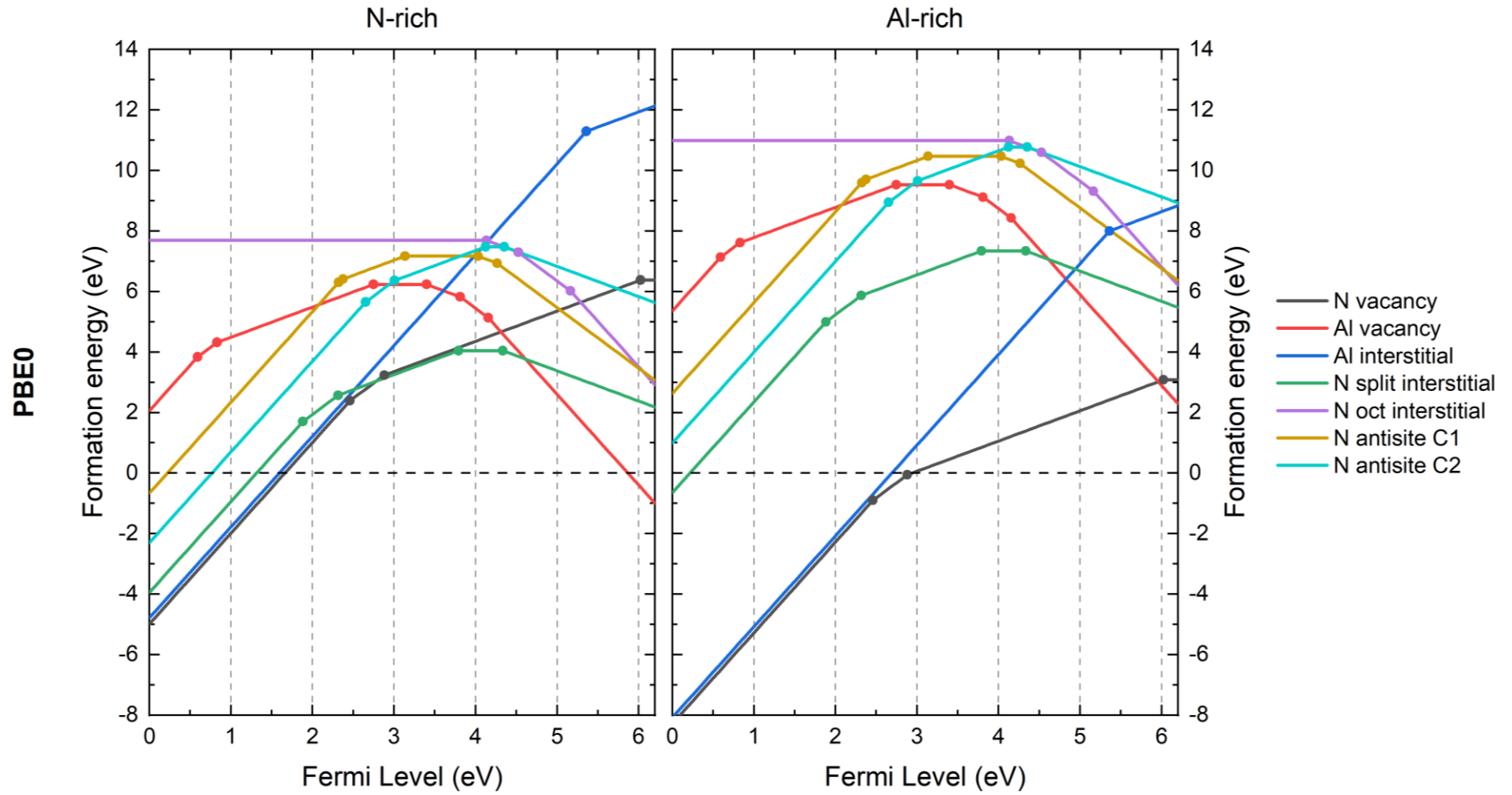
We begin the discussion of charge states of defects by first looking at the thermodynamic stability and charge transitions of the intrinsic defects, which are Al vacancy, N vacancy, Al interstitial, N interstitial, and N antisite. The defect charge transition diagrams show formation energies of these defects as function of the Fermi level (energy); respective plots using different hybrid functionals are presented in **Figure 6.2**. The diagram is a means to compare the degree of likelihood that the defects can be stabilised in the band gap of AlN forming deep defect states by using their calculated formation energies according to the reactions given in **Section 6.3**. In the following sections, individual defects will be discussed in turn, with detailed information of the calculated process and the comprehensive discussions of geometries and electronic configuration will be conducted. After that, diffused states, defect concentration, and defect processes are discussed. All our results are compared with previous calculation results and relevant experiment results.

#### (a) Al vacancy ( $V_{Al}$ )

Through our calculation, the Al vacancy ( $V_{Al}$ ) can be stable in seven charge states, from “-3” to “+3” (**Figure 6.2**). At the beginning of the calculation, an  $Al^{3+}$  ion at the centre of the cluster is taken out (leaving a  $V_{Al}^{3-}$  defect in the lattice). The electrostatic forces between the removed Al ion and the surrounding N ions become imbalanced, and these N ions start to repel each other with excess electrons localised on the lone pairs. The surrounding N ions can lose electrons (creating hole states) so that the charge state of the  $V_{Al}$  would become less negative. The first three electrons are removed successively from the three N ions on the same basal plane (N12, N16, N24 in **Figure 6.3**). Three hole states are localised at the three N ions separately, forming a spin quadruplet. For each hole localised, the corresponding N ion is pushed even more outwards by 3% compared to its respective AlN bond length in the -3 state (the bond length changes are presented in **Table 6.3**). Note that in calculations using B97-2 functional, the hole is not localising well in one of the charged states (see “-1” in **Figure 6.3**), and a small portion of the spin population is distributed to another ion. This can be improved by using a different hybrid functional with a higher HF exchange fraction (like PBE0 or BB1K), as shown in **Figure 6.4**.







(b)

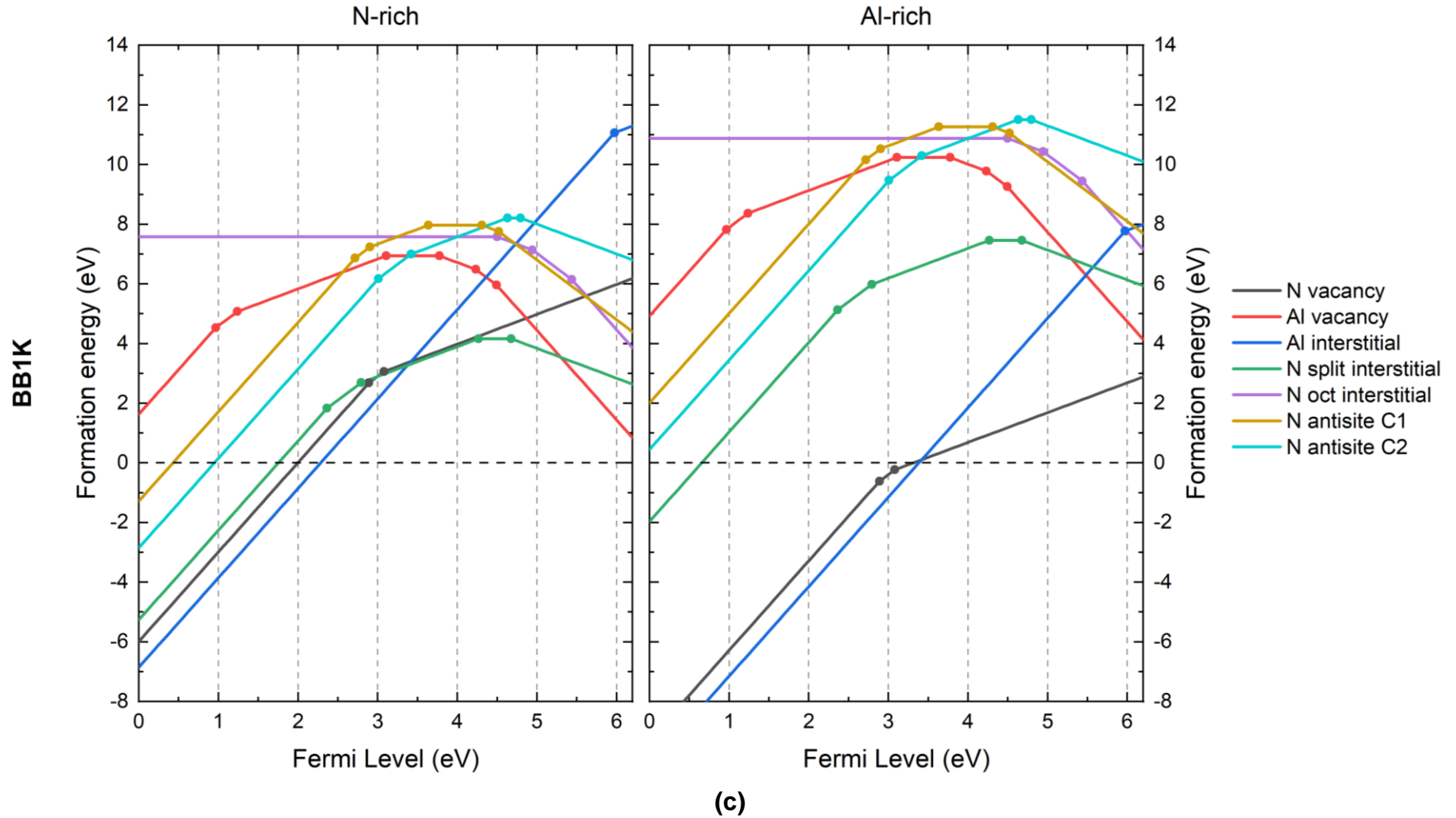


**Figure 6.2** The defect transition diagram showing formation energies of intrinsic defects in AlN as function of Fermi level in the band gap (functionals used: (a) B97-2; (b) PBE0; (c) BB1K). The Fermi level starts from the valence band maximum (VBM) on the left of the x-axis and ends at the conduction band minimum (CBM) on the right of the x-axis. The slopes of the lines indicate different charge states of the defect.

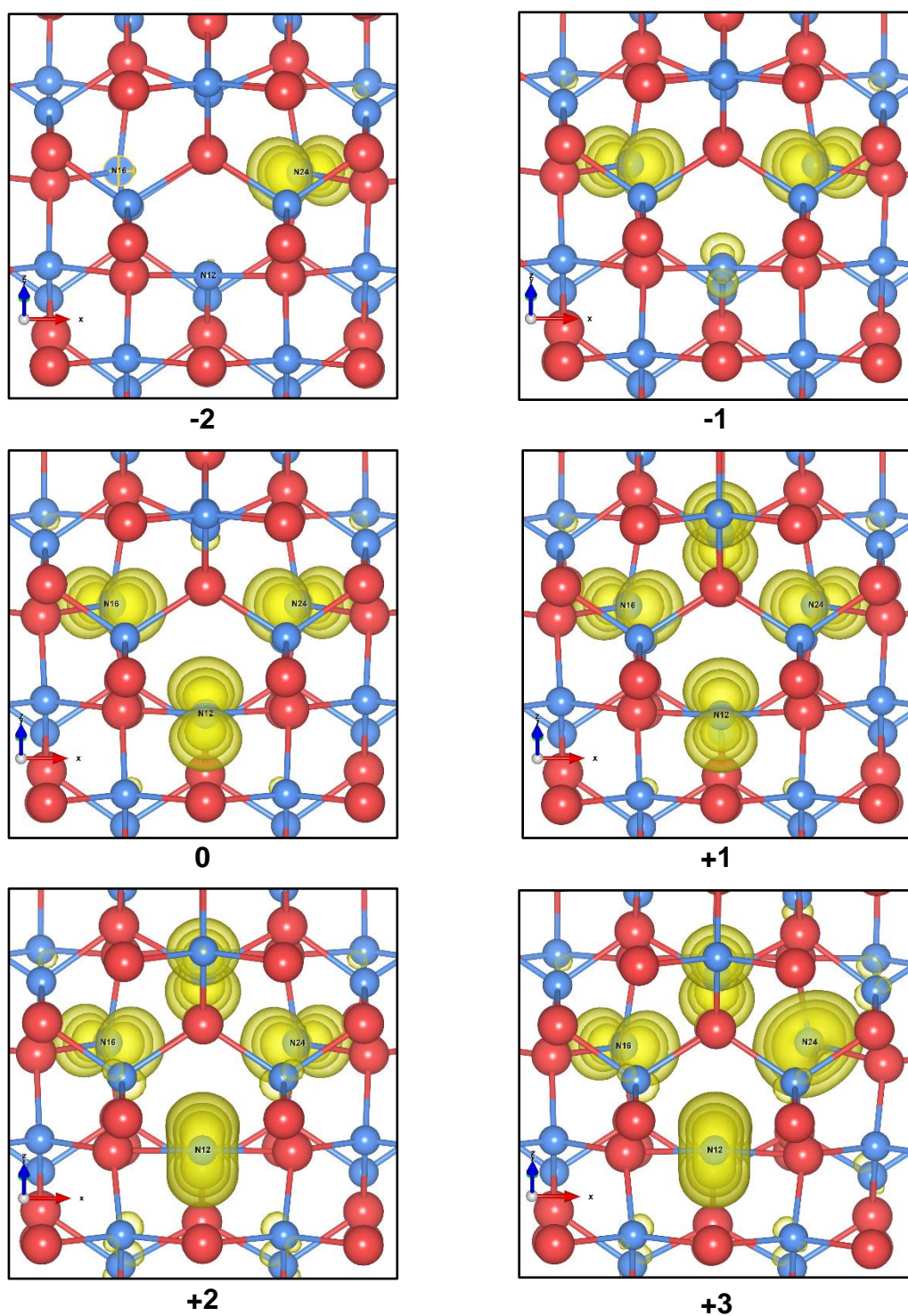


**Figure 6.3** Al vacancy in different charge states (-2 to +3). The spin density (yellow isosurfaces of 0.05, 0.025, and 0.01 a.u.), looking from the  $[01\bar{1}]$  direction, shows hole(s) localisation.

For both B97-2 and BB1K functionals, our calculation predicts the vacancy is more likely to become acceptor,  $V_{Al}^{3-}$ ,  $V_{Al}^{2-}$  and  $V_{Al}^{1-}$ , rather than a donor (**Figure**

**6.2).** From its neutral charge,  $V_{Al}^0$ , to positive charge states, the defect is more likely to behave like a donor. Sedhain, et al., states that  $V_{Al}(-2|-3)h$  is assigned as deep acceptor by PL spectroscopy. Aleksandrov, et al., speculates that the deep acceptor transition is  $V_{Al}(-1|-2)h$  by comparing their experimental data with DFT results. Our results agree with other theoretical results about the donor/acceptor behaviour of the defect.

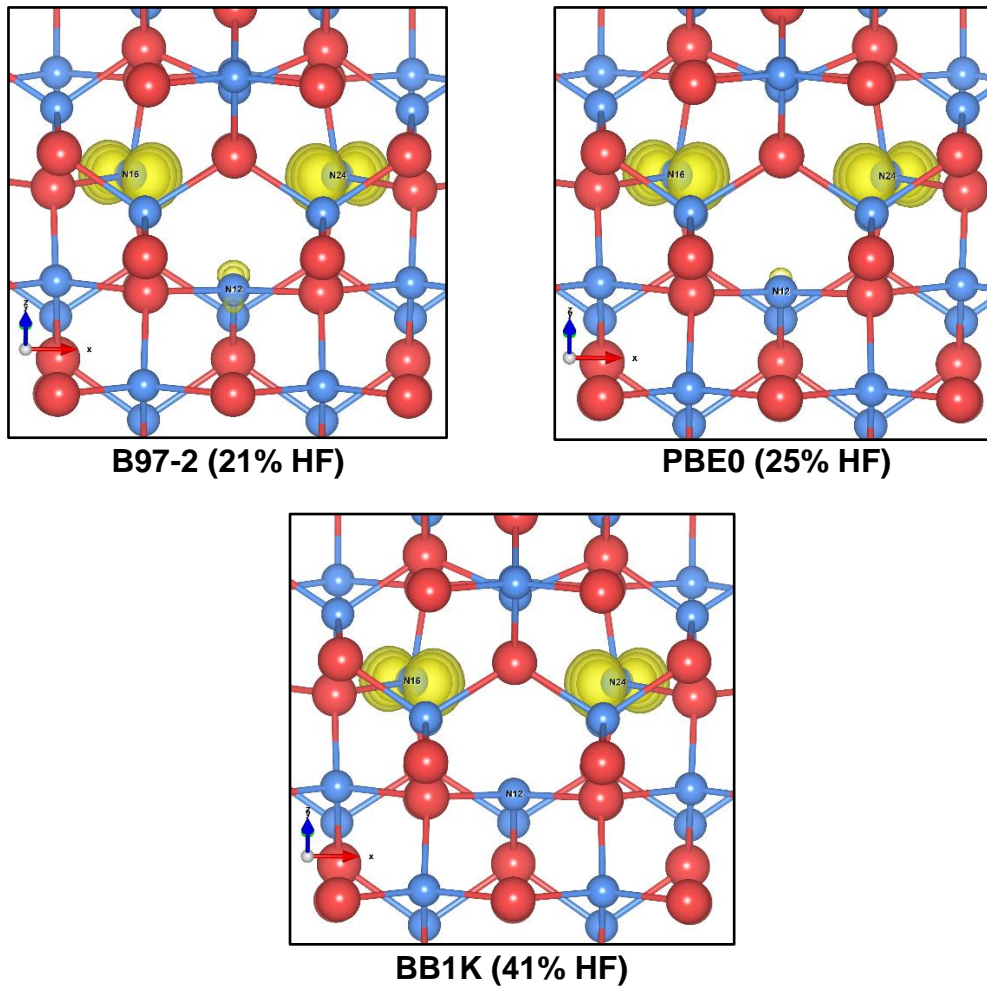


**Figure 6.4** Spin density of  $V_{Al}^{1-}$  using different functionals (yellow isosurfaces of 0.05, 0.03, and 0.02 a.u.), looking from the  $[01\bar{1}]$  direction. The N12 atom has lower share of the spin population as the HF exchange portion in the functional increases.

However, our calculated energy levels for charge transitions of  $V_{Al}$  are overall higher than previous DFT values obtained using the PBC method (**Table 6.4**). In those calculations, a shift to the CBM for the energy levels is seen as a higher-



run (more accurate) DFT functional (HSE) is used. We have proved that the higher portion of exact HF exchange results in stronger hole localisation (**Figure 6.4**), so the results obtained from using hybrid functionals are more reliable. Also, we obtained a 0.4-0.6 eV shift to the CBM compared to the latest PBC DFT results. In our QM/MM methods, geometry optimisation is carried out for each type of defect, so the VBM value is more accurate (deeper).

**Figure 6.5** presents the calculated ionization energies of all the stable charge states in the band gap using two different hybrid functionals B97-2 and BB1K. These energies are calculated by taking the energy difference from removing/adding electron from/to a stable defect at a certain charge state. As this is an adiabatic process, no geometry optimization is conducted after removing/adding electron. As a donor, deep states are formed by the formation of Al vacancy in charge state -3 to +1. And as an acceptor, deep states can also be seen in charge states -2 to +2.

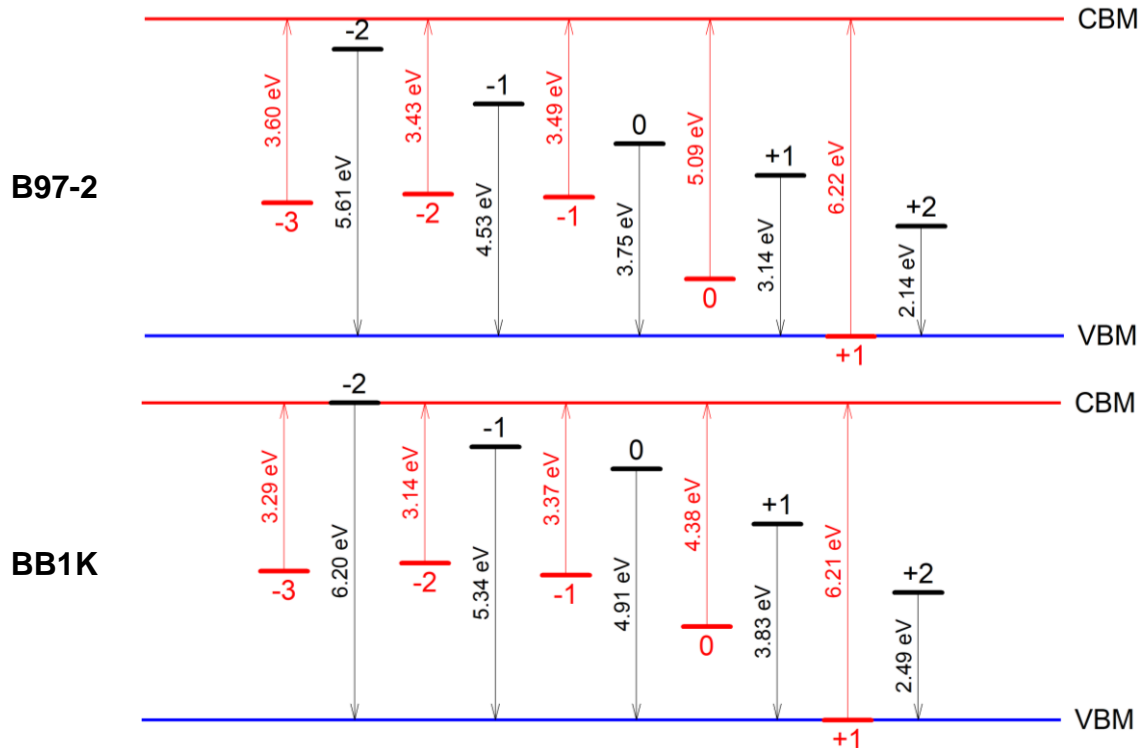


**Figure 6.5** Optical energy levels of Al vacancy with respect to band edges (based on vertical ionisation potential with respect to vacuum), calculated using the B97-2 and BB1K hybrid functionals. The vertical red lines indicate electron ionisation processes into the conduction band, and the vertical black lines the hole ionisation in the valence band.

**Table 6.3** Bond lengths (Å) between the  $V_{Al}$  site and the neighbouring N ions in the defect charge states -3, -2, -1, and 0. The last row is for the bond length between the central Al ion and its surrounding N ions without the defect in the cluster. The percentage number in parentheses indicates how much the bond length changes relative to corresponding perfect bond length.

Charge	Basal neigh. N24	Basal neigh. N16	Basal neigh. N12	z-axis neighbour
-3	2.198 (+15%)	2.198 (+15%)	2.197 (+15%)	2.443 (+28%)
-2	2.253 (+18%)	2.158 (+13%)	2.158 (+13%)	2.436 (+27%)
-1	2.237 (+17%)	2.237 (+17%)	2.101 (+10%)	2.416 (+26%)
0	2.248 (+18%)	2.247 (+18%)	2.247 (+18%)	2.382 (+24%)
Perfect	1.906	1.906	1.906	1.915

As shown in **Figure 6.2**,  $V_{Al}$  has the lowest formation energies among all the intrinsic defects in the upper one third of the band gap region from B97-2 and PBE0 calculations. One exception is seen from the BB1K calculation, in Al-rich condition, where  $V_{Al}$  does not have the lowest energy in the upper half of the band gap. Particularly in N-poor conditions,  $V_{Al}^{3-}$  is the predominant defect in the region 2.23 eV (by B97-2, and 2.07 eV by BB1K) below the CBM, as a triply charged acceptor. This is partly due to the large band gap of the material. Due to differences in the treatment of polarization and definition of the ionization potential in the QM/MM method, our formation energies for the charged defects can be different from previous calculations using PBC-based DFT methods, but there should not be much deviation in the energy of the neutral charge state. **Table 6.5** presents our results for the formation energy of the Al vacancy in the neutral charge state in comparison to results obtained using LDA (Perdew81), GGA (PBE), and a hybrid HSE06 (HF exchange portion tuned to 33%) functionals in our QM/MM setup. Our QM/MM results obtained using LDA and GGA functionals agree well with other computational results in the literature using the same functionals. Note though that our HSE values are appreciably smaller than those from the literature, which indicates possible problems with implementation of the functional in the molecular QM code, where it is not a popular choice. As the exchange fraction in the hybrid functional increases, the formation energy of the neutral Al vacancy increases. This trend can be seen by comparing our

results with literature HSE results, as the latter are in between the PBE0 and BB1K values. Nevertheless, somewhat counterintuitively, our QM/MM method implementing the BB1K functional delivers the best agreement with previous calculations for Al vacancy.

**Table 6.4** An overview of the defect energy level (eV) at the  $V_{Al}$  defect charge transition position with respect to the VBM.

	Present work			HSE (2020) 110	HSE (2014) 80	HSE (2013) 71	GGA (2008) 194	LDA (2009) 77
	B97-2	PBE0	BB1K					
$V_{Al}(-2 -3)h$	4.00	4.16	4.49	3.2	3.1	1.4	3.1	1.8
$V_{Al}(-1 -2)h$	3.64	3.81	4.23	2.9	2.8	1.1	2.6	1.1
$V_{Al}(0 -1)h$	3.32	3.40	3.78	2.5	2.4	0.8	2.4	0.9

**Table 6.5** Formation energies (eV) of  $V_{Al}^0$ . Previous calculated values reported in the literature as graphs are directly measured. (\*The HSE functional is an HSE06 type ( $\omega = 0.11$ ), with HF exchange fraction of 33%, as implemented in other recent work<sup>110</sup>.)

		Functional	$V_{Al}^{0,N-rich}$	$V_{Al}^{0,N-poor}$
QM/MM (Chemshell)	B97-2		6.02	9.32
	PBE0		6.24	9.53
	BB1K		6.94	10.24
	HSE*		5.84	9.14
	PBE (GGA type)		5.93	9.22
	Perdew81 (LDA type)		7.56	10.86
Previous work	HSE		6.87 <sup>110</sup> , 6.98 <sup>81</sup> , 6.81 <sup>71</sup> , 6.90 <sup>80</sup>	10.02 <sup>110</sup> , 10.12 <sup>71</sup> , 10.13 <sup>80</sup>
	PBE (GGA type)		6.00 <sup>171</sup> , 7.14 <sup>194</sup>	9.21 <sup>194</sup>
	Perdew81 (LDA type)		8.05 <sup>195</sup> , 6.53 <sup>77</sup>	10.20 <sup>77</sup>



**(a) N vacancy ( $V_N$ )**

In our calculation using the PBE0 and the B97-2 functionals, the N vacancy defect can be stable in 4 different charge states, +3, +2, +1, and 0. In the calculation using the BB1K functional, the neutral charge state of the defect is not formed deep in AlN (**Figure 6.2**). As an  $N^{3-}$  ion removed from the clean lattice, the removal of the three electrons of the anion results in the +3 state of the vacancy. The surrounding  $Al^{3+}$  ions are left with no electrons in their valence  $3s$  and  $3p$  orbitals. The triply positive charge vacancy pushes the surrounding Al ions outwards by 21-26% of their original AlN bond lengths (**Table 6.6**). As an electron is added to the system, this electron can easily be trapped at the vacancy site instead of at the surrounding Al cations. As shown in **Figure 6.6**, the trapped electron forms a hydrogen-like  $s$  orbital state around the vacancy site (subject to tetrahedral, trigonal in projection, deformation of the wurtzite lattice site). This is often termed as F-centre defect, where stable electronic states can be found in the void created by the vacancy defect. According to our calculation, the F-centre can trap one more electron, resulting in the  $V_N^{1+}$  defect state, and it tends to form a close-shell configuration of the F-centre by coupling two electrons.

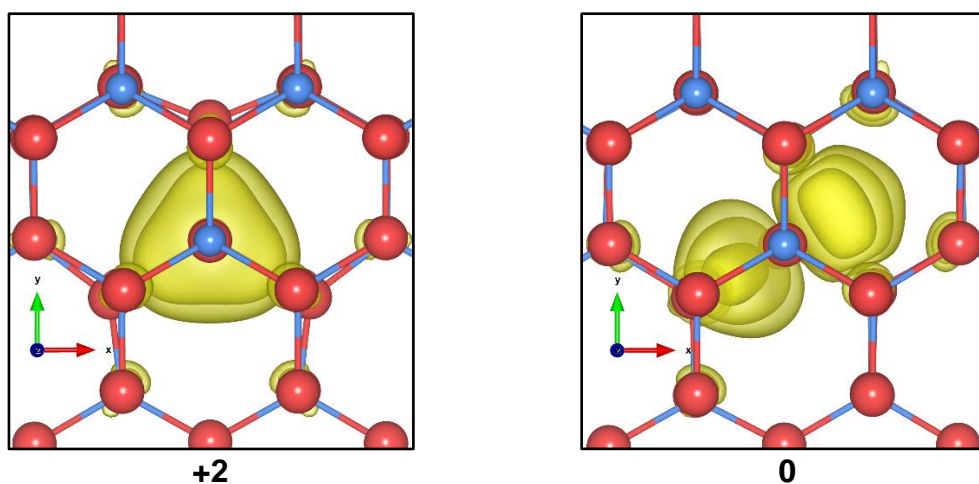


**Figure 6.6** N vacancy in charge states +2 and 0 in AlN. Electron localisation is shown with spin density of (yellow isosurfaces of 0.01, 0.005, and 0.0025 a.u.), looking from the  $[00\bar{1}]$  direction.

The third additional electron cannot localize at the F-centre. Instead, the population of the new spin is shared between the two surrounding Al-Al bonds evenly (**Figure 6.6**). In this neutral charge state, the shape of the spin population

wraps around the vacancy centre. Such electronic structure is formed in our calculations by the outermost diffuse atomic orbitals of the Al atoms. However, one might argue that the best way to construct F-centre defect states would be by implementation of a “ghost atom” at the vacancy centre. The ghost atom would bear the same wavefunction information as the removed atom but no other physical entity of a real atom. In such a way, the electronic information is described more accurately. However, as to date, the Chemshell interface to NWChem employed in our work does not support the ghost atom function, though work is underway.

**Table 6.6** Bond lengths (Å) between the  $V_N$  site and the neighbouring Al ions in the defect charge states +3, +2, +1, 0, and -1. The positive percentage number in the parentheses indicates how much the distance is increased relative to corresponding perfect bond length. The minus percentage number indicates how much they contract.

Charge	Basal neigh. avg.	z-axis neighbour
+3	2.409 (+26%)	2.310 (+21%)
+2	2.198 (+15%)	2.207 (+15%)
+1	2.036 (+7%)	2.018 (+5%)
0	1.943 (+2%)	1.916 (+0%)
-1	1.876 (-2%)	1.858 (-3%)
Perfect	1.906	1.915

As electrons are added to the defect, the surrounding Al ions gradually approach the defect centre, leading to reduction in the bond lengths. When the charge state becomes negative, the  $V_N$ -Al bond lengths are shorter than those in the perfect lattice. At this point, the vacancy defect starts to attract the surrounding positive charge Al ions, because of the negative central Madelung potential. This trend is presented in **Table 6.6**.

Out of all intrinsic defects (**Figure 6.2**),  $V_N^{3+}$ ,  $V_N^{2+}$  and  $V_N^{1+}$  are most likely to appear in the material in both *n*-type and *p*-type environment under thermodynamic

equilibrium. Their thermodynamic charge transition levels prove that the defect behaves as donor, as they are closer to the VBM (**Table 6.7**). **Table 6.7** and **Table 6.8** present the defect charge transition levels and the formation energy in neutral charge state respectively. The conclusion from the comparison with other literature results are like the one made for Al vacancy. Both Al vacancy and N vacancy are proved to be the most energetically favourable intrinsic defects in AlN, which coincides with the conclusion in **Chapter 6.4** where the Schottky defect pair is predicted to be most stable by GULP.

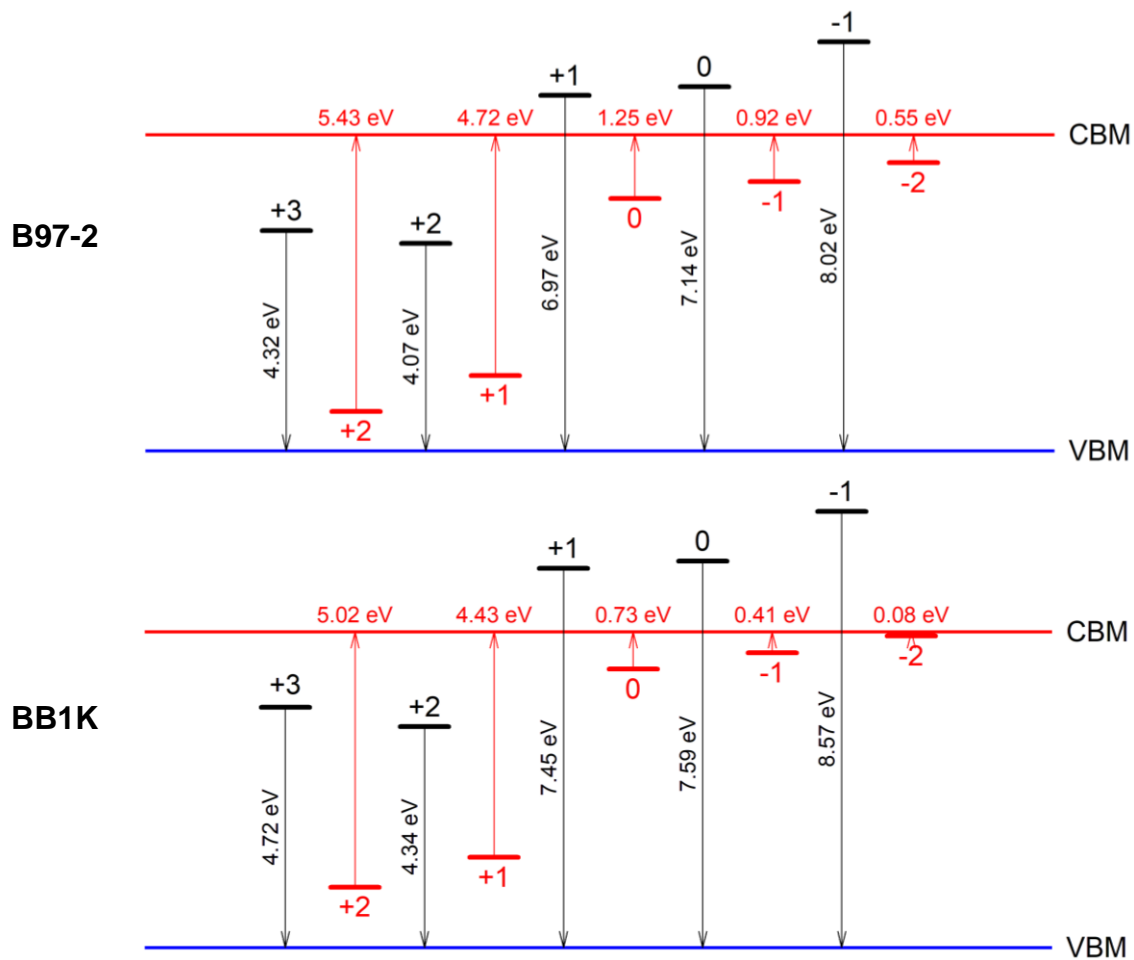


**Figure 6.7** Optical energy levels of N vacancy with respect to band edges (based on vertical ionisation potential with respect to vacuum), calculated using the B97-2 and BB1K hybrid functionals.

**Table 6.7** Defect energy levels (eV) of  $V_N$  with respect to the VBM.

	Present work			HSE (2020) <sup>110</sup>	HSE (2014) <sup>80</sup>	HSE (2013) <sup>71</sup>	LDA (2009) <sup>77</sup>	GGA (2008) <sup>194</sup>
	B97-2	PBE0	BB1K					
$V_N(+3 +2)e$	2.49	2.46	2.89	0.87	0.84	1.01	0.71 (+3 +1)	1.52 (+3 +1)
$V_N(+2 +1)e$	2.80	2.88	3.08	1.08	1.01	1.14		
$V_N(+1 0)e$	6.00	6.02	6.51	4.60	4.44	4.60	5.05	4.22

So far, there has been a number of experimental studies<sup>60,139,196–199</sup> corroborating the existence of F-centre type defects in AlN using the electron paramagnetic resonance (EPR) and the electron–nuclear double resonance (ENDOR) techniques. However, the optical properties and the relevant charge states obtained from their work are not consistent, where their detected optical absorption bands range from 350 nm (UV) to 450 nm (blue), which was proposed to be the reason for the yellow-to-red colour of the as-grown AlN crystals.

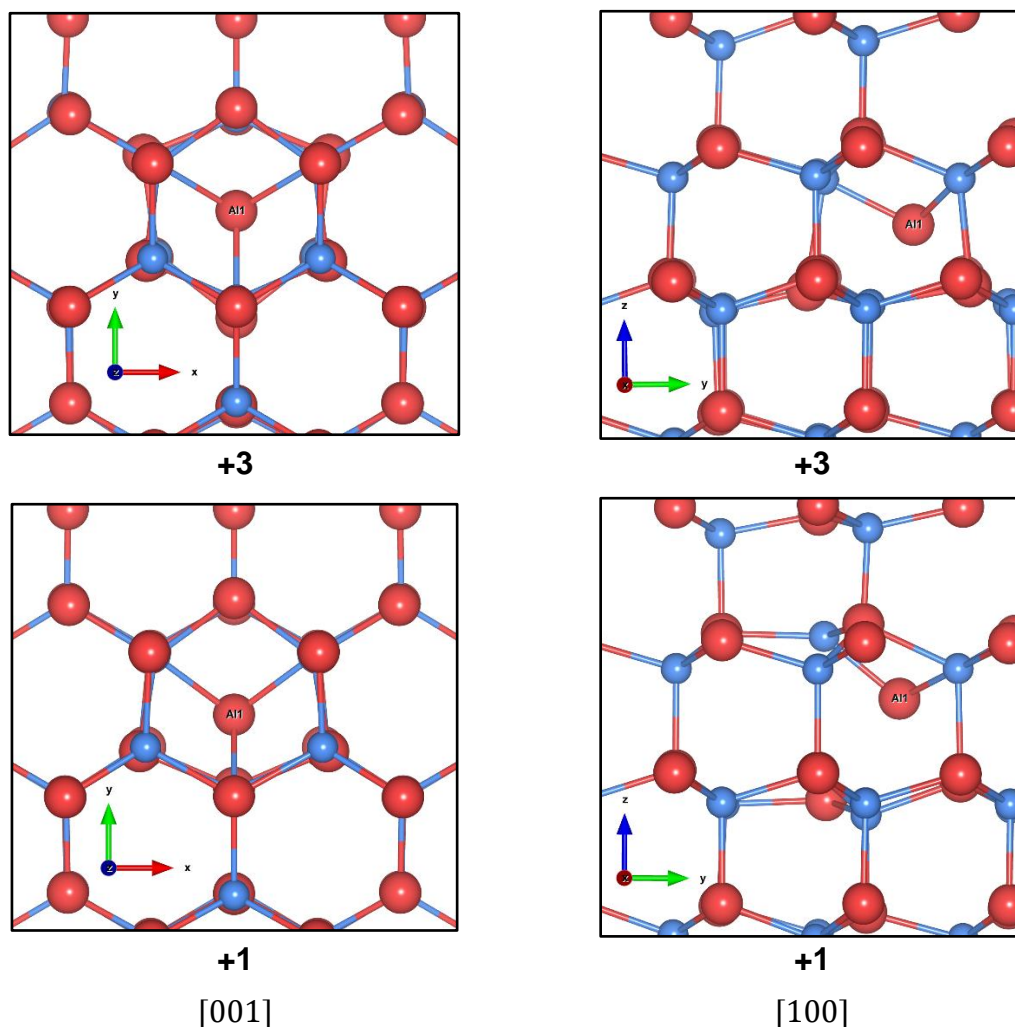
**Table 6.8** Formation energies (eV) of  $V_N^0$ .

	Present work			Previous work		
	B97-2	PBE0	BB1K	HSE	PBE0 <sup>171</sup>	LDA <sup>194</sup>
$V_N^{0,N-rich}$	6.32	6.38	6.49	6.61 <sup>110</sup> , 6.04 <sup>81</sup> , 6.57 <sup>71</sup> , 6.49 <sup>80</sup>	6.79	4.83
$V_N^{0,N-poor}$	3.03	3.08	3.19	3.50 <sup>110</sup> , 3.27 <sup>71</sup> , 3.32 <sup>80</sup>		2.75

### (b) Al interstitial ( $Al_i$ )

The Al interstitial defect ( $Al_i$ ) stabilizes in the octahedral void (**Figure 6.8**) in the wurtzite lattice (see **Chapter 2** and **Chapter 4** for the nomenclature of interstitial sites in the wurtzite crystal structure). Our QM/MM calculation proves that  $Al_i$  at the tetrahedral site has overall higher formation energy than that at the octahedral site. As shown in **Figure 6.2**, the  $Al_i$  can be formed in the +3 and +1 charge states. The  $Al_i^{2+}$  is a metastable state, as it is calculated to have a higher formation energy throughout the whole band gap region than the  $Al_i^{3+}$  and  $Al_i^{1+}$ . However, the electron can localize at  $Al_i^{2+}$  (**Figure 6.9**) forming  $sp$ -hybrid shape orbital, which can contribute to an optical transition state. The defect thus has a

direct charge transition between  $Al_i^{3+}$  and  $Al_i^{1+}$  in the upper region of the band gap. Therefore,  $Al_i$  is a donor type. This conclusion agrees with previous computational reports<sup>110</sup>.

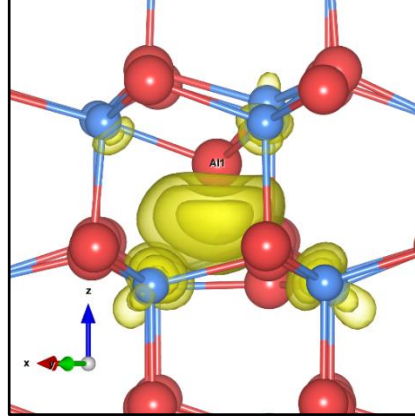


**Figure 6.8** Optimized geometry of Al interstitial defect at the octahedral site in charge states +3 and +1, looking from [001] and [100] directions. “Al1” label shows the interstitial defect species.

The octahedral  $Al_i^{3+}$  defect stabilizes at the centre of the  $c$ -channel. As the charge decreases, the defect starts to shift off centre, and the surrounding ions displace in response. This trend can be seen from **Table 6.9** and the relaxed geometry shown in **Figure 6.8**.

**Table 6.9** Off-centre displacements (Å) of  $Al_i$  in charge states +2, +1, and 0 from the ideal  $Al_i^{3+}$  position .

Charge	+2	+1	0
Displacement from $Al_i^{3+}$	0.326	0.493	0.572

**Figure 6.9** Spin density of charge state +2 of Al interstitial at the octahedral site (yellow isosurfaces of 0.02, 0.01, and 0.005 a.u.).

$Al_i$  has not been widely studied so far, as it is broadly considered chemically unstable in the material and calculated to have high energies of formation<sup>76</sup>. Here we present a contrasting result for both N-rich and N-poor condition (**Figure 6.2**). In the lower regions of the band gap, the formation energy of  $Al_i^{3+}$  is negative, and it is only about 0.8 eV higher than the  $V_N^{3+}$  from calculation of B97-2 functional. Such difference is even smaller in the calculations using the functionals with higher HF exchange portion (PBE0: 0.2 eV). Using BB1K, the formation energy of  $Al_i^{3+}$  is even lower by 0.9 eV than  $V_N^{3+}$ . In principle, the result obtained from B97-2 is generally more reliable for the thermodynamic problem, but the decrease of the formation energy difference might be an indication of the somewhat similar property of the two defects. There is only one experimental report assigning the  $Al_i^{2+}$  as a deep donor by EPR, but no optical line has been assigned to it to date<sup>200</sup>. From our calculation,  $Al_i^{2+}$  and  $Al_i^{1+}$  can be the source of a deep donor optical state (**Figure 6.10**). And  $Al_i^0$  is a possible shallow donor candidate as its optical level is 0.06 eV (BB1K) below the CBM. We will continue our discussion of

shallow donors in the next section on the diffuse defect states. The charge transition energy level and the formation energy in the neutral charge state are presented in **Table 6.10** and **Table 6.11** respectively, with a similar trend to what we have already observed for other defects reported above.

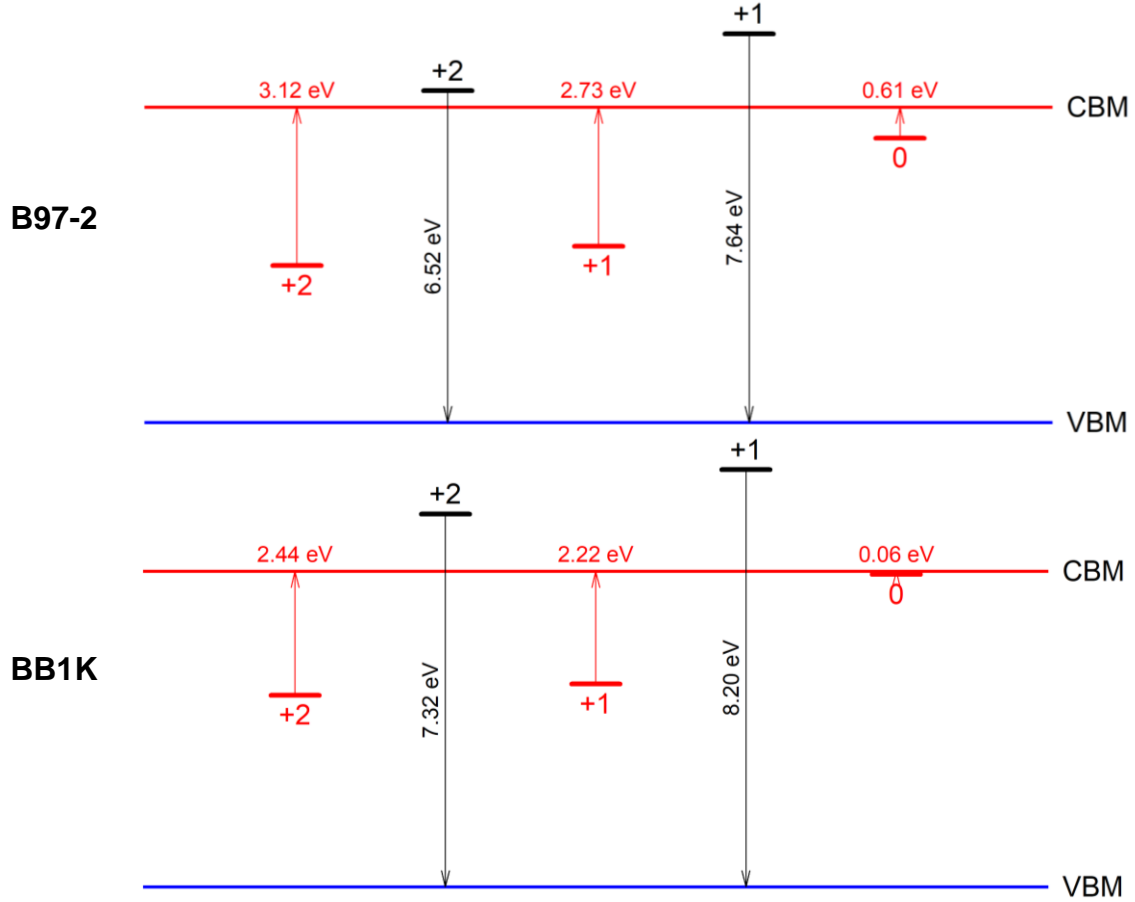


**Figure 6.10** Optical energy levels of Al interstitial with respect to band edges.

**Table 6.10** Defect levels (eV) of  $Al_i$  with respect to the VBM.

	Present work			HSE (2020) <sup>11</sup> 0
	B97-2	PBE0	BB1K	
$Al_i(+3 +1)e$	5.21	5.36	5.97	3.92
$Al_i(+1 0)e$	6.64	6.70	7.19	5.82

**Table 6.11** Formation energies (eV) of  $Al_i^0$ .

	Present work			Previous work	
	B97-2	PBE0	BB1K	HSE <sup>110</sup>	GGA <sup>76</sup>
$Al_i^{0,N-rich}$	12.94	12.64	12.29	14.16	14.30
$Al_i^{0,N-poor}$	9.65	9.34	8.99	11.09	10.76

**(c) N interstitial ( $N_i$ )**

There are two possible configurations of the N interstitial defect, an octahedral interstitial and a split interstitial. In the first configuration, a nitrogen ion stabilizes in the octahedral void of the wurtzite structure, around the same position as the Al interstitial discussed in the previous section (**Figure 6.11**). The octahedral N interstitial defect ( $N_{i,oct}$ ) is stable in three different charge states (-3, -2, -1, and 0) in the band gap, with the interstitial ion positioned in approximately the same location while the neighbouring ions displacing in response to the defect (**Figure 6.12**). Starting from the defect in its formal charge ( $N_{i,oct}^{3-}$ ), as electron is removed, a hole is localised on the defect (**Figure 6.12**) giving rise to energy states deep in the band gap (**Figure 6.13**). The three removed electrons are on the three Cartesian  $2p$  orbitals of the nitrogen atom and removing all of them in turns forms corresponding high spin states (up to 3 lone spins) of the defect. The localisation of the holes on the same atom in three charge states is seen from the shapes of spin densities in **Figure 6.12**. On further ionisation, of the neutral charge interstitial ( $N_{i,oct}^0$ ), we cannot find any stable configuration of the  $N_{i,oct}$  in any of the positive charge states. Comparing with all other types of defect states in the band gap in **Figure 6.2**, forming the  $N_{i,oct}$  defect requires almost the highest formation energy in N-poor conditions. Therefore, the  $N_{i,oct}$  defect is predicted to be most difficultly found in AlN, so it is discussed much less than other defect types in the literature.



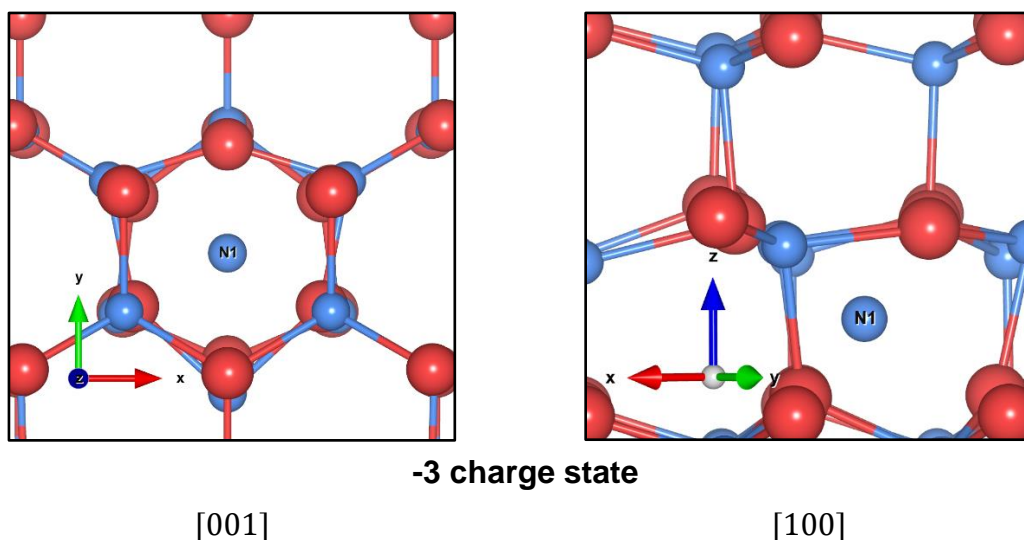


**Figure 6.11** Optimized geometry of N interstitial defect at the octahedral site in the -3 state, looking from [001] and [100] directions. The atom labelled "N1" is the interstitial defect species.

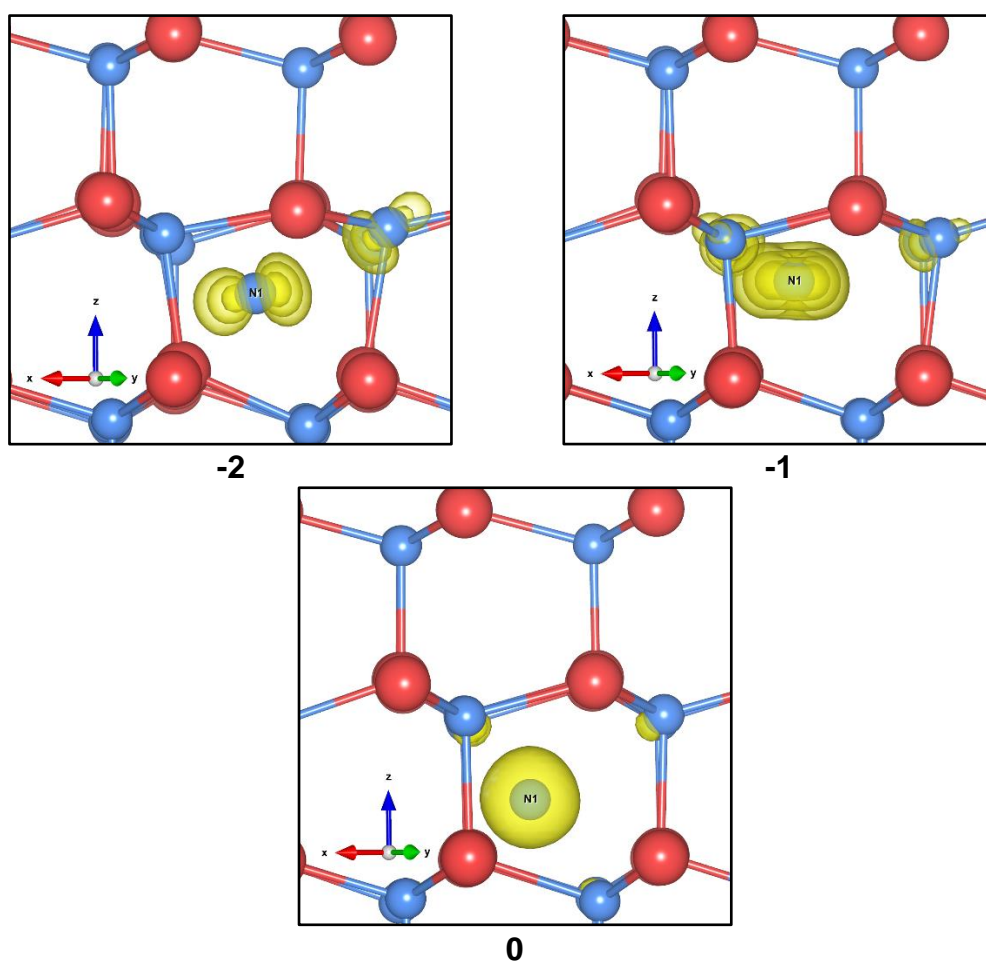


**Figure 6.12** N interstitial defect at the octahedral site in charge states -2, -1, and 0. Electron localisation is shown with spin density of (yellow isosurfaces of 0.1, 0.05, and 0.025 a.u.).

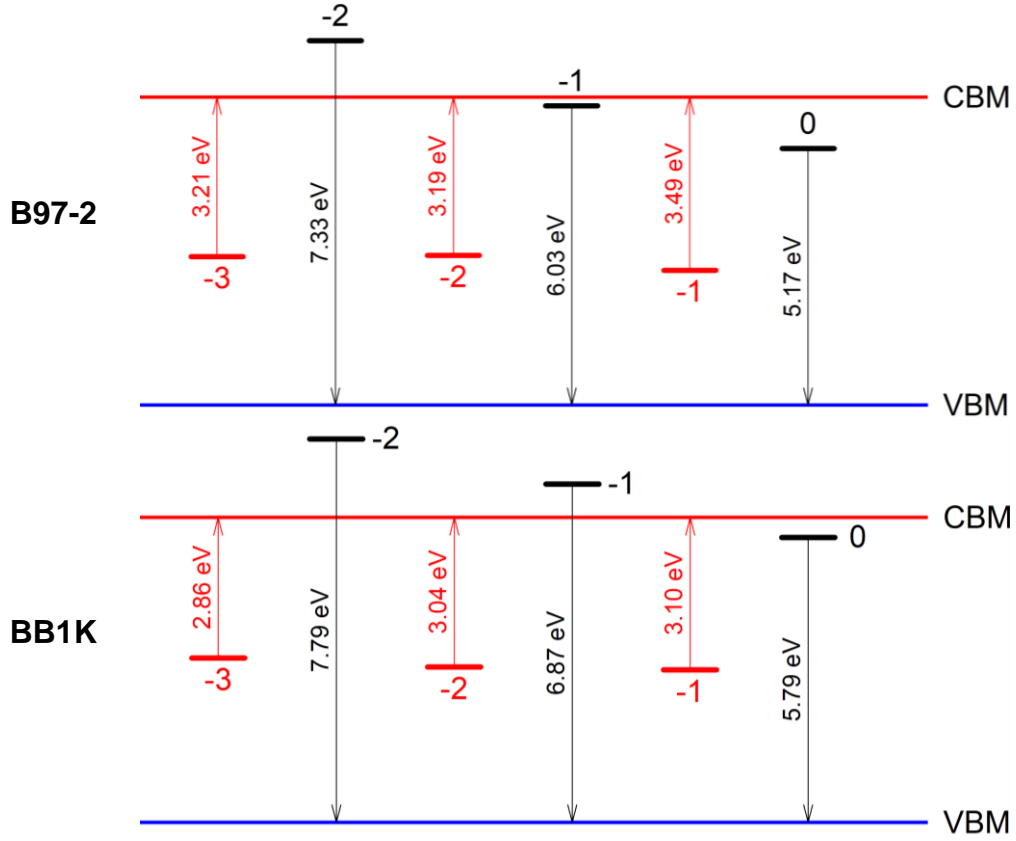
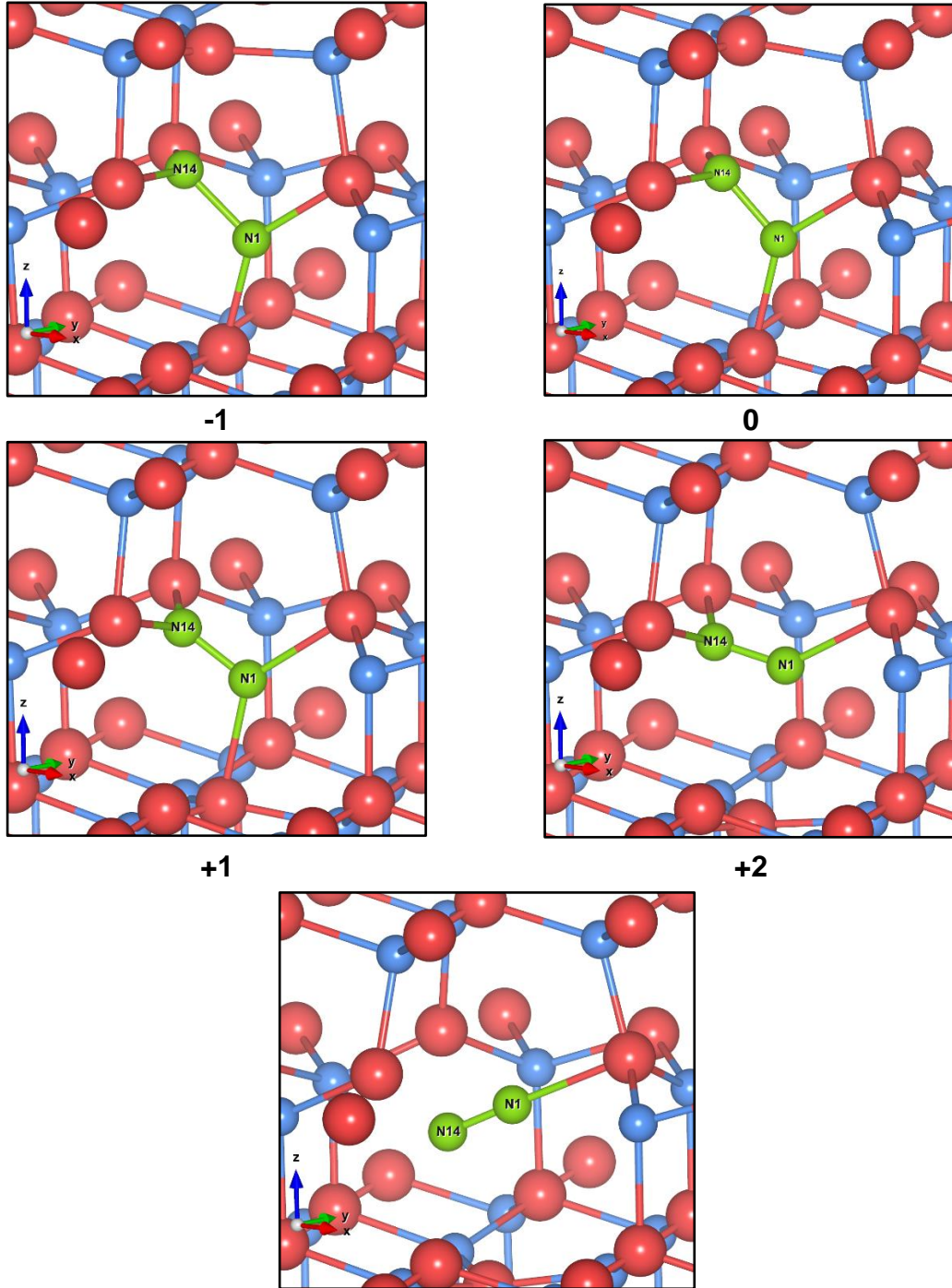


**Figure 6.13** Optical energy levels of N interstitial defect at the octahedral site with respect to band edges.

The N split interstitial defect ( $N_{i,split}$ ) is most stable in AlN in any of the charge states of the  $N_{i,oct}$  defect under CBM (**Figure 6.2**). The N atom introduced at the interstitial site can bond with one of the closest lattice N atoms, forming a N-N dimer structure (**Figure 6.14**) with a bond length slightly longer than that of a  $N_2$  gas molecule (**Table 6.12**). The  $N_{i,split}$  can be stabilized in charge states from -2 to +3. At charge +1, the  $N_{i,split}^{1+}$  has the lowest formation energy in the configuration where it bears two lone parallel spins (multiplicity of 3). As the charge state becomes 0 or +2, the lowest energy can be found with just one lone spin (multiplicity of 2). And in -1 and +3 charge states, the defect is most stable in the closed-shell electronic configuration. The spin densities of different charge states prove that the electronic configuration of the split interstitial is analogous to that of an  $N_2$  molecule. In charge states of 0, +1, and +2, the spin density adopts the shape of an anti-bonding  $\pi$  orbital (**Figure 6.15**). The  $N_{i,split}^{2-}$  does not form deep states under CBM, although a stable configuration can be found after geometry relaxation. The  $N_{i,split}$  defect is calculated to behave as the donor type.

The optical transition energies are those of a deep donor in the band gap region in any of the charge states (**Figure 6.16**). The charge transition energy levels are shallower towards CBM compared to previous reports (**Table 6.13**). For  $N_{i,split}^{3+}$ , our calculation shows it is as stable in the band gap, but it was reported as stable only once in the current literature<sup>76,81,110,115</sup>. **Table 6.14** shows the neutral defect formation energy, and our results are around 1eV lower than those reported in the literature.



**+3**

**Figure 6.14** Optimized geometry of N split interstitial defect site in the charge states of -1, 0, +1, +2, and +3. The split N-N configuration ions are shown in green. The atom labelled “N1” is the interstitial defect species, and “N11” is the bonded N atom from the lattice.

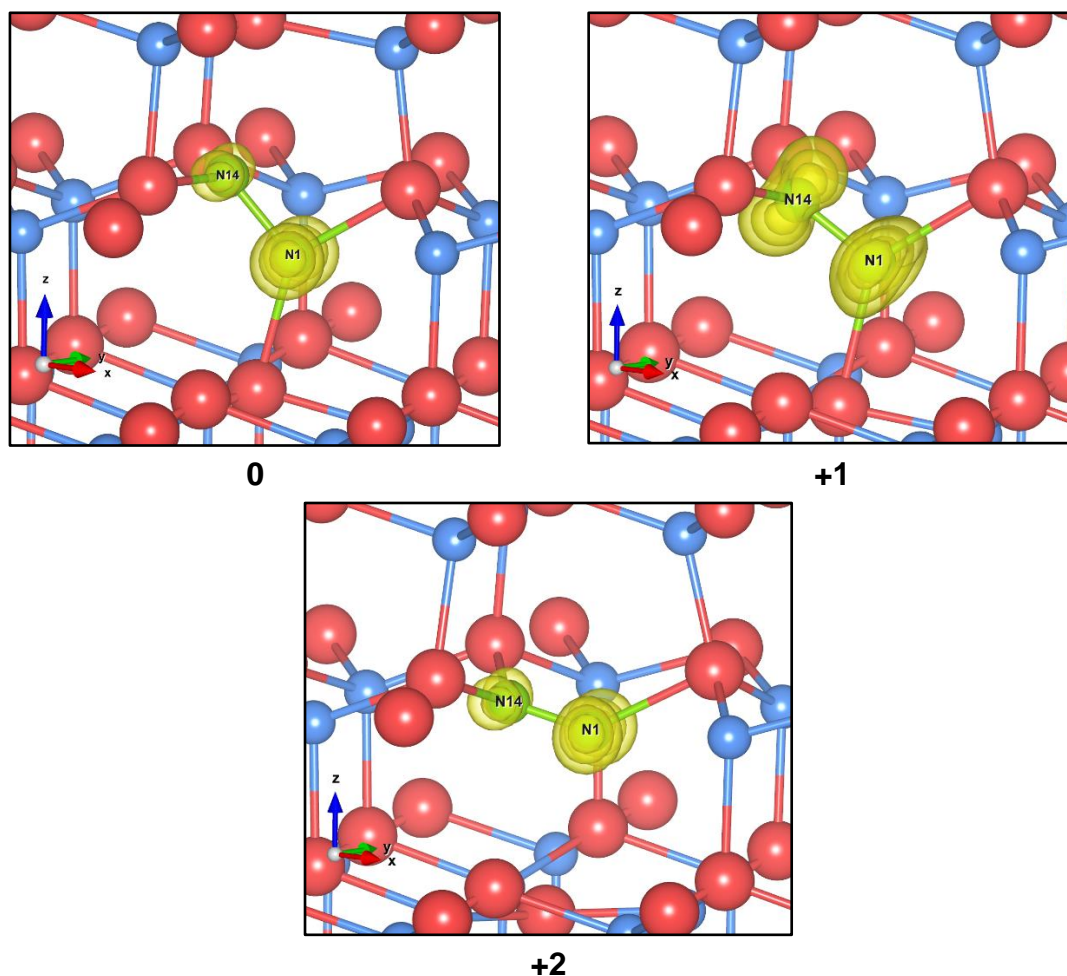


**Figure 6.15** N split interstitial defect in charge states 0, +1, and +2. Electron localisation is shown with spin density (yellow isosurfaces of 0.1, 0.05, and 0.025 a.u.).

In the +3 charge state, bond length of the N-N dimer is close to the bond length of  $N_2$  gas molecule ( $\sim 1.09 \text{ \AA}$ ). As the charge decreases (adding electrons on to the N-N dimer), the dimer is stretched. This trend is presented in **Table 6.12**, and the bond lengths in each charge states agree well with previous DFT results. The orientation of the N-N dimer is also changed in different charge states. The dimer rotates around the same N atom site of the perfect AlN lattice in the (110) plane. In the charge state -2, the bond between the N-N seems to break as the spin

density analysis shows the added electron is delocalized across the whole QM cluster region.

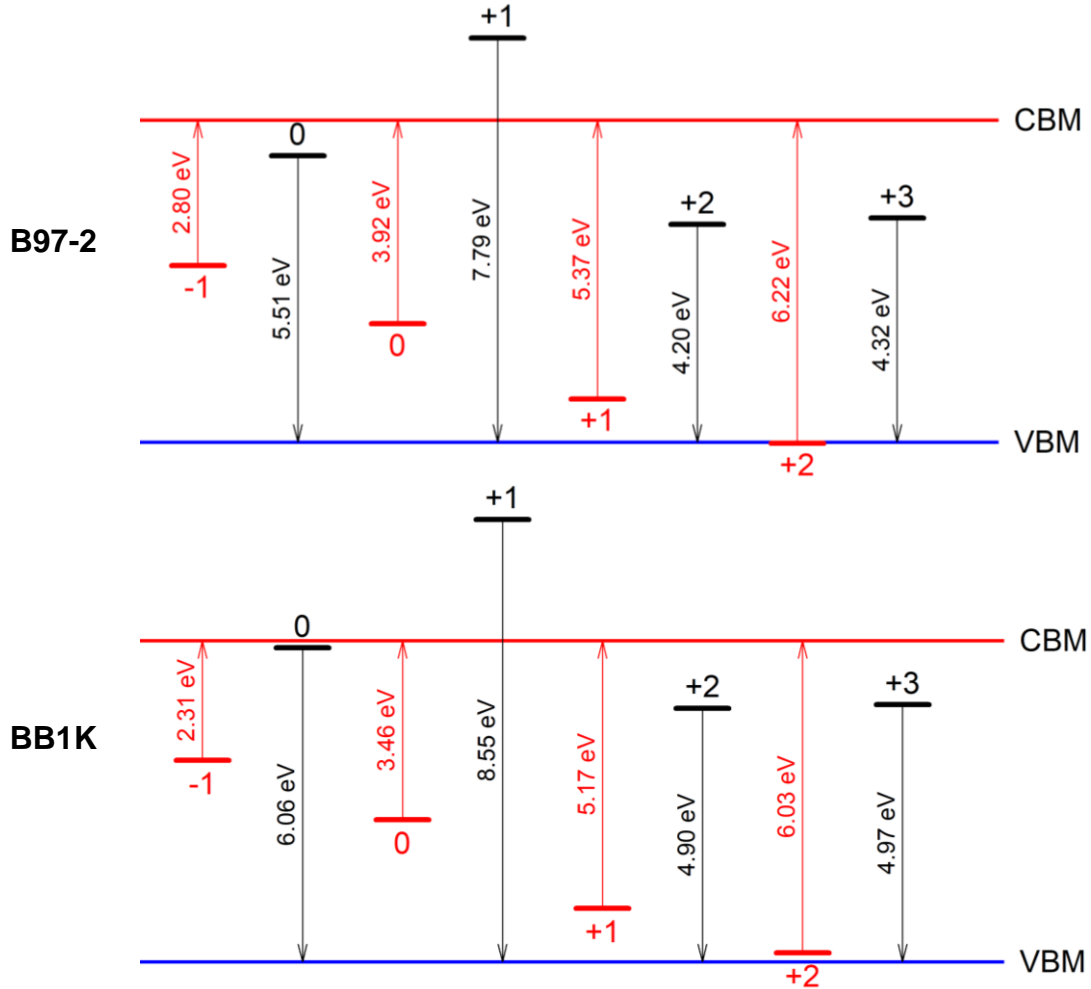


**Figure 6.16** Optical energy levels of N split interstitial defect with respect to band edges.

Though  $N_{i,split}$  defect is more stable throughout the band gap region compared to  $N_{i,oct}$  in the charge states of 0, -1, and -2. Particularly, in charge state -2, the defect formation energy of  $N_{i,oct}$  is 0.6 eV higher using the BB1K functional and 0.05 eV higher if B97-2 is used, than  $N_{i,split}$  counterparts. However, for  $N_{i,split}^{2-}$ , though it can be stable in our calculation, the charge transitions  $(-2|-1)$  occurs in the conduction band, which means it can autoionize very easily to becoming  $N_{i,split}^{1-}$ . The  $N_{i,split}^{3-}$  is not stable in our calculation, but both the  $N_{i,oct}^{2-}$  and  $N_{i,oct}^{3-}$  can be dominant N interstitial defect types (**Figure 6.2**). For the same charge

state of the two configurations, here a nudged elastic band calculation can be done in the future to find the transition energy between two configurations.

**Table 6.12** Bond lengths (Å) of the N-N dimer structure of the N split interstitial in charge states -2, -1, 0, +1, +2, and +3, calculated by B97-2 and BB1K functionals.

Charge	Bond length of N-N (Å)		
	Present work		Previous work <sup>115</sup>
	B97-2	BB1K	HSE06
-2	1.47	1.46	
-1	1.47	1.46	1.47
0	1.36	1.36	1.35
+1	1.26	1.25	1.27
+2	1.17	1.16	1.18
+3	1.10	1.09	

**Table 6.13** Defect energy levels (eV) of  $N_{i,split}$  and  $N_{i,oct}$  with respect to the VBM.

	Present work			Previous work			
	B97-2	PBE0	BB1K	HSE (2020) <sup>110</sup>	HSE (2019) <sup>81</sup>	HSE (2014) <sup>115</sup>	LDA (2002) <sup>76</sup>
$N_{i,split}(-1 0)e$	4.21	4.33	4.67	2.82	2.70	3.07	2.60
$N_{i,split}(0 +1)e$	3.68	3.79	4.27	2.16	2.12	2.69	1.84
$N_{i,split}(+1 +2)e$	2.24	2.32	2.79	0.94	1.88	0.70	1.45
$N_{i,split}(+2 +3)e$	1.83	1.88	2.36		1.17		
$N_{i,oct}(0 -1)h$	4.11	4.13	4.50				
$N_{i,oct}(-1 -2)h$	4.49	4.53	4.94				
$N_{i,oct}(-2 -3)h$	4.99	5.16	4.44				

**Table 6.14** Formation energies (eV) of  $N_{i,split}^0$  and  $N_{i,oct}^0$ .

	Present work			Previous work	
	B97-2	PBE0	BB1K	HSE	LDA <sup>76</sup>
$N_{i,split}^{0,N-rich}$	4.22	4.05	4.17	5.12 <sup>110</sup> , 5.16 <sup>81</sup> , 5.04 <sup>115</sup>	5.66
$N_{i,split}^{0,N-poor}$	7.51	7.34	7.46	8.28 <sup>110</sup> , 8.22 <sup>115</sup>	9.17
$N_{i,oct}^{0,N-rich}$	7.83	7.69	7.59		
$N_{i,oct}^{0,N-poor}$	11.13	10.99	10.88		

**(d) N antisite ( $N_{Al}$ )**

The N antisite defect is found to be stable in three different configurations in the lattice, all of which are stabilised by bonding with another neighbouring N atom and forming an N-N split interstitial defect complex in the lattice. Two different configurations are presented in **Figure 6.17** and **Figure 6.18** respectively. In the first configuration (termed here “config-A”, or  $N_{Al,A}$ ),  $N_{Al,A}$  is bonded with a basal N atom.  $N_{Al}$  is displaced towards the basal N atom, reducing the N-N bond distance.  $N_{Al,A}$  is calculated to be stable in charge states +3 to -2 in the band gap region (**Figure 6.2**), and it behaves donor-like. In charge state -2, the N-N bond distance is shorter than the perfect Al-N bond length by 0.57Å (30%), which is very close to “29%” from previous calculation for cubic AlN<sup>75</sup>. As the charge becomes more positive, the N-N bond distance becomes shorter, and the shortest value is reached in the neutral charge state at 1.17Å (1.14Å), which is close to the bond length of a N<sub>2</sub> gas molecule (**Table 6.15**). The spin density in charge states -2 and -1 adopts the shape of an anti-bonding  $\pi$  orbital, which proves the electronical similarity to N<sub>2</sub> molecule. In the charge state -3, the configuration is stable in the conduction band region, so the  $N_{Al,A}$  in such a state will be autoionized to more positive states.



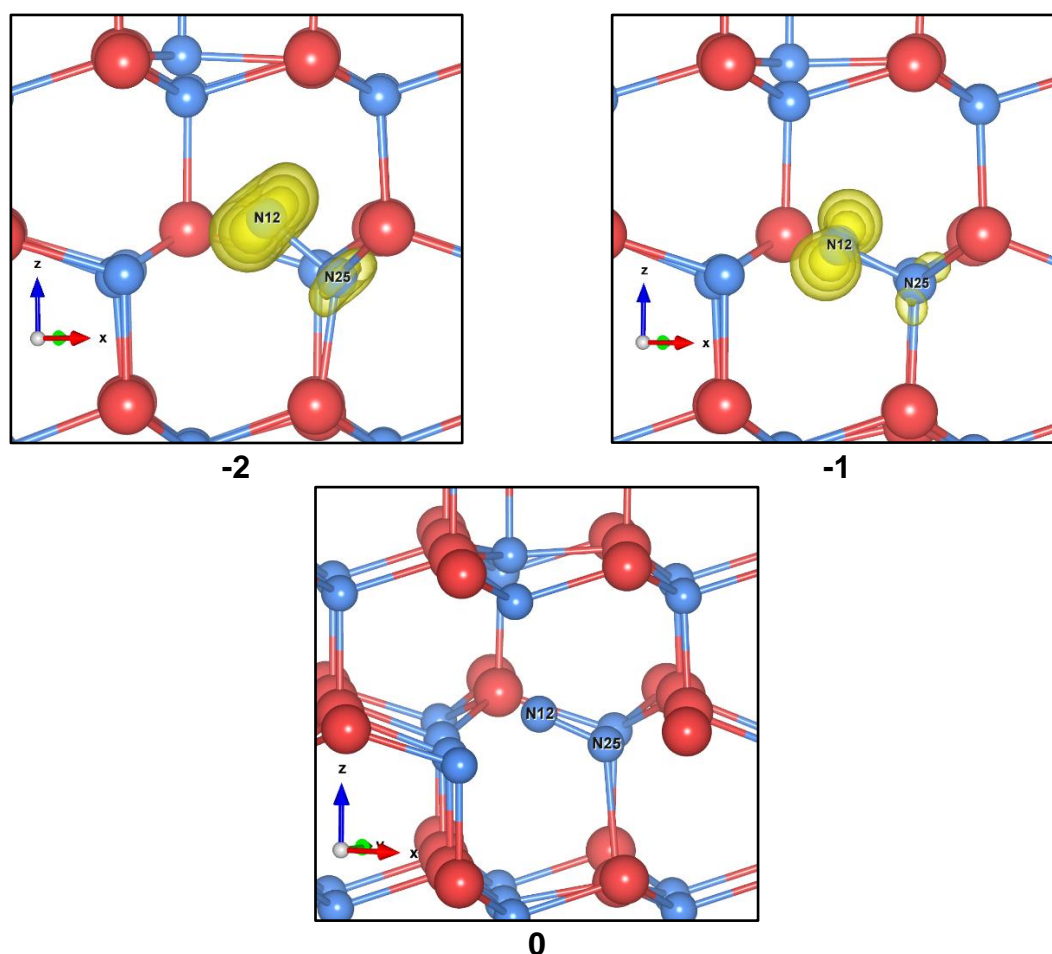


**Figure 6.17** Optimized geometry of N antisite defect in “Configuration A” in the charge states -2, -1, and 0. The spin density is presented for the defect in charge states -2 and -1 (yellow isosurfaces of 0.1, 0.05, and 0.025 a.u.).

From the charge state +1 of  $N_{Al,A}$ , the configuration becomes less stable than another configuration (“config-B”, or  $N_{Al,B}$ ), in which the N antisite defect bonds with the axial N atom and two basal N atoms in a trigonal configuration (**Figure 6.18**). The  $N_{Al,B}$  is stable in charge states from +3 to -1 in the band gap (**Figure 6.2**). In charge state +1, a hole is well localized on the  $N_{Al,B}$  defect where it forms by removing one of the two electrons from the 2s orbital of the N ion. It is very chemically difficult to remove more electrons from the electronic shell which is close to the core region, so in charge state +3, the hole localises on the N atom outside the trigonal bonded configuration.



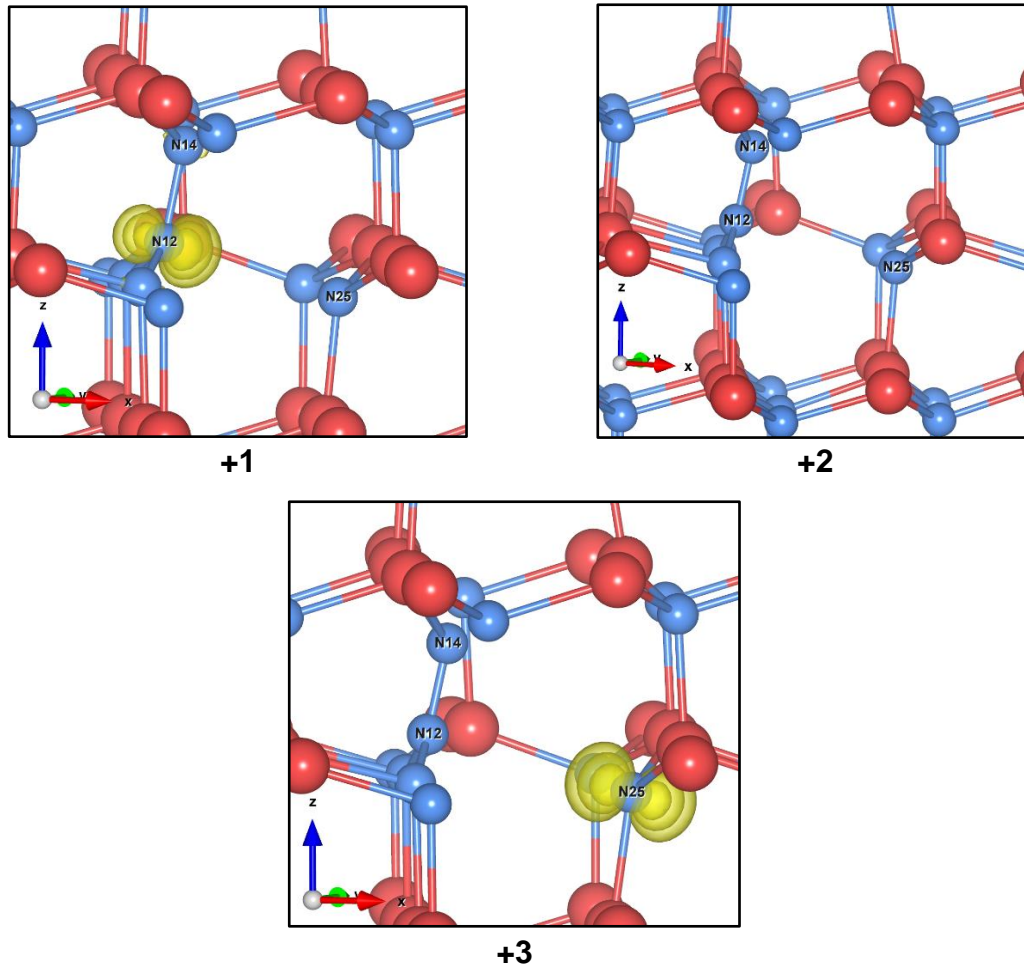


**Figure 6.18** Optimized geometry of N antisite defect in “Configuration B” in charge states +1, +2, and +3. Electron localisation in charge states +1 and +3 is shown with the spin density (yellow isosurfaces of 0.1, 0.05, and 0.025 a.u.).

There have been several theoretical studies of the  $N_{Al}$  in AlN, but only a few of them discuss the two configurations of the defect. Most of the early work investigate the defect only in the cubic phase of AlN<sup>75,76,201</sup>, and claim that there is small difference between the two structural phases<sup>76</sup>. The EL2 geometry of N antisite in cubic AlN in these reports is the closest configuration to our config-A and config-B types. More recent studies of the  $N_{Al}$  are either unclear about the geometry<sup>110</sup>, or only on the substitutional type<sup>81</sup>, which we found is generally less stable in the band gap. Therefore, we do not make a direct comparison of our results with others. The trend in the charge transition energies and the neutral charge defect formation energy from our QM/MM method compared to the PBC based DFT reports are consistent with those previously discussed for other defect

types. The relevant data are presented in **Table 6.16** and **Table 6.17**. Experimentally, there is still no identification of the N antisite defect in AlN.

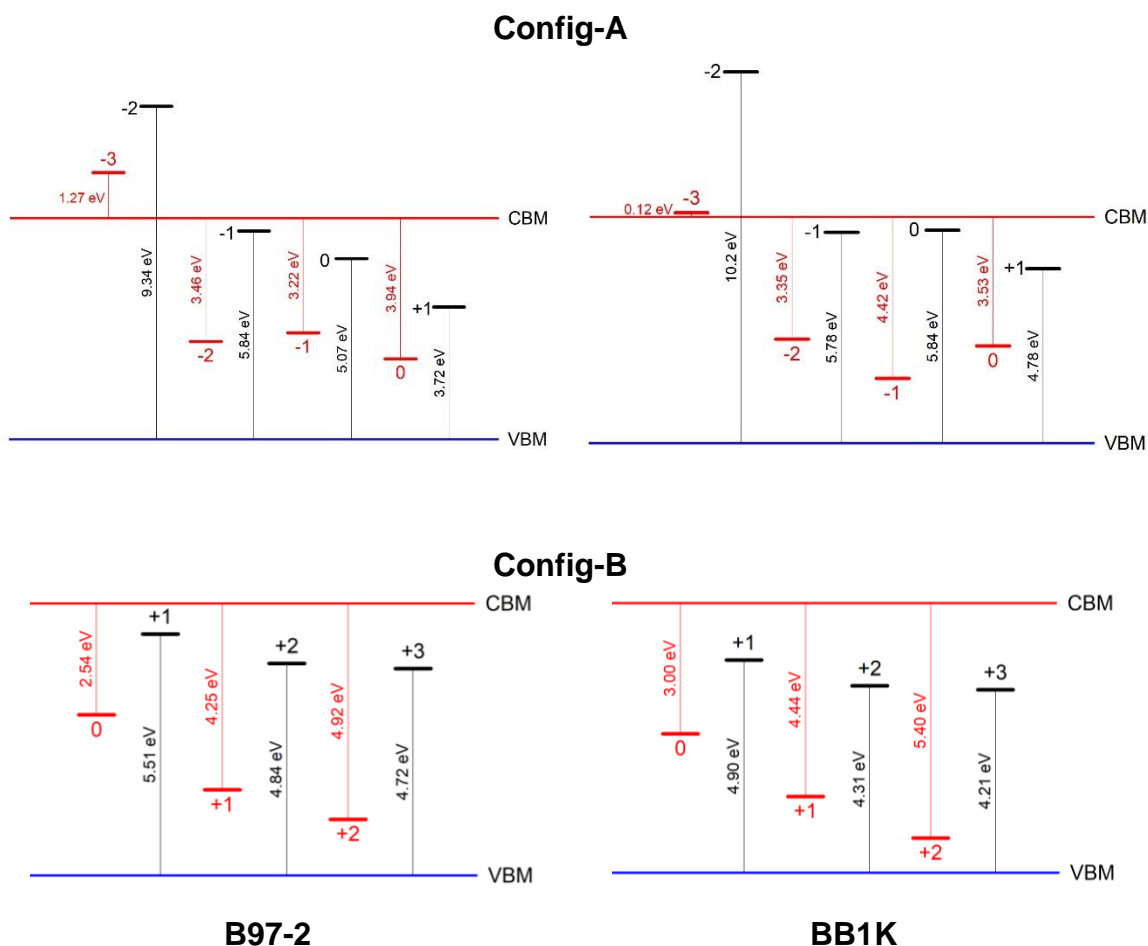


**Figure 6.19** Optical energy levels of N antisite defect with respect to band edges.

**Table 6.15** Bond lengths ( $\text{\AA}$ ) of the N-N dimer struture of the N antisite defect in two different configurations in charge states -2, -1, 0, +1, +2, and +3, calculated by B97-2 and BB1K functionals.

Charge	Bond length of N-N ( $\text{\AA}$ )			
	Config. A		Config. B	
	B97-2	BB1K	B97-2	BB1K
-2	1.32	1.31		
-1	1.24	1.31		
0	1.17	1.14	1.55	1.53

<b>+1</b>	1.45	1.42
<b>+2</b>	1.30	1.28
<b>+3</b>	1.32	1.30

**Table 6.16** Defect energy levels (eV) of N antisite with respect to the VBM.

	Present work			Previous work
	B97-2	PBE0	BB1K	HSE (2020) <sup>110</sup>
$N_{Al,A}(-2 -1)e$	4.21	4.26	4.52	3.63 (-2 0)2e
$N_{Al,A}(-1 0)e$	3.97	4.03	4.31	
$N_{Al,B}(-1 0)e$	4.05	4.35	4.79	
$N_{Al,A}(0 +1)e$	2.97	3.13	3.63	2.30
$N_{Al,B}(0 +1)e$	4.01	4.12	4.63	
$N_{Al,A}(+1 +2)e$	2.26	2.38	2.90	1.99
$N_{Al,B}(+1 +2)e$	2.98	3.01	3.42	
$N_{Al,A}(+2 +3)e$	2.20	2.32	2.72	
$N_{Al,B}(+2 +3)e$	2.55	2.65	3.01	

**Table 6.17** Formation energies (eV) of N antisite.

	Present work			Previous work	
	B97-2	PBE0	BB1K	HSE	LDA <sup>76</sup>
$N_{Al,A}^{0,N-rich}$	6.93	7.17	7.96	7.75 <sup>110</sup> , 6.73 <sup>81</sup>	5.71, 6.04
$N_{Al,B}^{0,N-rich}$	7.49	7.48	8.21		
$N_{Al,A}^{0,N-poor}$	10.23	10.47	11.27	14.03 <sup>110</sup>	12.84, 13.17
$N_{Al,B}^{0,N-poor}$	10.78	10.78	11.51		

### 6.4.3 Diffuse states of intrinsic defects

So far, we discussed “compact” states of defects, which are highly localised (and could be visualized as orbitals of small molecules). However, AlN is a dielectric material, so any charged defect can trap one or more electrons or holes in “diffuse”, atom like states of large effective radius. Such states of a charged defect can be modelled computationally using the effective mass theory, where an electron (or a hole) can be effectively represented by an atomic (e.g., hydrogenic) state centred on the compact charged defect. In the context of current defect calculations using the Chemshell embedded cluster approach, this idea was first realised in the previous QM/MM publication<sup>174</sup>, and a detailed theory can be found in the book by Stoneham<sup>202</sup>.

**Tables 6.18** and **6.19** present the binding energies of electrons and holes using this theory. Due to the lack of experimental values of effective masses of electrons and holes in AlN, we take the theoretical values from the previous literature, which are  $0.30m_0$  for the electron<sup>25</sup> and  $0.73m_0$  for the hole<sup>203</sup>. The binding energies are calculated through the formulae below:

$$E_H = -\frac{m^*}{2\varepsilon^2}Z^2 \quad \text{for } 1e \text{ or } 1h \text{ (H type),} \quad (6.15)$$

$$E_{He} = \frac{m^*}{\varepsilon^2}(I_{He}^{1st} + I_{He}^{2nd}) \quad \text{for } 2e \text{ or } 2h \text{ (He type),} \quad (6.16)$$

$$E_{Li,2} = \frac{m^*}{\varepsilon^2}(I_{Li}^{2nd} + I_{Li}^{3rd}) \quad \text{for } 2e \text{ or } 2h \text{ (Li type),} \quad (6.17)$$

$$E_{Li,3} = \frac{m^*}{\varepsilon^2}(I_{Li}^{1st} + I_{Li}^{2nd} + I_{Li}^{3rd}) \quad \text{for } 3e \text{ or } 3h \text{ (Li type),} \quad (6.18)$$

$$E_{Hydride} = \frac{m^*}{\varepsilon^2}(I_H + A_H) \quad \text{for } 2e \text{ or } 2h \text{ (H type),} \quad (6.19)$$

where  $E_H$ ,  $E_{He}$ ,  $E_{Li}$ , and  $E_{Hydride}$  are the binding energies of diffuse states,  $m^*$  is the respective effective mass of the electron or the hole,  $\varepsilon$  is dielectric constant (for adiabatic processes, 10.98 from our GULP calculations),  $Z$  is the charge of the compact defect state,  $I$  represents the ionisation potential, and  $A$  represents the electron affinity.

**Table 6.18** The binding energies (eV) of the diffuse electrons in AlN with respect to CBM.

Electron type	Defect charge, $Z$	Binding energy (eV)
1e (H type)	+1	-0.034
	+2	-0.135
	+3	-0.305
2e (Hydride type)	+1	-0.036
2e (He type)	+2	-0.197
2e (Li type)	+3	-0.493
3e (Li type)	+3	-0.506

**Table 6.19** The binding energies (eV) of the diffuse holes in AlN with respect to VBM.

Hole type	Defect charge	Binding energy (eV)
1h (H type)	-1	-0.082
	-2	-0.328
	-3	-0.738
2h (H type)	-1	-0.087
2h (He type)	-2	-0.476
2h (Li type)	-3	-1.195
3h (Li type)	-3	-1.227

**Table 6.20 – 6.26** list the calculated formation energies of all the diffused states of defects in different charge states with the corresponding compact states, where their formation stability can be compared directly to see which type is more favourable in each charge states.

**Table 6.20** Formation energies (eV) of compact and diffuse states of  $V_{Al}$  in AlN. The compact state energies are taken from the defect formation energies at VBM level. The hydrogenic state energies for diffuse electrons and holes are calculated with respect to the corresponding formation energies at VBM.

Defect charge	Defect type	Defect type	Functional		
			B97-2	PBE0	BB1K
0	Compact	$V_{Al}^0$	6.021	6.236	6.943
	Diffuse	$V_{Al}^{1+} + 1e_{(H)}$	3.392	3.455	3.803
		$V_{Al}^{1-} + 1h_{(H)}$	9.177	9.553	10.636
		$V_{Al}^{2-} + 2h_{(He)}$	12.424	12.970	14.472
		$V_{Al}^{3-} + 3h_{(Li)}$	15.675	16.375	18.212
1-	Compact	$V_{Al}^{1-}$	9.259	9.636	10.718
	Diffuse	$V_{Al}^{2-} + 1h_{(H)}$	12.572	13.118	14.620
		$V_{Al}^{3-} + 2h_{(He)}$	16.708	16.407	18.245
2-	Compact	$V_{Al}^{2-}$	12.900	13.446	14.948
	Diffuse	$V_{Al}^{3-} + 1h_{(H)}$	16.164	16.863	18.701
1+	Compact	$V_{Al}^{1+}$	3.426	3.489	3.837
	Diffuse	$V_{Al}^{1-} + 2h_{(H)}$	9.172	9.549	10.632

**Table 6.21** Formation energies (eV) of compact and diffuse states of  $V_N$  in AlN. The compact state energies are taken from the defect formation energies at CBM level. The hydrogenic state energies for diffuse electrons and holes are calculated with respect to the corresponding formation energies at CBM.

Defect charge	Defect type	Defect type	Functional		
			B97-2	PBE0	BB1K
0	Compact	$V_N^0$	6.326	6.379	6.490
	Diffuse	$V_N^{1-} + 1h_{(H)}$	12.465	12.658	13.110
		$V_N^{1+} + 1e_{(H)}$	6.490	6.522	6.150
		$V_N^{2+} + 2e_{(He)}$	9.730	9.679	9.108
		$V_N^{3+} + 3e_{(Li)}$	13.132	13.110	12.110
1+	Compact	$V_N^{1+}$	6.524	6.556	6.184
	Diffuse	$V_N^{2+} + 1e_{(H)}$	9.792	9.740	9.169
		$V_N^{3+} + 2e_{(Li)}$	13.145	13.134	12.123
2+	Compact	$V_N^{2+}$	9.927	9.876	9.305
	Diffuse	$V_N^{3+} + 1e_{(H)}$	13.333	13.312	12.312
1-	Compact	$V_N^{1-}$	6.347	6.540	6.992
	Diffuse	$V_N^{1+} + 2e_{(H)}$	6.488	6.520	6.149

**Table 6.22** Formation energies (eV) of compact and diffuse states of  $Al_i$  in AlN. The compact state energies are taken from the defect formation energies at CBM level. The hydrogenic state energies for diffuse electrons and holes are calculated with respect to the corresponding formation energies at CBM.

Defect charge	Defect type	Defect type	Functional		
			B97-2	PBE0	BB1K
0	Compact	$Al_i^0$	12.941	12.639	12.287
		$Al_i^{1+} + 1e_{(H)}$	12.469	12.103	11.262
	Diffuse	$Al_i^{2+} + 2e_{(He)}$	13.498	12.958	11.654
		$Al_i^{3+} + 3e_{(Li)}$	13.973	13.313	11.244
1+	Compact	$Al_i^{1+}$	12.503	12.137	11.296
		$Al_i^{2+} + 1e_{(H)}$	13.559	13.019	11.716
	Diffuse	$Al_i^{3+} + 2e_{(Li)}$	13.986	13.327	11.257
2+	Compact	$Al_i^{2+}$	13.695	13.154	11.851
	Diffuse	$Al_i^{3+} + 1e_{(H)}$	14.174	13.515	11.446

**Table 6.23** Formation energies (eV) of compact and diffuse states of  $N_{i,oct}$ . The compact state energies are taken from the defect formation energies at VBM level. The hydrogenic state energies for diffuse electrons and holes are calculated with respect to the corresponding formation energies at VBM.

Defect charge	Defect type	Defect type	Functional		
			B97-2	PBE0	BB1K
0	Compact	$N_{i,oct}^0$	7.833	7.693	7.586
		$N_{i,oct}^{1-} + 1h_{(H)}$	11.862	11.744	12.001
	Diffuse	$N_{i,oct}^{2-} + 2h_{(He)}$	15.962	15.875	16.549
		$N_{i,oct}^{3-} + 3h_{(Li)}$	20.199	20.288	21.235
1-	Compact	$N_{i,oct}^{1-}$	11.944	11.826	12.083
		$N_{i,oct}^{2-} + 1h_{(H)}$	16.110	16.023	16.697
	Diffuse	$N_{i,oct}^{3-} + 2h_{(Li)}$	20.232	21.320	21.267
2-	Compact	$N_{i,oct}^{2-}$	16.438	16.351	17.025
	Diffuse	$N_{i,oct}^{3-} + 1h_{(H)}$	20.688	20.777	21.723

**Table 6.24** Formation energies (eV) of compact and diffuse states of  $N_{i,split}$ . The compact state energies are taken from the defect formation energies at CBM level. The hydrogenic state energies for diffuse electrons and holes are calculated with respect to the corresponding formation energies at CBM.

Defect charge	Defect type		Functional		
			B97-2	PBE0	BB1K
0	Compact	$N_{i,split}^0$	4.217	4.048	4.165
		$N_{i,split}^{1+} + 1e_{(H)}$	6.698	6.422	6.065
	Diffuse	$N_{i,split}^{2+} + 2e_{(He)}$	10.499	10.144	9.310
		$N_{i,split}^{3+} + 3e_{(Li)}$	14.575	14.165	12.850
1+	Compact	$N_{i,split}^{1+}$	6.732	6.456	6.098
		$N_{i,split}^{2+} + 1e_{(H)}$	10.560	10.205	9.371
	Diffuse	$N_{i,split}^{3+} + 2e_{(Li)}$	14.871	14.462	12.146
2+	Compact	$N_{i,split}^{2+}$	10.696	10.340	9.506
	Diffuse	$N_{i,split}^{3+} + 1e_{(H)}$	14.871	14.462	13.146
1-	Compact	$N_{i,split}^{1-}$	2.230	2.181	2.639
	Diffuse	$N_{i,split}^{1+} + 2e_{(H)}$	6.696	6.420	6.063

**Table 6.25** Formation energies (eV) of compact and diffuse states of  $N_{Al,A}$ . The compact state energies are taken from the defect formation energies at CBM level. The hydrogenic state energies for diffuse electrons and holes are calculated with respect to the corresponding formation energies at CBM.

Defect charge	Defect type		Functional		
			B97-2	PBE0	BB1K
0	Compact	$N_{Al,A}^0$	6.930	7.171	7.790
		$N_{Al,A}^{1+} + 1e_{(H)}$	10.126	10.203	10.502
	Diffuse	$N_{Al,A}^{2+} + 2e_{(He)}$	13.898	13.994	13.766
		$N_{Al,A}^{3+} + 3e_{(Li)}$	17.584	17.433	16.811
1+	Compact	$N_{Al,A}^{1+}$	10.160	10.237	10.536
		$N_{Al,A}^{2+} + 1e_{(H)}$	13.959	13.926	13.698
	Diffuse	$N_{Al,A}^{3+} + 2e_{(Li)}$	17.597	17.447	17.012
2+	Compact	$N_{Al,A}^{2+}$	14.095	14.062	13.834
	Diffuse	$N_{Al,A}^{3+} + 1e_{(H)}$	17.785	17.635	17.012
1-	Compact	$N_{Al,A}^{1-}$	4.704	5.002	6.078
	Diffuse	$N_{Al,A}^{1+} + 2e_{(H)}$	10.124	10.202	10.500



**Table 6.26** Formation energies (eV) of compact and diffuse states of  $N_{Al,B}$ . The compact state energies are taken from the defect formation energies at CBM level. The hydrogenic state energies for diffuse electrons and holes are calculated with respect to the corresponding formation energies at CBM.

Defect charge	Defect type		Functional		
			B97-2	PBE0	BB1K
0	Compact	$N_{Al,B}^0$	7.487	7.481	8.212
		$N_{Al,B}^{1+} + 1e_{(H)}$	9.647	9.525	9.748
	Diffuse	$N_{Al,B}^{2+} + 2e_{(He)}$	12.709	12.556	12.366
		$N_{Al,B}^{3+} + 3e_{(Li)}$	16.049	15.794	15.247
1+	Compact	$N_{Al,B}^{1+}$	9.681	9.558	9.782
		$N_{Al,B}^{2+} + 1e_{(H)}$	12.770	12.617	12.427
	Diffuse	$N_{Al,B}^{3+} + 2e_{(Li)}$	16.062	15.807	15.261
2+	Compact	$N_{Al,B}^{2+}$	12.906	12.752	12.562
	Diffuse	$N_{Al,B}^{3+} + 1e_{(H)}$	16.250	15.996	15.449
1-	Compact	$N_{Al,B}^{1-}$	5.340	5.633	6.805
	Diffuse	$N_{Al,B}^{1+} + 2e_{(H)}$	9.646	9.523	9.746

From these results, we found the most types of the defects are in favour of their compact states.  $V_{Al}$ ,  $N_{i,oct}$ ,  $N_{i,split}$ ,  $N_{Al,A}$ , and  $N_{Al,B}$  show no preference to the diffuse state in any of their charge states, as their compact state energies are always lower than the diffuse variants. For  $Al_i$ , the energy of diffuse state is lower in the neutral charge state. Calculations using B97-2 and PBE0 functionals show only one electron diffused is more favourable to compact neutral  $Al_i$ , but BB1K calculations shows one, two and three electrons diffused are all more favourable. The different outcome from the BB1K calculations is also seen in other charge states of  $Al_i$ , where B97-2 and PBE0 calculations show different case. For  $V_N$ , from the B97-2 results in neutral charge state, the defect is more favourable to its diffuse state where a hole loosely bound (a shallow acceptor type defect), but the BB1K result shows one electron diffused is more favourable (a shallow donor type). The BB1K calculation shows another lower energy diffuse electron state in the charge state -1, while in the same charge state, PBE0 calculation shows the diffuse state is more favourable by only 0.02 eV. In conclusion, from these calculations, we found the diffuse states only appear in Al interstitial and N vacancy types of defects, where  $Al_i^0$  and  $V_N^{1-}$  is a possible shallow donor source, and the nature of  $V_N^0$  is still open for discussion.

#### 6.4.4 Defect concentrations

The calculated formation energies of intrinsic defects (**Figure 6.2**) can be used to calculate the thermodynamic equilibrium concentrations. At a given temperature, the equilibrium concentration of a defect can be described by the Boltzmann's equation. Meanwhile, the equilibrium concentrations of the charge carriers (i.e., electrons and holes) in the semiconductor material can be calculated by integrating the electronic density of states with the Fermi-Dirac distribution formula. In both equations, the Fermi energy is one of the common terms. Here, we apply the code SC-FERMI<sup>204</sup> to compute the self-consistent Fermi energy, given the condition of charge neutrality in the system:

$$[n_0] + [acceptors] = [p_0] + [donors] \quad , \quad (6.20)$$

where  $[n_0]$  and  $[p_0]$  are the equilibrium concentration of electrons and holes respectively. The code has been successfully applied in several other studies<sup>174,175,181,205,206</sup>. The density of electronic states used by the code is calculated using the VASP software<sup>207–210</sup>.

**Figure 6.20** shows the calculated equilibrium concentrations of the intrinsic defects and charge carriers, and the self-consistent Fermi energy as function of temperature from 300K to 2400K. In N-rich condition, the Fermi level is deep in the upper half of the band gap region, ranging from 3.55 to 3.93 eV (3.34-3.71 eV from B97-2) as the temperature increases. Using BB1K functional, the highest equilibrium concentration among all the intrinsic defects is the nitrogen split-interstitial, and the concentration of nitrogen vacancy defect is just about half an order of magnitude lower than  $[N_{i,split}]$ . Using B97-2 functional,  $[V_N]$  is about one order of magnitude higher than  $[N_{i,split}]$ . Therefore,  $V_N$  and  $N_{i,split}$  are the two intrinsic defect types that would be dominant in AlN from our calculation. In the range of the self-consistent Fermi energy,  $V_N^{1+}$  and  $N_{i,split}^{1+}$  are the most dominant charge states. However, at about 1000K, the concentrations of both defects are just at about  $10^4 \text{ cm}^{-3}$ . The Al vacancy is more dominant (by about four orders of magnitude) than the Al interstitial using B97-2 functional, while  $Al_i$  is more dominant than  $V_{Al}$  (by about seven orders of magnitude) using BB1K, but the concentration can only be above  $10^4 \text{ cm}^{-3}$  over 1500K.

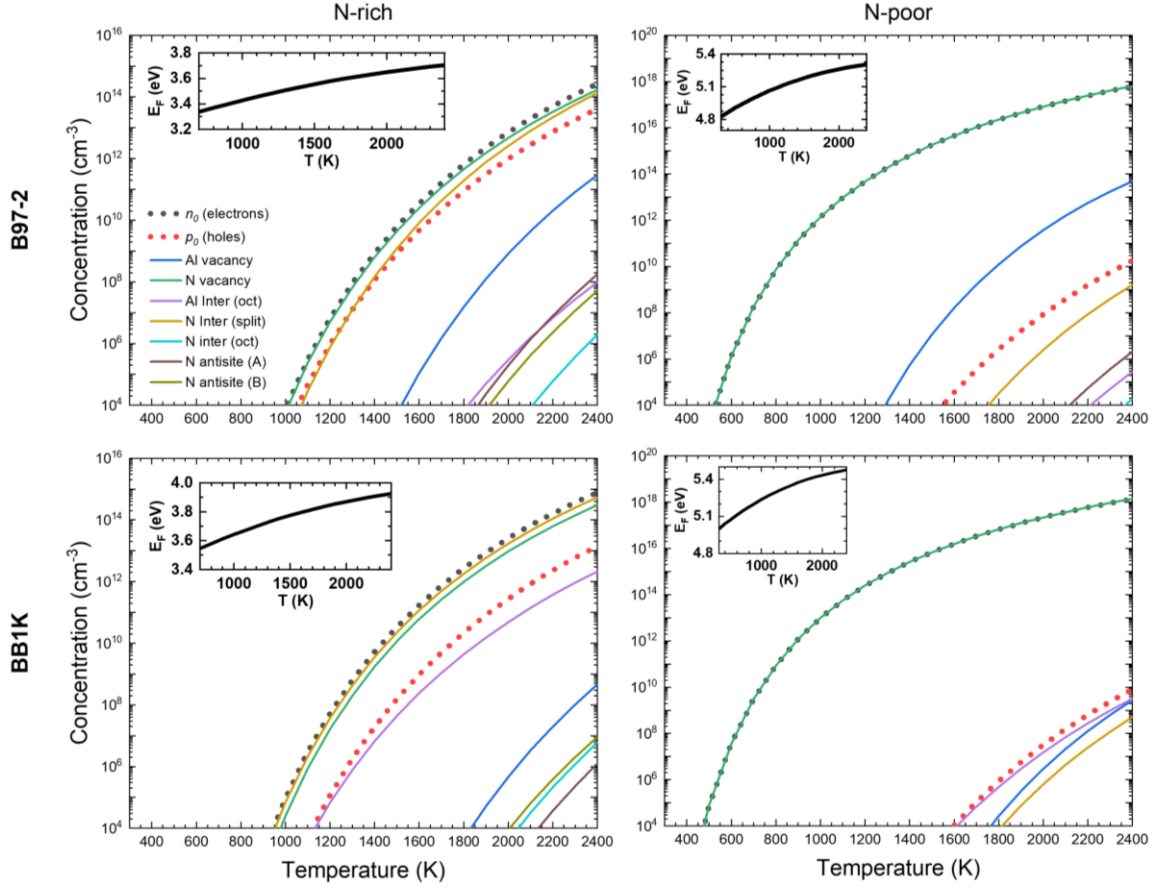


**Figure 6.20** The calculated equilibrium concentrations of charge carriers (electrons and holes) and the intrinsic defects as a function of temperature in N-rich and N-poor condition using B97-2 and BB1K hybrid functionals. The insets show the calculated self-consistent Fermi energies in each condition.

In N-poor condition, due to the lower formation energy of  $V_N$ , the equilibrium concentration of  $V_N$  is the highest among all the defects. The  $[V_N]$  is higher by about  $10^8 \text{ cm}^{-3}$  than it is in N-rich condition. The Fermi energy from 300 to 2400 K is ranging from 5.0 to 5.5 eV from BB1K functional (4.8-5.3 eV from B97-2), which is closer to the CBM and the electron carriers in turn increase. The concentrations of another charge carrier and other defects are becoming much lower due to the rise of the Fermi energy.  $V_N^{1+}$  is still the dominant charge state in the N-poor condition.

The results show lower concentration of charge carriers in AlN compared to GaN<sup>181</sup> which carrier concentration is calculated to be about one order of magnitude lower in N-poor condition and four orders of magnitude higher in N-rich

condition than AlN at 1400 K. Similar concentration difference is found in experiment where the n-type carrier concentrations are measured to be about same order of magnitude higher in GaN than in AlN deposited at 1100 °C<sup>211</sup>. In theory, the carrier density in intrinsic semiconductor (semiconductor without any defect) can be estimated through the Boltzmann distribution function based on the band gap energy and the density of states, which also estimates the intrinsic carrier density of AlN is lower by four orders of magnitude than GaN at 1400 K<sup>212</sup>. Several other experimental measurements of absolute carrier concentration in AlN were reported<sup>56,213–215</sup>, but none of them can compare directly with our results. The AlN samples in these reports are intentionally or unintentionally doped with extrinsic impurities like O, Si, Mg, and C, so their charge carrier concentrations are normally about eighteen orders of magnitude per cm<sup>3</sup>, much higher than our calculated results at common deposition temperature (around 1000-1400K). To our knowledge, there is no experimental research about native donor/acceptor in AlN to this date.

#### 6.4.5 Defect processes of intrinsic defects

In this section, we focus on the optical transitions of the intrinsic defects, as the thermodynamic results are primarily discussed in the previous sections. The configuration-coordinate diagram is used to picture the vertical ionization energy levels between different charge states of the defects, with the formation energies and the optimized geometries of the defects at their thermodynamic equilibrium conditions established in previous sections. The theory of configuration-coordinate diagram and the Franck-Condon principle are explained in **Chapter 2** (Section 2.8.4). Here for each type of the defects, the vertical transitions between multiple charge states are included in a single diagram. The energy states are represented by parabolic curves. The same approach is applied in the previous publication<sup>181</sup>.

In our configuration-coordinate diagrams, both the compact states and the diffuse atom like states (calculated in **Section 6.4.3**) are visualized. The diffuse state's configurational coordinate coincides with the corresponding compact energy state and with the lower ground state energies (by the amount of the binding energies).

As the carriers are still excited (or emitted) to the edges of the energy bands, curves of the diffuse states are represented narrower than the compact states, so that the carriers are ionized to the compact states.

Here are the notations that are used in the following sections:  $E_{PL}$  is the energy of the photoluminescence (PL) process, or the energy of an emitted photon when an electron goes vertically from CBM to a lower energy state.  $E_{ab}$  is the optical absorption (AB) energy when an electron is excited vertically from VBM to a higher energy state.  $E_{ZPL}$  is the energy of the “zero-phonon line” (ZPL) which is the energy difference between the initial and final ionized ground states of the defect.  $E_{rel}$  ( $E_{rel}^*$ ) is the relaxation energy after the defect is ionized. In the following sections, **Figure 6.22-6.28** show the selected vertical transitions in the configuration-coordinate diagram, and **Table 6.27-6.31** present all the ionization energies of the corresponding defect type.

## (a) Al vacancy

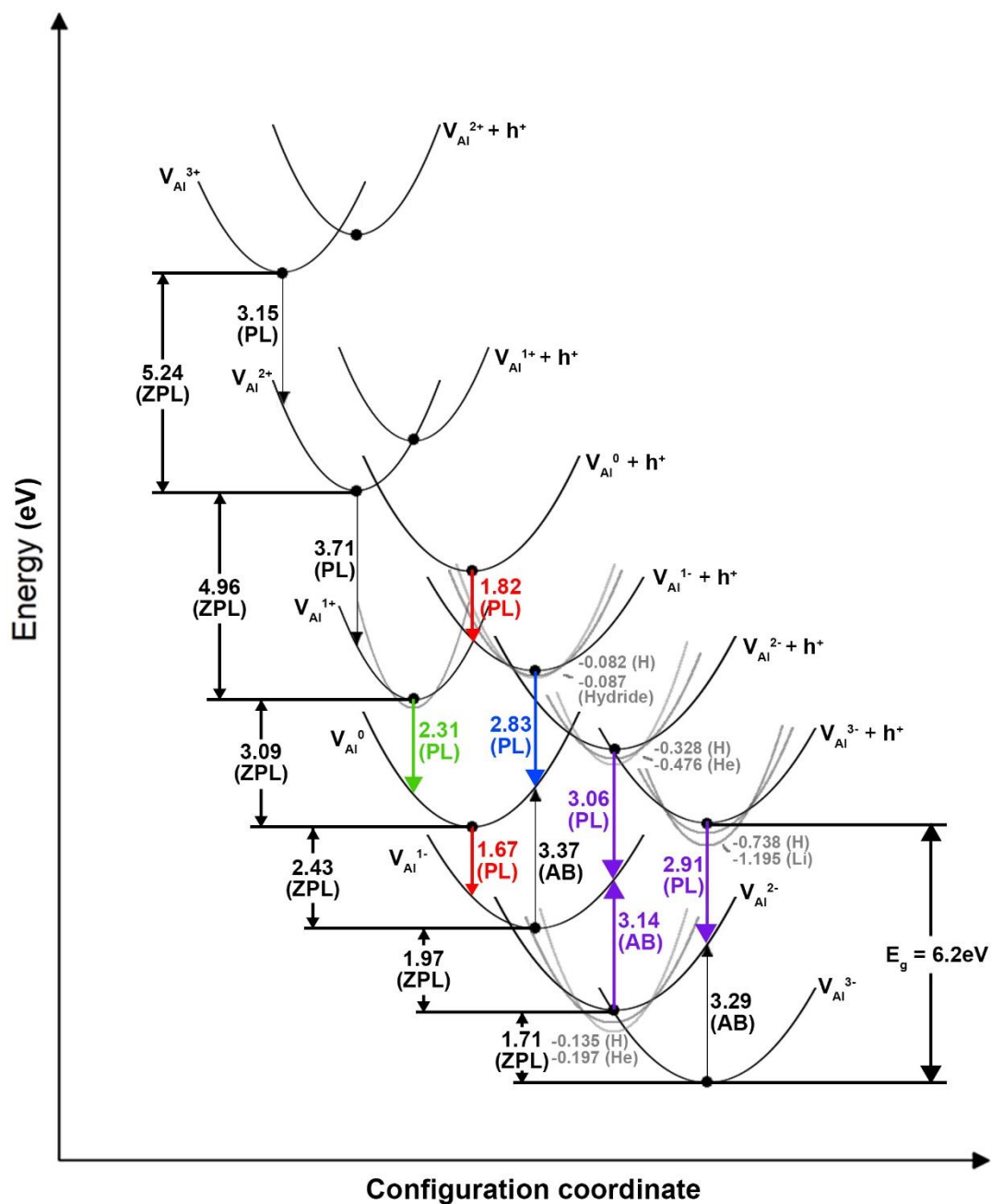


**Figure 6.21** Configuration-coordinate diagram for  $V_{Al}$  using BB1K functional. The coloured vertical arrows indicate the optical transitions of visible light. The grey curves are the diffuse states of corresponding compact defect states.

**Table 6.27** Ionization energies of  $V_{Al}$  in all charge states using B97-2 and BB1K functional. The underlined  $E_{PL}$  values are the energies falling in the visible light range (1.6-3.1 eV).

Defect States	$E_{PL}$	$E_{ab}$	$E_{ZPL}$	$E_{rel}$	$E_{rel}^*$
<b>B97-2</b>					
$V_{Al} (-3 -2) e$	0.592	3.603	2.198	1.606	1.405
$V_{Al} (-2 -1) e$	<u>1.667</u>	3.429	2.559	0.892	0.870
$V_{Al} (-1 0) e$	<u>2.447</u>	3.492	2.962	0.515	0.529
$V_{Al} (0 +1) e$	<u>3.062</u>	5.089	3.605	0.542	1.485
$V_{Al} (+1 +2) e$	4.057	6.216	5.413	1.356	0.803
$V_{Al} (+2 +3) e$	3.945	6.949	5.649	1.704	1.300
$V_{Al} (-2 -3) h$	<u>2.597</u>	5.608	4.002	1.405	1.606
$V_{Al} (-1 -2) h$	<u>2.771</u>	4.533	3.641	0.870	0.892
$V_{Al} (0 -1) h$	<u>2.708</u>	3.753	3.238	0.529	0.515
$V_{Al} (+1 0) h$	1.111	3.138	2.595	1.485	0.542
$V_{Al} (+2 +1) h$	-0.016	2.143	0.787	0.803	1.356
$V_{Al} (+3 +2) h$	-0.749	2.255	0.551	1.300	1.704
<b>BB1K</b>					
$V_{Al} (-3 -2) e$	0.001	3.292	1.709	1.707	1.584
$V_{Al} (-2 -1) e$	0.860	3.136	1.970	1.110	1.166
$V_{Al} (-1 0) e$	<u>1.672</u>	3.374	2.425	0.752	0.950
$V_{Al} (0 +1) e$	<u>2.311</u>	4.378	3.094	0.783	1.284
$V_{Al} (+1 +2) e$	3.713	6.209	4.962	1.250	1.246
$V_{Al} (+2 +3) e$	<u>3.148</u>	6.915	5.235	2.087	1.680
$V_{Al} (-2 -3) h$	<u>2.908</u>	6.199	4.491	1.584	1.707
$V_{Al} (-1 -2) h$	<u>3.064</u>	5.340	4.230	1.166	1.110
$V_{Al} (0 -1) h$	<u>2.826</u>	4.905	3.775	0.950	0.752
$V_{Al} (+1 0) h$	<u>1.822</u>	3.830	3.106	1.284	0.783
$V_{Al} (+2 +1) h$	-0.009	<u>2.487</u>	1.238	1.246	1.250
$V_{Al} (+3 +2) h$	-0.715	<u>3.052</u>	0.965	1.680	2.087

## (b) N vacancy

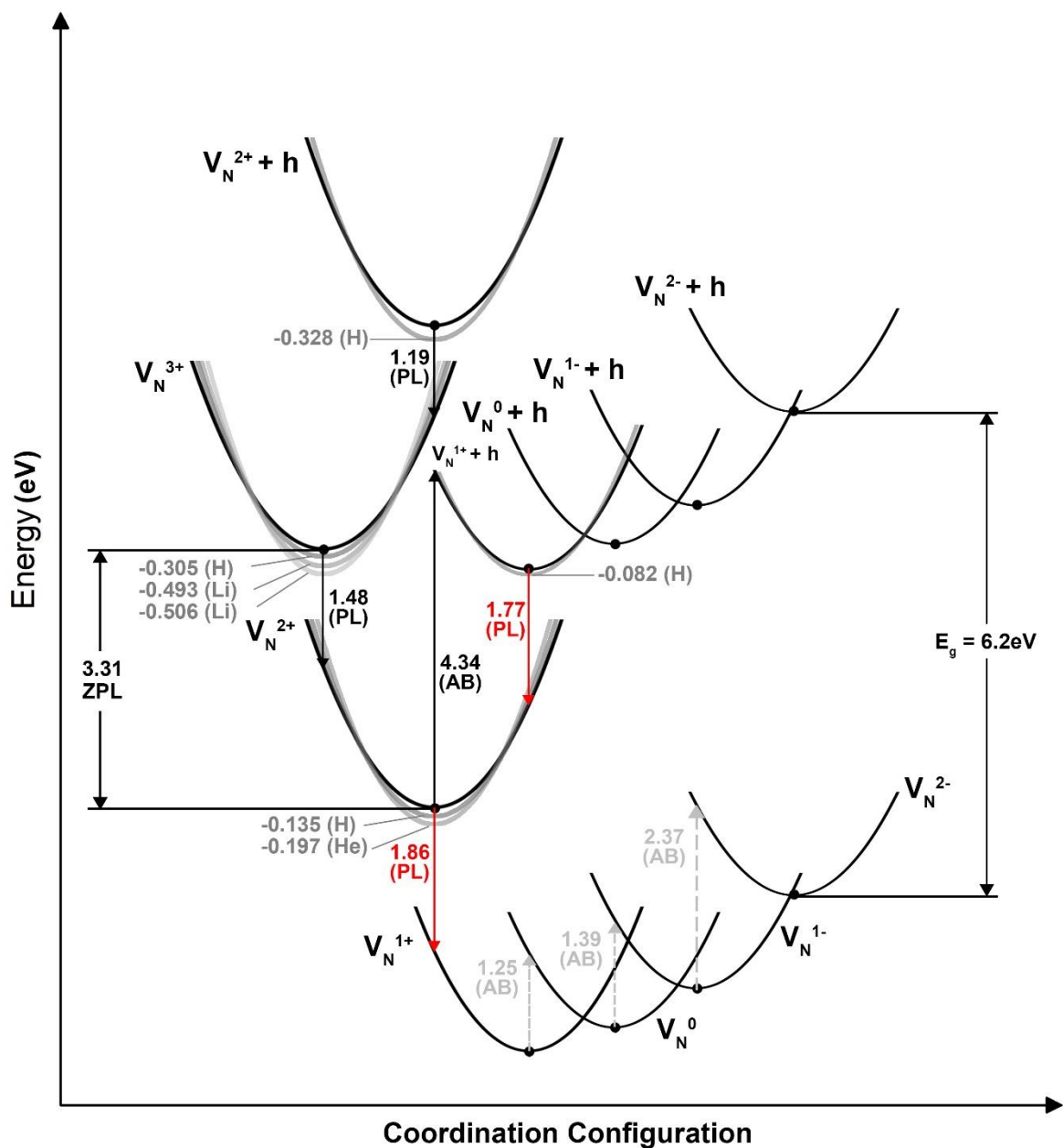


**Figure 6.22** Configuration-coordinate diagram for  $V_N$  using BB1K functional. The coloured vertical arrows indicate the optical transitions of visible light. The grey curves are the diffuse states of corresponding compact defect states.



**Table 6.28** Ionization energies of  $V_N$  in all charge states using B97-2 and BB1K functional. The underlined values are the energies falling in the visible light range (1.6-3.1 eV).

Defect States	$E_{PL}$	$E_{ab}$	$E_{ZPL}$	$E_{rel}$	$E_{rel}^*$
<b>B97-2</b>					
$V_N (-2 -1) e$	-1.821	0.551	-0.682	1.139	1.233
$V_N (-1 0) e$	-0.943	0.921	-0.021	0.922	0.942
$V_N (0 +1) e$	-0.772	1.252	0.198	0.970	1.054
$V_N (+1 +2) e$	<u>2.135</u>	4.723	3.403	1.268	1.320
$V_N (+2 +3) e$	<u>1.880</u>	5.428	3.711	1.831	1.717
$V_N (-1 -2) h$	5.649	8.021	6.882	1.233	1.139
$V_N (0 -1) h$	5.279	7.143	6.221	0.942	0.922
$V_N (+1 0) h$	4.948	6.972	6.002	1.054	0.970
$V_N (+2 +1) h$	1.477	4.065	2.797	1.320	1.268
$V_N (+3 +2) h$	0.772	4.320	2.489	1.717	1.831
<b>BB1K</b>					
$V_N (-2 -1) e$	-2.366	0.082	-1.206	1.161	1.288
$V_N (-1 0) e$	-1.391	0.414	-0.502	0.889	0.916
$V_N (0 +1) e$	-1.247	0.733	-0.306	0.941	1.039
$V_N (+1 +2) e$	<u>1.863</u>	4.428	3.121	1.257	1.308
$V_N (+2 +3) e$	1.482	5.015	3.312	1.829	1.704
$V_N (-1 -2) h$	6.118	8.566	7.406	1.288	1.161
$V_N (0 -1) h$	5.786	7.591	6.702	0.916	0.889
$V_N (+1 0) h$	5.467	7.447	6.506	1.039	0.941
$V_N (+2 +1) h$	<u>1.772</u>	4.337	3.079	1.308	1.257
$V_N (+3 +2) h$	1.185	4.718	2.888	1.704	1.829

## (c) Al interstitial

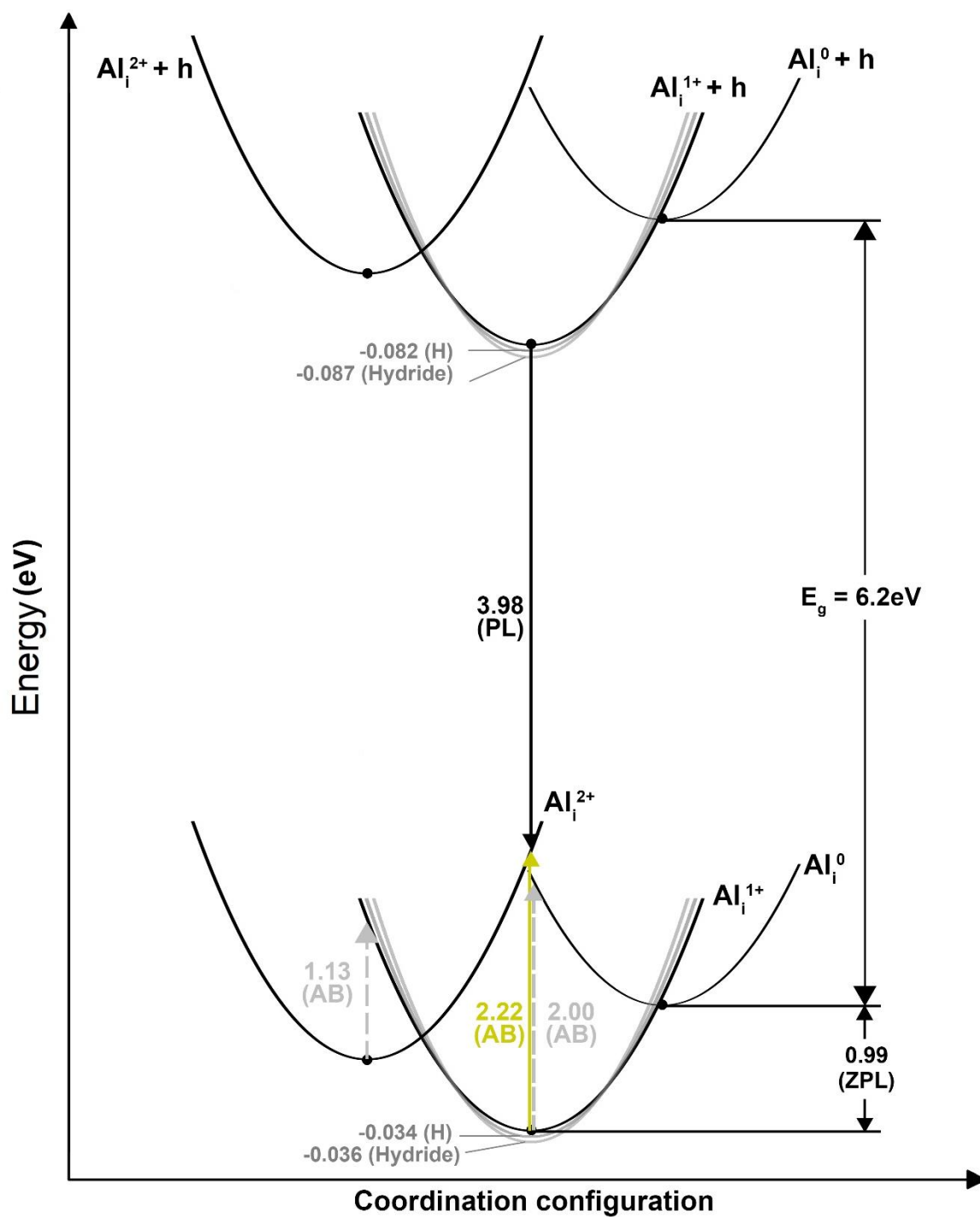


**Figure 6.23** Configuration-coordinate diagram for  $Al_i$  using BB1K functional. The coloured vertical arrows indicate the optical transitions of visible light. The grey curves are the diffuse states of corresponding compact defect states.

**Table 6.29** Ionization energies of  $Al_i$  in all charge states using B97-2 and BB1K functional. The underlined values are the energies falling in the visible light range (1.6-3.1 eV).

Defect States	$E_{PL}$	$E_{ab}$	$E_{ZPL}$	$E_{rel}$	$E_{rel}^*$
<b>B97-2</b>					
$Al_i (0 +1) e$	-1.443	0.606	-0.438	1.004	1.045
$Al_i (+1 +2) e$	-0.325	<u>2.733</u>	1.192	1.517	1.541
$Al_i (+2 +3) e$	N/A	3.118	0.784	N/A	2.333
$Al_i (+1 0) h$	5.594	7.643	6.638	1.045	1.004
$Al_i (+2 +1) h$	3.467	6.525	5.008	1.541	1.517
$Al_i (+3 +2) h$	<u>3.082</u>	N/A	5.416	2.333	N/A
<b>BB1K</b>					
$Al_i (0 +1) e$	-1.997	0.062	-0.991	1.006	1.053
$Al_i (+1 +2) e$	-1.125	<u>2.217</u>	0.555	1.680	1.662
$Al_i (+2 +3) e$		<u>2.436</u>	-0.101		2.537
$Al_i (+1 0) h$	6.138	8.197	7.191	1.053	1.006
$Al_i (+2 +1) h$	3.983	7.325	5.645	1.662	1.680
$Al_i (+3 +2) h$	3.764		6.301	2.537	

## (d) N interstitial

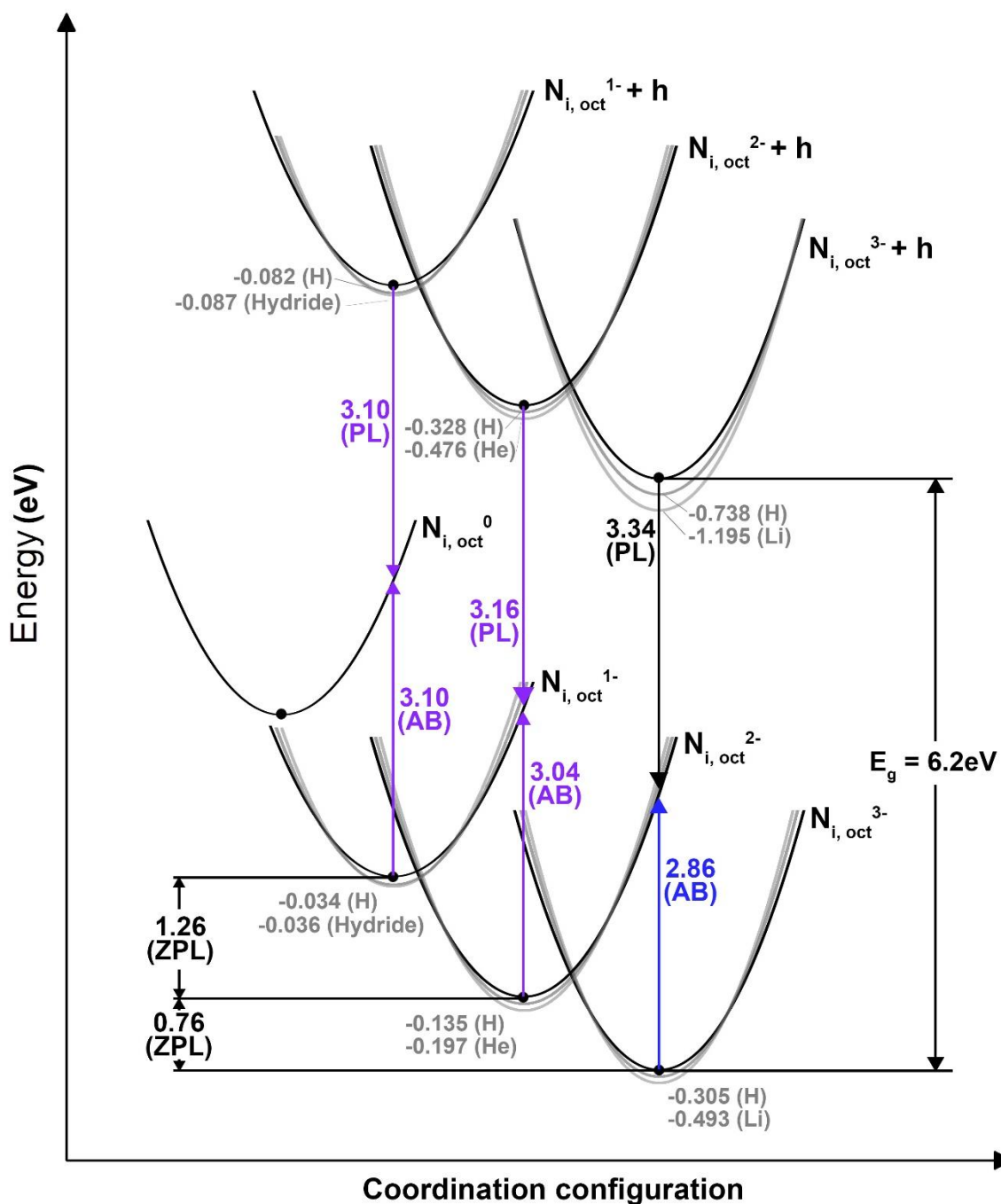


**Figure 6.24** Configuration-coordinate diagram for  $N_{i,oct}$  using BB1K functional. The coloured vertical arrows indicate the optical transitions of visible light. The grey curves are the diffuse states of corresponding compact defect states.

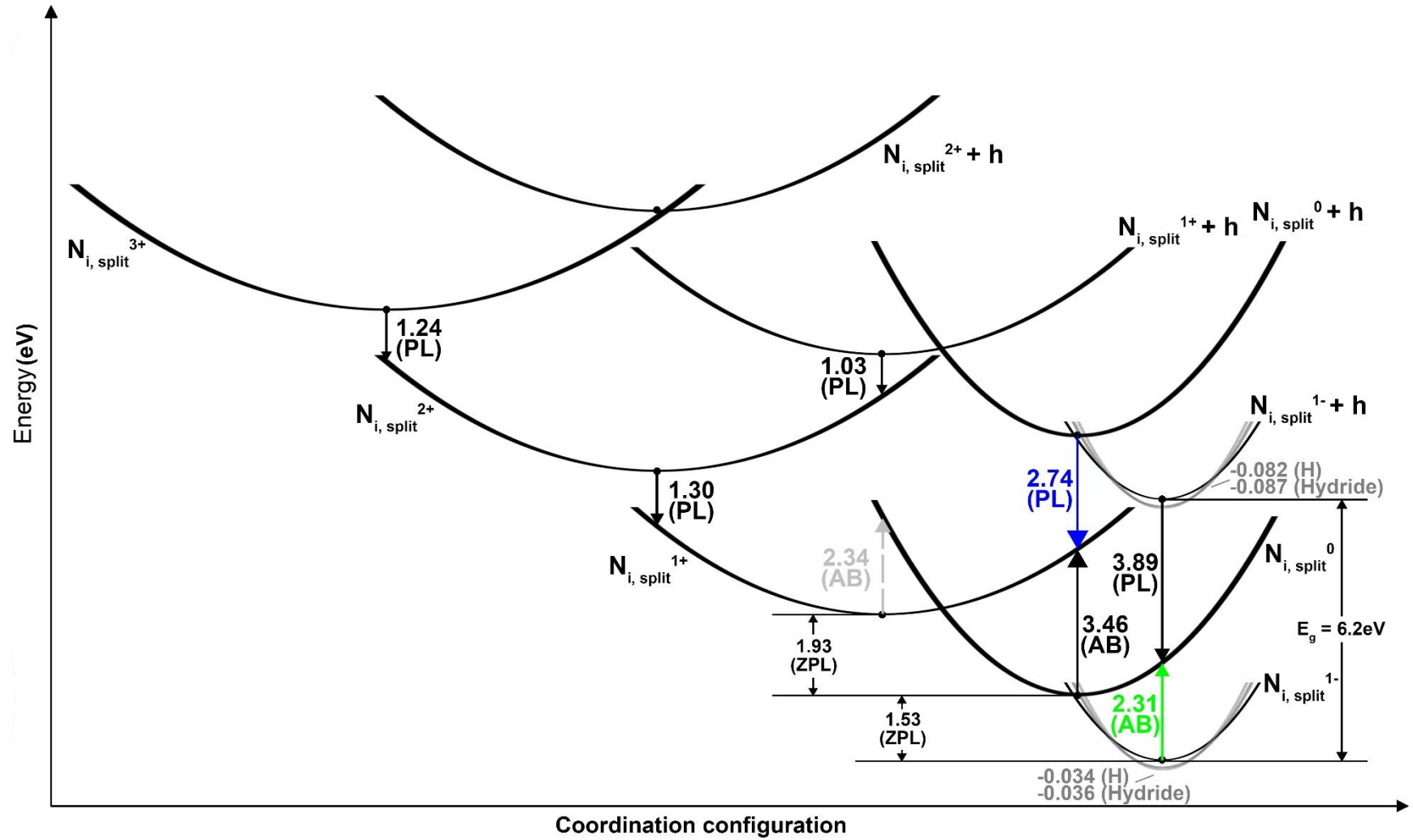


**Figure 6.25** Configuration-coordinate diagram for  $N_{i,split}$  using BB1K functional. The coloured vertical arrows indicate the optical transitions of visible light. The grey curves are the diffuse states of corresponding compact defect states.

**Table 6.30** Ionization energies of  $N_{i,oct}$  and  $N_{i,split}$  in all charge states using B97-2 and BB1K functional. The underlined values are the energies falling in the visible light range (1.6-3.1 eV).

Defect States	$E_{PL}$	$E_{ab}$	$E_{ZPL}$	$E_{rel}$	$E_{rel}^*$
<b>B97-2</b>					
$N_{i,oct} (-3 -2) e$	-1.135	3.213	1.212	2.347	2.001
$N_{i,oct} (-2 -1) e$	0.174	3.188	1.705	1.532	1.483
$N_{i,oct} (-1 0) e$	1.034	3.485	2.090	1.056	1.396
$N_{i,oct} (-2 -3) h$	<u>2.987</u>	7.335	4.988	2.001	2.347
$N_{i,oct} (-1 -2) h$	<u>3.012</u>	6.026	4.495	1.483	1.532
$N_{i,oct} (0 -1) h$	<u>2.715</u>	5.166	4.110	1.396	1.056
$N_{i,split} (-1 0) e$	0.685	<u>2.802</u>	1.987	1.301	0.815
$N_{i,split} (0 +1) e$	-1.588	3.922	2.515	4.103	1.407
$N_{i,split} (+1 +2) e$	<u>2.005</u>	5.368	3.964	1.959	1.404
$N_{i,split} (+2 +3) e$	<u>1.884</u>	6.225	4.372	2.488	1.853
$N_{i,split} (0 -1) h$	3.398	5.515	4.213	0.815	1.301
$N_{i,split} (+1 0) h$	<u>2.278</u>	7.788	3.685	1.407	4.103
$N_{i,split} (+2 +1) h$	0.832	4.195	2.236	1.404	1.959
<b>BB1K</b>					
$N_{i,oct} (-3 -2) e$	-1.595	<u>2.856</u>	0.764	2.358	2.092
$N_{i,oct} (-2 -1) e$	-0.674	<u>3.041</u>	1.257	1.932	1.784
$N_{i,oct} (-1 0) e$	0.405	<u>3.098</u>	1.703	1.298	1.395
$N_{i,oct} (-2 -3) h$	3.344	7.795	5.436	2.092	2.358
$N_{i,oct} (-1 -2) h$	3.159	6.874	4.943	1.784	1.932
$N_{i,oct} (0 -1) h$	<u>3.102</u>	5.795	4.497	1.395	1.298
$N_{i,split} (-1 0) e$	0.136	<u>2.307</u>	1.526	1.390	0.781
$N_{i,split} (0 +1) e$	-2.345	3.459	1.933	4.278	1.526
$N_{i,split} (+1 +2) e$	1.301	5.169	3.408	2.107	1.761
$N_{i,split} (+2 +3) e$	1.235	6.028	3.837	2.602	2.191
$N_{i,split} (0 -1) h$	3.893	6.064	4.674	0.781	1.390
$N_{i,split} (+1 0) h$	<u>2.741</u>	8.545	4.267	1.526	4.278
$N_{i,split} (+2 +1) h$	1.031	4.899	2.792	1.761	2.107
$N_{i,split} (+3 +2) h$	0.172	4.965	2.363	2.191	2.602



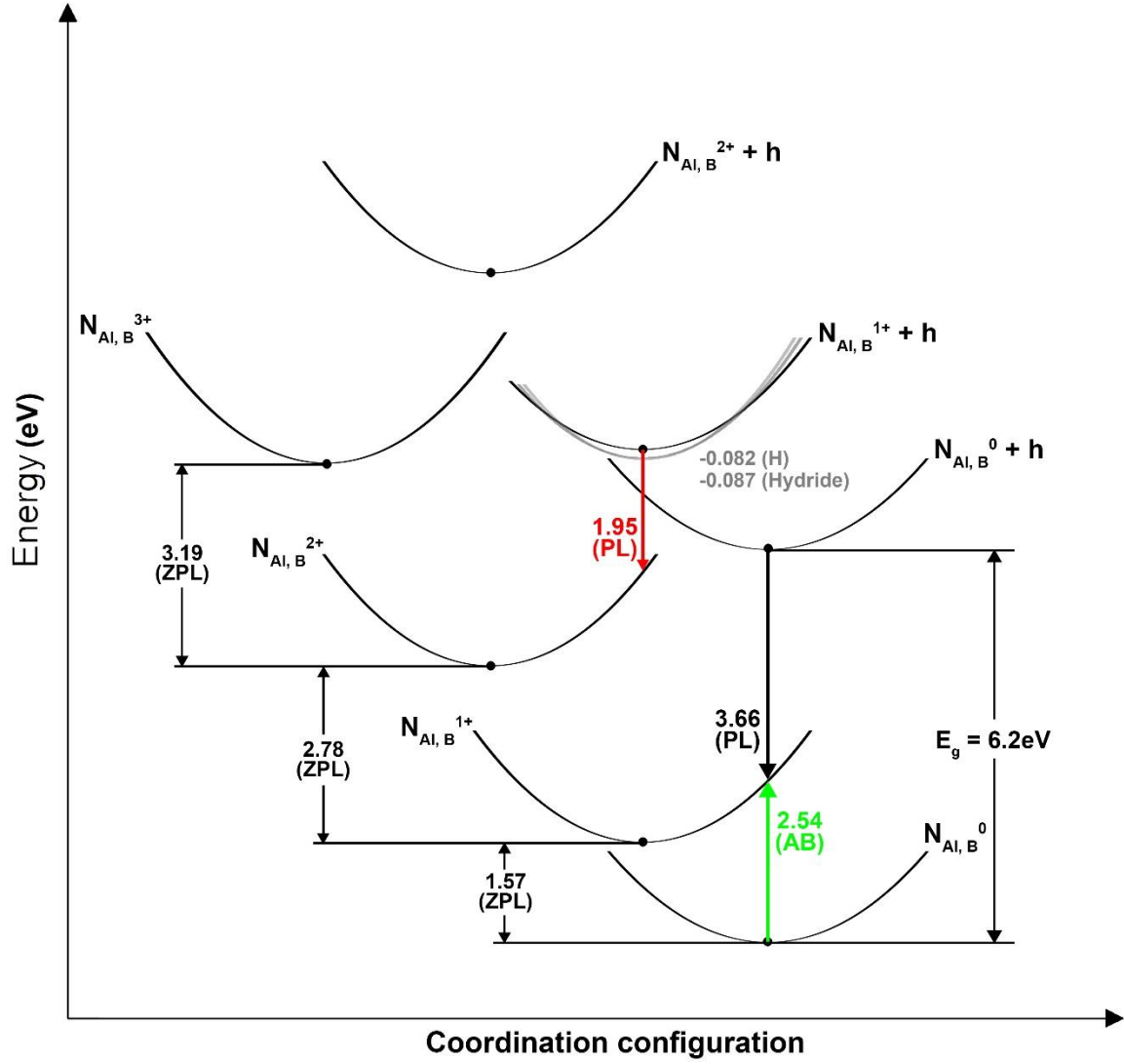


**Figure 6.27** Configuration-coordinate diagram for  $N_{Al,B}$  using BB1K functional. The coloured vertical arrows indicate the optical transitions of visible light. The grey curves are the diffuse states of corresponding compact defect states.



**Table 6.31** Ionization energies of  $N_{Al,A}$  and  $N_{Al,B}$  in all charge states using B97-2 and BB1K functional. The underlined values are the energies falling in the visible light range (1.6-3.1 eV).

Defect States	$E_{PL}$	$E_{ab}$	$E_{ZPL}$	$E_{rel}$	$E_{rel}^*$
<b>B97-2</b>					
$N_{Al,A} (-3 -2) e$	-3.144	-1.280	-2.213	0.931	0.933
$N_{Al,A} (-2 -1) e$	0.357	3.459	1.993	1.636	1.466
$N_{Al,A} (-1 0) e$	1.128	3.216	2.226	1.098	0.990
$N_{Al,A} (0 +1) e$	<u>2.485</u>	3.944	3.229	0.745	0.715
$N_{Al,A} (-2 -3) h$	7.480	9.344	8.413	0.933	0.931
$N_{Al,A} (-1 -2) h$	<u>2.741</u>	5.843	4.207	1.466	1.636
$N_{Al,A} (0 -1) h$	<u>2.984</u>	5.072	3.974	0.990	1.098
$N_{Al,A} (+1 0) h$	<u>2.256</u>	3.715	2.971	0.715	0.745
$N_{Al,B} (0 +1) e$	1.304	<u>3.002</u>	2.194	0.890	0.808
$N_{Al,B} (+1 +2) e$	<u>1.894</u>	4.444	3.224	1.330	1.220
$N_{Al,B} (+2 +3) e$	<u>1.990</u>	5.402	3.649	1.659	1.753
$N_{Al,B} (+1 0) h$	3.198	4.896	4.006	1.036	1.049
$N_{Al,B} (+2 +1) h$	<u>1.756</u>	4.306	2.976	1.260	2.234
$N_{Al,B} (+3 +2) h$	0.798	4.210	2.551	0.000	0.000
<b>BB1K</b>					
$N_{Al,A} (-3 -2) e$	-3.968	-0.116	-2.584	1.385	2.468
$N_{Al,A} (-2 -1) e$	0.422	3.348	1.680	1.258	1.668
$N_{Al,A} (-1 0) e$	0.364	4.419	1.892	1.528	2.527
$N_{Al,A} (0 +1) e$	1.419	3.534	2.565	1.146	0.968
$N_{Al,A} (-2 -3) h$	6.316	10.168	8.784	2.468	1.385
$N_{Al,A} (-1 -2) h$	<u>2.852</u>	5.778	4.520	1.668	1.258
$N_{Al,A} (0 -1) h$	<u>1.781</u>	5.836	4.308	2.527	1.528
$N_{Al,A} (+1 0) h$	<u>2.666</u>	4.781	3.635	0.968	1.146
$N_{Al,B} (0 +1) e$	0.695	<u>2.536</u>	1.570	0.875	0.966
$N_{Al,B} (+1 +2) e$	1.361	4.246	2.781	1.419	1.465
$N_{Al,B} (+2 +3) e$	1.484	4.917	3.192	1.708	1.726
$N_{Al,B} (+1 0) h$	3.664	5.505	4.630	1.237	1.398
$N_{Al,B} (+2 +1) h$	<u>1.954</u>	4.839	3.419	1.557	2.315
$N_{Al,B} (+3 +2) h$	1.283	4.716	3.008	0.000	0.000

## (f) Discussion

In experimental literature reporting optical transitions related to point defects- in undoped AlN, Al and N vacancies are considered most frequently to be responsible for the radiation absorption or emission. Al vacancy has been assigned to multiple photon emission energies. Aleksandrov, et al. proposes the  $V_{Al}(-1|-2)h$  is responsible for the 2 eV PL line by comparing their data with previous computational results<sup>64</sup>. Our calculation finds the PL energy from the  $V_{Al}(-1|-2)h$  transition is 3.06 eV, about 1 eV greater than that in their statement. Our closest PL energy is from  $V_{Al}(+1|0)h$  transition, which is 1.82 eV, within a 10% error (**Figure 6.21**). Sedhain, et al. assigns their 2.78 eV emission to  $V_{Al}(-2|-3)h$  transition<sup>65</sup>, and Yan, et al. confirms their conclusion by using DFT calculation with the HSE06 functional<sup>80</sup>. We find such a transition yields the PL energy of 2.91 eV, and a closer value of 2.83 eV is found from our  $V_{Al}(0|-1)h$  transition. In the same paper by Sedhain, et al.,  $V_{Al}(-3|-2)e$  is assigned to 2.9 – 3.3 eV absorption to the CBM<sup>65</sup>. We calculated 3.29 eV from such transition, and 3.14 eV of absorption energy from the  $V_{Al}(-2|-1)e$  transition, which both are in the range of the experiment.

One of the biggest problems with assignment of particular bands to Al vacancy in previous experimental work is the oxygen contamination of the samples. In the literature, Al vacancies tend to be linked with oxygen substitutional defects ( $O_N$ ) to form defect complexes. The oxygen concentration in the sample used in the report by Sedhain, et al. is measured to be about  $2 \times 10^{18} \text{ cm}^{-3}$ <sup>65</sup>. From our concentration calculation in **Figure 6.20**, Al vacancy concentration is much lower than N vacancy concentration, which implies that oxygen might be playing a key role in forming more Al vacancies in AlN. Our QM/MM investigation on the oxygen impurity will be expanded later in this work.

N vacancy is an important deep-level F-centre type defect in AlN<sup>139,196</sup>. The N vacancy was first assigned to the absorption band at 370 nm (~3.4 eV) as an F-centre defect<sup>139</sup>. Later, two absorption bands in the range of 5.0 – 5.8 eV and 2.7 – 3.5 eV were attributed to the same defect<sup>60,199,216</sup>, and it was proposed that the defect is responsible for the yellow-to-red colour of the as-grown AlN crystal samples. More recently, however, Berzina, et al.<sup>217</sup> have assigned the 415 nm

(~3.0 eV) and 390 nm (~3.2 eV) blue luminescence to the F-centre N vacancy. From our calculation, PL energies of 1.77 eV from  $V_{Al}(+2|+1)h$  transition and 1.86 eV from  $V_{Al}(+1|+2)e$  are found attributed to N vacancy (**Figure 6.22**), which is consistent with the “red” colour light seen in other experiments. For the optical absorption, we found UV band of 4.42 – 5.02 eV as donor (**Table 6.28**). No blue luminescence line is found from our N vacancy calculations.

For Al interstitial, N interstitial, and N antisite defects, there is no experimental assignment of optical transitions to date. From our calculations, all these defects can be strong candidates for deep states responsible for key optical transitions. Purple-to-blue luminescence and absorption can be found from defect process in both types of the N interstitial from 2.74 to 3.16 eV (2.86 - 3.10 eV for absorption) (**Figure 6.24 & 25**). Blue and red luminescence is found for the processes in the N antisite (**Figure 6.26 & 6.27**). Green absorption lines are seen for the processes in  $N_{i,split}(-1|0)e$  (2.31 eV) and  $N_{Al,B}(0|+1)e$  (2.54 eV). For Al interstitial, no visible light emission is found, and one yellow absorption (2.22 eV) is found for the  $Al_i(+1|+2)e$  process.

## 6.5 Conclusion

We present a systematic study of native point defects in AlN using the QM/MM embedded method in Chemshell. Defect formation energies, ionization energies, structures, electron densities, diffuse defect states, electron/hole concentrations are calculated and compared with extensive theoretical and previous experimental results. We found that in N-poor/Al-rich condition, the N vacancy is the most favourable defect, and in N-rich/Al-poor condition, the N vacancy and N split interstitial are both dominant in the material also. Both N vacancy and N split interstitial act as deep donor source. Other deep/shallow donor and acceptor behaviour of each defect is summarised below:

- $V_{Al}$ ,  $N_{i,oct}$  and both  $N_{Al}$  types have deep acceptor level.
- $N_{i,split}$  has deep acceptor level.
- $V_N$  (F-centre defect) and  $Al_i$  have shallow donor level. Therefore, the two defects can be the source of negative charge in AlN.

- $V_{Al}$ ,  $N_{i,oct}$ ,  $N_{i,split}$ ,  $N_{Al,A}$ , and  $N_{Al,B}$  show no preference to the diffuse state in any of their charge states.
- The diffuse states only appear in Al interstitial and N vacancy types of defects, where  $Al_i^0$  and  $V_N^{1-}$  is a possible shallow donor source, and the shallow nature of  $V_N^0$  varies according to the functional used.

Defect processes and ionization transition are also investigated. We can confirm the N-vacancy related purple-to-UV optical absorption band reported in previous experiments. The Al vacancy can also be assigned to many PL energies, but with a different charge transition compared to previous statements. Multiple optical lines have been identified to Al interstitial, N interstitial, and N antisite defect, but they have no experiment result to support.

# Chapter 7

## Summary and Conclusions

As mentioned in **Chapter 1**, the goal of this thesis is to use both MM and QM computational technique to systematically study the defects in wurtzite AlN. We have presented a full picture of all the native point defects in AlN, including Al vacancy, N vacancy, Al interstitial, N interstitial, and N antisite. Relevant properties of all the defects are discussed. We now summarise the main findings of each chapter.

In **Chapter 2** and **Chapter 3**, the structural and many other physical properties of the AlN were introduced. The physical quantities which were discussed in this chapter are the ones, which will be calculated in later chapters. In the last section, the related theory of defects is introduced. In **Chapter 3**, we introduced the theories of all computational techniques used for our calculations, including MM methods, QM methods, optimization techniques, and the QM/MM method.

Our key results and discussions began in **Chapter 4**. In this chapter, new 2-body and 3-body interatomic potential models were developed to predict a broad range of physical properties. We find that the 2-body potential model is inferior to the 3-body model for the off-diagonal elastic constants and bulk modulus, but for the Mott-Littleton defect calculations, the 3-body model can only apply with some additional correction. Therefore, the 2-body interatomic potential is primarily used for the defect energetic and defect migration calculations in **Chapter 5**. The key conclusion can be summarized as following:

- The N split interstitial is the more stable interstitial configuration.
- The formation energy of the Al and N vacancies can be calculated using the Mott-Littleton method. Depending on the electron affinities used for the N species, their formation energies can be very close to other DFT results.

- The Schottky defect complex has the lowest formation energies among all the defect complexes, indicating vacancies are the predominate type of defect in AlN.

In **Chapter 5**, we investigated the migration of native point defects in the AlN crystal lattice, by combining the RFO transition energy search with a steepest descents local minimum search. The migration paths and their activation energies are summarized here:

- For vacancies, the migration along the basal plane is more difficult than towards the axial atom. We argue that this trend is due to different changes in interatomic distances as the vacancies pass through different directions. However, there is no direct comparison to earlier work, but the trend is opposite to that found in a defect migration study of InN.
- For interstitials, we find the barrier for migrating along the axial channel is higher than for migrating via the interstitialcy mechanism. For the Al interstitial, such an interstitialcy mechanism is denoted a “knock-out” process. And for the N interstitial, such an interstitialcy mechanism is named as a “hand-over” process.

After the successful implementation of our new interatomic potential, in **Chapter 6**, the potential was implemented in the embedded QM/MM technique, with the QM DFT calculation as the central region, and the MM interatomic potential as an embedded environment, to investigate the electronic behaviour of charge defects in AlN. The thermodynamic defect formation energies, diffuse state energies, and defect concentrations are calculated. By combining all these results, we can predict the donor and acceptor behaviour of the defects, which are:

- $V_{Ga}$ ,  $N_{i,oct}$  and both  $N_{Ga}$  types have deep acceptor level.
- $N_{i,split}$  has deep acceptor level.
- $V_N$  (F-centre defect) and  $Al_i$  have shallow donor level.

Defect processes are investigated to gain a better understanding of the processes of electron ionization and optical transition. In the last section of Chapter 6, the configuration-coordinate diagrams of all the defects in all charge states are drawn, and we are able to compare our results with thermal and optical electronic transition energies from experiments.

In summary, a high quality interatomic potential model and an embedded cluster QM/MM model for precise defect calculations in AlN have been developed, and a detail study of the native point defects in AlN has been conducted in this work. Admittedly, these topics only represent the beginning. In the future, the same or an improved model can be extended into many other areas. Below, some will be briefly introduced as examples.

It is the most natural to expand the same methodology to studying defects in InN, as the In atom is only one row below the Ga in the periodic table. InN has a similar crystal structure but smaller band gap energy (1.97 eV at room temperature<sup>57</sup>) than AlN and GaN, which means the electron carriers are more easily excited to the conduction band, resulting in higher conductivity. Since the MM and QM/MM models for AlN and GaN are already readily available, by completing the study of InN, the results across three materials can be compared to one another and also to the experimental results. Moreover, one can start to look at the interfaces between any two of the three materials for many research problems such as energy band alignment, defect migration between different materials, etc. However, electrons and holes could be more delocalized compared to the other two nitrides, which might lead to potential problem in the embedded cluster QM/MM method.

Another topic to be explored is the high-spin state of the defect species in AlN. So far, the defects are only discussed at their thermodynamically most stable configuration. Recently, with the interest of quantum computing, computational techniques are applied to investigate the spin splitting effect in wide-band-gap material. This would require the QM interface of the QM/MM code to be able to distinguish and compute the high spin state defects, as the defect formation energy can be very high compared to the ones in low spin states. In **Chapter 6**, our QM/MM calculations have shown the high spin states of N vacancy are more thermodynamically favourable in the band gap, but we are not sure if the calculated energies of other types of defects are reliable in their higher spin states. To gain more accurate energy, the QM code used in this work must be adjusted. One direction is to add spin perturbation, so that the spin splitting states are more precise.

To extend the work directly, one can start to investigate the external impurities in AlN, namely O, C, Si, Mg, etc. In particular, the DX and AX defects in the material. In experiment, all the AlN samples have some degree of the concentrations of impurities. For example, oxygen, silicon, and carbon are the most found elementary impurities in AlN. It has been proved in experiments that these impurities can either form standalone point defects or bind with on-site elements forming defect complexes in the material. These impurity-related defects can also form deep/shallow energy states, additional to the ones assigned to native point defects. Like native point defects, the real behaviour of these impurities in the material is still under debate. We have shown a good agreement to the literature from our QM/MM calculation in **Chapter 6**. The calculations of the impurities and defect complexes enable us to make direct comparison to almost all the experimental results previously. This will be a huge impact to the material science community.



# Appendices

## A.1 GULP input script for physical property prediction

### Two-body interatomic potential:

```
opti conp prop comp
switch rfo gnorm 0.1
cell
3.112375 3.112375 4.982982 90.000000 90.000000 120.000000
fractional
Al core 2/3 1/3 0.50000000 3.00000000 1.00000 0.00000
N core 1/3 2/3 0.3801774 1.39999999 1.00000 0.00000
N shel 1/3 2/3 0.3796817 -4.4000000 1.00000 0.00000
space
P 63 M C
species 3
Al core 3.000000000
N core 1.400000000
N shel -4.400000000
buck4
N shel N shel 22764.3 0.1490 74.000000 3.5 4 5.0 15.0
buck
Al core N shel 1400 0.335 0.0000000 0.00 2.20
poly
1
Al core N shel 0.65 0.0 0.0 0.0 2.2
polynomial
```

5

*Al core N shel* 4639.617234 -9312.716462 &  
 7473.925473 -2992.993370 &  
 597.5182219 -47.55193364 0.0 2.20 2.80

*buck*

*Al core N shel* 640 0.382 0.0000000 2.80 3.30

*poly*

1

*Al core N shel* -0.07 0.0 0.0 2.8 3.3

*polynomial*

5

*Al core N shel* 122628.0146 -180945.3670 &  
 106770.4267 -31492.42111 &  
 4643.112012 -273.7457443 0.0 3.30 3.50

*lenn* 12 6

*Al core N shel* 10.421450 0.0 0.00 10.00

*spring*

*N* 63 50000

*accuracy* 20

*xtol opt* 6

*ftol opt* 8

*gtol opt* 6

*cutd* 6

### Three-body interatomic potential:

```

opti conp prop comp

switch rfo gnorm 0.1

cell

3.10221677 3.10221677 4.98056050 90.00000 90.00000 120.00000

fractional

Al core 2/3 1/3 0.500000000

N core 1/3 2/3 0.379209822

N shel 1/3 2/3 0.378874175

space

P 63 M C

species 3

Al core 3.000000000

N core 1.400000000

N shel -4.400000000

buck4

N shel N shel 22764.3 0.1490 74.000000 3.5 4 5.0 15.0

buck

Al core N shel 1776.7931 0.327033 0.0000000 0.00 2.20

polynomial

5

Al core N shel 2032.034156 -3965.360227 &
3110.779192 -1222.377777 &
240.119941 -18.84126698 0.0 2.20 2.80

buck

Al core N shel 2222.2544 0.327678 0.0000000 2.80 3.30

```

*poly*

1

*Al core N shel 0.35 0.0 0.0 0.0 2.2*

*poly*

1

*Al core N shel -0.07 0.0 0.0 2.8 3.3*

*polynomial*

5

*Al core N shel -16719.2965 24150.45089 &*

*-13939.8929 4019.231689 &*

*-578.87803 33.31894019 0.0 3.30 3.50*

*lenn 12 6*

*Al core N shel 10.421450 0.0 0.00 10.00*

*exp2 regular*

*Al core N shel N shel &*

*-0.144189 4.72633 1.89240 4.72633 1.89240 &*

*0.000 12.000 0.000 12.000 0.000 12.000*

*# The below Buckingham potential correction should be un-hashed while  
conducting the Mott-Littleton defect calculation.*

*# buck*

*# Al core N core 1.8e+14 0.05 0.0 0.00 12.0*

*spring*

*N 63 50000*

*accuracy 20*

*xtol opt 6*

*ftol opt 8*

*gtol opt 6*

*cutd 6*

## A.2 QM/MM basis set

*The basis set is based on the Def2-TZVP basis set. The outermost diffuse orbitals are removed (see Chapter 6).*

**For N atoms:**

*N1 S*

*19730.8006470 0.00021887984991*

*2957.8958745 0.0016960708803*

*673.22133595 0.0087954603538*

*190.68249494 0.035359382605*

*62.295441898 0.11095789217*

*22.654161182 0.24982972552*

*N1 S*

*8.9791477428 0.40623896148*

*3.6863002370 0.24338217176*

*N1 S*

*0.84660076805 1.0000000*

*N1 S*

*0.33647133771 1.0000000*

*N1 S*

*0.13647653675 1.0000000*

*N1 P*

*49.200380510 0.0055552416751*

*11.346790537 0.039318014098*

*3.4273972411 0.14953671029*

*1.1785525134 0.34949305230*

*N1 P*

0.41642204972    0.45843153697

*N1 P*

0.14260826011    0.24428771672

*N1 D*

1.65400000    1.0000000

*N1 D*

0.46900000    1.0000000

**For Al atoms:**

*Al1 S*

37792.5507720    0.00057047888709

5668.0682165    0.0044093016538

1289.8582841    0.022630967411

364.86596028    0.088025644295

118.57631515    0.25223701612

42.024867605    0.45960547169

15.499501629    0.33277886014

*Al1 S*

75.208026598    0.019250560190

23.031408972    0.087906743952

3.6348797649    -0.34246704535

*Al1 S*

1.6065049957    1.5106266058

0.76103394581    0.58071016470

*Al1 S*

0.16556708849    1.0000000

*Al1 S*

0.060041577113    1.0000000

*AI1 P*

452.52303192	0.0023110812466
107.08195049	0.018568641823
34.131021255	0.087216237035
12.587037428	0.26902101523
4.9811919704	0.52128324272

*AI1 P*

2.0070350900	0.60271687494
--------------	---------------

*AI1 P*

0.80083714374	1.00000000
---------------	------------

*AI1 P*

0.20178927472	1.00000000
---------------	------------

*AI1 P*

0.057895550392	1.00000000
----------------	------------

*AI1 D*

1.570000000	1.00000000
-------------	------------

*AI1 D*

0.333000000	1.00000000
-------------	------------

### **A.3 QM/MM ECP**

*bq\_AI2\_e nelec 0*

*bq\_AI2\_e ul*

1	25.000000	-36.000000
2	3.400000	42.600000
2	0.550000	0.450000

*bq\_AI2\_e s*

2	1.000000	0.0000001
---	----------	-----------

## Bibliography

- 1 F. Briegleb and A. Geuther, Ueber das Stickstoffmagnesium und die Affinitäten des Stickgases zu Metallen, *Justus Liebigs Ann. Chem.*, 1862, **123**, 228–241.
- 2 T. Koppe, H. Hofsäss and U. Vetter, Overview of band-edge and defect related luminescence in aluminum nitride, *J. Lumin.*, 2016, **178**, 267–281.
- 3 G. A. Slack, Nonmetallic crystals with high thermal conductivity, *J. Phys. Chem. Solids*, 1973, **34**, 321–335.
- 4 G. A. Slack and S. F. Bartram, Thermal expansion of some diamondlike crystals, *J. Appl. Phys.*, 1975, **46**, 89–98.
- 5 D. Gerlich, S. L. Dole and G. A. Slack, Elastic properties of aluminum nitride, *J. Phys. Chem. Solids*, 1986, **47**, 437–441.
- 6 G. A. Slack, R. A. Tanzilli, R. O. Pohl and J. W. Vandersande, The intrinsic thermal conductivity of AlN, *J. Phys. Chem. Solids*, 1987, **48**, 641–647.
- 7 R. Hahn, V. Glaw, A. Ginolas, M. Töpfer, K. Wittke and H. Reichl, High performance liquid cooled aluminium nitride heat sinks, *Microelectron. Int.*, 1999, **16**, 21–26.
- 8 J. Edwards, K. Kawabe, G. Stevens and R. H. Tredgold, Space charge conduction and electrical behaviour of aluminium nitride single crystals, *Solid State Commun.*, 1965, **3**, 99–100.
- 9 K. Tsubouchi, K. Sugai and N. Mikoshiba, in *1981 Ultrasonics Symposium*, 1981, pp. 375–380.
- 10 G. Bu, D. Ciplys, M. Shur, L. J. Schowalter, S. Schujman and R. Gaska, Electromechanical coupling coefficient for surface acoustic waves in single-crystal bulk aluminum nitride, *Appl. Phys. Lett.*, 2004, **84**, 4611–4613.
- 11 I. Akasaki and M. Hashimoto, Infrared lattice vibration of vapour-grown AlN, *Solid State Commun.*, 1967, **5**, 851–853.
- 12 A. T. Collins, E. C. Lightowers and P. J. Dean, Lattice vibration spectra of aluminum nitride, *Phys. Rev.*, 1967, **158**, 833–838.



- 13 S. Nakamura, M. Senoh and T. Mukai, P-GaN/N-InGaN/N-GaN Double-Heterostructure Blue-Light-Emitting Diodes, *Jpn. J. Appl. Phys.*, 1993, **32**, L8--L11.
- 14 S. Yoshida, S. Misawa and S. Gonda, Properties of  $\text{Al}_x\text{Ga}_{1-x}\text{N}$  films prepared by reactive molecular beam epitaxy, *J. Appl. Phys.*, 1982, **53**, 6844–6848.
- 15 M. Kneissl, T. Y. Seong, J. Han and H. Amano, The emergence and prospects of deep-ultraviolet light-emitting diode technologies, *Nat. Photonics*, 2019, **13**, 233–244.
- 16 J. R. Weber, W. F. Koehl, J. B. Varley, A. Janotti, B. B. Buckley, C. G. de Walle and D. D. Awschalom, Quantum computing with defects, *Proc. Natl. Acad. Sci.*, 2010, **107**, 8513–8518.
- 17 Y. Tu, Z. Tang, X. G. Zhao, Y. Chen, Z. Q. Zhu, J. H. Chu and J. C. Fang, A paramagnetic neutral  $\text{V}_{\text{Al}}\text{O}_{\text{N}}$  center in wurtzite AlN for spin qubit application, *Appl. Phys. Lett.*, 2013, **103**, 72103.
- 18 G. A. Slack and T. F. McNelly, Growth of high purity AlN crystals, *J. Cryst. Growth*, 1976, **34**, 263–279.
- 19 C. Fei, X. Liu, B. Zhu, D. Li, X. Yang, Y. Yang and Q. Zhou, AlN piezoelectric thin films for energy harvesting and acoustic devices, *Nano Energy*, 2018, **51**, 146–161.
- 20 M. A. Signore, G. Rescio, C. De Pascali, V. Iacovacci, P. Dario, A. Leone, F. Quaranta, A. Taurino, P. Siciliano and L. Francioso, Fabrication and characterization of AlN-based flexible piezoelectric pressure sensor integrated into an implantable artificial pancreas, *Sci. Rep.*, 2019, **9**, 17130.
- 21 M. Tinkham, *Group theory and quantum mechanics*, McGraw-Hill, New York, 1964.
- 22 D. L. Rousseau, R. P. Bauman and S. P. S. Porto, Normal mode determination in crystals, *J. Raman Spectrosc.*, 1981, **10**, 253–290.
- 23 L. C. Lew Yan Voon, M. Willatzen, M. Cardona and N. E. Christensen, Terms linear in  $k$  in the band structure of wurtzite-type semiconductors, *Phys. Rev. B*, 1996, **53**, 10703–10714.

- 
- 24 C. A. Arguello, D. L. Rousseau and S. P. S. Porto, First-Order Raman Effect in Wurtzite-Type Crystals, *Phys. Rev.*, 1969, **181**, 1351–1363.
- 25 I. Vurgaftman, J. R. Meyer and L. R. Ram-Mohan, Band parameters for III–V compound semiconductors and their alloys, *J. Appl. Phys.*, 2001, **89**, 5815–5875.
- 26 S. B. Zhang and J. E. Northrup, Chemical potential dependence of defect formation energies in GaAs: Application to Ga self-diffusion, *Phys. Rev. Lett.*, 1991, **67**, 2339–2342.
- 27 J. A. Van Vechten and C. D. Thurmond, Entropy of ionization and temperature variation of ionization levels of defects in semiconductors, *Phys. Rev. B*, 1976, **14**, 3539–3550.
- 28 F. Jensen, *Introduction to computational chemistry*, Wiley, Chichester, UK, 3rd edn., 2017.
- 29 J. D. Gale, GULP: A computer program for the symmetry-adapted simulation of solids, *J. Chem. Soc. Faraday Trans.*, 1997, **93**, 629–637.
- 30 P. P. Ewald, Die Berechnung optischer und elektrostatischer Gitterpotentiale, *Ann. Phys.*, 1921, **369**, 253–287.
- 31 B. G. Dick and A. W. Overhauser, Theory of the Dielectric Constants of Alkali Halide Crystals, *Phys. Rev.*, 1958, **112**, 90–103.
- 32 J. D. Gale, General Utility Lattice Program, [http://gulp.curtin.edu.au/gulp/help/gulp5.0\\_manual.pdf](http://gulp.curtin.edu.au/gulp/help/gulp5.0_manual.pdf), (accessed 13 December 2018).
- 33 P. Hohenberg and W. Kohn, Inhomogeneous Electron Gas, *Phys. Rev.*, 1964, **136**, B864–B871.
- 34 W. Kohn and L. J. Sham, Self-Consistent Equations Including Exchange and Correlation Effects, *Phys. Rev.*, 1965, **140**, A1133–A1138.
- 35 J. P. Perdew, M. Ernzerhof and K. Burke, Rationale for mixing exact exchange with density functional approximations, *J. Chem. Phys.*, 1996, **105**, 9982–9985.

- 36 C. Adamo and V. Barone, Toward reliable density functional methods without adjustable parameters: The PBE0 model, *J. Chem. Phys.*, 1999, **110**, 6158–6170.
- 37 P. J. Wilson, T. J. Bradley and D. J. Tozer, Hybrid exchange-correlation functional determined from thermochemical data and ab initio potentials, *J. Chem. Phys.*, 2001, **115**, 9233–9242.
- 38 A. D. Becke, Density-functional thermochemistry. V. Systematic optimization of exchange-correlation functionals, *J. Chem. Phys.*, 1997, **107**, 8554–8560.
- 39 Y. Zhao, B. J. Lynch and D. G. Truhlar, Development and Assessment of a New Hybrid Density Functional Model for Thermochemical Kinetics, *J. Phys. Chem. A*, 2004, **108**, 2715–2719.
- 40 A. D. Becke, Density-functional exchange-energy approximation with correct asymptotic behavior, *Phys. Rev. A*, 1988, **38**, 3098–3100.
- 41 A. D. Becke, Density - functional thermochemistry. IV. A new dynamical correlation functional and implications for exact - exchange mixing, *J. Chem. Phys.*, 1996, **104**, 1040–1046.
- 42 J. Heyd, G. E. Scuseria and M. Ernzerhof, Hybrid functionals based on a screened Coulomb potential, *J. Chem. Phys.*, 2003, **118**, 8207–8215.
- 43 F. Weigend and R. Ahlrichs, Balanced basis sets of split valence, triple zeta valence and quadruple zeta valence quality for H to Rn: Design and assessment of accuracy, *Phys. Chem. Chem. Phys.*, 2005, **7**, 3297–3305.
- 44 A. Schäfer, C. Huber and R. Ahlrichs, Fully optimized contracted Gaussian basis sets of triple zeta valence quality for atoms Li to Kr, *J. Chem. Phys.*, 1994, **100**, 5829–5835.
- 45 K. Eichkorn, F. Weigend, O. Treutler and R. Ahlrichs, Auxiliary basis sets for main row atoms and transition metals and their use to approximate Coulomb potentials, *Theor. Chem. Acc.*, 1997, **97**, 119–124.
- 46 T. H. Dunning, Gaussian basis sets for use in correlated molecular calculations. I. The atoms boron through neon and hydrogen, *J. Chem. Phys.*, 1989, **90**, 1007–1023.

- 
- 47 P. Sherwood, A. H. de Vries, M. F. Guest, G. Schreckenbach, C. R. A. Catlow, S. A. French, A. A. Sokol, S. T. Bromley, W. Thiel, A. J. Turner, S. Billeter, F. Terstegen, S. Thiel, J. Kendrick, S. C. Rogers, J. Casci, M. Watson, F. King, E. Karlsen, M. Sjøvoll, A. Fahmi, A. Schäfer and C. Lennartz, QUASI: A general purpose implementation of the QM/MM approach and its application to problems in catalysis, *J. Mol. Struct. THEOCHEM*, 2003, **632**, 1–28.
- 48 A. A. Sokol, S. T. Bromley, S. A. French, C. R. A. Catlow and P. Sherwood, Hybrid QM/MM embedding approach for the treatment of localized surface states in ionic materials, *Int. J. Quantum Chem.*, 2004, **99**, 695–712.
- 49 Y. Lu, M. R. Farrow, P. Fayon, A. J. Logsdail, A. A. Sokol, C. R. A. Catlow, P. Sherwood and T. W. Keal, Open-Source, Python-Based Redevelopment of the ChemShell Multiscale QM/MM Environment, *J. Chem. Theory Comput.*, 2019, **15**, 1317–1328.
- 50 J. H. Harding, A. H. Harker, P. B. Keegstra, R. Pandey, J. M. Vail and C. Woodward, Hartree-Fock cluster computations of defect and perfect ionic crystal properties, *Phys. B+C*, 1985, **131**, 151–156.
- 51 A. H. Edwards, P. V Sushko, A. L. Shluger and V. B. Sulimov, Embedding techniques for irradiation-induced defects in crystalline SiO<sub>2</sub>, *IEEE Trans. Nucl. Sci.*, 2002, **49**, 1383–1388.
- 52 J. L. Pascual and L. Seijo, Ab initio model potential embedded cluster calculations including lattice relaxation and polarization: Local distortions on Mn<sup>2+</sup> - doped CaF<sub>2</sub>, *J. Chem. Phys.*, 1995, **102**, 5368–5376.
- 53 J. Kästner, J. M. Carr, T. W. Keal, W. Thiel, A. Wander and P. Sherwood, DL-FIND: An Open-Source Geometry Optimizer for Atomistic Simulations, *J. Phys. Chem. A*, 2009, **113**, 11856–11865.
- 54 W. Jost, Diffusion and Electrolytic Conduction in Crystals (Ionic Semiconductors), *J. Chem. Phys.*, 1933, **1**, 466–475.
- 55 T. Takano, T. Mino, J. Sakai, N. Noguchi, K. Tsubaki and H. Hirayama, Deep-ultraviolet light-emitting diodes with external quantum efficiency higher than 20% at 275 nm achieved by improving light-extraction efficiency, *Appl. Phys. Express*, 2017, **10**, 31002.

- 
- 56 Y. Taniyasu, M. Kasu and T. Makimoto, An aluminium nitride light-emitting diode with a wavelength of 210 nanometres, *Nature*, 2006, **441**, 325–328.
- 57 Q. Guo and A. Yoshida, Temperature Dependence of Band Gap Change in InN and AlN, *Jpn. J. Appl. Phys.*, 1994, **33**, 2453–2456.
- 58 P. B. Perry and R. F. Rutz, The optical absorption edge of single - crystal AlN prepared by a close - spaced vapor process, *Appl. Phys. Lett.*, 1978, **33**, 319–321.
- 59 E. Kuokstis, J. Zhang, Q. Fareed, J. W. Yang, G. Simin, M. A. Khan, R. Gaska, M. Shur, C. Rojo and L. Schowalter, Near-band-edge photoluminescence of wurtzite-type AlN, *Appl. Phys. Lett.*, 2002, **81**, 2755–2757.
- 60 S. M. Evans, N. C. Giles, L. E. Halliburton, G. A. Slack, S. B. Schujman and L. J. Schowalter, Electron paramagnetic resonance of a donor in aluminum nitride crystals, *Appl. Phys. Lett.*, 2006, **88**, 62112.
- 61 N. T. Son, A. Gali, Á. Szabó, M. Bickermann, T. Ohshima, J. Isoya and E. Janzén, Defects at nitrogen site in electron-irradiated AlN, *Appl. Phys. Lett.*, 2011, **98**, 242116.
- 62 M. Lamprecht, V. N. Jmerik, R. Collazo, Z. Sitar, S. V Ivanov and K. Thonke, Model for the deep defect-related emission bands between 1.4 and 2.4 eV in AlN, *Phys. status solidi*, 2017, **254**, 1600714.
- 63 G. Liu, C. Yan, G. Zhou, J. Wen, Z. Qin, Q. Zhou, B. Li, R. Zheng, H. Wu and Z. Sun, Broadband White-Light Emission from Alumina Nitride Bulk Single Crystals, *ACS Photonics*, 2018, **5**, 4009–4013.
- 64 I. A. Aleksandrov, V. G. Mansurov, V. F. Plyusnin and K. S. Zhuravlev, Time-resolved photoluminescence characterization of 2 eV band in AlN, *Phys. status solidi c*, 2015, **12**, 353–356.
- 65 A. Sedhain, L. Du, J. H. Edgar, J. Y. Lin and H. X. Jiang, The origin of 2.78 eV emission and yellow coloration in bulk AlN substrates, *Appl. Phys. Lett.*, 2009, **95**, 262104.
- 66 S. Tojo, R. Yamamoto, R. Tanaka, Q. T. Thieu, R. Togashi, T. Nagashima, T. Kinoshita, R. Dalmau, R. Schlessner, H. Murakami, R. Collazo, A. Koukitu, B.

- Monemar, Z. Sitar and Y. Kumagai, Influence of high-temperature processing on the surface properties of bulk AlN substrates, *J. Cryst. Growth*, 2016, **446**, 33–38.
- 67 J.-M. Mäki, I. Makkonen, F. Tuomisto, A. Karjalainen, S. Suihkonen, J. Räisänen, T. Y. Chemekova and Y. N. Makarov, Identification of the  $V_{\text{Al}}\text{-O}_{\text{N}}$  defect complex in AlN single crystals, *Phys. Rev. B*, 2011, **84**, 81204.
- 68 J. S. Harris, J. N. Baker, B. E. Gaddy, I. Bryan, Z. Bryan, K. J. Mirrieles, P. Reddy, R. Collazo, Z. Sitar and D. L. Irving, On compensation in Si-doped AlN, *Appl. Phys. Lett.*, 2018, **112**, 152101.
- 69 S. Ichikawa, M. Funato and Y. Kawakami, Dominant Nonradiative Recombination Paths and Their Activation Processes in  $\text{Al}_x\text{Ga}_{1-x}\text{N}$ -related Materials, *Phys. Rev. Appl.*, 2018, **10**, 64027.
- 70 D. Alden, J. S. Harris, Z. Bryan, J. N. Baker, P. Reddy, S. Mita, G. Callsen, A. Hoffmann, D. L. Irving, R. Collazo and Z. Sitar, Point-Defect Nature of the Ultraviolet Absorption Band in AlN, *Phys. Rev. Appl.*, 2018, **9**, 54036.
- 71 B. E. Gaddy, Z. Bryan, I. Bryan, R. Kirste, J. Xie, R. Dalmau, B. Moody, Y. Kumagai, T. Nagashima, Y. Kubota, T. Kinoshita, A. Koukitu, Z. Sitar, R. Collazo and D. L. Irving, Vacancy compensation and related donor-acceptor pair recombination in bulk AlN, *Appl. Phys. Lett.*, 2013, **103**, 161901.
- 72 Y. Xue, H. Wang, N. Xie, Q. Yang, F. Xu, B. Shen, J. Shi, D. Jiang, X. Dou, T. Yu and B. Sun, Single-Photon Emission from Point Defects in Aluminum Nitride Films, *J. Phys. Chem. Lett.*, 2020, **11**, 2689–2694.
- 73 R. Collazo, J. Xie, B. E. Gaddy, Z. Bryan, R. Kirste, M. Hoffmann, R. Dalmau, B. Moody, Y. Kumagai, T. Nagashima, Y. Kubota, T. Kinoshita, A. Koukitu, D. L. Irving and Z. Sitar, On the origin of the 265 nm absorption band in AlN bulk crystals, *Appl. Phys. Lett.*, 2012, **100**, 191914.
- 74 T. Mattila and R. M. Nieminen, Point-defect complexes and broadband luminescence in GaN and AlN, *Phys. Rev. B*, 1997, **55**, 9571–9576.
- 75 I. Gorczyca, A. Svane and N. E. Christensen, Theory of point defects in GaN, AlN, and BN: Relaxation and pressure effects, *Phys. Rev. B*, 1999, **60**, 8147–8157.

- 
- 76 C. Stampfl and C. G. Van de Walle, Theoretical investigation of native defects, impurities, and complexes in aluminum nitride, *Phys. Rev. B*, 2002, **65**, 155212.
- 77 K. Laaksonen, M. G. Ganchenkova and R. M. Nieminen, Vacancies in wurtzite GaN and AlN, *J. Phys. Condens. Matter*, 2009, **21**, 15803.
- 78 C. G. Van de Walle and J. Neugebauer, First-principles calculations for defects and impurities: Applications to III-nitrides, *J. Appl. Phys.*, 2004, **95**, 3851–3879.
- 79 M. A. Caro, S. Schulz and E. P. O'Reilly, Hybrid functional study of the elastic and structural properties of wurtzite and zinc-blende group-III nitrides, *Phys. Rev. B*, 2012, **86**, 14117.
- 80 Q. Yan, A. Janotti, M. Scheffler and C. G. Van de Walle, Origins of optical absorption and emission lines in AlN, *Appl. Phys. Lett.*, 2014, **105**, 111104.
- 81 Y. Gao, D. Sun, X. Jiang and J. Zhao, Point defects in group III nitrides: A comparative first-principles study, *J. Appl. Phys.*, 2019, **125**, 215705.
- 82 A. Walsh, C. R. A. Catlow, A. A. Sokol and S. M. Woodley, Physical Properties, Intrinsic Defects, and Phase Stability of Indium Sesquioxide, *Chem. Mater.*, 2009, **21**, 4962–4969.
- 83 Q. Hou, J. Buckeridge, T. Lazauskas, D. Mora-Fonz, A. A. Sokol, S. M. Woodley and C. R. A. Catlow, Defect formation in  $\text{In}_2\text{O}_3$  and  $\text{SnO}_2$ : a new atomistic approach based on accurate lattice energies, *J. Mater. Chem. C*, 2018, **6**, 12386–12395.
- 84 A. Walsh, S. M. Woodley, C. R. A. Catlow and A. A. Sokol, Potential energy landscapes for anion Frenkel-pair formation in ceria and india, *Solid State Ionics*, 2011, **184**, 52–56.
- 85 A. N. Cormack, Intrinsic Disorder in Aluminum Nitride, *J. Am. Ceram. Soc.*, 1989, **72**, 1730–1732.
- 86 J. A. Chisholm, D. W. Lewis and P. D. Bristowe, Classical simulations of the properties of group-III nitrides, *J. Phys. Condens. Matter*, 1999, **11**, L235--L239.
- 87 F. Benkabou, H. Aourag, P. J. Becker and M. Certier, Molecular Dynamics Study of Zinc-Blende GaN, AlN and InN, *Mol. Simul.*, 2000, **23**, 327–341.

- 
- 88 F. Benkabou, M. Certier and H. Aourag, Elastic Properties of Zinc-blende GaN, AlN and InN from Molecular Dynamics, *Mol. Simul.*, 2003, **29**, 201–209.
- 89 S. Goumri-Said, M. B. Kanoun, A. E. Merad, G. Merad and H. Aourag, Prediction of structural and thermodynamic properties of zinc-blende AlN: molecular dynamics simulation, *Chem. Phys.*, 2004, **302**, 135–141.
- 90 D. Powell, M. A. Migliorato and A. G. Cullis, Optimized Tersoff potential parameters for tetrahedrally bonded III-V semiconductors, *Phys. Rev. B*, 2007, **75**, 115202.
- 91 J. Kioseoglou, P. Komninou and T. Karakostas, Interatomic potential calculations of III(Al, In)–N planar defects with a III-species environment approach, *Phys. status solidi*, 2008, **245**, 1118–1124.
- 92 M. Tungare, Y. Shi, N. Tripathi, P. Suvarna and F. (Shadi) Shahedipour-Sandvik, A Tersoff-based interatomic potential for wurtzite AlN, *Phys. status solidi*, 2011, **208**, 1569–1572.
- 93 P. Vashishta, R. K. Kalia, A. Nakano and J. P. Rino, Interaction potential for aluminum nitride: A molecular dynamics study of mechanical and thermal properties of crystalline and amorphous aluminum nitride, *J. Appl. Phys.*, 2011, **109**, 33514.
- 94 P. Ruterana, B. Barbaray, A. Béré, P. Vermaut, A. Hairie, E. Paumier, G. Nouet, A. Salvador, A. Botchkarev and H. Morkoç, Formation mechanism and relative stability of the  $\{11\bar{2}0\}$  stacking fault atomic configurations in wurtzite (Al,Ga,In) nitrides, *Phys. Rev. B*, 1999, **59**, 15917–15925.
- 95 K. Choudhary, T. Liang, K. Mathew, B. Revard, A. Chernatynskiy, S. R. Phillpot, R. G. Hennig and S. B. Sinnott, Dynamical properties of AlN nanostructures and heterogeneous interfaces predicted using COMB potentials, *Comput. Mater. Sci.*, 2016, **113**, 80–87.
- 96 J. D. Gale and A. L. Rohl, The General Utility Lattice Program (GULP), *Mol. Simul.*, 2003, **29**, 291–341.
- 97 M. Born and K. Huang, *Dynamical Theory of Crystal Lattices*, Oxford University Press, Oxford, Revised., 1998.



- 
- 98 G. V Lewis and C. R. A. Catlow, Potential models for ionic oxides, *J. Phys. C Solid State Phys.*, 1985, **18**, 1149–1161.
- 99 N. C. Pyper and A. D. Buckingham, Relativistic AB Initio calculations of the properties of ionic solids, *Philos. Trans. R. Soc. London. Ser. A, Math. Phys. Sci.*, 1986, **320**, 107–158.
- 100 J. C. Slater and J. G. Kirkwood, The Van Der Waals Forces in Gases, *Phys. Rev.*, 1931, **37**, 682–697.
- 101 M. Miskufova, University College of London, 2011.
- 102 M. Schwoerer-Böhning, A. T. Macrander, M. Pabst and P. Pavone, Phonons in Wurtzite Aluminum Nitride, *Phys. status solidi*, 1999, **215**, 177–180.
- 103 V. Y. Davydov, Y. E. Kitaev, I. N. Goncharuk, A. N. Smirnov, J. Graul, O. Semchinova, D. Uffmann, M. B. Smirnov, A. P. Mirgorodsky and R. A. Evarestov, Phonon dispersion and Raman scattering in hexagonal GaN and AlN, *Phys. Rev. B*, 1998, **58**, 12899–12907.
- 104 H. Schulz and K. H. Thiemann, Crystal structure refinement of AlN and GaN, *Solid State Commun.*, 1977, **23**, 815–819.
- 105 L. E. Mcneil, C. Hill, N. Carolina and R. H. French, Vibrational Spectroscopy of Aluminum Nitride, *J. Am. Ceram. Soc.*, 1993, **76**, 1132–1136.
- 106 G. Bu, D. Ciplys, M. Shur, L. J. Schowalter, S. Schujman and R. Gaska, Surface acoustic wave velocity in single-crystal AlN substrates, *IEEE Trans. Ultrason. Ferroelectr. Freq. Control*, 2006, **53**, 251–254.
- 107 M. E. Levinshtein, S. L. Rumyantsev, M. Shur, V. Bougrov and A. Zubrilov, *Properties of Advanced Semiconductor Materials: GaN, AlN, InN, BN, SiC, SiGe*, John Wiley Sons Inc, New York, 1st edn., 2001.
- 108 L. Xinjiao, X. Zechuan, H. Ziyu, C. Huazhe, S. Wuda, C. Zhongcai, Z. Feng and W. Enguang, On the properties of AlN thin films grown by low temperature reactive r.f. sputtering, *Thin Solid Films*, 1986, **139**, 261–274.
- 109 A. F. Wright, Elastic properties of zinc-blende and wurtzite AlN, GaN, and InN, *J. Appl. Phys.*, 1997, **82**, 2833–2839.

- 
- 110 I. A. Aleksandrov and K. S. Zhuravlev, Luminescence line shapes of band to deep centre and donor–acceptor transitions in AlN, *J. Phys. Condens. Matter*, 2020, **32**, 435501.
- 111 A. Zoroddu, F. Bernardini, P. Ruggerone and V. Fiorentini, First-principles prediction of structure, energetics, formation enthalpy, elastic constants, polarization, and piezoelectric constants of AlN, GaN, and InN: Comparison of local and gradient-corrected density-functional theory, *Phys. Rev. B*, 2001, **64**, 45208.
- 112 I. Supryadkina, K. Abgaryan, D. Bazhanov and I. Mutigullin, Ab initio study of macroscopic polarization of AlN, GaN and AlGaIn, *Phys. status solidi c*, 2014, **11**, 307–311.
- 113 N. F. Mott and M. J. Littleton, Conduction in polar crystals. I. Electrolytic conduction in solid salts, *Trans. Faraday Soc.*, 1938, **34**, 485–499.
- 114 S. Limpijumnong and C. G. Van de Walle, Diffusivity of native defects in GaN, *Phys. Rev. B*, 2004, **69**, 35207.
- 115 A. Szállás, K. Szász, X. T. Trinh, N. T. Son, E. Janzén and A. Gali, Characterization of the nitrogen split interstitial defect in wurtzite aluminum nitride using density functional theory, *J. Appl. Phys.*, 2014, **116**, 113702.
- 116 C. I. Wu and A. Kahn, Electronic states at aluminum nitride (0001)-1×1 surfaces, *Appl. Phys. Lett.*, 1999, **74**, 546–548.
- 117 S. P. Grabowski, M. Schneider, H. Nienhaus, W. Mönch, R. Dimitrov, O. Ambacher and M. Stutzmann, Electron affinity of Al<sub>x</sub>Ga<sub>1-x</sub>N(0001) surfaces, *Appl. Phys. Lett.*, 2001, **78**, 2503–2505.
- 118 M. Mishra, S. Krishna, N. Aggarwal and G. Gupta, Influence of metallic surface states on electron affinity of epitaxial AlN films, *Appl. Surf. Sci.*, 2017, **407**, 255–259.
- 119 J. R. Rumble, *CRC Handbook of Chemistry and Physics*, CRC Press/Taylor & Francis, Boca Raton, FL, USA, 102nd edn., 2020.
- 120 A. Fara, F. Bernardini and V. Fiorentini, Theoretical evidence for the semi-insulating character of AlN, *J. Appl. Phys.*, 1999, **85**, 2001–2003.

- 
- 121 D. F. Hevia, C. Stampfl, F. Viñes and F. Illas, Microscopic origin of n-type behavior in Si-doped AlN, *Phys. Rev. B*, 2013, **88**, 85202.
- 122 M. Sterntzke and G. Müller, EELS Study of Oxygen Diffusion in Aluminum Nitride, *J. Am. Ceram. Soc.*, 1994, **77**, 737–742.
- 123 E. N. Mokhov, M. K. Rabchinskiy, S. S. Nagalyuk, M. R. Gafurov and O. P. Kazarova, Effect of the Beryllium Acceptor Impurity upon the Optical Properties of Single-Crystal AlN, *Semiconductors*, 2020, **54**, 278–281.
- 124 S. S. Dohyung Kim, Heesub Lee, Yoshiki Naoi, High Temperature Diffusion in  $\text{Al}_x\text{Ga}_{1-x}\text{N}$  and P-Type AlGaN by  $\text{Al}_4\text{C}_3$ , *Int. J. Mater. Sci. Appl.*, 2014, **3**, 177–182.
- 125 M. G. Ganchenkova and R. M. Nieminen, Nitrogen Vacancies as Major Point Defects in Gallium Nitride, *Phys. Rev. Lett.*, 2006, **96**, 196402.
- 126 K. H. Warnick, Y. Puzyrev, T. Roy, D. M. Fleetwood, R. D. Schrimpf and S. T. Pantelides, Room-temperature diffusive phenomena in semiconductors: The case of AlGaIn, *Phys. Rev. B*, 2011, **84**, 214109.
- 127 A. Kyrtos, M. Matsubara and E. Bellotti, Migration mechanisms and diffusion barriers of carbon and native point defects in GaN, *Phys. Rev. B*, 2016, **93**, 245201.
- 128 I. A. Aleksandrov, T. V Malin, K. S. Zhuravlev, S. V Trubina, S. B. Erenburg, B. Pecz and Y. V Lebiadok, Diffusion in GaN/AlN superlattices: DFT and EXAFS study, *Appl. Surf. Sci.*, 2020, **515**, 146001.
- 129 C. G. Van de Walle, S. Limpijumnong and J. Neugebauer, First-principles studies of beryllium doping of GaN, *Phys. Rev. B*, 2001, **63**, 245205.
- 130 R. Hrytsak, P. Kempisty, E. Grzanka, M. Leszczynski and M. Sznajder, DFT study on point defects migration through the pseudomorphic and lattice-matched InN/GaN interfaces, *Comput. Mater. Sci.*, 2021, **186**, 110039.
- 131 T. Koyama, M. Sugawara, T. Hoshi, A. Uedono, J. F. Kaeding, R. Sharma, S. Nakamura and S. F. Chichibu, Relation between Al vacancies and deep emission bands in AlN epitaxial films grown by  $\text{NH}_3$ -source molecular beam epitaxy, *Appl. Phys. Lett.*, 2007, **90**, 241914.

- 
- 132 T. Hoshi, T. Koyama, M. Sugawara, A. Uedono, J. F. Kaeding, R. Sharma, S. Nakamura and S. F. Chichibu, Correlation between the violet luminescence intensity and defect density in AlN epilayers grown by ammonia-source molecular beam epitaxy, *Phys. status solidi c*, 2008, **5**, 2129–2132.
- 133 B. Bastek, F. Bertram, J. Christen, T. Hempel, A. Dadgar and A. Krost, Analysis of point defects in AlN epilayers by cathodoluminescence spectroscopy, *Appl. Phys. Lett.*, 2009, **95**, 32106.
- 134 S. F. Chichibu, K. Hazu, Y. Ishikawa, M. Tashiro, T. Ohtomo, K. Furusawa, A. Uedono, S. Mita, J. Xie, R. Collazo and Z. Sitar, Excitonic emission dynamics in homoepitaxial AlN films studied using polarized and spatio-time-resolved cathodoluminescence measurements, *Appl. Phys. Lett.*, 2013, **103**, 142103.
- 135 M. Bickermann, B. M. Epelbaum, O. Filip, P. Heimann, S. Nagata and A. Winnacker, Point defect content and optical transitions in bulk aluminum nitride crystals, *Phys. status solidi*, 2009, **246**, 1181–1183.
- 136 A. Sedhain, J. Y. Lin and H. X. Jiang, Nature of optical transitions involving cation vacancies and complexes in AlN and AlGaIn, *Appl. Phys. Lett.*, 2012, **100**, 221107.
- 137 Q. Hu, S. Tanaka, T. Yoneoka and T. Noda, Study of radiation defects for AlN ceramics under O<sup>+</sup> irradiation, *Nucl. Instruments Methods Phys. Res. Sect. B Beam Interact. with Mater. Atoms*, 2000, **166–167**, 70–74.
- 138 U. Vetter, S. Müller, M. Brötzmann, H. Hofsäss and J. B. Gruber, Effective reduction of AlN defect luminescence by fluorine implantation, *Diam. Relat. Mater.*, 2011, **20**, 782–784.
- 139 K. Atobe, M. Honda, N. Fukuoka, M. Okada and M. Nakagawa, F-Type Centers in Neutron-Irradiated AlN, *Jpn. J. Appl. Phys.*, 1990, **29**, 150–152.
- 140 J. A. Freitas, Optical studies of bulk and homoepitaxial films of III–V nitride semiconductors, *J. Cryst. Growth*, 2005, **281**, 168–182.
- 141 K. B. Nam, M. L. Nakarmi, J. Y. Lin and H. X. Jiang, Deep impurity transitions involving cation vacancies and complexes in AlGaIn alloys, *Appl. Phys. Lett.*, 2005, **86**, 222108.

- 
- 142 N. Nepal, M. L. Nakarmi, J. Y. Lin and H. X. Jiang, Photoluminescence studies of impurity transitions in AlGa<sub>N</sub> alloys, *Appl. Phys. Lett.*, 2006, **89**, 92107.
- 143 S. Bellucci, A. I. Popov, C. Balasubramanian, G. Cinque, A. Marcelli, I. Karbovnyk, V. Savchyn and N. Krutyak, Luminescence, vibrational and XANES studies of AlN nanomaterials, *Radiat. Meas.*, 2007, **42**, 708–711.
- 144 A. Sedhain, N. Nepal, M. L. Nakarmi, T. M. Al tahtamouni, J. Y. Lin, H. X. Jiang, Z. Gu and J. H. Edgar, Photoluminescence properties of AlN homoepilayers with different orientations, *Appl. Phys. Lett.*, 2008, **93**, 41905.
- 145 A. Uedono, S. Ishibashi, S. Keller, C. Moe, P. Cantu, T. M. Katona, D. S. Kamber, Y. Wu, E. Letts, S. A. Newman, S. Nakamura, J. S. Speck, U. K. Mishra, S. P. DenBaars, T. Onuma and S. F. Chichibu, Vacancy-oxygen complexes and their optical properties in AlN epitaxial films studied by positron annihilation, *J. Appl. Phys.*, 2009, **105**, 54501.
- 146 I. A. Weinstein, A. S. Vokhmintsev and D. M. Spiridonov, Thermoluminescence kinetics of oxygen-related centers in AlN single crystals, *Diam. Relat. Mater.*, 2012, **25**, 59–62.
- 147 L. Shen, N. Wang and X. Xiao, Strong orange luminescence from AlN whiskers, *Mater. Lett.*, 2013, **94**, 150–153.
- 148 Z. Wu, W. Zhang, H. Hu, S. Zuo, F. Wang, P. Yan, J. Wang, R. Zhuo and D. Yan, Effect of temperature on growth and ultraviolet photoluminescence of Zn doped AlN nanostructures, *Mater. Lett.*, 2014, **136**, 95–98.
- 149 W.-Y. Wang, P. Jin, G.-P. Liu, W. Li, B. Liu, X.-F. Liu and Z.-G. Wang, Effect of high-temperature annealing on AlN thin film grown by metalorganic chemical vapor deposition, *Chinese Phys. B*, 2014, **23**, 87810.
- 150 J. Pastrňák, S. Pačesová and L. Roskovcová, Luminescent properties of the oxygen impurity centres in AlN, *Czechoslov. J. Phys. B*, 1974, **24**, 1149–1161.
- 151 R. A. Youngman and J. H. Harris, Luminescence Studies of Oxygen-Related Defects In Aluminum Nitride, *J. Am. Ceram. Soc.*, 1990, **73**, 3238–3246.
- 152 M. Benabdesselam, P. Iacconi, D. Lapraz, P. Grosseau and B. Guilhot, Thermoluminescence of AlN - Influence of Synthesis Processes, *J. Phys. Chem.*, 1995, **99**, 10319–10323.

- 
- 153 Q. Hu, S. Tanaka, T. Yoneoka and V. Grismanovs, In-situ luminescence measurement for AlN ceramics under reactor irradiation, *Radiat. Eff. Defects Solids*, 1999, **147**, 283–292.
- 154 S. Schweizer, U. Rogulis, J.-M. Spaeth, L. Trinkler and B. Berzina, Investigation of Oxygen-Related Luminescence Centres in AlN Ceramics, *Phys. status solidi*, 2000, **219**, 171–180.
- 155 Y. G. Cao, X. L. Chen, Y. C. Lan, J. Y. Li, Y. P. Xu, T. Xu, Q. L. Liu and J. K. Liang, Blue emission and Raman scattering spectrum from AlN nanocrystalline powders, *J. Cryst. Growth*, 2000, **213**, 198–202.
- 156 B. Berzina, L. Trinkler, J. Sils and E. Palcevskis, Oxygen-related defects and energy accumulation in aluminum nitride ceramics, *Radiat. Eff. Defects Solids*, 2001, **156**, 241–247.
- 157 A. Dadgar, A. Krost, J. Christen, B. Bastek, F. Bertram, A. Krtischil, T. Hempel, J. Bläsing, U. Haboeck and A. Hoffmann, MOVPE growth of high-quality AlN, *J. Cryst. Growth*, 2006, **297**, 306–310.
- 158 B. E. Gaddy, Z. Bryan, I. Bryan, J. Xie, R. Dalmau, B. Moody, Y. Kumagai, T. Nagashima, Y. Kubota, T. Kinoshita, A. Koukitu, R. Kirste, Z. Sitar, R. Collazo and D. L. Irving, The role of the carbon-silicon complex in eliminating deep ultraviolet absorption in AlN, *Appl. Phys. Lett.*, 2014, **104**, 202106.
- 159 S. Tungasmita, P. O. Å. Persson, L. Hultman and J. Birch, Pulsed low-energy ion-assisted growth of epitaxial aluminum nitride layer on 6H-silicon carbide by reactive magnetron sputtering, *J. Appl. Phys.*, 2002, **91**, 3551–3555.
- 160 X. Tang, F. Hossain, K. Wongchotigul and M. G. Spencer, Near band-edge transition in aluminum nitride thin films grown by metal organic chemical vapor deposition, *Appl. Phys. Lett.*, 1998, **72**, 1501–1503.
- 161 T. Nagashima, Y. Kubota, T. Kinoshita, Y. Kumagai, J. Xie, R. Collazo, H. Murakami, H. Okamoto, A. Koukitu and Z. Sitar, Structural and Optical Properties of Carbon-Doped AlN Substrates Grown by Hydride Vapor Phase Epitaxy Using AlN Substrates Prepared by Physical Vapor Transport, *Appl. Phys. Express*, 2012, **5**, 125501.

- 
- 162 K. Kornitzer, W. Limmer, K. Thonke, R. Sauer, D. G. Ebling, L. Steinke and K. W. Benz, AlN on sapphire and on SiC: CL and Raman study, *J. Cryst. Growth*, 1999, **201–202**, 441–443.
- 163 M. Bickermann, B. M. Epelbaum, O. Filip, B. Tautz, P. Heimann and A. Winnacker, Faceting in AlN bulk crystal growth and its impact on optical properties of the crystals, *Phys. status solidi c*, 2012, **9**, 449–452.
- 164 I. Gorczyca, N. E. Christensen, E. L. Peltzer y Blancá and C. O. Rodriguez, Optical phonon modes in GaN and AlN, *Phys. Rev. B*, 1995, **51**, 11936–11939.
- 165 L. Gordon, J. L. Lyons, A. Janotti and C. G. de Walle, Hybrid functional calculations of DX centers in AlN and GaN, *Phys. Rev. B*, 2014, **89**, 85204.
- 166 P. G. Moses, M. Miao, Q. Yan and C. G. Van de Walle, Hybrid functional investigations of band gaps and band alignments for AlN, GaN, InN, and InGaN, *J. Chem. Phys.*, 2011, **134**, 84703.
- 167 L. Silvestri, K. Dunn, S. Praver and F. Ladouceur, Hybrid functional study of Si and O donors in wurtzite AlN, *Appl. Phys. Lett.*, 2011, **99**, 122109.
- 168 A. Kyrtos, M. Matsubara and E. Bellotti, Band offsets of  $\text{Al}_x\text{Ga}_{1-x}\text{N}$  alloys using first-principles calculations, *J. Phys. Condens. Matter*, 2020, **32**, 365504.
- 169 P. C. Bowes, Y. Wu, J. N. Baker, J. S. Harris and D. L. Irving, Space charge control of point defect spin states in AlN, *Appl. Phys. Lett.*, 2019, **115**, 52101.
- 170 J. B. Varley, A. Janotti and C. G. Van de Walle, Defects in AlN as candidates for solid-state qubits, *Phys. Rev. B*, 2016, **93**, 161201.
- 171 H. Seo, M. Govoni and G. Galli, Design of defect spins in piezoelectric aluminum nitride for solid-state hybrid quantum technologies, *Sci. Rep.*, 2016, **6**, 20803.
- 172 S. Lany and A. Zunger, Assessment of correction methods for the band-gap problem and for finite-size effects in supercell defect calculations: Case studies for ZnO and GaAs, *Phys. Rev. B*, 2008, **78**, 235104.
- 173 J. Buckeridge, C. R. A. Catlow, D. O. Scanlon, T. W. Keal, P. Sherwood, M. Miskufova, A. Walsh, S. M. Woodley and A. A. Sokol, Determination of the

- Nitrogen Vacancy as a Shallow Compensating Center in GaN Doped with Divalent Metals, *Phys. Rev. Lett.*, 2015, **114**, 16405.
- 174 J. Buckeridge, C. R. A. Catlow, M. R. Farrow, A. J. Logsdail, D. O. Scanlon, T. W. Keal, P. Sherwood, S. M. Woodley, A. A. Sokol and A. Walsh, Deep vs shallow nature of oxygen vacancies and consequent n-type carrier concentrations in transparent conducting oxides, *Phys. Rev. Mater.*, 2018, **2**, 54604.
- 175 Q. Hou, J. Buckeridge, A. Walsh, Z. Xie, Y. Lu, T. W. Keal, J. Guan, S. M. Woodley, C. R. A. Catlow and A. A. Sokol, *Front. Chem.*, 2021, **9**, 1102.
- 176 No Title, [https://www.github.com/logsdail/fit\\_my\\_ecp](https://www.github.com/logsdail/fit_my_ecp), (accessed 22 February 2022).
- 177 N. S. Kanhe, A. B. Nawale, R. L. Gawade, V. G. Puranik, S. V. Bhoraskar, A. K. Das and V. L. Mathe, Understanding the growth of micro and nano-crystalline AlN by thermal plasma process, *J. Cryst. Growth*, 2012, **339**, 36–45.
- 178 E. Aprà, E. J. Bylaska, W. A. de Jong, N. Govind, K. Kowalski, T. P. Straatsma, M. Valiev, H. J. J. van Dam, Y. Alexeev, J. Anchell, V. Anisimov, F. W. Aquino, R. Atta-Fynn, J. Autschbach, N. P. Bauman, J. C. Becca, D. E. Bernholdt, K. Bhaskaran-Nair, S. Bogatko, P. Borowski, J. Boschen, J. Brabec, A. Bruner, E. Cauët, Y. Chen, G. N. Chuev, C. J. Cramer, J. Daily, M. J. O. Deegan, T. H. Dunning, M. Dupuis, K. G. Dylla, G. I. Fann, S. A. Fischer, A. Fonari, H. Früchtl, L. Gagliardi, J. Garza, N. Gawande, S. Ghosh, K. Glaesemann, A. W. Götz, J. Hammond, V. Helms, E. D. Hermes, K. Hirao, S. Hirata, M. Jacquelin, L. Jensen, B. G. Johnson, H. Jónsson, R. A. Kendall, M. Klemm, R. Kobayashi, V. Konkov, S. Krishnamoorthy, M. Krishnan, Z. Lin, R. D. Lins, R. J. Littlefield, A. J. Logsdail, K. Lopata, W. Ma, A. V. Marenich, J. Martin del Campo, D. Mejia-Rodriguez, J. E. Moore, J. M. Mullin, T. Nakajima, D. R. Nascimento, J. A. Nichols, P. J. Nichols, J. Nieplocha, A. Otero-de-la-Roza, B. Palmer, A. Panyala, T. Pirojsirikul, B. Peng, R. Peverati, J. Pittner, L. Pollack, R. M. Richard, P. Sadayappan, G. C. Schatz, W. A. Shelton, D. W. Silverstein, D. M. A. Smith, T. A. Soares, D. Song, M. Swart, H. L. Taylor, G. S. Thomas, V. Tipparaju, D. G. Truhlar, K. Tsemekhman, T. Van Voorhis, Á. Vázquez-Mayagoitia, P. Verma, O. Villa, A. Vishnu, K. D. Vogiatzis, D. Wang, J. H.



- Weare, M. J. Williamson, T. L. Windus, K. Woliński, A. T. Wong, Q. Wu, C. Yang, Q. Yu, M. Zacharias, Z. Zhang, Y. Zhao and R. J. Harrison, NWChem: Past, present, and future, *J. Chem. Phys.*, 2020, **152**, 184102.
- 179 M. F. Guest, I. J. Bush, H. J. J. Van Dam, P. Sherwood, J. M. H. Thomas, J. H. Van Lenthe, R. W. A. Havenith and J. Kendrick, The GAMESS-UK electronic structure package: algorithms, developments and applications, *Mol. Phys.*, 2005, **103**, 719–747.
- 180 Z. Xie, Y. Sui, J. Buckeridge, C. R. A. Catlow, T. W. Keal, P. Sherwood, A. Walsh, D. O. Scanlon, S. M. Woodley and A. A. Sokol, Demonstration of the donor characteristics of Si and O defects in GaN using hybrid QM/MM, *Phys. status solidi*, 2017, **214**, 1600445.
- 181 Z. Xie, Y. Sui, J. Buckeridge, C. R. A. Catlow, T. W. Keal, P. Sherwood, A. Walsh, M. R. Farrow, D. O. Scanlon, S. M. Woodley and A. A. Sokol, Donor and acceptor characteristics of native point defects in GaN, *J. Phys. D. Appl. Phys.*, 2019, **52**, 335104.
- 182 A. A. Sokol, S. A. French, S. T. Bromley, C. R. A. Catlow, H. J. J. van Dam and P. Sherwood, Point defects in ZnO, *Faraday Discuss.*, 2007, **134**, 267–282.
- 183 D. J. Wilson, A. A. Sokol, S. A. French and C. R. A. Catlow, The Role of Defects in Photographic Latent Image Formation, *MRS Proc.*, 2004, **848**, FF7.6.
- 184 C. R. A. Catlow, A. A. Sokol and A. Walsh, Microscopic origins of electron and hole stability in ZnO, *Chem. Commun.*, 2011, **47**, 3386–3388.
- 185 A. J. Logsdail, C. A. Downing, T. W. Keal, P. Sherwood, A. A. Sokol and C. R. A. Catlow, Modelling the chemistry of Mn-doped MgO for bulk and (100) surfaces, *Phys. Chem. Chem. Phys.*, 2016, **18**, 28648–28660.
- 186 CRC Handbook, *CRC Handbook of Chemistry and Physics*, CRC Press/Taylor & Francis, Boca Raton, FL, USA, 102nd edn., 2021.
- 187 M. S. Miao, A. Janotti and C. G. Van De Walle, Reconstructions and origin of surface states on AlN polar and nonpolar surfaces, *Phys. Rev. B - Condens. Matter Mater. Phys.*, 2009, **80**, 1–9.

- 
- 188 P. Strak, P. Kempisty, K. Sakowski and S. Krukowski, Ab initio determination of electron affinity of polar nitride surfaces, clean and under Cs coverage, *J. Vac. Sci. Technol. A*, 2017, **35**, 21406.
- 189 C. I. Wu, A. Kahn, E. S. Hellman and D. N. E. Buchanan, Electron affinity at aluminum nitride surfaces, *Appl. Phys. Lett.*, 1998, **73**, 1346–1348.
- 190 C. I. Wu and A. Kahn, Negative electron affinity and electron emission at cesiated GaN and AlN surfaces, *Appl. Surf. Sci.*, 2000, **162–163**, 250–255.
- 191 T. Kozawa, T. Mori, T. Ohwaki, Y. Taga and N. Sawaki, UV Photoemission Study of AlGa<sub>N</sub> Grown by Metalorganic Vapor Phase Epitaxy, *Jpn. J. Appl. Phys.*, 2000, **39**, L772–L774.
- 192 P. Reddy, I. Bryan, Z. Bryan, J. Tweedie, S. Washiyama, R. Kirste, S. Mita, R. Collazo and Z. Sitar, Charge neutrality levels, barrier heights, and band offsets at polar AlGa<sub>N</sub>, *Appl. Phys. Lett.*, 2015, **107**, 91603.
- 193 M. C. Benjamin, C. Wang, R. F. Davis and R. J. Nemanich, Observation of a negative electron affinity for heteroepitaxial AlN on  $\alpha(6H)$  - SiC(0001), *Appl. Phys. Lett.*, 1994, **64**, 3288–3290.
- 194 Y. Zhang, W. Liu and H. Niu, Native defect properties and p-type doping efficiency in group-IIA doped wurtzite AlN, *Phys. Rev. B*, 2008, **77**, 35201.
- 195 P. Boguslawski, E. Briggs, T. A. White, M. G. Wensell and J. Bernholc, Native Defects in Wurtzite GaN And AlN, *MRS Online Proc. Libr.*, 1994, **339**, 693–698.
- 196 S. Nakahata, K. Sogabe, T. Matsuura and A. Yamakawa, Electron Spin Resonance Analysis of Lattice Defects in Polycrystalline Aluminum Nitride, *J. Am. Ceram. Soc.*, 1997, **80**, 1612–1614.
- 197 P. M. Mason, H. Przybylinska, G. D. Watkins, W. J. Choyke and G. A. Slack, Optically detected electron paramagnetic resonance of AlN single crystals, *Phys. Rev. B*, 1999, **59**, 1937–1947.
- 198 V. A. Soltamov, I. V. Ilyin, A. A. Soltamova, E. N. Mokhov and P. G. Baranov, Identification of the deep level defects in AlN single crystals by electron paramagnetic resonance, *J. Appl. Phys.*, 2010, **107**, 113515.

- 
- 199 V. A. Soltamov, I. V. Ilyin, A. A. Soltamova, D. O. Tolmachev, N. G. Romanov, A. S. Gurin, V. A. Khramtsov, E. N. Mokhov, Y. N. Makarov, G. V. Mamin, S. B. Orlinskii and P. G. Baranov, Shallow Donors and Deep-Level Color Centers in Bulk AlN Crystals: EPR, ENDOR, ODMR and Optical Studies, *Appl. Magn. Reson.*, 2013, **44**, 1139–1165.
- 200 S. B. Orlinskii, P. G. Baranov, A. P. Bundakova, M. Bickermann and J. Schmidt, Defects in AlN: High-frequency EPR and ENDOR studies, *Phys. B Condens. Matter*, 2009, **404**, 4873–4876.
- 201 T. Mattila and R. M. Nieminen, Ab initio study of oxygen point defects in GaAs, GaN, and AlN, *Phys. Rev. B*, 1996, **54**, 16676–16682.
- 202 A. M. Stoneham, *Theory of Defects in Solids: Electronic Structure of Defects in Insulators and Semiconductors*, Oxford: Clarendon Press, Oxford, New., 2001.
- 203 K. Kim, W. R. L. Lambrecht, B. Segall and M. van Schilfgaarde, Effective masses and valence-band splittings in GaN and AlN, *Phys. Rev. B*, 1997, **56**, 7363–7375.
- 204 J. Buckeridge, SC-FERMI, <https://github.com/jbuckeridge/sc-fermi>.
- 205 F. H. Taylor, J. Buckeridge and C. R. A. Catlow, Defects and oxide ion migration in the solid oxide fuel cell cathode material LaFeO<sub>3</sub>, *Chem. Mater.*, 2016, **28**, 8210–8220.
- 206 J. Buckeridge, D. Jevdokimovs, C. R. A. Catlow and A. A. Sokol, Nonstoichiometry and Weyl fermionic behavior in TaAs, *Phys. Rev. B*, 2016, **94**, 180101.
- 207 G. Kresse and J. Hafner, Ab initio molecular dynamics for liquid metals, *Phys. Rev. B*, 1993, **47**, 558–561.
- 208 G. Kresse and J. Hafner, Ab initio molecular-dynamics simulation of the liquid-metal--amorphous-semiconductor transition in germanium, *Phys. Rev. B*, 1994, **49**, 14251–14269.
- 209 G. Kresse and J. Furthmüller, Efficiency of ab-initio total energy calculations for metals and semiconductors using a plane-wave basis set, *Comput. Mater. Sci.*, 1996, **6**, 15–50.

- 210 G. Kresse and J. Furthmüller, Efficient iterative schemes for ab initio total-energy calculations using a plane-wave basis set, *Phys. Rev. B*, 1996, **54**, 11169–11186.
- 211 R. Collazo, S. Mita, J. Xie, A. Rice, J. Tweedie, R. Dalmau and Z. Sitar, Progress on n-type doping of AlGa<sub>N</sub> alloys on AlN single crystal substrates for UV optoelectronic applications, *Phys. status solidi c*, 2011, **8**, 2031–2033.
- 212 R. T. Kemerley, H. B. Wallace and M. N. Yoder, Impact of wide bandgap microwave devices on DoD systems, *Proc. IEEE*, 2002, **90**, 1059–1064.
- 213 R. Radhakrishnan Sumathi, Native seeding and silicon doping in bulk growth of AlN single crystals by PVT method, *Phys. status solidi c*, 2014, **11**, 545–548.
- 214 Y. Taniyasu, M. Kasu and T. Makimoto, Electrical conduction properties of n-type Si-doped AlN with high electron mobility ( $>100\text{cm}^2\cdot\text{V}^{-1}\cdot\text{s}^{-1}$ ), *Appl. Phys. Lett.*, 2004, **85**, 4672–4674.
- 215 T. Ive, O. Brandt, H. Kostial, K. J. Friedland, L. Däweritz and K. H. Ploog, Controlled n-type doping of AlN:Si films grown on 6H-SiC(0001) by plasma-assisted molecular beam epitaxy, *Appl. Phys. Lett.*, 2005, **86**, 24106.
- 216 M. Bickermann, B. M. Epelbaum and A. Winnacker, Characterization of bulk AlN with low oxygen content, *J. Cryst. Growth*, 2004, **269**, 432–442.
- 217 B. Berzina, L. Trinkler, V. Korsaks and R. Ruska, Nitrogen vacancy type defect luminescence of AlN nanopowder, *Opt. Mater. (Amst)*, 2020, **108**, 110069.

